Technische Universität München
Fakultät für Informatik

Lehrstuhl für Sensorbasierte Robotersysteme
und Intelligente Assistenzsysteme

Whole-Body Control of Orbital Robots

Alessandro Massimo Giordano

Vollständiger Abdruck der von der Fakultät für Informatik der Technischen Universität München zur Erlangung des akademischen Grades eines Doktors der Naturwisseschaften (Dr. rer. nat.) genehmigten Dissertation.

Vorsitzende(r):

Prof. Dr.-Ing. Matthias Althoff

Prüfer der Dissertation:

1. Prof. Dr.-Ing. Alin Albu-Schäffer
2. Prof. Dr. Kazuya Yoshida

Die Dissertation wurde am 11.05.2020 bei der Technischen Universität München eingereicht und durch die Fakultät für Informatik am 18.09.2020 angenommen.

Preface

This thesis is based on research activity undertaken at the Institute of Robotics and Mechatronics of the German Aerospace Center (DLR). The institute provided a vibrant and stimulating environment, together with the best tools required for conducting top-level robotics research.

I am deeply grateful to Prof. Alin Albu-Schäffer for my enrollment, and, especially, for his enlightened supervision of my research. His passion and his truly scientific mind provided me inspiration, put me on the right track, and were an example of excellence. When talking about excellence, I shall also express my gratitude to Dr. Christian Ott. Our technical discussions were fundamental for the development of the backbone of this research.

I thank the OOS team, with whom I had the pleasure to work. Especially, I thank my colleagues Jordi Artigas, Marco De Stefano, Roberto Lampariello, Hrishik Mishra: each of them teached me something. I further thank the rest of the people of the team who made possible to work with an amazing facility such as the OOS-Sim. I wish to thank Gianluca Garofalo for his initial guidance, and for his very valuable work. I thank also my former student Davide Calzolari for his trust, and for his excellent feedback. Best thanks also to Philipp Stratman and the rest of the TUM team.

I am nothing but another witness of the fascinating interplay between dreams and intelligence, whose name is science. I am thankful to all great minds who created this.

Thanks and love to Nora, for giving me meaning and love. Among other things, it would have been impossible to realize this work without her trust, support, and motivation. Thanks and love to my brother Fabrizio, and to Nino and Marilù, who gave me a family. Thanks to my friends, who gave me another family, and also many laughs.

Munich, April 2020 — Alessandro Massimo Giordano

Abstract

Arm-equipped orbital robots are complex systems merging the nonlinear dynamics behavior of classical terrestrial robots with the complexities of the control architecture of space systems. From the one hand, their dynamics is characterized by nonlinearity and by the microgravity behavior; from the other hand, their control architecture relies on highly heterogeneous actuation and limited sensing capability. Tremendous impetus has characterized the research of the last decades towards the realization of such systems; many solutions have been investigated both theoretically and experimentally. Still, the solutions were investigated in a somewhat decoupled fashion stemming from the different points of view of the robotics and the space communities. Centralized control systems taking into account both aspects altogether, and exploiting their features, need to be developed for a successful deployment of the technology.

The main contribution of this thesis is to define a unifying framework for designing controllers that better exploit the dynamics and actuation properties of the orbital robots. The framework leverages on the whole-body quantities of the system, and on their conservation laws. The robot requirements are enforced by introducing the innovative tasks of momentum dumping and control of the center-of-mass of the whole robot, which are more natural and thus more fuel efficient than the classical spacecraft positioning tasks. Thrusters-decoupled actuators allocation structures are further defined and used for the design of coordinated controllers that limit the allocation of thrusters. Within this framework, whole-body controllers are derived, which merge the advantages of common free-floating and free-flying strategies, while solving their main limitations. The derived controllers allow reducing the thrusters use and the fuel consumption of robotic operations, thereby allowing an extended life and reduced cost of orbital robotics missions.

Beyond the conceptual innovation, attention is posed also to the theoretical and practical stability of the controllers. The actuators allocation is formulated in a way that main structural properties of the system are preserved, and thus can be exploited in the stability analysis. The theoretical stability is proven for some of the classical controller and for the whole-body controllers analyzed in the thesis. The practical stability and effectiveness of the controllers considering a realistic set of thrusters is analyzed via extensive numerical simulation. The practical stability and effectiveness of the controllers considering a real arm is validated with hardware experiments on a 3D robotic motion simulator of on-orbit servicing scenarios.

Contents

List of Figures

List of Tables

CHAPTER 1

Introduction

Arm-equipped orbital robots are a fundamental technology for future space missions. The employment of only human astronauts is prohibitive for certain missions, due to high risks to human safety and costs. Examples of missions that will need orbital robots are on-orbit servicing of existing satellites, in-orbit assembly of space structures (see Fig. 1.1), berthing with orbital stations (see Fig. 1.2), and active removal of space debris (see Figs 1.3 and 1.4).

Orbital robots feature a complex dynamic behavior, which stems from the lack of a fixed-based base, and differs substantially from the behavior of on-ground robots. The two major dynamics implications caused by the lack of a fixed-base are a coupling of the motion of the robot manipulator(s) into the motion of the sustaining spacecraft, and the necessity of locomoting in the inertial space via usage of thrusters. In addition to the complex dynamic behavior, the control architecture of such systems is characterized by heterogeneous actuation, limited resources, and limited capability of exteroceptive sensing. Thus, in order to realize orbital robotics missions, there is the need of developing suitable controllers which are capable of tackling the complexity of the dynamics and of the control architecture.

1.1. Related work

Commonly, orbital robots were classified [UY89, DP93, WKCGR18] as **free-floating** or **free-flying** robots, depending on whether thrusters are completely turned off, or are used to control the supporting spacecraft; five categories can be identified and are listed in Table 1.1.

Note that the differentiation among the categories was done on the basis of the different activation of the external forces and torques provided by the thrusters, with the aim of enforcing different translational and rotational requirements *on the spacecraft.*
Free-flying strategies that control the translation of the spacecraft (i.e., cases 4 and 5 in Table 1.1) have the advantage of endowing the robot with the capability of reaching any position in the inertial space. Free-flying strategies that control the rotation of the spacecraft (i.e., cases 3 and 5 in Table 1.1) have the advantage of ensuring eventual pointing requirements of practical on-board equipment, such as antennas, spacecraft-mounted

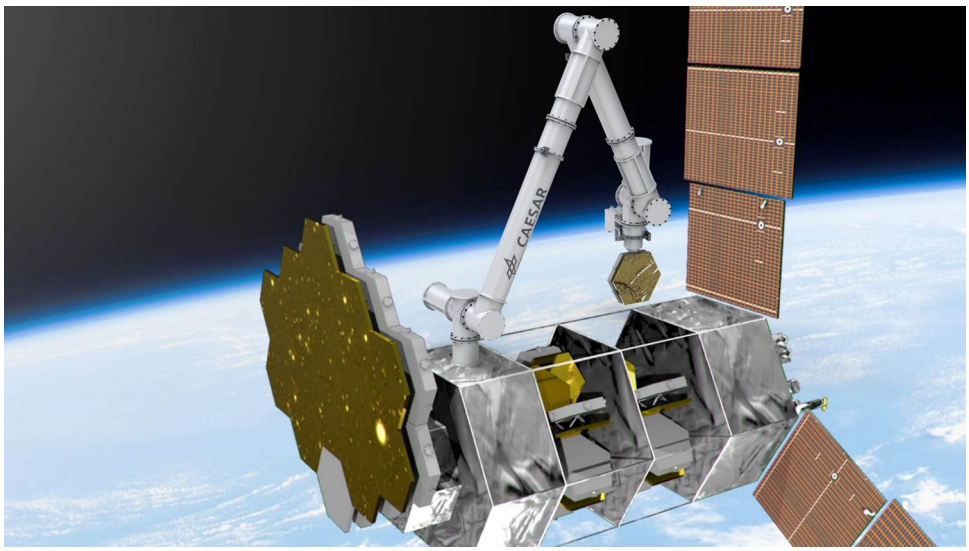

Figure 1.1.: In-orbit assembly of a space telescope: the DLR CAESAR mounted on the ESA PULSAR spacecraft.

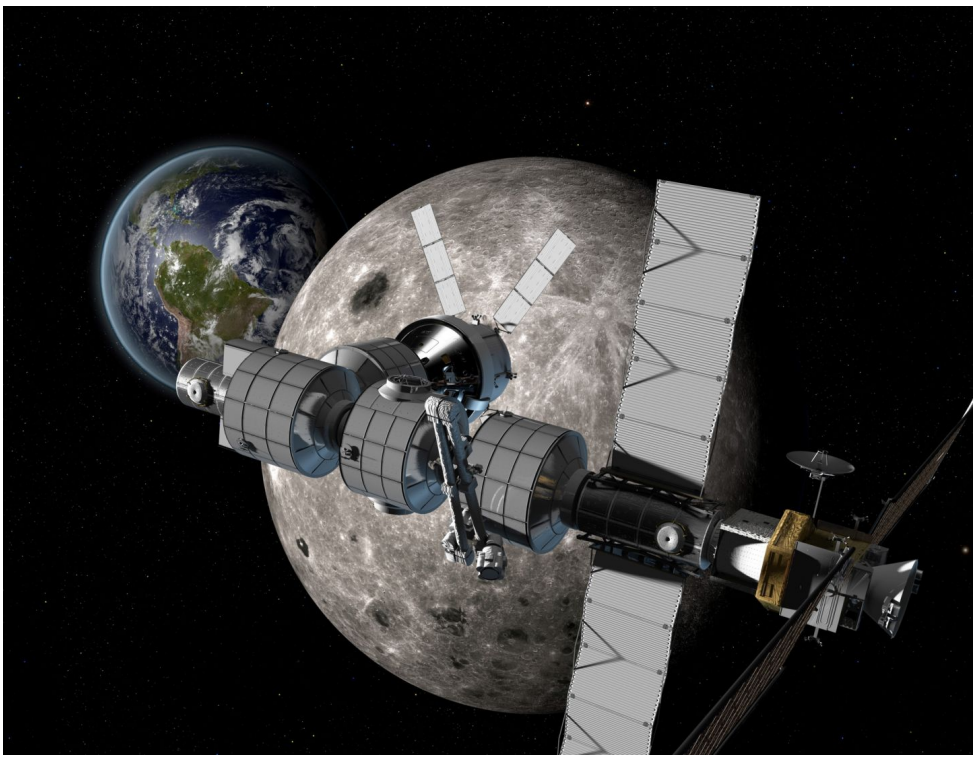

Figure 1.2.: Berthing with lunar orbiting station envisioned in NASA Deep Space Gateway mission.

Case number	Category	Thrusters force	Thrusters torque	Spacecraft translation	Spacecraft rotation
1	Free-floating	0	0	Uncontrolled	Uncontrolled
2	Free-floating	0	0	Uncontrolled	Controlled[a]
3	Free-flying	0	$\neq 0$	Uncontrolled	Controlled
4	Free-flying	$\neq 0$	0	Controlled	Uncontrolled
5	Free-flying	$\neq 0$	$\neq 0$	Controlled	Controlled

[a] The rotation of the spacecraft is controlled only by exploiting redundancy provided by momentum-exchange devices (e.g., reaction wheels, control-moment gyros, variable speed control moment gyros), or by redundancy in the manipulators' joints.

Table 1.1.: Classification of orbital robots based on the use of the thrusters and on the requirements enforced on the spacecraft.

relative sensors, or photovoltaic arrays. Related works for the Free-flying case 3 in Table 1.1 are [XSLK92, Oda96, Oda97, Agh09a, Agh09b]; related works for the Free-flying case 5 are [AJ87, VD89, DT90, SA90, DT91, PD91a, ES93, PM94, MP97, RA06, NY06a, NY06b, AVT19]; to the author's knowledge, control methods for the Free-flying case 4 were not thoroughly investigated in the literature due to a somewhat limited applicability in common scenarios.
Despite their advantages, the free-flying strategies are affected by several limitations:

Fuel usage The Reaction Control System (RCS) of a spacecraft is composed of chemical thrusters, which make use of nonrenewable fuel. Fuel in space is a limited resource because it has to be entirely carried during the launch phase, and has to last for the entire time of the robot's mission; an excessive use of the thrusters may reduce the operational life of the robot.

Low control rate Thrusters in space are normally operated in a discrete on/off mode, modulation techniques are normally employed to map the spacecraft control signal into a discrete on/off one to be commanded to the thrusters' valves. These techniques impose limits on the maximum sampling rate of the signal to be discretized, resulting in a very low rate of the spacecraft control signal compared to the high rate of the joint control one. Free-flying strategies that actuate the thrusters and the joint torques in a coupled way[1] might result in a severe limitation of the performance of the arm due to the low-rate control signal of the spacecraft.

Saturation The motors of the joints are normally capable of providing high torques, whereas the thrusters are capable of providing low-to-moderate thrusts, which in turn result in low-to-moderate forces and torques realized on the spacecraft. Free-flying strategies that actuate the thrusters and the joint torques in a coupled way might result in a severe limitation of the performance of the arm due to possible occurrence of saturation of the thrusters.

Plume impingement Impingement of the thrusters' plume onto the target object can induce an excitation of the target rotational state, and can push it away from the

[1] The concept of thrusters-coupled actuation is later explained in detail in Section 3.2.4 and Section 4.1.1.

servicer robot. In general, the problem cannot be addressed only by design of the RCS hardware; constraints on the trajectory planning and mission operations can be necessary to overcome the problem. Due to overuse of thrusters actuation, free-flying strategies might cause substantial plume impingement, and may make the capture phase difficult.

To overcome the above-mentioned limitations, the robot may be operated based on free-floating strategies, in which the thrusters are completely turned off (i.e., the cases 1 and 2 in Table 1.1). In some free-floating strategies [UY87, VD87, UY89, MMA89b, VD90, PD91b, XS91, YSKU92, NM93, CS01, YNU+04, SK05, NY06a, ALH06, XWZY13, GGDS+16, LMO+18], the robot is steered towards desired location while the position and attitude of the spacecraft displace freely in reaction to the motion of the manipulator. In some other others [LLZ87, NYU91, NUY92, XSLK92, Yos94, DY04a, DY04b, YDN06, ONY07, ONY08, Agh09a, Agh09b, ONY10, SN16], reactionless motion of a redundant arm and/or momentum exchange devices are used to control the attitude of the spacecraft during maneuvers of the manipulator.
By completely avoiding the use of the thrusters, the free-floating strategies have the advantage of consuming no fuel at all and causing no plume impingement. Furthermore, the manipulator can be operated at its maximum speed because it is not limited by the low rate and saturation of the reaction control system. Despite these advantages, the free-floating strategies might have limited applicability in practical scenarios due to the following aspects:

Zero momentum assumption To avoid drifts in the inertial space, and thus ensure stability of the system for an indefinite time, free-floating strategies rely on the assumption of a zero initial linear momentum (cases 1 and 2), and zero initial angular momentum (case 1). This assumption is based on the idea that, prior to the proximity operations, the robot would be "placed" in a zero momentum condition by a single- or multi-body free-flying controller during a previous rendezvous phase. However, an exact zero momentum condition cannot be achieved with the present-day reaction control systems employed in rendezvous operations, because of the low resolution of the chemical thrusters. Chemical thrusters are characterized by a minimum impulse that can be actuated, as quantified by the so-called Minimum Impulse Bit (MIB), below which no more momentum can be extracted from the system, resulting in a nonzero residual momentum. Furthermore, orbital environmental forces act on the robot, causing an accumulation of nonzero momentum.

Contact Accidental or voluntary contact transfers momentum to the system. Due to the transferred momentum, a fast drift of the spacecraft and the joints may be induced during and/or after contact, which may lead to singularity and workspace limits within few seconds.

Limited workspace In a free-floating strategy, the workspace of the manipulator would be a bounded region of the inertial space. In scenarios in which the robot is requested to operate on different distant objects, a free-floating strategy alone cannot be employed, switching to a free-flying one is needed.

1.2. Idea: Whole-Body Control of Orbital Robots

The above-mentioned free-floating and free-flying categorization implicitly builds upon the idea that the thrusters can be used only to enforce requirements on the spacecraft; however, in a multibody robotic system, thrusters might be instead used to achieve other tasks that own different properties. This *spacecraft-centric* perspective, probably originated as a heritage of previous pioneering research in single-body space robotics, might dim the analysis of the core-features of a multi-body system, and might inhibit the development of new classes of controllers that better exploit those features.
In this doctoral thesis, a step is taken towards a different framing of the problem with the aim of exploring innovative control solutions. By looking at the system from a *whole-body-centric* perspective, new control tasks are conceived and new coordination methods of the actuators are derived, which allow developing a new control strategy merging the advantages of the free-floating and the free-flying ones.
By looking at the system in its entirety rather than focusing on the behavior of the spacecraft, it is possible to identify a more general set of control requirements needed to ensure the success of an on-orbit robotic operation. An orbital robot shall be able to

(R1) control the translation, the rotation, or both, of the end-effector of the manipulator(s), and

(R2) ensure that no drift happen that may result in workspace limits, and

(R3) provide a mean of moving the robot in the inertial space, and

(R4) if needed, control the translation, or the rotation, or both, of one or other bodies of the robot other than the end-effector, and

(R5) provide a mean of avoiding collisions.

The requirement (R2) is needed, for instance, for ensuring safety during the post-contact phase[2]; the requirement (R3) endows the robot with the capability of reaching distant objects; the requirement (R4) guarantees eventual pointing or proximity constraints of body-mounted devices and may not necessarily be the spacecraft; the requirement (R5) guarantees the robot be safely maneuverable nearby objects when no explicit requirements are imposed on the spacecraft.
Finally, in addition to the above-mentioned requirements, the controller of an orbital robot shall have the important feature of **limiting the use of the thrusters**, to reduce the consumption of nonrenewable fuel, and to limit performance deterioration caused by the limitation of the thrusters.
A class of whole-body controllers is derived in this thesis, which allows satisfying most of the stated requirements without necessarily resorting to a free-flying strategy, i.e., without necessarily enforcing a control of the position and/or the rotation of the spacecraft. In the next chapters, by leveraging on the two core ideas of **thrusters-decoupled actuation** and **invariant task**, a class of whole-body controllers is derived, which integrates the natural floating-base behavior of the system into a fully actuated strategy, and allows to drastically reduce the thrusters use. By doing so, a single unified controller for the pre- and post-contact phases of an orbital robot is obtained, which bypasses or mitigates the limitations of the free-floating and free-flying strategies, and merges their advantages.

[2]This aspect will be analyzed in detail in Section 3.1.3 and in Chapters 7 and 8.

1.3. Overview and Contribution

The thesis contributes to both theory and experimental validation in the field. The organization of the thesis is as follows. First, the free-flying and free-floating strategies are reported, as well their limitations. Second, the general framework for the derivation of the Whole-Body controllers is presented. Then, a series of new controllers are derived as an application of the general framework to specific control cases. Finally, the validation of new controllers with numerical and hardware simulations is reported. The thesis is organized in such a way to have a uniform notation.

Chapter 2 treats the modeling of the orbital robot, and introduces the methodology for deriving the controllers. Therein, the main kinematics and dynamics equations are described, as well as the underlying assumptions and notation. The transformation of the dynamics into a new space – the *allocation* space – is addressed, in a similar way as done for the Operational Space Formulation [Kha87].

Chapter 3 deals with the free-floating and free-flying strategies, and analyzes their limitations. The common transposed-Jacobian free-floating controller [MMA89b] is extended for use of with nonzero linear and angular momenta, and for the use with redundant arms; both extensions are a contribution. The common coordinated free-flying controller [PD91a] is extended for use with a redundant manipulator, a mathematically rigorous stability analysis is provided, and the limitation arising from the thrusters-coupled actuation of the free-flying strategy is pointed out. To the best of the author's knowledge, the extension to the redundant manipulator and the stability analysis are a contribution.

Chapter 4 describes the core idea of the class of Whole-Body controllers derived herein, and defines the framework for their derivation. First, the concepts of thrusters-decoupled actuation and invariant task are made mathematically precise. Second, an external-internal actuator decomposition is presented for achieving complete thrusters-decoupling. Third, a centroid-circumcentroidal actuator decomposition is presented for achieving partial thrusters-decoupling. The three derivations are a contribution.

Chapter 5 presents two Whole-Body controllers for an orbital robot equipped with thrusters; the controllers are derived by application of the general framework presented in Chapter 4. The first controller adopts an external-internal actuator decomposition, and allows enforcing the whole-body requirements (R1)-(R3) listed in Section 1.2 with minimalistic use of the thrusters. By doing so, the safety advantages of the free-flying strategy are merged with the fuel efficiency advantage of a free-floating one. The second controller adopts a centroid-circumcentroidal actuator decomposition, and it allows enforcing the additional requirement (R4) for the particular case of attitude control of the base, which is needed in certain missions. Compared to a free-floating strategy, or to the free-flying strategies with partial underactuation (i.e., cases 3 and 4 in Table 1.1), the controllers guarantee a safe post-contact phase; compared to a free-flying strategy with complete actuation (i.e., case 5 in the same table), the controllers drastically reduce the thrusters use and fuel consumption during the pre-contact maneuvering. The two controllers are a contribution; the stability analysis of the second controller is a contribution.

Chapter 6 presents a Whole-Body controller for an orbital robot equipped with thrusters and reaction wheels; similarly as in Chapter 5, the controller is derived by application of the general framework presented in Chapter 4. Thanks to the additional redundancy provided by the reaction wheels, an external-internal actuator decomposition can be used instead of a centroid-circumcentroidal one, and the requirement (R4) of attitude control of the base is enforced without using thrusters. By doing so, the thrusters usage and the

Reference	Description
Journal [GDOA20]	A. M. Giordano, A. Dietrich, C. Ott, and A. Albu-Schäffer. Coordination of thrusters, reaction wheels, and arm in orbital robots. *Journal of Robotics and Autonomous Systems*, 2020
Journal [GOA19]	A. M. Giordano, C. Ott, and A. Albu-Schäffer. Coordinated control of spacecraft's attitude and end-effector for space robots. *IEEE Robotics and Automation Letters*, 4(2):2108–2115, April 2019
Conference [GCAS18]	A. M. Giordano, D. Calzolari, and A. Albu-Schäffer. Workspace fixation for free-floating space robot operations. In *2018 IEEE International Conference on Robotics and Automation (ICRA)*, May 2018
Conference [GGAS17]	A. M. Giordano, G. Garofalo, and A. Albu-Schäffer. Momentum dumping for space robots. In *2017 IEEE 56th Annual Conference on Decision and Control (CDC)*, pages 5243–5248, Dec 2017
Conference [GGDS$^+$16]	A. M. Giordano, G. Garofalo, M De Stefano, C. Ott, and A. Albu-Schäffer. Dynamics and control of a free-floating space robot in presence of nonzero linear and angular momenta. In *Proceedings of the 55th IEEE Conference on Decision and Control*, Dec 2016
Conference [ADSR$^+$15]	J. Artigas, M. De Stefano, W. Rackl, R. Lampariello, B. Brunner, W. Bertleff, R. Burger, O. Porges, A. Giordano, C. Borst, and A. Albu-Schäffer. The OOS-SIM: An on-ground simulation facility for on-orbit servicing robotic operations. In *2015 IEEE International Conference on Robotics and Automation (ICRA)*, May 2015

Table 1.2.: List of publications on which this thesis is based.

fuel consumption during pre-contact phase are drastically reduced also in missions which require attitude pointing. The controller and its stability proof are contributions.

Chapter 7 presents the validation of the controllers via numerical simulation. The functional differences among controllers are first analyzed via ideal simulation; then, an extensive validation with realistic thrusters and noise models is reported, which validates the reduced thrusters usage and fuel consumption of the Whole-Body controllers.

Chapter 8 reports the results of the experimental validation performed on the On-Orbit Servicing Simulator (OOS-Sim) hardware-in-the-loop simulation facility at German Aerospace Center (DLR). The experimental validation proves the applicability of the proposed controllers considering a robot composed of a seven degrees-of-freedom (DOF) arm mounted on a 6DOF moving spacecraft, and is a contribution.

Chapter 9 summarizes the key differences among the presented controllers and draws the main conclusions.

The research findings reported in this thesis resulted in two journal articles and four conference papers in the main robotics and control congresses; they are listed in Table 1.2. Furthermore, one book chapter, two journal articles and thirteen conference papers have been co-authored, which are related to the topic but not integrated in the thesis; they are listed in Table 1.3.

Reference	Description
Book chapter [DSRB+20]	M. De Stefano, M. A. Roa, R. Balachandran, A. M. Giordano, H. Mishra, N. Oumer, B. Brunner, M. Lingenauber, M. Stelzer, and R. Lampariello. Design and validation of orbital robotic missions. In Xiu Yan and G. Visentin, editors, *Space Robotics (in press)*. Springer, 2020
Journal [CGA20]	D. Calzolari, A. M. Giordano, and A. Albu-Schäffer. Error bounds for pd-controlled mechanical systems under bounded disturbances using interval arithmetic. *IEEE Robotics and Automation Letters*, 5(2):1231–1238, April 2020
Journal [JLR+18]	S. Jaekel, R. Lampariello, W. Rackl, M. De Stefano, N. Oumer, A. M. Giordano, O. Porges, M. Pietras, B. Brunner, J. Ratti, Q. Muehlbauer, M. Thiel, S. Estable, R. Biesbroek, and A. Albu-Schaeffer. Design and operational elements of the robotic subsystem for the e.deorbit debris removal mission. *Frontiers in Robotics and AI*, 5:100, 2018
Conference [MGDS+20]	H. Mishra, A.M. Giordano, M. De Stefano, R. Lampariello, and C. Ott. Inertially-decoupled equations for hardware-in-the-loop simulation of an orbital robot with external forces. In *2020 IEEE/RSJ International Conference on Intelligent Robots and Systems (IROS)*, 2020
Conference [CLG20]	D. Calzolari, R. Lampariello, and A. M. Giordano. Singularity maps of space robots and their application to gradient-based trajectory planning. In *Robotics: Science and Systems*, 2020
Conference [MDGO20]	H. Mishra, M. De Stefano, A. M. Giordano, and C. Ott. A geometric controller for fully-actuated robotic capture of a tumbling target. In *2020 Annual American Control Conference (ACC)*, June 2020
Conference [CGM19b]	F. Cavenago, A. M. Giordano, and M. Massari. Contact force observer for space robots. In *2019 IEEE 58th Conference on Decision and Control (CDC)*, pages 2528–2535, Dec 2019
Conference [CHC+19]	J. Cieslak, D. Henry, P. Colmenarejo, N. Santos, J. Branco, P. Serra, J. Telaar, H. Strauch, A.M. Giordano, M. De Stefano, C. Ott, M. J. Reiner, J. Jaworski, E. Papadopoulos, G. Visentin, F. Ankersen, and J. Gil. Assessment of a supervisory fault-hiding scheme in a classical guidance, navigation and control setup: the e.deorbit mission. In *2019 4th International Conference on Control and Fault-Tolerant Systems (SYSTOL)*, 2019
Conference [MDGO19]	H. Mishra, M. De Stefano, A. M. Giordano, and C. Ott. A nonlinear observer for free-floating target motion using only pose measurements. In *2019 Annual American Control Conference (ACC)*, June 2019
Conference [HCZ+19]	D. Henry, J. Cieslak, J. Zenteno Torres, P. Colmenarejo, J. Branco, N. Santos, P. Serra, J. Telaar, H. Strauch, A.M. Giordano, M. De Stefano, C. Ott, M. J. Reiner, J. Jaworski, E. Papadopoulos, G. Visentin, F. Ankersen, and J. Gil. Model-based fault diagnosis and tolerant control: the esa's e.deorbit mission. In *2019 European Control Conference (ECC)*, June 2019

continued on next page

continued from previous page

Reference	Description
Conference [GMGL19]	A.P. Gallardo, H. Mishra, A. M. Giordano, and R. Lampariello. Robust estimation of motion states for free-floating tumbling target capture. In *2019 IEEE Aerospace Conference*, March 2019
Conference [CGM19a]	F. Cavenago, A. M. Giordano, and M. Massari. An approach to contact detection and isolation for free-floating robots based on momentum monitoring. In *2019 IEEE Aerospace Conference*, March 2019
Conference [CBS+18]	P. Colmenarejo, J. Branco, N. Santos, P. Serra, J. Telaar, H. Strauch, A. M. Giordano, M. De Stefano, C. Ott, M. Rainer, D. Henry, J. Jaworski, E. Papadopoulos, G. Visentin, F. Ankersen, and J. Gil-Fernandez. Methods and outcomes of the comrade project - design of robust combined control for robotic spacecraft and manipulator in servicing missions. In *69th International Astronautical Congress*, Sept 2018
Conference [MDSGO18]	H. Mishra, M. De Stefano, A. M. Giordano, and Christian Ott. Tracking control with robotic systems for a moving target: A vector lyapunov function approach. volume 51, pages 471 – 478, 2018. 12th IFAC Symposium on Robot Control SYROCO 2018
Conference [DBG+18]	M. De Stefano, R. Balachandran, A. M. Giordano, C. Ott, and C. Secchi. An energy-based approach for the multi-rate control of a manipulator on an actuated base. In *2018 IEEE International Conference on Robotics and Automation (ICRA)*, pages 1072–1077, May 2018
Conference [DSAG+15]	M. De Stefano, J. Artigas, A. Giordano, R. Lampariello, and A. Albu-Schaeffer. On- ground experimental verification of a torque controlled free-floating robot. In *13th Symposium on Advanced Space Technologies in Robotics and Automation 2015 (ASTRA)*, May 2015

Table 1.3.: List of publications closely related to the thesis.

1.4. Orbital Robotics Mission

The Engineering Test Satellite VII (ETS-VII) [OKY96, Yos03] was the first mission demonstrating in orbit the robotic capturing of a target satellite by means of an arm-equipped orbital robot. It provided validation of a number of robotic tasks, including: teleoperation from the ground with a large time delay; robotic servicing such as replacement of satellite units and deployment of a space structure; dynamically coordinated control between the manipulator's reaction and the satellite's response; capture and berthing of a cooperative target satellite.

After the ETS-VII mission, a number of activities in the world were conducted to demonstrate in orbit the robotic capture of a noncooperative target satellite. The Deutsche Orbitale Servicing Mission (DEOS) [SBS+10, RMNL11] of the German Space Agency (DLR) was designed up to technology readiness level B2, with the aim of demonstrating the robotic capture of a noncooperative tumbling satellite in orbit. The ESA e.deorbit [JLR+18] activity was started to capture and deorbit the ESA-owned defunct satellite ENVISAT, which represents a large noncooperative tumbling satellite; the activity envisions the capture of the satellite by means of an arm-equipped orbital robot. The ESA

COMRADE project [CBS+18] was conducted to design the combined[3] and coordinated[4] control system for the ESA e.deorbit mission.

The present thesis was developed within the context of the DLR DEOS, ESA e.deorbit, and ESA COMRADE projects. More specifically, the free-floating controller presented in Section 3.1, and the Whole-Body controller presented in Section 5.1, were developed by the author to tackle the impedance control problem in the DLR DEOS mission; the free-flying controller in Section 3.2 was adapted for application with a large tumbling target and implemented in the ESA COMRADE project; the Whole-Body controllers in Section 5.2 and Section 6.1 were developed by the author for improving the performance, fuel consumption, and plume impingement compatibly with the attitude requirement envisioned in the ESA e.deorbit project.

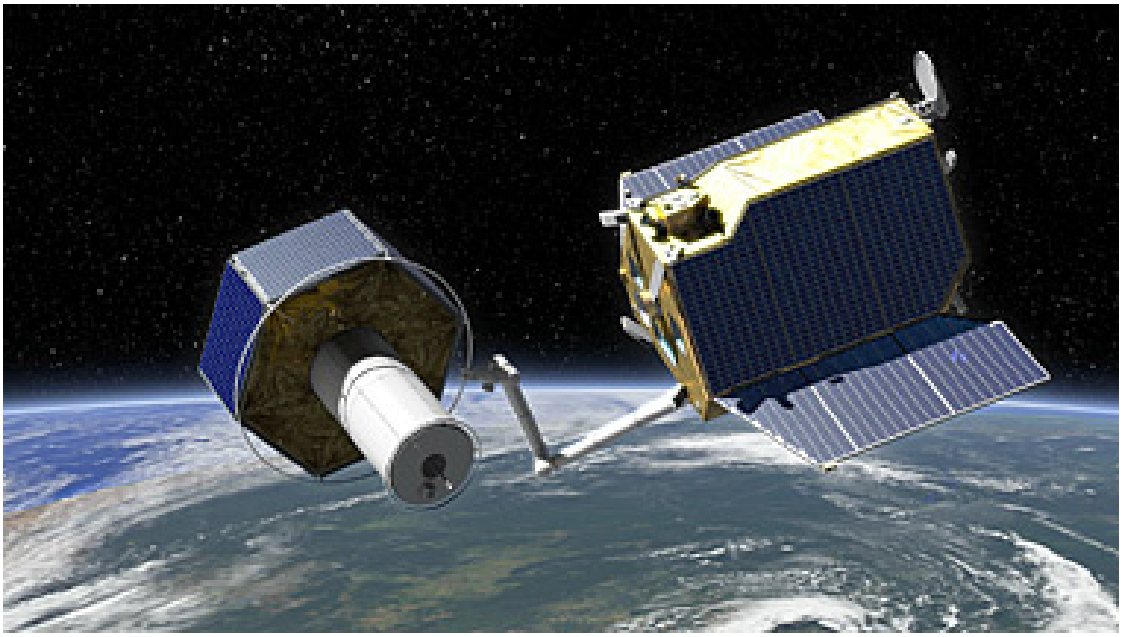

Figure 1.3.: Robotic capture scenario of the DLR DEOS mission: the robotic arm tracks the grasping point of the tumbling satellite while the base of the orbital robot is left free-floating.

[3] *Combined* means that the controller is implemented on a single computer unit which has access to both the spacecraft's and arm's sensors and actuators.

[4] *Coordinated* means the control tasks are shared among both spacecraft and arm actuators, to fully exploit the system redundancy.

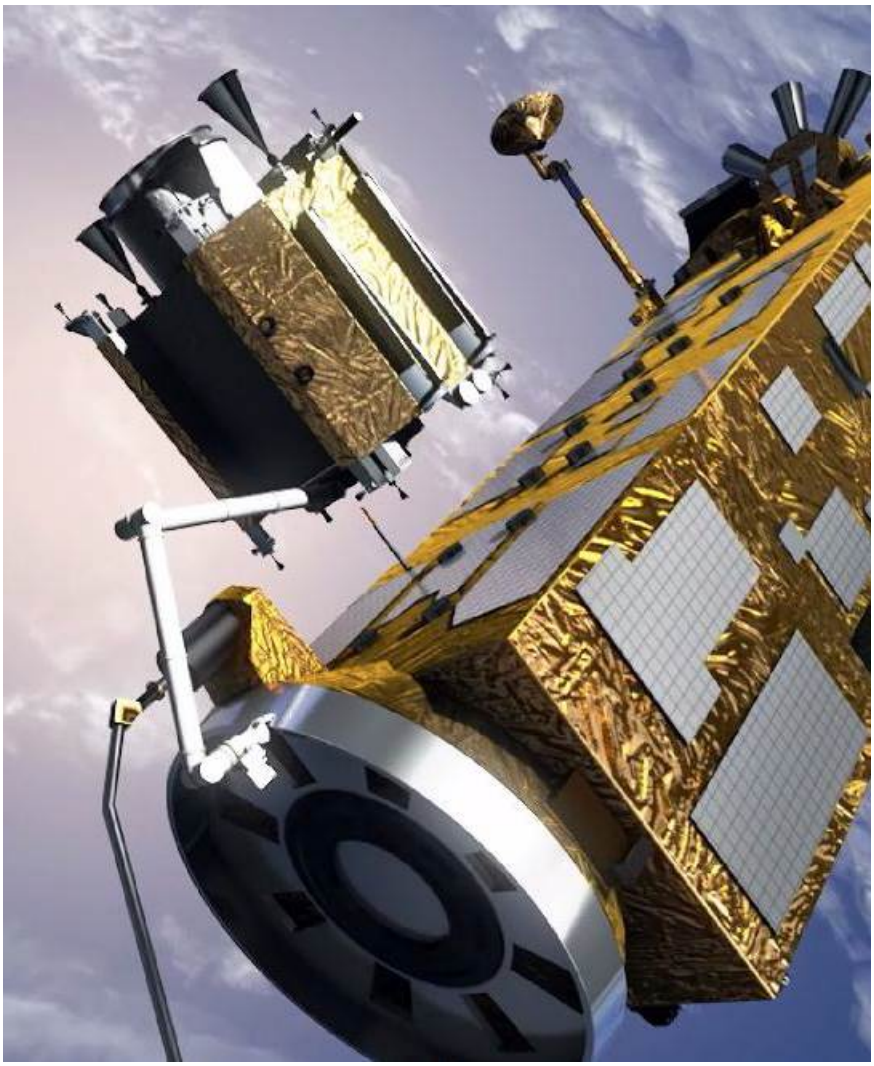

Figure 1.4.: Robotic capture scenario of the ESA e.deorbit mission: to avoid collisions with the large tumbling satellite, the orbital robot has to perform a synchronized flight during the robotic capture; the relative attitude shall be further controlled to ensure LIDAR pointing.

CHAPTER 2

Modelling and methodology

2.1. Derivation of the Kinematics Model

In this section, the kinematics equations used throughout the thesis are described. Let us first describe the scenario, the references frames, and the assumptions used for the derivation of the kinematics model. The scenario considered in this work involves a robot in proximity of a target object in orbit (see Fig. 2.1).

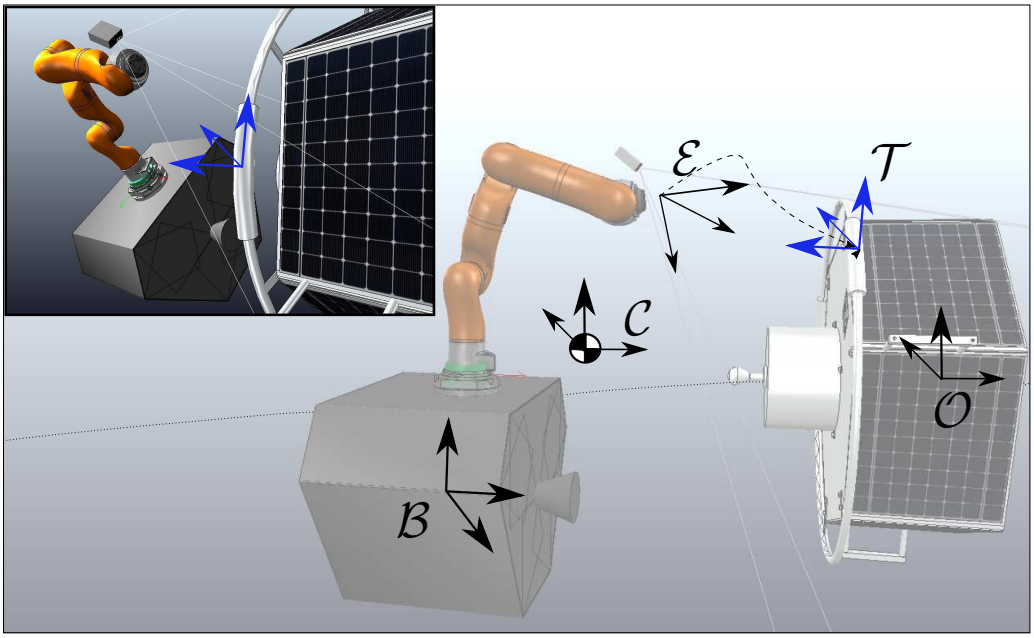

Figure 2.1.: Scenario: robotic capture of a target object in orbit.

An orbital frame $\mathcal{O}$ is defined having inertial axes and located on an orbit which at the initial time coincides with the orbit of the target. The orbital motion is slow compared to the robot maneuvers, and, in turn, the effects of the noninertiality of $\mathcal{O}$ resulting in the dynamics of the system relative to $\mathcal{O}$ are small compared to the actuation forces. Thus,

the following assumption is made:

Assumption 2.1. *The frame $\mathcal{O}$ is inertial.*

The following frames are considered: a body-fixed "base" frame $\mathcal{B}$ attached to the spacecraft; an end-effector frame $\mathcal{E}$; a body-fixed frame $\mathcal{T}$ attached to the target object; a frame $\mathcal{C}$ having inertial axes and located on the CoM of the orbital robot, i.e., the CoM of the spacecraft-arm multibody system. Furthermore, the body-fixed frame of the general j^{th} body of the robot is denoted by $\mathcal{J}$. Note that arbitrary axes and origin can be chosen for the body-fixed frames $\mathcal{B}$, $\mathcal{T}$, and $\mathcal{J}$, because the equations developed throughout the text are general.
The main focus of the thesis is to investigate the coordination of the actuation in an orbital robot; to simplify the formulation, the following additional assumption is made.

Assumption 2.2. *The target object is stationary w. r. t. $\mathcal{O}$, thus the frame $\mathcal{T}$ is inertial.*

For noninertial target objects, e.g. tumbling target objects, a disturbance would appear in the closed loop due to the noninertiality of the frame $\mathcal{T}$. The assumption 2.2 may be removed and the controllers derived herein may be applied, for instance, by adding a disturbance compensation term in the feedback law. This was done in [GML+20] for a free-flying controller. Further details about the extension to a noninertial target are provided in Chapter 9.
For moderate lengths, the distributed flexibility along the links of the arm has a minor effect compared to the concentrated flexibility in the joints [Mor16]. The modeling and compensation of the lumped flexibility in the joints was treated in detail in [ASOH07b]. Herein, it is assumed that in practical implementations the control algorithms derived in this thesis are used in combination with a joint inner control loop which implements such compensation methods. Based on this, it is assumed that:

Assumption 2.3. *The space robot is modeled as a chain of rigid bodies, no structural flexibility is modeled.*

2.1.1. Rigid Body Motion

The modeling of the rigid body motion is based on [MLS94]. This section is not intended to provide a comprehensive treatment of the topic, but to clarify the conventions and recurrent formulas used throughout the text. Let us consider the general reference frames $\mathcal{X}$, $\mathcal{Y}$, and $\mathcal{Z}$, as depicted in Fig. 2.2.

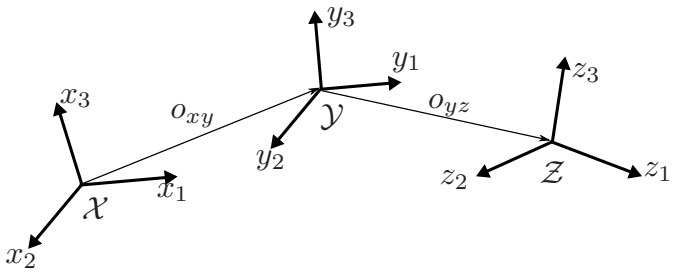

Figure 2.2.: Description of the rigid body motion.

The translation of a frame $\mathcal{Y}$ relative to a frame $\mathcal{X}$ is described by the position vector from the origin of the frame $\mathcal{X}$ to the origin of the frame $\mathcal{Y}$. This vector is represented

using a vector of coordinates $\boldsymbol{o}_{xy} \in \mathbb{R}^3$ that is expressed in the axes of the frame $\mathcal{X}$. When necessary, the notation ${}_z\boldsymbol{o}_{xy} \in \mathbb{R}^3$ will be used to denote that the vector is expressed in the axes of another frame, e.g. $\mathcal{Z}$.
The rotation of $\mathcal{Y}$ with respect to $\mathcal{X}$ is described by a matrix $\boldsymbol{R}_{xy} = \begin{bmatrix} {}_x\boldsymbol{y}_1 & {}_x\boldsymbol{y}_2 & {}_x\boldsymbol{y}_3 \end{bmatrix}$, where ${}_x\boldsymbol{y}_i$ is the vector of coordinates in the frame $\mathcal{X}$ of the unit vector that is collinear to the i^{th} direction of the frame $\mathcal{Y}$. The matrix $\boldsymbol{R}_{xy}$ is the so-called rotation matrix, and is an element of the special orthogonal group $\mathrm{SO}(3) = \left\{ \boldsymbol{R} \in \mathbb{R}^{3\times 3} : \boldsymbol{R}\boldsymbol{R}^T = \boldsymbol{E}, \det(\boldsymbol{R}) = 1 \right\}$. Note that the inverse of $\boldsymbol{R}_{xy}$ can be computed as $\boldsymbol{R}_{yx} = \boldsymbol{R}_{xy}^{-1} = \boldsymbol{R}_{xy}^T$.
The translational and rotational velocities are represented by vectors $\boldsymbol{v}_{xy} \in \mathbb{R}^3$ and $\boldsymbol{\omega}_{xy} \in \mathbb{R}^3$, respectively, and are related to the position and to the rotation matrix by

$$\boldsymbol{v}_{xy} = \boldsymbol{R}_{xy}^T \, \dot{\boldsymbol{o}}_{xy}, \tag{2.1}$$

$$[\boldsymbol{\omega}_{xy}]^\wedge = \boldsymbol{R}_{xy}^T \, \dot{\boldsymbol{R}}_{xy}. \tag{2.2}$$

The vector $\boldsymbol{v}_{xy}$ is called **body linear velocity** of $\mathcal{Y}$ w. r. t. $\mathcal{X}$, and is expressed in the axes of $\mathcal{Y}$. The vector $\boldsymbol{\omega}_{xy}$ is called **body angular velocity** of $\mathcal{Y}$ w. r. t. $\mathcal{X}$, and is expressed in the axes of $\mathcal{Y}$. The operator $[\cdot]^\wedge : \mathbb{R}^3 \to \mathfrak{so}(3)$ maps a $\mathbb{R}^3$-vector to an element of the Lie algebra $\mathfrak{so}(3)$, which is an infinitesimal generator of SO(3), and has the form of a skew-symmetric matrix

$$[\boldsymbol{\omega}_{xy}]^\wedge = \begin{bmatrix} 0 & -\omega_{xy}^3 & \omega_{xy}^2 \\ \omega_{xy}^3 & 0 & -\omega_{xy}^1 \\ -\omega_{xy}^2 & \omega_{xy}^1 & 0 \end{bmatrix} \in \mathfrak{so}(3), \qquad \boldsymbol{\omega}_{xy} = \begin{bmatrix} \omega_{xy}^1 \\ \omega_{xy}^2 \\ \omega_{xy}^3 \end{bmatrix} \in \mathbb{R}^3. \tag{2.3}$$

For later reference, it is convenient to also let $[\cdot]^\vee : \mathfrak{so}(3) \to \mathbb{R}^3$ denote the inverse operator

$$\begin{bmatrix} 0 & -\omega_{xy}^3 & \omega_{xy}^2 \\ \omega_{xy}^3 & 0 & -\omega_{xy}^1 \\ -\omega_{xy}^2 & \omega_{xy}^1 & 0 \end{bmatrix}^\vee = \begin{bmatrix} \omega_{xy}^1 \\ \omega_{xy}^2 \\ \omega_{xy}^3 \end{bmatrix} = \boldsymbol{\omega}_{xy}. \tag{2.4}$$

The pose of $\mathcal{Y}$ with respect to $\mathcal{X}$ is a composition of translation and rotation, and is described by the matrix

$$\boldsymbol{H}_{xy} = \begin{bmatrix} \boldsymbol{R}_{xy} & \boldsymbol{o}_{xy} \\ \boldsymbol{0} & 1 \end{bmatrix} \in \mathrm{SE}(3), \tag{2.5}$$

which is the so-called **homogeneous representation** of a rigid transformation, and is an element of the special Euclidean group[1] $\mathrm{SE}(3) = \mathrm{SO}(3) \rtimes \mathbb{R}^3$. With slight abuse of notation, let $[\cdot]^\wedge : \mathbb{R}^6 \to \mathfrak{se}(3)$ denote the operator which maps a $\mathbb{R}^6$-vector to an element of the Lie algebra $\mathfrak{se}(3)$, which is an infinitesimal generator of SE(3), such that

$$[\boldsymbol{\nu}_{xy}]^\wedge = \begin{bmatrix} [\boldsymbol{\omega}_{xy}]^\wedge & \boldsymbol{v}_{xy} \\ \boldsymbol{0} & \boldsymbol{0} \end{bmatrix} \in \mathfrak{se}(3), \qquad \boldsymbol{\nu}_{xy} = \begin{bmatrix} \boldsymbol{v}_{xy} \\ \boldsymbol{\omega}_{xy} \end{bmatrix} \in \mathbb{R}^6. \tag{2.6}$$

The 6DOF velocity of $\mathcal{Y}$ w. r. t. $\mathcal{X}$ is represented by a vector $\boldsymbol{\nu}_{xy} = \begin{bmatrix} \boldsymbol{v}_{xy} \\ \boldsymbol{\omega}_{xy} \end{bmatrix} \in \mathbb{R}^6$, which is related to $\boldsymbol{H}_{xy}$ by

$$[\boldsymbol{\nu}_{xy}]^\wedge = \boldsymbol{H}_{xy}^{-1} \dot{\boldsymbol{H}}_{xy}. \tag{2.7}$$

[1] With the homogeneous representation, SE(3) is the semi-direct product between groups [Ott08, p.14], and its group operation is given by the matrix multiplication of the homogeneous matrices.

The vector $\boldsymbol{\nu}_{xy}$ is called **body velocity**[2] of the $\mathcal{Y}$ frame relative to the frame $\mathcal{X}$. The time derivative $\dot{\boldsymbol{\nu}}_{xy}$ of the body velocity is called **body acceleration** of the frame $\mathcal{Y}$ relative to the frame $\mathcal{X}$.
Formulas for the transformation of the relative poses, velocities, and accelerations between multiple frames are now provided. Let us preliminary define the so-called Adjoint matrices[3] $\boldsymbol{A}_{xy} \in \mathbb{R}^{6\times6}$ and $\boldsymbol{a}_{xy} \in \mathbb{R}^{6\times6}$, as

$$\boldsymbol{A}_{xy} = \begin{bmatrix} \boldsymbol{R}_{xy} & [\boldsymbol{o}_{xy}]^\wedge \boldsymbol{R}_{xy} \\ \boldsymbol{0} & \boldsymbol{R}_{xy} \end{bmatrix}, \qquad \boldsymbol{a}_{xy} = \begin{bmatrix} [\boldsymbol{\omega}_{xy}]^\wedge & [\boldsymbol{v}_{xy}]^\wedge \\ \boldsymbol{0} & [\boldsymbol{\omega}_{xy}]^\wedge \end{bmatrix}, \tag{2.8}$$

for which the properties hold

$$\boldsymbol{A}_{xy}^{-1} = \boldsymbol{A}_{yx}, \qquad \dot{\boldsymbol{A}}_{xy} = \boldsymbol{A}_{xy}\boldsymbol{a}_{xy}, \qquad \boldsymbol{a}_{xy}\boldsymbol{\nu}_{xy} = \boldsymbol{0}. \tag{2.9}$$

Then, given three frames $\mathcal{X}, \mathcal{Y}$, and $\mathcal{Z}$, their mutual relative poses, velocities, and accelerations are related by

$$\boldsymbol{H}_{xz} = \boldsymbol{H}_{xy}\boldsymbol{H}_{yz}, \tag{2.10}$$
$$\boldsymbol{\nu}_{xz} = \boldsymbol{A}_{zy}\boldsymbol{\nu}_{xy} + \boldsymbol{\nu}_{yz}, \tag{2.11}$$
$$\dot{\boldsymbol{\nu}}_{xz} = \boldsymbol{A}_{zy}\dot{\boldsymbol{\nu}}_{xy} + \boldsymbol{A}_{zy}\boldsymbol{a}_{zy}\boldsymbol{\nu}_{zy} + \dot{\boldsymbol{\nu}}_{yz}. \tag{2.12}$$

Similar relations hold for the adjoint matrices[4]:

$$\boldsymbol{A}_{xz} = \boldsymbol{A}_{xy}\boldsymbol{A}_{yz}. \tag{2.13}$$
$$\boldsymbol{a}_{xz} = \boldsymbol{A}_{zy}\boldsymbol{a}_{xy}\boldsymbol{A}_{zy}^{-1} + \boldsymbol{a}_{yz}. \tag{2.14}$$

As a conclusive remark, note that when only one subscript is used on the right of the notations $\boldsymbol{o}_y$, $\boldsymbol{R}_y$, $\boldsymbol{H}_y$, $\boldsymbol{v}_y$, $\boldsymbol{\omega}_y$, $\boldsymbol{\nu}_y$, then it is intended that the quantities are relative to the orbital frame $\mathcal{O}$.

2.1.2. Forward Kinematics

In this section the kinematics model of an orbital robot is derived. The orbital robot considered herein is a free open mechanical chain with n revolute joints that are distributed on multiple branches[5]. The unconstrained motion of the chain is modeled as a free joint between the base frame $\mathcal{B}$ and the orbital frame $\mathcal{O}$, and its configuration is represented by the homogeneous transformation matrix $\boldsymbol{H}_b \in \mathrm{SE}(3)$. The joints of the chain are modeled as angles between two adjacent bodies of the chain, and are represented by a vector $\boldsymbol{q} \in \mathbb{R}^n$. The configuration set of the robot is therefore $\mathrm{SE}(3) \times \mathbb{R}^n$. The velocity of the base is modeled by means of its velocity $\boldsymbol{\nu}_b \in \mathbb{R}^6$, while the velocity of the joints is modeled as the time derivative $\dot{\boldsymbol{q}} \in \mathbb{R}^n$. Based on this, the velocity of the robot is represented by the stacked vector[6] $\boldsymbol{\upsilon} = \begin{bmatrix} \boldsymbol{\nu}_b^T & \dot{\boldsymbol{q}}^T \end{bmatrix}^T \in \mathbb{R}^{6+n}$.

[2] Other parametrizations of the velocity exist, e.g. the spatial velocity and the hybrid velocity [MLS94], but are not used in the present work.
[3] The matrices $\boldsymbol{A}_{xy}$ and $\boldsymbol{a}_{xy}$ are known in the literature as "Adjoint" and "small Adjoint", respectively.
[4] See Appendix E for the proof.
[5] This is the case of the manipulator-equipped spacecraft with momentum exchange devices treated herein, or, for example, of a robot equipped with multiple manipulators.
[6] Note that the symbol $\boldsymbol{\upsilon}$ denotes a general motion, whereby the symbol $\boldsymbol{v}$ used in Section 2.1.1 denotes the particular case of linear velocity.

The static and differential forward kinematics equations of the robot relate the pose and the velocity, respectively, of the j^{th} body frame to the configuration variables $\boldsymbol{H}_b$ and $\boldsymbol{q}$, and to the generalized velocities $\boldsymbol{\upsilon}$. They are given by[7]

$$\boldsymbol{H}_j = \boldsymbol{H}_b \boldsymbol{H}_{bj}(\boldsymbol{q}), \tag{2.16a}$$
$$\boldsymbol{\nu}_j = \boldsymbol{A}_{jb}(\boldsymbol{q})\boldsymbol{\nu}_b + \boldsymbol{J}_{jq}(\boldsymbol{q})\dot{\boldsymbol{q}} \tag{2.16b}$$
$$= \boldsymbol{J}_j(\boldsymbol{q})\boldsymbol{\upsilon}, \tag{2.16c}$$

where

$$\boldsymbol{J}_j(\boldsymbol{q}) = \begin{bmatrix} \boldsymbol{A}_{jb}(\boldsymbol{q}) & \boldsymbol{J}_{jq}(\boldsymbol{q}) \end{bmatrix} \in \mathbb{R}^{6\times(6+n)}, \tag{2.17}$$

and where $\boldsymbol{J}_{jq}(\boldsymbol{q}) \in \mathbb{R}^{6\times n}$ is the body Jacobian[8] matrix that linearly maps the joint motion into a body velocity relative to the base, i.e., $\boldsymbol{\nu}_{bj} = \boldsymbol{J}_{jq}(\boldsymbol{q})\dot{\boldsymbol{q}}$; it corresponds to the j^{th} body Jacobian matrix of the fixed-base robot. By convention, the 0^{th} frame is defined coincident with the base frame $\mathcal{B}$; in turn, it is $\boldsymbol{A}_{0b} = \boldsymbol{E}$ and $\boldsymbol{J}_{0q} = \boldsymbol{0}$. Notice that $\boldsymbol{J}_j(\boldsymbol{q})$ does not depend on the configuration of the base, but it depends only on the joint angles, this is an advantage of the body velocity representation adopted herein.
The main task of the robot will be specified in the end-effector frame, also referred to as "tool frame". The end-effector frame is attached on the body $j = j_e$ of the robot onto which the tool is mounted. With this purpose, the static and differential kinematics equations for the end-effector will be used. Similarly as done for the j^{th} frame, they can be expressed as

$$\boldsymbol{H}_e = \boldsymbol{H}_b \boldsymbol{H}_{be}(\boldsymbol{q}), \tag{2.18a}$$
$$\boldsymbol{\nu}_e = \boldsymbol{A}_{eb}(\boldsymbol{q})\boldsymbol{\nu}_b + \boldsymbol{J}_{eq}(\boldsymbol{q})\dot{\boldsymbol{q}} \tag{2.18b}$$
$$= \boldsymbol{J}_e(\boldsymbol{q})\boldsymbol{\upsilon}, \tag{2.18c}$$

where

$$\boldsymbol{J}_e(\boldsymbol{q}) = \begin{bmatrix} \boldsymbol{A}_{eb}(\boldsymbol{q}) & \boldsymbol{J}_{eq}(\boldsymbol{q}) \end{bmatrix} \in \mathbb{R}^{6\times(6+n)}, \tag{2.19}$$

and where $\boldsymbol{J}_{eq}(\boldsymbol{q}) \in \mathbb{R}^{6\times n}$ is the Jacobian matrix that linearly maps the joint motion into the velocity of the end-effector relative to the base, i.e., $\boldsymbol{\nu}_{be} = \boldsymbol{J}_{eq}(\boldsymbol{q})\dot{\boldsymbol{q}}$; it corresponds to the end-effector body Jacobian matrix of the fixed-base robot. The end-effector maps are computed as $\boldsymbol{H}_{be}(\boldsymbol{q}) = \boldsymbol{H}_{bj_e}\boldsymbol{H}_{j_e e}(\boldsymbol{q})$, and $\boldsymbol{J}_{eq}(\boldsymbol{q}) = \boldsymbol{A}_{j_e e}\boldsymbol{J}_{j_e q}(\boldsymbol{q}_m) \in \mathbb{R}^{6\times n}$, where $\boldsymbol{H}_{j_e e}$ and $\boldsymbol{A}_{ej_e}$ are constant matrices and j_e is the index of the body to which the end effector is attached.
The equations (2.16) and (2.18) hold for a general kinematic structure. In order to specify those relations for a specific structure, all that is required is to compute $\boldsymbol{J}_j(\boldsymbol{q})$ for all bodies based on the constraints imposed by each joint. The algorithm used for the computation is the one in [GOA13], and is done recursively by propagating it from the root to the leaves of the tree structured robot. This is equivalent to the outward recursion of the Newton-Euler algorithm. The parent of the j^{th} body is specified by associating to the

[7] For later reference, let us report the translational part of (2.16a), as

$$\boldsymbol{o}_j = \boldsymbol{o}_b + \boldsymbol{R}_{ob}\,\boldsymbol{o}_{bj}(\boldsymbol{q}) \tag{2.15}$$

[8] Note that the legacy term "Jacobian" is somewhat imprecise because it is not the differential of any mapping.

index j an index p_j which refers to the parent of the j^{th} body. Then, the $\boldsymbol{J}_j(\boldsymbol{q})$ matrix is defined by iteration of the equations

$$\left.\begin{array}{rll} \boldsymbol{J}_j & = \boldsymbol{\Xi}_j, & j = 0, \\ \boldsymbol{J}_j(\boldsymbol{q}) & = \boldsymbol{A}_{jp_j}(q_j)\boldsymbol{J}_{p_j}(\boldsymbol{q}) + \boldsymbol{\Xi}_j, & j = 1, \ldots, n, \end{array}\right\} \tag{2.20}$$

where $\boldsymbol{\Xi}_j \in \mathbb{R}^{6\times(6+n)}$ is the matrix mapping $\boldsymbol{\upsilon}$ into the velocity of the j^{th} frame relative to the p_j^{th} frame, i.e., such that $\boldsymbol{\nu}_{p_j j} = \boldsymbol{\Xi}_j \boldsymbol{\upsilon}$. Note that this matrix is completely determined by the type of interconnection of the bodies, and is always constant for revolute joints and for free joints. For the computation of the dynamics model, the time derivative of $\dot{\boldsymbol{J}}_j(\boldsymbol{q})$ is required. This can be also computed in the recursion, using the relation

$$\left.\begin{array}{rll} \dot{\boldsymbol{J}}_j & = \boldsymbol{0}, & j = 0, \\ \dot{\boldsymbol{J}}_j(\boldsymbol{q}) & = \boldsymbol{A}_{jp_j}(q_j)\dot{\boldsymbol{J}}_{p_j}(\boldsymbol{q}) - \boldsymbol{a}_{jp_j}(q_j)\boldsymbol{A}_{jp_j}(q_j)\boldsymbol{J}_{p_j}(\boldsymbol{q}), & j = 1, \ldots, n, \end{array}\right\} \tag{2.21}$$

Further detailed information regarding the algorithm can be found in [GOA13].

2.2. Derivation of the Dynamics Model

In this section the dynamics model used for the design and the analysis of the controller is derived. For the derivation of the dynamics model the following assumptions are made.

Assumption 2.4. *No orbital environmental[9] forces act on the robot and on the target object.*

The assumption is justified by the fact that the actuation forces of an arm-equipped orbital robot are considerably higher the orbital environmental forces.

Assumption 2.5. *No fuel dynamics is modeled, e.g. the sloshing and the decrease of the mass of the fuel are neglected.*

The sloshing disturbance is negligible when proper design of the tanks is adopted; the decrease of the fuel mass is small compared to the total mass of the system, and can be neglected during robot maneuvers.

Assumption 2.6. *The rotor dynamics is modeled only for the joints of the reaction wheels, no rotor dynamics is modeled for the joints of the arm. The rotor of each reaction wheel is a rotational symmetric rigid body, whose rotation and symmetry axes coincide.*

Assumption 2.7. *No friction is modeled in the joints.*

The modeling and control in presence of the rotor dynamics and the friction were treated in detail in [ASOH07a, LADH08]. Herein, it is assumed that in practical implementations the control algorithms derived in this thesis are used in combination with a joint inner control loop which takes into account the rotor dynamics and the friction.

[9] With "orbital environmental forces" are meant the forces and torques resulting from the atmospheric drag, the solar pressure, the magnetic field, and the gravity gradient.

2.2.1. Equations of Motion

The derivation of the model is the one in [GOA13]. Let us preliminary define the following symbols: $\boldsymbol{f}_y \in \mathbb{R}^3$ denotes the force acting on the origin of the frame $\mathcal{Y}$ and expressed in the axes of $\mathcal{Y}$; $\boldsymbol{m}_y \in \mathbb{R}^3$ denotes the moment acting around the origin of $\mathcal{Y}$ and expressed in the axes of $\mathcal{Y}$; $\boldsymbol{\mathcal{F}}_y = \begin{bmatrix}\boldsymbol{f}_y^T & \boldsymbol{m}_y^T\end{bmatrix}^T \in \mathbb{R}^6$ denotes the so-called wrench acting on $\mathcal{Y}$. Based on the Newton-Euler equations in body coordinates, $n+1$ equations of motion are written as

$$\frac{d}{dt}\left(\boldsymbol{A}_{oj}^{-T}(\boldsymbol{H}_b, \boldsymbol{q})\boldsymbol{\Lambda}_j^{(j)}\boldsymbol{\nu}_j\right) = \boldsymbol{A}_{oj}^{-T}(\boldsymbol{H}_b, \boldsymbol{q})\boldsymbol{\mathcal{F}}_j^t, \qquad j = 0, \dots, n \tag{2.22}$$

where $\boldsymbol{\mathcal{F}}_j^t = \boldsymbol{\mathcal{F}}_j^c + \boldsymbol{\mathcal{F}}_j + \boldsymbol{\mathcal{F}}_j^{ext}$ is the total wrench acting on the j^{th} body around the j^{th} frame, $\boldsymbol{\mathcal{F}}_j^c$ is the wrench resulting from mechanical constraints, $\boldsymbol{\mathcal{F}}_j$ is the wrench resulting from the actuators, and $\boldsymbol{\mathcal{F}}_j^{ext}$ is the wrench resulting from uncontrolled external forces[10], e.g. contact. The symbol $\boldsymbol{\Lambda}_j^{(j)} \in \mathbb{R}^{6\times6}$ denotes the inertia of the j^{th} body around its frame $\mathcal{J}$; it is given by

$$\boldsymbol{\Lambda}_j^{(j)} = \begin{bmatrix} m^{(j)}\boldsymbol{E} & -m^{(j)}\left[\boldsymbol{o}_{jc_j}\right]^\wedge \\ m^{(j)}\left[\boldsymbol{o}_{jc_j}\right]^\wedge & \boldsymbol{I}_j^{(j)} \end{bmatrix}, \tag{2.23}$$

where $m^{(j)} \in \mathbb{R}$ denotes the mass of the j^{th} body, $\boldsymbol{I}_j^{(j)} \in \mathbb{R}^{3\times3}$ denotes its rotational inertia around the origin of $\mathcal{J}$ and expressed in the axes of $\mathcal{J}$, and $\boldsymbol{o}_{jc_j} \in \mathbb{R}^3$ denotes the position vector from the origin of $\mathcal{J}$ to the CoM of the j^{th} body. By computing the time derivative in (2.22), and by pre-multiplying by $\boldsymbol{A}_{oj}(\boldsymbol{H}_b, \boldsymbol{q})^T$, it is obtained

$$\boldsymbol{\Lambda}_j^{(j)}\dot{\boldsymbol{\nu}}_j - \boldsymbol{a}_{oj}(\boldsymbol{\nu}_j)^T\boldsymbol{\Lambda}_j^{(j)}\boldsymbol{\nu}_j = \boldsymbol{\mathcal{F}}_j^t, \tag{2.24}$$

where (2.9) is used together with the property $\frac{d}{dt}(\cdot)^{-1} = -(\cdot)^{-1}\frac{d(\cdot)}{dt}(\cdot)^{-1}$ of the derivative of an inverse. By exploiting the property $\boldsymbol{a}_{oj}(\boldsymbol{\nu}_j)\boldsymbol{\nu}_j = \boldsymbol{0}$, (2.24) is rewritten as

$$\boldsymbol{\Lambda}_j^{(j)}\dot{\boldsymbol{\nu}}_j + \boldsymbol{\Psi}_j^{(j)}(\boldsymbol{\nu}_j)\boldsymbol{\nu}_j = \boldsymbol{\mathcal{F}}_j^t, \tag{2.25}$$

where $\boldsymbol{\Psi}_j^{(j)}(\boldsymbol{\nu}_j) = \boldsymbol{\Lambda}_j^{(j)}\boldsymbol{a}_{oj}(\boldsymbol{\nu}_j) - \boldsymbol{a}_{oj}(\boldsymbol{\nu}_j)^T\boldsymbol{\Lambda}_j^{(j)} \in \mathbb{R}^{6\times6}$ is a skew-symmetric matrix. Note that, in turn, it holds $\dot{\boldsymbol{\Lambda}}_j^{(j)} = \boldsymbol{\Psi}_j^{(j)}(\boldsymbol{\nu}_j) + \boldsymbol{\Psi}_j^{(j)}(\boldsymbol{\nu}_j)^T$. The equations of motions (2.25) of each body can be stacked in a unique one, as

$$\boldsymbol{\Lambda}\dot{\boldsymbol{\nu}} + \boldsymbol{\Psi}(\boldsymbol{\nu})\boldsymbol{\nu} = \boldsymbol{\mathcal{F}}^t, \tag{2.26}$$

where [11] $\boldsymbol{\Lambda} = \text{blkdiag}(\boldsymbol{\Lambda}_j^{(j)}) \in \mathbb{R}^{6(n+1)\times6(n+1)}$, $\boldsymbol{\Psi} = \text{blkdiag}(\boldsymbol{\Psi}_j^{(j)}(\boldsymbol{\nu}_j)) \in \mathbb{R}^{6(n+1)\times6(n+1)}$, $\boldsymbol{\nu} = \text{col}(\boldsymbol{\nu}_j) \in \mathbb{R}^{6(n+1)}$, and $\boldsymbol{\mathcal{F}}^t = \text{col}(\boldsymbol{\mathcal{F}}_j^t) \in \mathbb{R}^{6(n+1)}$. The $n+1$ kinematics constraints (2.16c) can also be stacked in a compact form, as

$$\boldsymbol{\nu} = \boldsymbol{J}(\boldsymbol{q})\boldsymbol{\upsilon}, \tag{2.27}$$

[10] For brevity, this quantity will be sometimes referred to simply as "external wrench".

[11] The following notation is intended:

$$\text{blkdiag}(\boldsymbol{B}_j) = \begin{bmatrix} \boldsymbol{B}_1 & \boldsymbol{0} & \dots & \boldsymbol{0} \\ \boldsymbol{0} & \boldsymbol{B}_2 & \dots & \boldsymbol{0} \\ \vdots & \vdots & \ddots & \vdots \\ \boldsymbol{0} & \boldsymbol{0} & \boldsymbol{0} & \boldsymbol{B}_n \end{bmatrix}, \quad \text{col}(\boldsymbol{B}_j) = \begin{bmatrix} \boldsymbol{B}_1 \\ \boldsymbol{B}_2 \\ \vdots \\ \boldsymbol{B}_n \end{bmatrix}, \quad j = 0, \dots, n.$$

where $\boldsymbol{J}(\boldsymbol{q}) = \text{col}(\boldsymbol{J}_j(\boldsymbol{q})) \in \mathbb{R}^{6(n+1)\times(6+n)}$. Then, the kinematic constraints can be applied to the dynamics by projecting (2.26) to the space orthogonal to the constraint reaction forces. This is done by inserting (2.27) and its derivative into (2.26), and by pre-multiplying by $\boldsymbol{J}(\boldsymbol{q})^T$, obtaining

$$\boldsymbol{J}(\boldsymbol{q})^T \left[\boldsymbol{\Lambda}\boldsymbol{J}(\boldsymbol{q})\dot{\boldsymbol{\upsilon}} + \left(\boldsymbol{\Psi}(\boldsymbol{\nu})\boldsymbol{J}(\boldsymbol{q}) + \boldsymbol{\Lambda}\dot{\boldsymbol{T}}(\boldsymbol{q})\right)\boldsymbol{\upsilon}\right] = \boldsymbol{J}(\boldsymbol{q})^T\boldsymbol{\mathcal{F}}^t. \tag{2.28}$$

Finally, by denoting as $\boldsymbol{\varsigma} = \boldsymbol{J}(\boldsymbol{q})^T\boldsymbol{\mathcal{F}} \in \mathbb{R}^{6+n}$ the vector of the actuation generalized forces, where $\boldsymbol{\mathcal{F}} = \text{col}(\boldsymbol{\mathcal{F}}_j) \in \mathbb{R}^{6(n+1)}$, and by noting that the constraint reaction wrenches disappear after the projection, i.e., $\boldsymbol{J}_j(\boldsymbol{q})^T\boldsymbol{\mathcal{F}}_j^c = \boldsymbol{0}$, the equation (2.28) is compactly written as

$$\boldsymbol{M}(\boldsymbol{q})\dot{\boldsymbol{\upsilon}} + \boldsymbol{C}(\boldsymbol{q},\boldsymbol{\upsilon})\boldsymbol{\upsilon} = \boldsymbol{\varsigma} + \sum_{j=0}^{n} \boldsymbol{J}_j(\boldsymbol{q})^T\boldsymbol{\mathcal{F}}_j^{ext}, \tag{2.29}$$

where

$$\boldsymbol{M}(\boldsymbol{q}) = \sum_{j=0}^{n} \boldsymbol{J}_j(\boldsymbol{q})^T\boldsymbol{\Lambda}_j^{(j)}\boldsymbol{J}_j(\boldsymbol{q}) \in \mathbb{R}^{(6+n)\times(6+n)}, \tag{2.30}$$

$$\boldsymbol{C}(\boldsymbol{q},\boldsymbol{\upsilon}) = \sum_{j=0}^{n} \boldsymbol{J}_j(\boldsymbol{q})^T\boldsymbol{\Psi}_j^{(j)}(\boldsymbol{\nu}_j)\boldsymbol{J}_j(\boldsymbol{q}) + \boldsymbol{J}_j(\boldsymbol{q})^T\boldsymbol{\Lambda}_j^{(j)}\dot{\boldsymbol{J}}_j(\boldsymbol{q}) \in \mathbb{R}^{(6+n)\times(6+n)}, \tag{2.31}$$

and where with an abuse notation the same matrix symbol is used after substitution of the $\boldsymbol{\nu}$ dependency, i.e., by using (2.27) it is written $\boldsymbol{C}(\boldsymbol{q},\boldsymbol{\nu}) = \boldsymbol{C}\left(\boldsymbol{q},\boldsymbol{J}(\boldsymbol{q})\boldsymbol{\upsilon}\right) := \boldsymbol{C}(\boldsymbol{q},\boldsymbol{\upsilon})$. For the derivation of the controllers the time derivatives of the inertia matrix is occasionally used; this can be computed as

$$\dot{\boldsymbol{M}}(\boldsymbol{q}) = \sum_{j=0}^{n} \dot{\boldsymbol{J}}_j(\boldsymbol{q})^T\boldsymbol{\Lambda}_j^{(j)}\boldsymbol{J}_j(\boldsymbol{q}) + \boldsymbol{J}_j(\boldsymbol{q})^T\boldsymbol{\Lambda}_j^{(j)}\dot{\boldsymbol{J}}_j(\boldsymbol{q}). \tag{2.32}$$

The equation (2.29) represents the dynamics of the system in terms of the generalized velocities $\boldsymbol{\upsilon}$, and will be used as the basis for the derivation of model-based controllers. Note that the dynamics does not depend on the configuration of the base $\boldsymbol{H}_b$, as a consequence of the body representation used to model the base velocity; this property is very useful in simplifying the analysis of the closed-loop of the derived controllers.

Partitioning of the dynamics

It is useful to partition the dynamics (2.29) in base and joint components, as

$$\underbrace{\begin{bmatrix}\boldsymbol{M}_b(\boldsymbol{q}) & \boldsymbol{M}_{bq}(\boldsymbol{q})\\ \boldsymbol{M}_{bq}(\boldsymbol{q})^T & \boldsymbol{M}_q(\boldsymbol{q})\end{bmatrix}}_{\boldsymbol{M}(\boldsymbol{q})}\begin{bmatrix}\dot{\boldsymbol{\nu}}_b\\ \ddot{\boldsymbol{q}}\end{bmatrix} + \underbrace{\begin{bmatrix}\boldsymbol{C}_b(\boldsymbol{q},\boldsymbol{\nu}_b,\dot{\boldsymbol{q}}) & \boldsymbol{C}_{bq}(\boldsymbol{q},\boldsymbol{\nu}_b,\dot{\boldsymbol{q}})\\ \boldsymbol{C}_{qb}(\boldsymbol{q},\boldsymbol{\nu}_b,\dot{\boldsymbol{q}}) & \boldsymbol{C}_q(\boldsymbol{q},\boldsymbol{\nu}_b,\dot{\boldsymbol{q}})\end{bmatrix}}_{\boldsymbol{C}(\boldsymbol{q},\boldsymbol{\upsilon})}\underbrace{\begin{bmatrix}\boldsymbol{\nu}_b\\ \dot{\boldsymbol{q}}\end{bmatrix}}_{\boldsymbol{\upsilon}} = \underbrace{\begin{bmatrix}\boldsymbol{\mathcal{F}}_b\\ \boldsymbol{\tau}\end{bmatrix}}_{\boldsymbol{\varsigma}} + \sum_{j=0}^{n}\begin{bmatrix}\boldsymbol{A}_{jb}(\boldsymbol{q})^T\\ \boldsymbol{J}_{jq}(\boldsymbol{q})^T\end{bmatrix}\boldsymbol{\mathcal{F}}_j^{ext}, \tag{2.33}$$

where $\boldsymbol{\mathcal{F}}_b$ is the external wrench around the base acted upon by a system of spacecraft-mounted thrusters, and $\boldsymbol{\tau} \in \mathbb{R}^n$ are the torques acting in the joints. The sub-blocks of the

inertia matrix are expressed as

$$\boldsymbol{M}_b(\boldsymbol{q}) = \sum_{j=0}^{n} \boldsymbol{A}_{jb}(\boldsymbol{q})^T \boldsymbol{\Lambda}_j^{(j)} \boldsymbol{A}_{jb}(\boldsymbol{q}) \quad \in \mathbb{R}^{6\times 6}, \tag{2.34a}$$

$$\boldsymbol{M}_{bq}(\boldsymbol{q}) = \sum_{j=0}^{n} \boldsymbol{A}_{jb}(\boldsymbol{q})^T \boldsymbol{\Lambda}_j^{(j)} \boldsymbol{J}_{jq}(\boldsymbol{q}) \quad \in \mathbb{R}^{6\times n}, \tag{2.34b}$$

$$\boldsymbol{M}_q(\boldsymbol{q}) = \sum_{j=0}^{n} \boldsymbol{J}_{jq}(\boldsymbol{q})^T \boldsymbol{\Lambda}_j^{(j)} \boldsymbol{J}_{jq}(\boldsymbol{q}) \quad \in \mathbb{R}^{n\times n}. \tag{2.34c}$$

From (2.34) it can be seen that the block $\boldsymbol{M}_b(\boldsymbol{q})$ is equivalent to the inertia of the whole robot around the $\mathcal{B}$ frame, and the block $\boldsymbol{M}_q(\boldsymbol{q})$ is equivalent to the fixed-base generalized inertia of the mechanism. The block $\boldsymbol{M}_{bq}(\boldsymbol{q})$ is the coupling between the base and the joints motion. By further partitioning $\boldsymbol{M}_b(\boldsymbol{q})$ and $\boldsymbol{M}_{bq}(\boldsymbol{q})$ in translational and rotational components, it is written

$$\begin{aligned} \boldsymbol{M}_b(\boldsymbol{q}) &= \begin{bmatrix} \boldsymbol{M}_v & \boldsymbol{M}_{v\omega}(\boldsymbol{q}) \\ \boldsymbol{M}_{v\omega}(\boldsymbol{q})^T & \boldsymbol{M}_\omega(\boldsymbol{q}) \end{bmatrix}, & \boldsymbol{M}_v &= m\boldsymbol{E} \in \mathbb{R}^{3\times 3} \\ \boldsymbol{M}_{bq}(\boldsymbol{q}) &= \begin{bmatrix} \boldsymbol{M}_{vq}(\boldsymbol{q}) \\ \boldsymbol{M}_{\omega q}(\boldsymbol{q}) \end{bmatrix} & \boldsymbol{M}_{v\omega}(\boldsymbol{q}) &= -m\left[\boldsymbol{o}_{bc}(\boldsymbol{q})\right]^\wedge \in \mathbb{R}^{3\times 3} \end{aligned} \tag{2.35}$$

where $m = \sum_{j=0}^{n} m^{(j)} \in \mathbb{R}$ is the mass of the whole robot, and where $\boldsymbol{o}_{bc}(\boldsymbol{q})$ is the position vector from $\mathcal{B}$ to $\mathcal{C}$; its derivation is explained in the next section. The expressions of $\boldsymbol{M}_\omega(\boldsymbol{q}) \in \mathbb{R}^{3\times 3}$, $\boldsymbol{M}_{vq}(\boldsymbol{q}) \in \mathbb{R}^{3\times n}$, and $\boldsymbol{M}_{\omega q}(\boldsymbol{q}) \in \mathbb{R}^{3\times n}$ are omitted for brevity.

2.2.2. CoM and Momentum

The position of the CoM of the whole robot is defined as the point located at the mass-weighted average position of all bodies, as

$$\boldsymbol{o}_c := \frac{1}{m} \sum_{j=0}^{n} m^{(j)} \boldsymbol{o}_j. \tag{2.36}$$

The position vector from $\mathcal{B}$ to $\mathcal{C}$ is computed as[12] $\boldsymbol{o}_{bc}(\boldsymbol{q}) = \boldsymbol{R}_b^T (\boldsymbol{o}_c - \boldsymbol{o}_b)$, which by applying (2.36) and (2.15) results in the form

$$\boldsymbol{o}_{bc}(\boldsymbol{q}) = \frac{1}{m} \sum_{j=0}^{n} m^{(j)} \boldsymbol{o}_{bj}(\boldsymbol{q}). \tag{2.37}$$

Based on this, the position of the CoM can be expressed as a function of the rotation of the base and of the joint angles, as

$$\boldsymbol{o}_c = \boldsymbol{o}_b + \boldsymbol{R}_b \, \boldsymbol{o}_{bc}(\boldsymbol{q}). \tag{2.38}$$

The total momentum $\boldsymbol{h}_c = \begin{bmatrix} \boldsymbol{p} \\ \boldsymbol{l}_c \end{bmatrix} \in \mathbb{R}^6$ of the whole robot around its CoM – also referred to as "centroidal" momentum [OGL13] – is defined as

$$\boldsymbol{h}_c := \sum_{j=0}^{n} \boldsymbol{A}_{cj}(\boldsymbol{R}_b, \boldsymbol{q})^{-T} \boldsymbol{h}_j^{(j)} = \sum_{j=0}^{n} \boldsymbol{A}_{cb}(\boldsymbol{R}_b, \boldsymbol{q})^{-T} \boldsymbol{A}_{bj}(\boldsymbol{q})^{-T} \boldsymbol{\Lambda}_j^{(j)} \boldsymbol{\nu}_j, \tag{2.39}$$

[12] Remark that the frame $\mathcal{C}$ is aligned with the inertial frame $\mathcal{O}$ by definition, i.e., it holds $\boldsymbol{R}_c = \boldsymbol{E}$ and thus $\boldsymbol{R}_b = \boldsymbol{R}_b$.

where $\boldsymbol{p}, \boldsymbol{l}_c \in \mathbb{R}^3$ are the total linear momentum and the total angular momentum around $\mathcal{C}$, respectively, both expressed in the frame $\mathcal{C}$, and where $\boldsymbol{h}_j^{(j)} = \boldsymbol{\Lambda}_j^{(j)} \boldsymbol{\nu}_j \in \mathbb{R}^6$ is the momentum of the j^{th} body around its body frame $\mathcal{J}$. Note that $\boldsymbol{A}_{cb}(\boldsymbol{R}_b, \boldsymbol{q})$ is only function of the rotation of the base and of the joint angles; by applying the property $\boldsymbol{R}[\boldsymbol{o}]^\wedge \boldsymbol{R}^T = [\boldsymbol{R}\boldsymbol{o}]^\wedge$ of a skew-symmetric matrix, it can be written

$$\boldsymbol{A}_{cb}(\boldsymbol{R}_b, \boldsymbol{q}) = \begin{bmatrix} \boldsymbol{R}_b & -\boldsymbol{R}_b \left[\boldsymbol{o}_{bc}(\boldsymbol{q})\right]^\wedge \\ \boldsymbol{0} & \boldsymbol{R}_b \end{bmatrix}. \tag{2.40}$$

The velocity of the CoM, i.e., $\boldsymbol{v}_c = \frac{d}{dt}(\boldsymbol{o}_c)$, is related to the momentum by

$$\boldsymbol{v}_c = \frac{1}{m}\boldsymbol{p} = \frac{1}{m}\boldsymbol{S}_v \boldsymbol{h}_c, \tag{2.41}$$

where $\boldsymbol{S}_v = \begin{bmatrix} \boldsymbol{E} & \boldsymbol{0} \end{bmatrix} \in \mathbb{R}^{3\times 6}$. By using the kinematics equations (2.16b), the momentum can be expressed in terms of the motions of the base and of the joints, as

$$\boldsymbol{h}_c = \left(\boldsymbol{A}_{cb}(\boldsymbol{R}_b, \boldsymbol{q})^{-T} \sum_{j=0}^{n} \boldsymbol{A}_{jb}(\boldsymbol{q})^T \boldsymbol{\Lambda}_j^{(j)} \boldsymbol{A}_{jb}(\boldsymbol{q}) \right) \boldsymbol{\nu}_b + \left(\boldsymbol{A}_{cb}(\boldsymbol{R}_b, \boldsymbol{q})^{-T} \sum_{j=0}^{n} \boldsymbol{A}_{jb}(\boldsymbol{q})^T \boldsymbol{\Lambda}_j^{(j)} \boldsymbol{J}_{jq}(\boldsymbol{q}) \right) \dot{\boldsymbol{q}}. \tag{2.42a}$$

By using the expressions of the partitioned matrices in (2.34) and (2.35) it is straightforward to see that the CoM position, velocity, and the momentum are compactly related to the inertia matrix by

$$\boldsymbol{o}_c = \boldsymbol{o}_b - \boldsymbol{R}_b \boldsymbol{M}_v^{-1} \left[\boldsymbol{M}_{v\omega}(\boldsymbol{q})\right]^\vee, \tag{2.43a}$$

$$\boldsymbol{h}_c = \boldsymbol{L}(\boldsymbol{R}_b, \boldsymbol{q}) \begin{bmatrix} \boldsymbol{\nu}_b \\ \dot{\boldsymbol{q}} \end{bmatrix} = \boldsymbol{L}(\boldsymbol{R}_b, \boldsymbol{q}) \boldsymbol{v}, \tag{2.43b}$$

$$\boldsymbol{v}_c = \boldsymbol{L}_v(\boldsymbol{R}_b, \boldsymbol{q}) \begin{bmatrix} \boldsymbol{v}_b \\ \boldsymbol{\omega}_b \\ \dot{\boldsymbol{q}} \end{bmatrix} = \boldsymbol{L}_v(\boldsymbol{R}_b, \boldsymbol{q}) \boldsymbol{v}. \tag{2.43c}$$

where the matrices $\boldsymbol{L}(\boldsymbol{R}_b, \boldsymbol{q}) \in \mathbb{R}^{6\times(6+n)}$ and $\boldsymbol{L}_v(\boldsymbol{R}_b, \boldsymbol{q}) \in \mathbb{R}^{3\times(6+n)}$ are given by

$$\boldsymbol{L}(\boldsymbol{R}_b, \boldsymbol{q}) = \boldsymbol{A}_{cb}(\boldsymbol{R}_b, \boldsymbol{q})^{-T} \begin{bmatrix} \boldsymbol{M}_b(\boldsymbol{q}) & \boldsymbol{M}_{bq}(\boldsymbol{q}) \end{bmatrix}, \tag{2.44a}$$

$$\boldsymbol{L}_v(\boldsymbol{R}_b, \boldsymbol{q}) = \frac{1}{m}\boldsymbol{S}_v \boldsymbol{L}(\boldsymbol{R}_b, \boldsymbol{q}) = \boldsymbol{R}_b \frac{1}{m} \begin{bmatrix} \boldsymbol{M}_v & \boldsymbol{M}_{v\omega}(\boldsymbol{q}) & \boldsymbol{M}_{vq}(\boldsymbol{q}) \end{bmatrix}. \tag{2.44b}$$

For later reference, the expression (2.44b) is further simplified by using the expressions of $\boldsymbol{M}_v$ and $\boldsymbol{M}_{v\omega}(\boldsymbol{q})$ in (2.35), as

$$\boldsymbol{L}_v(\boldsymbol{R}_b, \boldsymbol{q}) = \boldsymbol{R}_b \begin{bmatrix} \boldsymbol{E} & -\left[\boldsymbol{o}_{bc}(\boldsymbol{q})\right]^\wedge & \frac{1}{m}\boldsymbol{M}_{vq}(\boldsymbol{q}) \end{bmatrix}. \tag{2.44c}$$

2.2.3. Properties of the dynamic matrices

In this section some properties of the dynamic matrices are stated, which are important for the simplification of the analysis of the controllers.

Property 2.1 (Positive definiteness)**.** *The inertia matrix $\boldsymbol{M}(\boldsymbol{q})$ is symmetric and positive definite, i.e.,*

$$\boldsymbol{M}(\boldsymbol{q}) = \boldsymbol{M}(\boldsymbol{q})^T, \quad \boldsymbol{y}^T \boldsymbol{M}(\boldsymbol{q}) \boldsymbol{y} > 0 \qquad \forall \boldsymbol{q} \in \mathbb{R}^n, \forall \boldsymbol{y} \neq \boldsymbol{0} \in \mathbb{R}^{6+n}.$$

Property 2.2 (Skew symmetry or Passivity)**.** *The matrix* $\dot{\boldsymbol{M}}(\boldsymbol{q}) - 2\boldsymbol{C}(\boldsymbol{q}, \boldsymbol{\upsilon})$ *is skew symmetric, i.e.,*

$$\boldsymbol{y}^T \left(\dot{\boldsymbol{M}}(\boldsymbol{q}) - 2\boldsymbol{C}(\boldsymbol{q}, \boldsymbol{\upsilon}) \right) \boldsymbol{y} = 0 \qquad \forall \boldsymbol{q} \in \mathbb{R}^n,\ \forall \boldsymbol{y}, \boldsymbol{\upsilon} \in \mathbb{R}^{6+n},$$

or, equivalently,

$$\dot{\boldsymbol{M}}(\boldsymbol{q}) = \boldsymbol{C}(\boldsymbol{q}, \boldsymbol{\upsilon}) + \boldsymbol{C}(\boldsymbol{q}, \boldsymbol{\upsilon})^T \qquad \forall \boldsymbol{q} \in \mathbb{R}^n,\ \forall \boldsymbol{\upsilon} \in \mathbb{R}^{6+n}.$$

Proof. Notice that $\boldsymbol{J}_j(\boldsymbol{q})^T \boldsymbol{\Psi}_j^{(j)}(\boldsymbol{\nu}_j) \boldsymbol{J}_j(\boldsymbol{q})$ in (2.31) is a skew-symmetric matrix, then

$$\boldsymbol{C}(\boldsymbol{q}, \boldsymbol{\upsilon}) + \boldsymbol{C}(\boldsymbol{q}, \boldsymbol{\upsilon})^T = \sum_{j=0}^{n} \dot{\boldsymbol{J}}_j(\boldsymbol{q})^T \boldsymbol{\Lambda}_j^{(j)} \boldsymbol{J}_j(\boldsymbol{q}) + \boldsymbol{J}_j(\boldsymbol{q})^T \boldsymbol{\Lambda}_j^{(j)} \dot{\boldsymbol{J}}_j(\boldsymbol{q}) = \dot{\boldsymbol{M}}(\boldsymbol{q}).$$

□

Property 2.3 (Boundedness of inertia)**.** *The eigenvalues* $\lambda_i(\boldsymbol{M}(\boldsymbol{q})) \in \mathbb{R}_+, i = 1, \ldots, 6+n$, *keep bounded, i.e., there exists* $\lambda_{M,min}, \lambda_{M,max} \in \mathbb{R}_+$ *such that*

$$0 < \lambda_{M,min} \leq \lambda_i(\boldsymbol{M}(\boldsymbol{q})) \leq \lambda_{M,max}, \qquad \forall i = 1, \ldots, 6+n,\ \forall \boldsymbol{q} \in \mathbb{R}^n,$$

where

$$\lambda_{M,min} = \inf_{\boldsymbol{q} \in \mathbb{R}^n} \min_{i=1,\ldots,6+n} \lambda_i(\boldsymbol{M}((\boldsymbol{q})), \qquad \lambda_{M,max} = \sup_{\boldsymbol{q} \in \mathbb{R}^n} \max_{i=1,\ldots,6+n} \lambda_i(\boldsymbol{M}(\boldsymbol{q})). \tag{2.45}$$

Property 2.1, Property 2.2, and Property 2.3 are standard in the context of fixed-base manipulators [SSVO09], and have been formalized also in the context of vehicle-manipulator systems [FGP14].

Property 2.4 (Conservation structure)**.** *For the maps* $\boldsymbol{L}(\boldsymbol{R}_b, \boldsymbol{q})$ *and* $\boldsymbol{L}_v(\boldsymbol{R}_b, \boldsymbol{q})$*, it hold*

$$\left(\dot{\boldsymbol{L}}(\boldsymbol{R}_b, \boldsymbol{q}) - \boldsymbol{L}(\boldsymbol{R}_b, \boldsymbol{q}) \boldsymbol{M}(\boldsymbol{q})^{-1} \boldsymbol{C}(\boldsymbol{q}, \boldsymbol{\upsilon}) \right) \boldsymbol{\upsilon} = \boldsymbol{0}, \tag{2.46a}$$

$$\left(\dot{\boldsymbol{L}}_v(\boldsymbol{R}_b, \boldsymbol{q}) - \boldsymbol{L}_v(\boldsymbol{R}_b, \boldsymbol{q}) \boldsymbol{M}(\boldsymbol{q})^{-1} \boldsymbol{C}(\boldsymbol{q}, \boldsymbol{\upsilon}) \right) \boldsymbol{\upsilon} = \boldsymbol{0}, \tag{2.46b}$$

$\forall \boldsymbol{q} \in \mathbb{R}^n,\ \forall \boldsymbol{\upsilon} \in \mathbb{R}^{6+n}$.

Proof. According to Newton's third law, only external wrenches do change the total momentum of the system. Therefore, projecting around $\mathcal{C}$ all external forces acting on the system, it must be

$$\dot{\boldsymbol{h}}_c = \boldsymbol{A}_{bc}(\boldsymbol{R}_b, \boldsymbol{q})^T \boldsymbol{\mathcal{F}}_b + \sum_{j=0}^{n} \boldsymbol{A}_{jc}(\boldsymbol{R}_b, \boldsymbol{q})^T \boldsymbol{\mathcal{F}}_j^{ext}. \tag{2.47}$$

Let us now re-derive $\dot{\boldsymbol{h}}_c$ by taking the time derivative of (2.43b), as

$$\begin{aligned} \dot{\boldsymbol{h}}_c = \dot{\boldsymbol{L}}(\boldsymbol{R}_b, \boldsymbol{q}) \boldsymbol{\upsilon} + \boldsymbol{L}(\boldsymbol{R}_b, \boldsymbol{q}) \dot{\boldsymbol{\upsilon}} = \left(\dot{\boldsymbol{L}}(\boldsymbol{R}_b, \boldsymbol{q}) - \boldsymbol{L}(\boldsymbol{R}_b, \boldsymbol{q}) \boldsymbol{M}(\boldsymbol{q})^{-1} \boldsymbol{C}(\boldsymbol{q}, \boldsymbol{\upsilon}) \right) \boldsymbol{\upsilon} + \\ + \boldsymbol{L}(\boldsymbol{R}_b, \boldsymbol{q}) \boldsymbol{M}(\boldsymbol{q})^{-1} \boldsymbol{\varsigma} + \boldsymbol{L}(\boldsymbol{R}_b, \boldsymbol{q}) \boldsymbol{M}(\boldsymbol{q})^{-1} \sum_{j=0}^{n} \boldsymbol{J}_j(\boldsymbol{q})^T \boldsymbol{\mathcal{F}}_j^{ext}, \end{aligned} \tag{2.48}$$

where (2.29) is used. The inverse $\boldsymbol{M}(\boldsymbol{q})^{-1}$ can be obtained by inversion of the partitioned inertia matrix in (2.33), as

$$\boldsymbol{M}(\boldsymbol{q})^{-1}=\begin{bmatrix}\boldsymbol{M}_b(\boldsymbol{q})^{-1}+\boldsymbol{M}_b(\boldsymbol{q})^{-1}\boldsymbol{M}_{bq}(\boldsymbol{q})\boldsymbol{M}_q^*(\boldsymbol{q})^{-1}\boldsymbol{M}_{bq}(\boldsymbol{q})^T\boldsymbol{M}_b(\boldsymbol{q})^{-1} & -\boldsymbol{M}_b(\boldsymbol{q})^{-1}\boldsymbol{M}_{bq}(\boldsymbol{q})\boldsymbol{M}_q^*(\boldsymbol{q})^{-1} \\ -\boldsymbol{M}_q^*(\boldsymbol{q})^{-1}\boldsymbol{M}_{bq}(\boldsymbol{q})^T\boldsymbol{M}_b(\boldsymbol{q})^{-1} & \boldsymbol{M}_q^*(\boldsymbol{q})^{-1}\end{bmatrix} \tag{2.49}$$

where

$$\boldsymbol{M}_q^*(\boldsymbol{q}) = \boldsymbol{M}_q - \boldsymbol{M}_{bq}(\boldsymbol{q})^T\boldsymbol{M}_b(\boldsymbol{q})^{-1}\boldsymbol{M}_{bq} \in \mathbb{R}^{(6+n)\times(6+n)}.$$

is the reduced joint inertia. Then, by combining the equations (2.44a) and (2.49) it results $\boldsymbol{L}(\boldsymbol{R}_b,\boldsymbol{q})\boldsymbol{M}(\boldsymbol{q})^{-1} = \begin{bmatrix}\boldsymbol{A}_{bc}(\boldsymbol{R}_b,\boldsymbol{q})^T & \boldsymbol{0}\end{bmatrix}$, and in turn (2.48) reduces to

$$\dot{\boldsymbol{h}}_c = \Big(\dot{\boldsymbol{L}}(\boldsymbol{R}_b,\boldsymbol{q}) - \boldsymbol{L}(\boldsymbol{R}_b,\boldsymbol{q})\boldsymbol{M}(\boldsymbol{q})^{-1}\boldsymbol{C}(\boldsymbol{q},\boldsymbol{\upsilon})\Big)\,\boldsymbol{\upsilon} + \boldsymbol{A}_{bc}(\boldsymbol{R}_b,\boldsymbol{q})^T\boldsymbol{\mathcal{F}}_b + \boldsymbol{A}_{jc}(\boldsymbol{R}_b,\boldsymbol{q})^T\boldsymbol{\mathcal{F}}_j^{ext}. \tag{2.50}$$

where (2.17) is used. Comparing (2.47) and (2.50) for all $\boldsymbol{\upsilon}\in\mathbb{R}^{6+n}$, $\boldsymbol{\mathcal{F}}_b\in\mathbb{R}^6$, and $\boldsymbol{\mathcal{F}}_j^{ext}\in\mathbb{R}^6$, a constraint for the motion is then obtained as

$$\Big(\dot{\boldsymbol{L}}(\boldsymbol{R}_b,\boldsymbol{q}) - \boldsymbol{L}(\boldsymbol{R}_b,\boldsymbol{q})\boldsymbol{M}(\boldsymbol{q})^{-1}\boldsymbol{C}(\boldsymbol{q},\boldsymbol{\upsilon})\Big)\,\boldsymbol{\upsilon} = \boldsymbol{0}, \tag{2.51}$$

thereby proving (2.46a). A similar constraint is obtained straightforwardly for the CoM velocity by pre-multiplying (2.51) by $\frac{1}{m}\boldsymbol{S}_v$, as

$$\Big(\dot{\boldsymbol{L}}_v(\boldsymbol{R}_b,\boldsymbol{q}) - \boldsymbol{L}_v(\boldsymbol{R}_b,\boldsymbol{q})\boldsymbol{M}(\boldsymbol{q})^{-1}\boldsymbol{C}(\boldsymbol{q},\boldsymbol{\upsilon})\Big)\,\boldsymbol{\upsilon} = \boldsymbol{0}, \tag{2.52}$$

wherein the relation (2.44b) is used, as well as its time derivative $\dot{\boldsymbol{L}}_v(\boldsymbol{q}) = \frac{1}{m}\boldsymbol{S}_v\dot{\boldsymbol{L}}(\boldsymbol{q})$, are applied. This concludes the proof of also (2.46b) □

2.3. Model of a robot with an arm and reaction wheels

In this section, the kinematics and dynamics models are written for the particular case of a space robot equipped with one manipulator with $n_m \in \mathbb{N}$ degrees of freedom and an additional set of $n_w \in \mathbb{N}$ spacecraft-mounted reaction wheels (see Fig. 2.3).

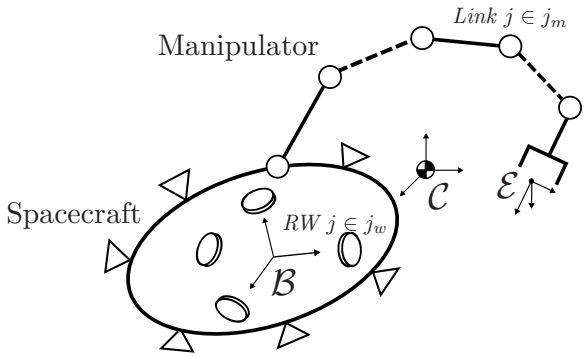

Figure 2.3.: Schematic representation of components of the orbital robot equipped with one arm and a set of spacecraft-mounted Reaction Wheels (RWs).

By denoting as $\boldsymbol{q}_w \in \mathbb{R}^{n_w}$ and $\boldsymbol{q}_m \in \mathbb{R}^{n_m}$ the joint angles of the wheels and of the manipulator, respectively, the robot is thus composed of $n = n_w + n_m$ joints with angles

$\boldsymbol{q} = \begin{bmatrix}\boldsymbol{q}_w^T & \boldsymbol{q}_m^T\end{bmatrix}^T \in \mathbb{R}^{n_w+n_m}$. The indexes of the wheels' rotating bodies are listed in a set $j_w \subset \mathbb{N}$, whereas the indexes of the links of the arm are listed in a set $j_m \subset \mathbb{N}$. The motion of the robot is represented by $\boldsymbol{\upsilon} = \begin{bmatrix}\boldsymbol{\nu}_b^T & \dot{\boldsymbol{q}}_w^T & \dot{\boldsymbol{q}}_m^T\end{bmatrix}^T \in \mathbb{R}^{6+n_w+n_m}$.
The j^{th} Jacobian $\boldsymbol{J}_{jq}(\boldsymbol{q}_m) \in \mathbb{R}^{6\times(n_w+n_m)}$ is partitioned in wheels and arm components, as

$$\boldsymbol{J}_{jq}(\boldsymbol{q}_m) = \begin{bmatrix}\boldsymbol{J}_{jw} & \boldsymbol{J}_{jm}(\boldsymbol{q}_m)\end{bmatrix}, \tag{2.53}$$

where $\boldsymbol{J}_{jw} \in \mathbb{R}^{6\times n_w}$ and $\boldsymbol{J}_{jm}(\boldsymbol{q}_m) \in \mathbb{R}^{6\times n_m}$ are the components associated to the joints of the wheels and of the manipulators, respectively. Note that for $j \in j_w$ it is $\boldsymbol{J}_{jm}(\boldsymbol{q}_m) = \boldsymbol{0}$, and for $j \in j_m$ it is $\boldsymbol{J}_{jw} = \boldsymbol{0}$. Accordingly, the end-effector Jacobian $\boldsymbol{J}_{eq}(\boldsymbol{q}_m) \in \mathbb{R}^{6\times(n_w+n_m)}$ is partitioned as

$$\boldsymbol{J}_{eq}(\boldsymbol{q}_m) = \begin{bmatrix}\boldsymbol{0} & \boldsymbol{J}_{em}(\boldsymbol{q}_m)\end{bmatrix}, \tag{2.54}$$

where $\boldsymbol{J}_{em}(\boldsymbol{q}_m) \in \mathbb{R}^{6\times n_m}$ is equivalent to the fixed-base end-effector Jacobian of the arm. Similarly, the blocks $\boldsymbol{M}_{bq}(\boldsymbol{q}_m) \in \mathbb{R}^{6\times(n_w+n_m)}$ and $\boldsymbol{M}_q(\boldsymbol{q}_m) \in \mathbb{R}^{(n_w+n_m)\times(n_w+n_m)}$ of the inertia, are partitioned in wheels and manipulator components, as

$$\boldsymbol{M}_{bq}(\boldsymbol{q}_m) = \begin{bmatrix}\boldsymbol{M}_{bw} & \boldsymbol{M}_{bm}(\boldsymbol{q}_m)\end{bmatrix}, \tag{2.55a}$$

$$\boldsymbol{M}_q(\boldsymbol{q}_m) = \begin{bmatrix}\boldsymbol{M}_w & \boldsymbol{0} \\ \boldsymbol{0} & \boldsymbol{M}_m(\boldsymbol{q}_m)\end{bmatrix}, \tag{2.55b}$$

where $\boldsymbol{M}_{bw} \in \mathbb{R}^{6\times n_w}$ and $\boldsymbol{M}_{bm}(\boldsymbol{q}_m) \in \mathbb{R}^{6\times n_m}$ are the base-wheels and base-arm inertia couplings, respectively, and where $\boldsymbol{M}_w \in \mathbb{R}^{n_w\times n_w}$ and $\boldsymbol{M}_m(\boldsymbol{q}_m) \in \mathbb{R}^{n_m\times n_m}$ are the wheels and arm inertias, respectively. The couplings are partitioned in translation and rotation, as

$$\boldsymbol{M}_{bw} = \begin{bmatrix}\boldsymbol{0} \\ \boldsymbol{M}_{\omega w}\end{bmatrix}, \qquad \boldsymbol{M}_{bm}(\boldsymbol{q}_m) = \begin{bmatrix}\boldsymbol{M}_{vm}(\boldsymbol{q}_m) \\ \boldsymbol{M}_{\omega m}(\boldsymbol{q}_m)\end{bmatrix}, \tag{2.56}$$

where $\boldsymbol{M}_{vm}(\boldsymbol{q}_m) \in \mathbb{R}^{3\times n_m}$ is the coupling between the linear velocity of the base and the joints of the arm, $\boldsymbol{M}_{\omega m}(\boldsymbol{q}_m) \in \mathbb{R}^{3\times n_m}$ is the coupling between the angular velocity of the base and the joints of the arm, and $\boldsymbol{M}_{\omega w} \in \mathbb{R}^{3\times n_w}$ is the coupling between the angular velocity of the base and the joints of the reaction wheels. Notice that the joint inertia in (2.55b) is block-decoupled because the wheels and the arm are on separate branches of the kinematic chain; furthermore, notice that translational coupling of the reaction wheels in (2.56) is zero because they rotate around a fixed axis.
Based on the above partitionings, the kinematics of the end-effector is given by

$$\boldsymbol{H}_e = \boldsymbol{H}_b\boldsymbol{H}_{be}(\boldsymbol{q}_m), \tag{2.57a}$$

$$\boldsymbol{\nu}_e = \boldsymbol{A}_{eb}(\boldsymbol{q}_m)\begin{bmatrix}\boldsymbol{v}_b \\ \boldsymbol{\omega}_b\end{bmatrix} + \boldsymbol{J}_{em}(\boldsymbol{q}_m)\dot{\boldsymbol{q}}_m, \tag{2.57b}$$

and the dynamics equations are given by

$$\underbrace{\begin{bmatrix}\boldsymbol{M}_b(\boldsymbol{q}_m) & \boldsymbol{M}_{bw} & \boldsymbol{M}_{bm}(\boldsymbol{q}_m) \\ \boldsymbol{M}_{bw}^T & \boldsymbol{M}_w & \boldsymbol{0} \\ \boldsymbol{M}_{bm}(\boldsymbol{q}_m)^T & \boldsymbol{0} & \boldsymbol{M}_m(\boldsymbol{q}_m)\end{bmatrix}}_{\boldsymbol{M}(\boldsymbol{q}_m)}\begin{bmatrix}\dot{\boldsymbol{\nu}}_b \\ \ddot{\boldsymbol{q}}_w \\ \ddot{\boldsymbol{q}}_m\end{bmatrix} + \underbrace{\begin{bmatrix}\boldsymbol{C}_b(\boldsymbol{q}_m,\boldsymbol{\upsilon}) & \boldsymbol{C}_{bw}(\boldsymbol{q}_m,\boldsymbol{\upsilon}) & \boldsymbol{C}_{bm}(\boldsymbol{q}_m,\boldsymbol{\upsilon}) \\ \boldsymbol{C}_{wb}(\boldsymbol{q}_m,\boldsymbol{\upsilon}) & \boldsymbol{C}_w(\boldsymbol{q}_m,\boldsymbol{\upsilon}) & \boldsymbol{C}_{wm}(\boldsymbol{q}_m,\boldsymbol{\upsilon}) \\ \boldsymbol{C}_{mb}(\boldsymbol{q}_m,\boldsymbol{\upsilon}) & \boldsymbol{C}_{mw}(\boldsymbol{q}_m,\boldsymbol{\upsilon}) & \boldsymbol{C}_m(\boldsymbol{q}_m,\boldsymbol{\upsilon})\end{bmatrix}}_{\boldsymbol{C}(\boldsymbol{q}_m,\boldsymbol{\upsilon})}\underbrace{\begin{bmatrix}\boldsymbol{\nu}_b \\ \dot{\boldsymbol{q}}_w \\ \dot{\boldsymbol{q}}_m\end{bmatrix}}_{\boldsymbol{\upsilon}} =$$

$$= \begin{bmatrix}\boldsymbol{\mathcal{F}}_b \\ \boldsymbol{\tau}_w \\ \boldsymbol{\tau}_m\end{bmatrix} + \sum_{j=0}^{n}\begin{bmatrix}\boldsymbol{A}_{jb}(\boldsymbol{q}_m)^T \\ \boldsymbol{J}_{jw}^T \\ \boldsymbol{J}_{jm}(\boldsymbol{q}_m)^T\end{bmatrix}\boldsymbol{\mathcal{F}}_j^{ext}, \tag{2.58}$$

where $\boldsymbol{\tau}_w \in \mathbb{R}^{n_w}$ and $\boldsymbol{\tau}_m \in \mathbb{R}^{n_m}$ denote the torques in the joints of the wheels and the arm, respectively, and where $\boldsymbol{\mathcal{F}}_b$ denotes the resulting wrench realized by a set of spacecraft-mounted thrusters. The inertia and Coriolis matrices have dimensions $\boldsymbol{M}(\boldsymbol{q}_m) \in \mathbb{R}^{n_m \times n_m}$ and $\boldsymbol{C}(\boldsymbol{q}_m, \boldsymbol{\upsilon}) \in \mathbb{R}^{n_m \times n_m}$, respectively. The momentum and CoM velocity maps have dimensions $\boldsymbol{L}(\boldsymbol{R}_b, \boldsymbol{q}_m) \in \mathbb{R}^{6\times(n_w+n_m)}$ and $\boldsymbol{L}_v(\boldsymbol{R}_b, \boldsymbol{q}_m) \in \mathbb{R}^{3\times(n_w+n_m)}$, respectively, and have the form

$$\boldsymbol{L}(\boldsymbol{R}_b, \boldsymbol{q}_m) = \boldsymbol{A}_{cb}(\boldsymbol{R}_b, \boldsymbol{q}_m)^{-T} \begin{bmatrix} \boldsymbol{M}_b(\boldsymbol{q}_m) & \boldsymbol{M}_{bw} & \boldsymbol{M}_{bm}(\boldsymbol{q}_m) \end{bmatrix}, \tag{2.59a}$$

$$\boldsymbol{L}_v(\boldsymbol{R}_b, \boldsymbol{q}_m) = \frac{1}{m}\boldsymbol{S}_v\boldsymbol{L}(\boldsymbol{R}_b, \boldsymbol{q}_m) = \boldsymbol{R}_b\frac{1}{m}\begin{bmatrix} \boldsymbol{M}_v & \boldsymbol{M}_{v\omega}(\boldsymbol{q}_m) & \boldsymbol{0} & \boldsymbol{M}_{vm}(\boldsymbol{q}_m) \end{bmatrix}. \tag{2.59b}$$

Lastly, the position of the CoM is given by

$$\boldsymbol{o}_c = \boldsymbol{o}_b - \boldsymbol{R}_b\boldsymbol{M}_v^{-1}\left[\boldsymbol{M}_{v\omega}(\boldsymbol{q}_m)\right]^\vee. \tag{2.60}$$

Notice that all quantities in the above relations are not functionally depending on the joint angles of the wheels, as a consequence of Assumption 2.6. However, the Coriolis/centrifugal matrix still depends of the joint velocities of the reaction wheels, which are dynamically coupled with the rest of the system via gyroscopic effects.

2.4. Model of a robot with an arm

In this section, the model is written for the particular case of a space robot equipped with one manipulator (see Fig. 2.4).

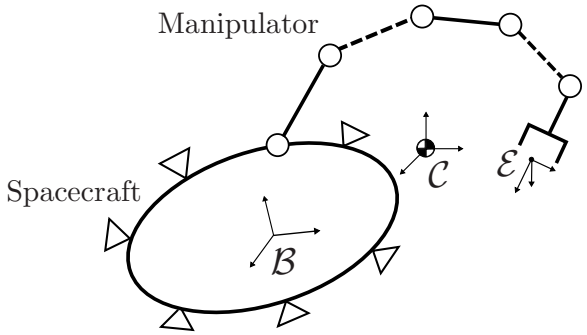

Figure 2.4.: Schematic representation of components of the orbital robot equipped with one arm.

The joint angles are trivially $\boldsymbol{q} = \boldsymbol{q}_m \in \mathbb{R}^{n_m}$, the motion of the robot is represented by the vector $\boldsymbol{\upsilon} = \begin{bmatrix}\boldsymbol{\nu}_b^T & \dot{\boldsymbol{q}}_m^T\end{bmatrix}^T \in \mathbb{R}^{6+n_m}$. The Jacobians, and the coupling and joint inertia matrices are trivially given by

$$\boldsymbol{J}_{jq}(\boldsymbol{q}_m) = \boldsymbol{J}_{jm}(\boldsymbol{q}_m), \tag{2.61a}$$

$$\boldsymbol{J}_{eq}(\boldsymbol{q}_m) = \boldsymbol{J}_{em}(\boldsymbol{q}_m), \tag{2.61b}$$

$$\boldsymbol{M}_{bq}(\boldsymbol{q}_m) = \boldsymbol{M}_{bm}(\boldsymbol{q}_m), \tag{2.61c}$$

$$\boldsymbol{M}_q(\boldsymbol{q}_m) = \boldsymbol{M}_m(\boldsymbol{q}_m). \tag{2.61d}$$

Note that manipulator sub-blocks are the same as the case of robot with reaction wheels. For later use, let us mention that the translation and rotation components of $\boldsymbol{M}_{bq}(\boldsymbol{q}_m)$

given by (2.35), are

$$\boldsymbol{M}_{vq}(\boldsymbol{q}_m) = \boldsymbol{M}_{vm}(\boldsymbol{q}_m), \tag{2.61e}$$
$$\boldsymbol{M}_{\omega q}(\boldsymbol{q}_m) = \boldsymbol{M}_{\omega m}(\boldsymbol{q}_m). \tag{2.61f}$$

The kinematics of the end-effector is given by the same relations as in (2.57), whereas the dynamics equations simplify to

$$\underbrace{\begin{bmatrix} \boldsymbol{M}_b(\boldsymbol{q}_m) & \boldsymbol{M}_{bm}(\boldsymbol{q}_m) \\ \boldsymbol{M}_{bm}(\boldsymbol{q}_m)^T & \boldsymbol{M}_m(\boldsymbol{q}_m) \end{bmatrix}}_{\boldsymbol{M}(\boldsymbol{q}_m)} \begin{bmatrix} \dot{\boldsymbol{\nu}}_b \\ \ddot{\boldsymbol{q}}_m \end{bmatrix} + \underbrace{\begin{bmatrix} \boldsymbol{C}_b(\boldsymbol{q}_m, \boldsymbol{\upsilon}) & \boldsymbol{C}_{bm}(\boldsymbol{q}_m, \boldsymbol{\upsilon}) \\ \boldsymbol{C}_{mb}(\boldsymbol{q}_m, \boldsymbol{\upsilon}) & \boldsymbol{C}_m(\boldsymbol{q}_m, \boldsymbol{\upsilon}) \end{bmatrix} \begin{bmatrix} \boldsymbol{\nu}_b \\ \dot{\boldsymbol{q}}_m \end{bmatrix}}_{\boldsymbol{C}(\boldsymbol{q}_m, \boldsymbol{\upsilon})\ \boldsymbol{\upsilon}} = \begin{bmatrix} \boldsymbol{\mathcal{F}}_b \\ \boldsymbol{\tau}_m \end{bmatrix} + \sum_{j=0}^{n} \begin{bmatrix} \boldsymbol{A}_{jb}(\boldsymbol{q}_m)^T \\ \boldsymbol{J}_{jm}(\boldsymbol{q}_m)^T \end{bmatrix} \boldsymbol{\mathcal{F}}_j^{ext}, \tag{2.62}$$

The inertia and Coriolis matrices have dimensions $\boldsymbol{M}(\boldsymbol{q}_m) \in \mathbb{R}^{n_m \times n_m}$ and $\boldsymbol{C}(\boldsymbol{q}_m, \boldsymbol{\upsilon}) \in \mathbb{R}^{n_m \times n_m}$, respectively. The momentum and CoM velocity maps have dimensions $\boldsymbol{L}(\boldsymbol{R}_b, \boldsymbol{q}_m) \in \mathbb{R}^{6 \times n_m}$ and $\boldsymbol{L}_v(\boldsymbol{R}_b, \boldsymbol{q}_m) \in \mathbb{R}^{3 \times n_m}$, respectively, and have the form

$$\boldsymbol{L}(\boldsymbol{R}_b, \boldsymbol{q}_m) = \boldsymbol{A}_{cb}(\boldsymbol{R}_b, \boldsymbol{q}_m)^{-T} \begin{bmatrix} \boldsymbol{M}_b(\boldsymbol{q}_m) & \boldsymbol{M}_{bm}(\boldsymbol{q}_m) \end{bmatrix}, \tag{2.63a}$$
$$\boldsymbol{L}_v(\boldsymbol{R}_b, \boldsymbol{q}_m) = \frac{1}{m} \boldsymbol{S}_v \boldsymbol{L}(\boldsymbol{R}_b, \boldsymbol{q}_m) = \boldsymbol{R}_b \frac{1}{m} \begin{bmatrix} \boldsymbol{M}_v & \boldsymbol{M}_{v\omega}(\boldsymbol{q}_m) & \boldsymbol{M}_{vm}(\boldsymbol{q}_m) \end{bmatrix}. \tag{2.63b}$$

The CoM position is expressed by the same relation as in (2.60). With slight abuse of notation, the same symbols $\boldsymbol{M}(\boldsymbol{q}_m)$, $\boldsymbol{C}(\boldsymbol{q}_m, \boldsymbol{\upsilon})$, $\boldsymbol{L}(\boldsymbol{R}_b, \boldsymbol{q}_m)$, and $\boldsymbol{L}_v(\boldsymbol{R}_b, \boldsymbol{q}_m)$ are used to denote the dynamic matrices for the robot cases with or without reaction wheels.

2.5. Control Allocation

In this section, the methodology adopted for the control design is described. A widespread design method adopted in robotics is the task-space control, by which the control design can be directly performed at the task level – see the Operational Space Formulation in [Kha87] for the seminal work in the field of fixed-base manipulators, [SK05] for floating-base robots, and [Ott08] for further development in the field of flexible-joint and redundant manipulators, and without feedback linearization. The advantage of such an approach is that the dynamics is transformed into a new form in which some structural properties of the system are maintained in the closed-loop dynamics, thereby facilitating the design of asymptotically stable controllers; furthermore, the method allows allocating the actuators in such a way that the control design is facilitated when the performance requirements are specified in the operational space rather than in the joint space.
A similar approach is adopted herein; the adopted approach allows maintaining the structural properties of the dynamics in the closed-loop dynamics, but it allows a more general control allocation that has advantageous properties when considering heterogeneous actuators.
The dynamics of the system, given in (2.29) in $\boldsymbol{\upsilon}, \boldsymbol{\varsigma} \in \mathbb{R}^{6+n}$ variables, is mapped to a new space, referred to as **allocation space**, which is described by the variables $\boldsymbol{\chi}, \boldsymbol{\Upsilon} \in \mathbb{R}^{6+n}$: $\boldsymbol{\chi}$ is a coordinate of the new motion in which the dynamics is represented while keeping some structural properties of the dynamics in the original space; $\boldsymbol{\Upsilon}$ defines a new control input – also referred to as **virtual actuator** – by which the control tasks are assigned. The details of the dynamics transformation are addressed in the next section, whereas the definition of the control tasks is addressed case by case in the control applications in Chapters 3, 5, and 6. The rationale of the approach is schematically represented in

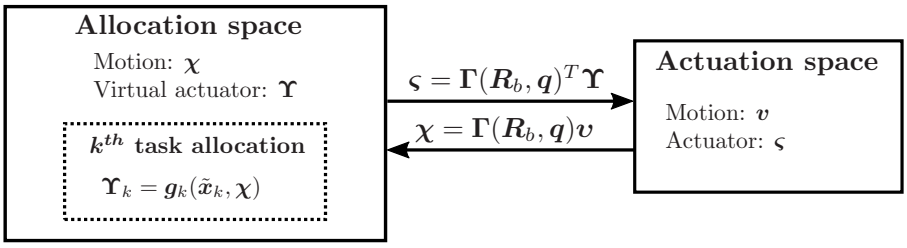

Figure 2.5.: Approach for the control design: the control task is designed in an *allocation space*, and then assigned to the actuators. The functions $\boldsymbol{g}_k(\tilde{\boldsymbol{x}}_k, \boldsymbol{\chi})$ enforce the k^{th} control requirement.

Fig. 2.5.
A number of task errors $\tilde{\boldsymbol{x}}_k$ are defined to specify control tasks; differently from the common task-space formulations, herein the k^{th} transformed motion $\boldsymbol{\chi}_k$ is not defined such that the k^{th} time derivative $\dot{\tilde{\boldsymbol{x}}}_k$ is a function of only the motion $\boldsymbol{\chi}_k$, but it can be a more general function of the entire motion[13] $\boldsymbol{\chi}$. Furthermore, the k^{th} motion is not defined necessarily as a velocity, but can also be a momentum. The advantages of the control allocation in presence of heterogeneous actuators will be treated in detail in Chapter 4.

2.5.1. Allocation Space

By defining a mapping $\boldsymbol{\Gamma}(\boldsymbol{R}_b, \boldsymbol{q}) \in \mathbb{R}^{(6+n)\times(6+n)}$, let us define a new generalized motion[14] $\boldsymbol{\chi} \in \mathbb{R}^{6+n}$, as

$$\boldsymbol{\chi} = \boldsymbol{\Gamma}(\boldsymbol{R}_b, \boldsymbol{q}) \boldsymbol{\upsilon}. \tag{2.64}$$

Let us consider a region $\mathcal{Q}$ in which $\boldsymbol{\Gamma}(\boldsymbol{R}_b, \boldsymbol{q})$ is nonsingular, given by

$$\mathcal{Q} = \left\{ \boldsymbol{R}_b \in \mathrm{SO}(3),\, \boldsymbol{q} \in \mathbb{R}^n : \min_{i=1,\dots,6+n} \sigma_i \left(\boldsymbol{\Gamma}(\boldsymbol{R}_b, \boldsymbol{q}) \right) \geq \sigma_{\Gamma,min} \right\}, \tag{2.65}$$

for some $\sigma_{\Gamma,min} \in \mathbb{R}_+$. In $\mathcal{Q}$ the inverse of $\boldsymbol{\Gamma}(\boldsymbol{R}_b, \boldsymbol{q})$ exists, and it is possible to write the inverse relation of (2.64), as

$$\boldsymbol{\upsilon} = \boldsymbol{\Gamma}(\boldsymbol{R}_b, \boldsymbol{q})^{-1} \boldsymbol{\chi}. \tag{2.66}$$

The time derivative of (2.66) is given by

$$\dot{\boldsymbol{\upsilon}} = \boldsymbol{\Gamma}(\boldsymbol{R}_b, \boldsymbol{q})^{-1} \dot{\boldsymbol{\chi}} - \boldsymbol{\Gamma}(\boldsymbol{R}_b, \boldsymbol{q})^{-1} \dot{\boldsymbol{\Gamma}}(\boldsymbol{R}_b, \boldsymbol{q}) \boldsymbol{\Gamma}(\boldsymbol{R}_b, \boldsymbol{q})^{-1} \boldsymbol{\chi}. \tag{2.67}$$

The dynamics equation of the system in the allocation space is obtained by inserting (2.66) and (2.67) into (2.29), and by pre-multiplying it by $\boldsymbol{\Gamma}(\boldsymbol{R}_b, \boldsymbol{q})^{-T}$, resulting in

$$\boldsymbol{M}_\chi(\boldsymbol{R}_b, \boldsymbol{q}) \dot{\boldsymbol{\chi}} + \boldsymbol{C}_\chi(\boldsymbol{R}_b, \boldsymbol{q}, \boldsymbol{\upsilon}) \boldsymbol{\chi} = \boldsymbol{\Upsilon} + \boldsymbol{\Gamma}(\boldsymbol{R}_b, \boldsymbol{q})^{-T} \sum_{j=0}^{n} \boldsymbol{J}_j(\boldsymbol{q})^T \boldsymbol{\mathcal{F}}_j^{ext}, \tag{2.68}$$

where the transformed inertia and Coriolis/centrifugal matrices are given by

$$\boldsymbol{M}_\chi(\boldsymbol{R}_b, \boldsymbol{q}) = \boldsymbol{\Gamma}(\boldsymbol{R}_b, \boldsymbol{q})^{-T} \boldsymbol{M}(\boldsymbol{q}) \boldsymbol{\Gamma}(\boldsymbol{R}_b, \boldsymbol{q})^{-1}, \tag{2.69a}$$

$$\boldsymbol{C}_\chi(\boldsymbol{R}_b, \boldsymbol{q}, \boldsymbol{\upsilon}) = \boldsymbol{\Gamma}(\boldsymbol{R}_b, \boldsymbol{q})^{-T} \left(\boldsymbol{C}(\boldsymbol{q}, \boldsymbol{\upsilon}) - \boldsymbol{M}(\boldsymbol{q}) \boldsymbol{\Gamma}(\boldsymbol{R}_b, \boldsymbol{q})^{-1} \dot{\boldsymbol{\Gamma}}(\boldsymbol{R}_b, \boldsymbol{q}) \right) \boldsymbol{\Gamma}(\boldsymbol{R}_b, \boldsymbol{q})^{-1}, \tag{2.69b}$$

[13] For the sake of simplicity, a more rigorous mathematical explanation of this aspect is postponed to the control applications.

[14] It is called **motion** a quantity which is either a velocity or a momentum; in turn, "generalized motion" means that $\boldsymbol{\chi}$ is the stacked vector of either velocity or momentum array vectors.

and where $\boldsymbol{\Upsilon}$ is a new set of control inputs which is dual to $\boldsymbol{\chi}$, and is related to the generalized forces by

$$\boldsymbol{\varsigma} = \boldsymbol{\Gamma}(\boldsymbol{R}_b, \boldsymbol{q})^T \boldsymbol{\Upsilon}. \tag{2.69c}$$

The mapping $\boldsymbol{\Gamma}^T(\boldsymbol{q})$ is also referred to as **actuation mapping**. The dynamics (2.68) depends on $\boldsymbol{\upsilon}$ via the Coriolis/centrifugal matrix. To write it entirely in terms of $\boldsymbol{\chi}$, (2.66) is used to replace the functional argument as $\boldsymbol{C}_\chi(\boldsymbol{R}_b, \boldsymbol{q}, \boldsymbol{\upsilon}) = \boldsymbol{C}_\chi\left(\boldsymbol{R}_b, \boldsymbol{q}, \boldsymbol{\Gamma}(\boldsymbol{R}_b, \boldsymbol{q})^{-1}\boldsymbol{\chi}\right) := \boldsymbol{C}_\chi(\boldsymbol{R}_b, \boldsymbol{q}, \boldsymbol{\chi})$; with an abuse notation the same symbol is used to denote the matrix after the substitution of the argument. Then, it is written

$$\boldsymbol{M}_\chi(\boldsymbol{R}_b, \boldsymbol{q})\dot{\boldsymbol{\chi}} + \boldsymbol{C}_\chi(\boldsymbol{R}_b, \boldsymbol{q}, \boldsymbol{\chi})\boldsymbol{\chi} = \boldsymbol{\Upsilon} + \boldsymbol{\Gamma}(\boldsymbol{R}_b, \boldsymbol{q})^{-T} \sum_{j=0}^{n} \boldsymbol{J}_j(\boldsymbol{q})^T \boldsymbol{\mathcal{F}}_j^{ext}. \tag{2.70}$$

An important feature of the transformation (2.69) is that the properties of positive definiteness and skew-symmetry of the dynamics matrices are preserved in the transformed dynamics (2.70).

Proposition 2.1. *The matrices $\boldsymbol{M}_\chi(\boldsymbol{R}_b, \boldsymbol{q})$ and $\boldsymbol{C}_\chi(\boldsymbol{R}_b, \boldsymbol{q}, \boldsymbol{\chi})$ in (2.70) $\forall \boldsymbol{R}_b, \boldsymbol{q} \in \mathcal{Q}$ satisfy the properties*

$$\boldsymbol{M}_\chi(\boldsymbol{R}_b, \boldsymbol{q}) = \boldsymbol{M}_\chi(\boldsymbol{R}_b, \boldsymbol{q})^T, \quad \boldsymbol{y}^T \boldsymbol{M}_\chi(\boldsymbol{R}_b, \boldsymbol{q})\boldsymbol{y} > 0 \qquad \forall \boldsymbol{y} \neq \boldsymbol{0} \in \mathbb{R}^{6+n}, \tag{2.71a}$$

$$\dot{\boldsymbol{M}}_\chi(\boldsymbol{R}_b, \boldsymbol{q}) = \boldsymbol{C}_\chi(\boldsymbol{R}_b, \boldsymbol{q}, \boldsymbol{\chi}) + \boldsymbol{C}_\chi(\boldsymbol{R}_b, \boldsymbol{q}, \boldsymbol{\chi})^T, \qquad \forall \boldsymbol{\chi} \in \mathbb{R}^{6+n} \tag{2.71b}$$

Proof. The matrix $\boldsymbol{M}_\chi(\boldsymbol{R}_b, \boldsymbol{q})$ exists because $\boldsymbol{\Gamma}(\boldsymbol{R}_b, \boldsymbol{q})$ is nonsingular in $\mathcal{Q}$. The symmetry of $\boldsymbol{M}_\chi(\boldsymbol{R}_b, \boldsymbol{q})$ follows from the congruence transformation (2.69a) of the symmetric matrix $\boldsymbol{M}(\boldsymbol{q})$. By the Sylvester's law of the inertia, the matrix $\boldsymbol{M}_\chi(\boldsymbol{R}_b, \boldsymbol{q})$ is positive definite because $\boldsymbol{M}(\boldsymbol{R}_b, \boldsymbol{q})$ is positive definite and $\boldsymbol{\Gamma}(\boldsymbol{R}_b, \boldsymbol{q})$ is nonsingular in $\mathcal{Q}$. So (2.71a) is proven.
To prove the skew symmetry property (2.71b). The matrix $\boldsymbol{C}_\chi(\boldsymbol{R}_b, \boldsymbol{q}, \boldsymbol{\chi})$ exists because $\boldsymbol{\Gamma}(\boldsymbol{R}_b, \boldsymbol{q})$ is nonsingular in $\mathcal{Q}$. In the remaining proof the arguments of the matrices are dropped in order to simplify the notation. The term $\boldsymbol{M}_\chi$ in (2.71b) is written by taking the time derivative of (2.69a), as

$$\begin{aligned}\dot{\boldsymbol{M}}_\chi &= \frac{d}{dt}\boldsymbol{\Gamma}^{-T}\boldsymbol{M}\boldsymbol{\Gamma}^{-1} + \boldsymbol{\Gamma}^{-T}\dot{\boldsymbol{M}}\boldsymbol{\Gamma}^{-1} + \boldsymbol{\Gamma}^{-T}\boldsymbol{M}\frac{d}{dt}\boldsymbol{\Gamma}^{-1} \\ &= -\boldsymbol{\Gamma}^{-T}\dot{\boldsymbol{\Gamma}}^T\boldsymbol{\Gamma}^{-T}\boldsymbol{M}\boldsymbol{\Gamma}^{-1} + \boldsymbol{\Gamma}^{-T}\dot{\boldsymbol{M}}\boldsymbol{\Gamma}^{-1} - \boldsymbol{\Gamma}^{-T}\boldsymbol{M}\boldsymbol{\Gamma}^{-1}\dot{\boldsymbol{\Gamma}}\boldsymbol{\Gamma}^{-1},\end{aligned}$$

where the property $\frac{d}{dt}(\cdot)^{-1} = -(\cdot)^{-1}\frac{d(\cdot)}{dt}(\cdot)^{-1}$ is used. The term $\boldsymbol{C}_\chi + \boldsymbol{C}_\chi^T$ is given by

$$\boldsymbol{C}_\chi + \boldsymbol{C}_\chi^T = \boldsymbol{\Gamma}^{-T}\left(\boldsymbol{C} + \boldsymbol{C}^T\right)\boldsymbol{\Gamma}^{-1} - \boldsymbol{\Gamma}^{-T}\boldsymbol{M}\boldsymbol{\Gamma}^{-1}\dot{\boldsymbol{\Gamma}}\boldsymbol{\Gamma}^{-1} - \boldsymbol{\Gamma}^{-T}\dot{\boldsymbol{\Gamma}}^T\boldsymbol{\Gamma}^{-T}\boldsymbol{M}\boldsymbol{\Gamma}^{-1}.$$

Then, it results

$$\dot{\boldsymbol{M}}_\chi - \boldsymbol{C}_\chi - \boldsymbol{C}_\chi^T = \boldsymbol{\Gamma}^{-T}\left(\dot{\boldsymbol{M}} - \boldsymbol{C} - \boldsymbol{C}^T\right)\boldsymbol{\Gamma}^{-1} = 0$$

where Property 2.2 is applied. Then, (2.71b) is proven. □

If, additionally, the transformation $\boldsymbol{\Gamma}(\boldsymbol{R}_b, \boldsymbol{q}) \in \mathbb{R}^{(6+n)\times(6+n)}$ is bounded, i.e., if it exists $\sigma_{\Gamma,max} \in \mathbb{R}_+$ such that

$$\sup_{\boldsymbol{R}_b \in \mathrm{SO}(3),\, \boldsymbol{q} \in \mathbb{R}^n} \max_{i=1,\dots,6+n} \sigma_i(\boldsymbol{\Gamma}(\boldsymbol{R}_b, \boldsymbol{q})) \leq \sigma_{\Gamma,max}, \tag{2.72}$$

then also the boundedness property of the inertia is preserved.

Proposition 2.2. *If it exists* $\sigma_{\Gamma,max} \in \mathbb{R}_+$ *satisfying* (2.72)*, it holds*

$$0 < \lambda_{M_\chi,min} \leq \sigma_i(\boldsymbol{M}_\chi(\boldsymbol{R}_b, \boldsymbol{q})) \leq \lambda_{M_\chi,max}, \qquad \forall i = 1, \ldots, 6+n. \tag{2.73a}$$

for some $\lambda_{M_\chi,min}, \lambda_{M_\chi,max} \in \mathbb{R}_+$.

Proof. The boundedness of $\boldsymbol{M}_\chi(\boldsymbol{R}_b, \boldsymbol{q})$ follows directly from the definition (2.69a) together with the Property 2.3, the assumption (2.72), and the restriction $\boldsymbol{R}_b, \boldsymbol{q} \in \mathcal{Q}$. □

2.6. Summary

In this chapter, the kinematics and dynamics modelling of an orbital robot was discussed. The kinematics modeling of [MLS94] and the dynamics modeling of [GOA13] were applied to derive the equations. First, the kinematics and dynamics equations were derived for a general free open mechanical chain with multiple branches; then, two particular cases of single-arm robot with and without reaction wheels were reported as subcases of the general equations. All the assumptions were described in detail. Finally, some properties of the dynamical matrices (e.g. positive definiteness, skew symmetry) and of the motion (conservation structure), which are of great interest for the controller design, were pointed out.

In a second part of the chapter, the methodology for the transformation of the dynamics into a new space was described; equations for the transformation of the dynamics and of the actuators were provided. These equations form the basis of the derivation of the controllers in the next chapters.

CHAPTER 3

The Free-Floating and Free-Flying Approaches

The free-floating and free-flying strategies are described herein to outline their concept and to point out their limitations. Two controllers are analyzed:

(C1) Free-floating control,

(C2) Free-flying control with requirements on the pose of the base.

Key aspects for the solution of the limitations are identified, motivating the development of the innovative design idea presented later in the thesis.
In order to use an uniform methodology and notation throughout the thesis, the mathematical derivation adopted herein slightly differs from the original formulation of the strategies; however, this does not alter their rationale. The strategies presented herein were derived for a robot equipped with an arm but no reaction wheels; therefore, herein the derivation is restricted to this case and the dynamics model in 2.4 is used.

3.1. The Free-Floating Approach

In a free-floating control strategy the use of the thrusters is completely avoided, i.e., $\boldsymbol{\mathcal{F}}_b = \mathbf{0}$. A method for the control of the end-effector of a free-floating robot was derived in [MMA89a, MMA89b] by using the so-called generalized Jacobian matrix [UY89]

$$\boldsymbol{J}^*_{em}(\boldsymbol{q}_m) = \boldsymbol{J}_{em}(\boldsymbol{q}_m) - \boldsymbol{A}_{eb}(\boldsymbol{q}_m)\boldsymbol{M}_b(\boldsymbol{q}_m)^{-1}\boldsymbol{M}_{bm}(\boldsymbol{q}_m) \in \mathbb{R}^{6\times n_m} \tag{3.1}$$

under the assumption of zero linear and angular momenta. The method was extended to the case of control in presence of nonzero linear and angular momenta in [GGDS$^+$16]; in the following, the details for this more general case are reported. Further studies analyzing the free-floating approach in presence of nonzero angular momentum are [MS01, NP11].

3.1.1. Transformation of the dynamics

The derivation of the equations of the free-floating controller is restricted to the case of zero uncontrolled external forces, i.e., $\boldsymbol{\mathcal{F}}^{ext}_j = \mathbf{0}$.
To control the pose of the end-effector in presence of nonzero momenta, the dynamics is

transformed to an allocation space of dimension $6 + n_m$, which models both the velocity of the end-effector and the momentum of the system.
For a robot without reaction wheels, by using (2.18c), (2.61b), (2.43b), and (2.63a) the momentum $\boldsymbol{h}_c \in \mathbb{R}^6$ and the end-effector velocity $\boldsymbol{\nu}_e \in \mathbb{R}^6$, are expressed as

$$\boldsymbol{h}_c = \boldsymbol{L}(\boldsymbol{R}_b, \boldsymbol{q}_m)\boldsymbol{\upsilon}, \tag{3.2}$$
$$\boldsymbol{\nu}_e = \boldsymbol{J}_e(\boldsymbol{q}_m)\boldsymbol{\upsilon}, \tag{3.3}$$

where $\boldsymbol{L}(\boldsymbol{R}_b, \boldsymbol{q}_m) \in \mathbb{R}^{6\times(6+n_m)}$ and $\boldsymbol{J}_e(\boldsymbol{q}_m) \in \mathbb{R}^{6\times(6+n_m)}$. The momentum and end-effector velocities are six-dimensional vectors, and together form a twelve-dimensional motion. For a redundant arm it is $n_m > 6$; thus an additional motion of dimension $r = n_m - 6$ is required to construct an allocation space of dimension $6 + n_m$.
Let $\boldsymbol{\upsilon}_n \in \mathbb{R}^r$ denote such an additional motion, and let us express it as

$$\boldsymbol{\upsilon}_n = \boldsymbol{J}_n(\boldsymbol{q}_m)\boldsymbol{\upsilon}, \tag{3.4}$$

where $\boldsymbol{J}_n(\boldsymbol{q}_m) \in \mathbb{R}^{r\times(6+n_m)}$. To limit interference with the end-effector, one may define $\boldsymbol{\upsilon}_n$ as being a dynamically-consistent [Kha87] null-space velocity of the end-effector. Furthermore, to be actuable by a free-floating robot, $\boldsymbol{\upsilon}_n$ is further defined to be dynamically-consistent null-space velocity of the momentum[1]. These two requirements are satisfied by choosing a mapping $\boldsymbol{J}_n(\boldsymbol{q}_m)$ that satisfies the following condition:

$$\begin{bmatrix} \boldsymbol{L}(\boldsymbol{R}_b, \boldsymbol{q}) \\ \boldsymbol{J}_e(\boldsymbol{q}_m) \end{bmatrix} \boldsymbol{M}(\boldsymbol{q}_m)^{-1} \boldsymbol{J}_n(\boldsymbol{q}_m)^T = \boldsymbol{0}. \tag{3.5}$$

Based on the above definitions, $\boldsymbol{h}_c$, $\boldsymbol{\nu}_e$, and $\boldsymbol{\upsilon}_n$ form an allocation space $\boldsymbol{\chi} = \begin{bmatrix}\boldsymbol{h}_c^T & \boldsymbol{\nu}_e^T & \boldsymbol{\upsilon}_n{}^T\end{bmatrix}^T$ of dimension $6 + n_m$, which can be expressed as

$$\boldsymbol{\chi} = \begin{bmatrix} \boldsymbol{h}_c \\ \boldsymbol{\nu}_e \\ \boldsymbol{\upsilon}_n \end{bmatrix} = \boldsymbol{\Gamma}(\boldsymbol{R}_b, \boldsymbol{q}_m)\boldsymbol{\upsilon}, \qquad \text{where} \quad \boldsymbol{\Gamma}(\boldsymbol{R}_b, \boldsymbol{q}_m) = \begin{bmatrix} \boldsymbol{L}(\boldsymbol{R}_b, \boldsymbol{q}_m) \\ \boldsymbol{J}_e(\boldsymbol{q}_m) \\ \boldsymbol{J}_n(\boldsymbol{q}_m) \end{bmatrix} \in \mathbb{R}^{(6+n_m)\times(6+n_m)}. \tag{3.6}$$

In a region $\mathcal{Q}$ where the mapping $\boldsymbol{\Gamma}(\boldsymbol{R}_b, \boldsymbol{q}_m)$ is nonsingular (see (2.65)), the inverse of $\boldsymbol{\Gamma}(\boldsymbol{R}_b, \boldsymbol{q}_m)$ exists. Thus, the dynamics in the allocation space is obtained by applying (2.69) and obtaining the form

$$\underbrace{\begin{bmatrix} \boldsymbol{M}_h & \boldsymbol{M}_{he} & \boldsymbol{0} \\ \boldsymbol{M}_{he}^T & \boldsymbol{M}_e & \boldsymbol{0} \\ \boldsymbol{0} & \boldsymbol{0} & \boldsymbol{M}_n \end{bmatrix}}_{\boldsymbol{M}_\chi(\boldsymbol{R}_b, \boldsymbol{q}_m)} \begin{bmatrix} \dot{\boldsymbol{h}}_c \\ \dot{\boldsymbol{\nu}}_e \\ \dot{\boldsymbol{\upsilon}}_n \end{bmatrix} + \underbrace{\begin{bmatrix} \boldsymbol{C}_h & \boldsymbol{C}_{he} & -\boldsymbol{C}_{nh}^T \\ \boldsymbol{C}_{eh} & \boldsymbol{C}_e & -\boldsymbol{C}_{ne}^T \\ \boldsymbol{C}_{nh} & \boldsymbol{C}_{ne} & \boldsymbol{C}_n \end{bmatrix}}_{\boldsymbol{C}_\chi(\boldsymbol{R}_b, \boldsymbol{q}_m, \boldsymbol{h}_c, \boldsymbol{\nu}_e, \boldsymbol{\upsilon}_n)} \begin{bmatrix} \boldsymbol{h}_c \\ \boldsymbol{\nu}_e \\ \boldsymbol{\upsilon}_n \end{bmatrix} = \begin{bmatrix} \boldsymbol{\alpha}_c \\ \boldsymbol{\mathcal{F}}_e \\ \boldsymbol{\varsigma}_n \end{bmatrix}, \tag{3.7}$$

where $\boldsymbol{\alpha}_c \in \mathbb{R}^6$, $\boldsymbol{\mathcal{F}}_e \in \mathbb{R}^6$, and $\boldsymbol{\varsigma}_n \in \mathbb{R}^r$ are the virtual actuators associated to $\boldsymbol{h}_c$, $\boldsymbol{\nu}_e$, and $\boldsymbol{\upsilon}_n$, respectively. They are related to the actuators by a mapping

$$\begin{bmatrix} \boldsymbol{\mathcal{F}}_b \\ \boldsymbol{\tau}_m \end{bmatrix} = \underbrace{\begin{bmatrix} \boldsymbol{M}_b(\boldsymbol{q}_m)\boldsymbol{A}_{cb}(\boldsymbol{R}_b, \boldsymbol{q}_m)^{-1} & \boldsymbol{A}_{eb}(\boldsymbol{q}_m)^T & \boldsymbol{J}_{nb}(\boldsymbol{q}_m)^T \\ \boldsymbol{M}_{bm}(\boldsymbol{q}_m)^T\boldsymbol{A}_{cb}(\boldsymbol{R}_b, \boldsymbol{q}_m)^{-1} & \boldsymbol{J}_{em}(\boldsymbol{q}_m)^T & \boldsymbol{J}_{nm}(\boldsymbol{q}_m)^T \end{bmatrix}}_{\boldsymbol{\Gamma}(\boldsymbol{R}_b, \boldsymbol{q}_m)^T} \begin{bmatrix} \boldsymbol{\alpha}_c \\ \boldsymbol{\mathcal{F}}_e \\ \boldsymbol{\varsigma}_n \end{bmatrix}. \tag{3.8}$$

[1] The rationale behind this is explained in detail in Chapter 4.

where the partitionings of $\boldsymbol{L}(\boldsymbol{R}_b, \boldsymbol{q}_m)$ and $\boldsymbol{J}_e(\boldsymbol{q}_m)$ resulting from (2.63a), (2.19), (2.61b), and where $\boldsymbol{J}_{nb}(\boldsymbol{q}_m) \in \mathbb{R}^{r\times 6}$ and $\boldsymbol{J}_{nm}(\boldsymbol{q}_m) \in \mathbb{R}^{r\times n_m}$ are the sub-blocks associated to the partitioning $\boldsymbol{J}_n(\boldsymbol{q}_m) = \begin{bmatrix}\boldsymbol{J}_{nb}(\boldsymbol{q}_m) & \boldsymbol{J}_{nm}(\boldsymbol{q}_m)\end{bmatrix}$. Notice in (3.7) that the choice of the dynamically-consistent null-space velocity $\boldsymbol{\upsilon}_n$ leads to a decoupled matrix $\boldsymbol{M}_\chi(\boldsymbol{q})$; however, the momentum and end-effector systems are still coupled. In [GHEO15] it was observed how in a floating robot the momentum and joint dynamics are inertially decoupled, thus the inertial coupling in (3.7) between the momentum and the end-effector comes somewhat as surprise. This is only an apparent contradiction. In Chapter 4 this aspect will be analyzed in detail, and it will be explained how to obtain an inertially-decoupled structure for the momentum and end-effector.
To enforce the underactuation, the condition $\boldsymbol{\mathcal{F}}_b = \boldsymbol{0}$ is imposed in the relation (3.8), obtaining $\boldsymbol{\alpha}_c = -\boldsymbol{A}_{cb}(\boldsymbol{R}_b, \boldsymbol{q}_m)\boldsymbol{M}_b(\boldsymbol{q}_m)^{-1}\boldsymbol{A}_{eb}(\boldsymbol{q}_m)^T\boldsymbol{\mathcal{F}}_e - \boldsymbol{A}_{cb}(\boldsymbol{R}_b, \boldsymbol{q}_m)\boldsymbol{M}_b(\boldsymbol{q}_m)^{-1}\boldsymbol{J}_{nb}(\boldsymbol{q}_m)^T\boldsymbol{\varsigma}_n$, and in turn the actuator commands reduce to (See Appendix C.1)

$$\boldsymbol{\mathcal{F}}_b = \boldsymbol{0}, \tag{3.9a}$$

$$\boldsymbol{\tau}_m = \boldsymbol{J}^*_{em}(\boldsymbol{q}_m)^T\boldsymbol{\mathcal{F}}_e + \boldsymbol{J}^*_{nm}(\boldsymbol{q}_m)^T\boldsymbol{\varsigma}_n, \tag{3.9b}$$

where the condition (C.3) is applied, and where $\boldsymbol{J}^*_{nm}(\boldsymbol{q}_m) \in \mathbb{R}^{r\times n_m}$ is the dynamically-consistent null-space mapping of the generalized Jacobian $\boldsymbol{J}^*_{em}(\boldsymbol{q}_m)$ and is defined in (C.4b). In agreement with $\boldsymbol{\mathcal{F}}_b = \boldsymbol{0}$, it must be $\dot{\boldsymbol{h}}_c = \boldsymbol{0}$, and thus the dynamics (3.7) reduces to

$$\boldsymbol{M}_{\bar{\chi}}(\boldsymbol{q}_m)\begin{bmatrix}\dot{\boldsymbol{\nu}}_e\\ \dot{\boldsymbol{\upsilon}}_n\end{bmatrix} + \boldsymbol{C}_{\bar{\chi}}(\boldsymbol{R}_b, \boldsymbol{q}_m, \boldsymbol{h}_c, \boldsymbol{\nu}_e, \boldsymbol{\upsilon}_n)\begin{bmatrix}\boldsymbol{\nu}_e\\ \boldsymbol{\upsilon}_n\end{bmatrix} + \boldsymbol{C}_{\bar{\chi}h}(\boldsymbol{R}_b, \boldsymbol{q}_m, \boldsymbol{h}_c, \boldsymbol{\nu}_e, \boldsymbol{\upsilon}_n)\boldsymbol{h}_c = \begin{bmatrix}\boldsymbol{\mathcal{F}}_e\\ \boldsymbol{\varsigma}_n\end{bmatrix}, \tag{3.10}$$

where $\boldsymbol{M}_{\bar{\chi}}(\boldsymbol{q}_m) \in \mathbb{R}^{n_m\times n_m}$, $\boldsymbol{C}_{\bar{\chi}}(\boldsymbol{R}_b, \boldsymbol{q}_m, \boldsymbol{h}_c, \boldsymbol{\nu}_e, \boldsymbol{\upsilon}_n) \in \mathbb{R}^{n_m\times 6}$, $\boldsymbol{C}_{\bar{\chi}h}(\boldsymbol{R}_b, \boldsymbol{q}_m, \boldsymbol{h}_c, \boldsymbol{\nu}_e, \boldsymbol{\upsilon}_n) \in \mathbb{R}^{n_m\times 6}$.
As a consequence of the dynamically-consistent null space, the inertia matrix has the decoupled form:

$$\boldsymbol{M}_{\bar{\chi}}(\boldsymbol{q}_m) = \begin{bmatrix}\left(\boldsymbol{J}^*_{em}(\boldsymbol{q}_m)\boldsymbol{M}^*_m(\boldsymbol{q}_m)^{-1}\boldsymbol{J}^*_{em}(\boldsymbol{q}_m)^T\right)^{-1} & \boldsymbol{0}\\ \boldsymbol{0} & \boldsymbol{Z}_m(\boldsymbol{q}_m)\boldsymbol{M}^*_m(\boldsymbol{q}_m)\boldsymbol{Z}_m(\boldsymbol{q}_m)^T\end{bmatrix}, \tag{3.11}$$

where $\boldsymbol{Z}_m \in \mathbb{R}^{r\times(n_m)}$ is a null-space base matrix[2] and where

$$\boldsymbol{M}^*_m(\boldsymbol{q}_m) = \boldsymbol{M}_m - \boldsymbol{M}_{bm}(\boldsymbol{q}_m)^T\boldsymbol{M}_b(\boldsymbol{q}_m)^{-1}\boldsymbol{M}_{bm}(\boldsymbol{q}_m) \in \mathbb{R}^{(n_m\times n_m)} \tag{3.12}$$

is the reduced joint inertia of the manipulator [MMA89b]. Note that in (3.11) the part of the inertia associated to the end-effector is equivalent to the end-effector inertia [MMA89b] of the free-floating robot with zero momentum; the part associated to the null space can be interpreted similarly. So, (3.10) has the same inertia as the free-floating robot with zero momentum. Furthermore, as a consequence of Proposition 2.1, the dynamics matrices in (3.10) satisfy the skew-symmetry property

$$\dot{\boldsymbol{M}}_{\bar{\chi}}(\boldsymbol{R}_b, \boldsymbol{q}_m) = \boldsymbol{C}_{\bar{\chi}}(\boldsymbol{R}_b, \boldsymbol{q}_m, \boldsymbol{h}_c, \boldsymbol{\nu}_e, \boldsymbol{\upsilon}_n) + \boldsymbol{C}_{\bar{\chi}}(\boldsymbol{R}_b, \boldsymbol{q}_m, \boldsymbol{h}_c, \boldsymbol{\nu}_e, \boldsymbol{\upsilon}_n)^T. \tag{3.13}$$

Notice in (3.10) that, differently than the classical free-floating dynamics in [MMA89b], the robot dynamics is affected by an additional Coriolis/centrifugal term that depends on the momentum. This term represents a nonvanishing disturbance for the end-effector and null-space dynamics and needs to be compensated or taken into account in the control design and analysis of free-floating controllers in presence of nonzero momentum.

[2] See Appendix C.1 for exact definition.

3.1.2. Design of the controller

The objective of the control is to regulate the pose of the frame $\mathcal{E}$ around a desired frame that is fixed in the target frame $\mathcal{T}$. Furthermore, the null-space motion shall be stopped. Towards this aim, let us consider an error coordinate $\tilde{\boldsymbol{x}}_e \in \mathbb{R}^6$ for the end-effector, and an associated velocity error $\tilde{\boldsymbol{\nu}}_e \in \mathbb{R}^6$. The definition of all error coordinates used throughout the thesis are reported in Appendix B. Note that, as a consequence of Assumption 2.2, it is $\tilde{\boldsymbol{\nu}}_e = \boldsymbol{\nu}_{e_d e} = \boldsymbol{\nu}_e$. For the null space, the velocity error is $\tilde{\boldsymbol{\upsilon}}_n = \boldsymbol{\upsilon}_n$.
The nonvanishing momentum disturbance leads to final control errors when the classical transposed-Jacobian PD-like control as in [MMA89a, MMA89b] is used. Herein, the disturbance is compensated by feedback to eliminate such error. The controller is designed as

$$\begin{bmatrix} \boldsymbol{\mathcal{F}}_e \\ \boldsymbol{\varsigma}_n \end{bmatrix} = \begin{bmatrix} -\boldsymbol{J}_{\tilde{x}_e}(\tilde{\boldsymbol{x}}_e)^T \boldsymbol{K}_e \tilde{\boldsymbol{x}}_e - \boldsymbol{D}_e \tilde{\boldsymbol{\nu}}_e \\ -\boldsymbol{D}_n \tilde{\boldsymbol{\upsilon}}_n \end{bmatrix} + \boldsymbol{C}_{\bar{\chi}h}(\boldsymbol{R}_b, \boldsymbol{q}_m, \boldsymbol{h}_c, \tilde{\boldsymbol{\nu}}_e, \tilde{\boldsymbol{\upsilon}}_n)\boldsymbol{h}_c, \tag{3.14}$$

where $\boldsymbol{K}_e \in \mathbb{R}^{6\times 6}$ is a symmetric, positive-definite stiffness matrix, $\boldsymbol{D}_e \in \mathbb{R}^{6\times 6}$ and $\boldsymbol{D}_n \in \mathbb{R}^{r\times r}$ are positive-definite damping matrices, and $\boldsymbol{J}_x(\tilde{\boldsymbol{x}}_e) \in \mathbb{R}^{6\times 6}$ is the Jacobian of the end-effector error. The resulting closed-loop dynamics has the form

$$\boldsymbol{M}_{\bar{\chi}}(\boldsymbol{q}_m) \begin{bmatrix} \dot{\tilde{\boldsymbol{\nu}}}_e \\ \dot{\tilde{\boldsymbol{\upsilon}}}_n \end{bmatrix} + \boldsymbol{C}_{\bar{\chi}}(\boldsymbol{R}_b, \boldsymbol{q}_m, \boldsymbol{h}_c, \tilde{\boldsymbol{\nu}}_e, \tilde{\boldsymbol{\upsilon}}_n) \begin{bmatrix} \tilde{\boldsymbol{\nu}}_e \\ \tilde{\boldsymbol{\upsilon}}_n \end{bmatrix} + \boldsymbol{D}_e \tilde{\boldsymbol{\nu}}_e + \boldsymbol{J}_{\tilde{x}}(\tilde{\boldsymbol{x}}_e)^T \boldsymbol{K}_e \tilde{\boldsymbol{x}}_e = \boldsymbol{0}, \tag{3.15}$$

The disturbed task-space dynamics of a free-floating robot in presence of momentum, as well as the disturbance compensation method described herein, were first derived in [GGDS+16].

3.1.3. Limitations of a Free-Floating Approach

Equation (3.15) has the structure of a passive task-space dynamics, and one may be tempted to conclude that the system is stable. However, (3.15) represents the dynamics of the system only partially and does not say anything regarding the behavior of the whole system. In presence of linear and angular momenta, the base and joint motion of the system keep moving and cannot reach a rest position. As a matter of fact, by inverting (3.8) it is possible to see that, when the end-effector and the null space converge, the base and joint motions converge to

$$\boldsymbol{\nu}_b \to \boldsymbol{A}_{eb}(\boldsymbol{q}_m)^{-1} \boldsymbol{J}_{em}(\boldsymbol{q}_m) \boldsymbol{J}^*_{em}(\boldsymbol{q}_m)^{\#} \boldsymbol{A}_{eb}(\boldsymbol{q}_m) \boldsymbol{M}_b(\boldsymbol{q}_m)^{-1} \boldsymbol{A}_{cb}(\boldsymbol{R}_b, \boldsymbol{q}_m)^T \boldsymbol{h}_c, \tag{3.16}$$

$$\dot{\boldsymbol{q}}_m \to \boldsymbol{J}^*_{em}(\boldsymbol{q}_m)^{\#} \boldsymbol{A}_{eb}(\boldsymbol{q}_m) \boldsymbol{M}_b(\boldsymbol{q}_m)^{-1} \boldsymbol{A}_{cb}(\boldsymbol{R}_b, \boldsymbol{q}_m)^T \boldsymbol{h}_c, \tag{3.17}$$

where $\boldsymbol{J}^*_{em}(\boldsymbol{q}_m)^{\#} \in \mathbb{R}^{n_m \times 6}$ is the weighted pseudoinverse of the generalized Jacobian with weight $\boldsymbol{M}^*_m(\boldsymbol{q}_m)$, and is given by

$$\boldsymbol{J}^*_{em}(\boldsymbol{q}_m)^{\#} = \boldsymbol{M}^*_m(\boldsymbol{q}_m)^{-1} \boldsymbol{J}^*_{em}(\boldsymbol{q}_m)^T \left(\boldsymbol{J}^*_{em}(\boldsymbol{q}_m) \boldsymbol{M}^*_m(\boldsymbol{q}_m)^{-1} \boldsymbol{J}^*_{em}(\boldsymbol{q}_m)^T \right)^{-1}. \tag{3.18}$$

Due to the nonzero $\dot{\boldsymbol{q}}_m$, the path taken by the joint angles $\boldsymbol{q}_m$ may converge to a singular configuration, or to workspace or joint limits. Furthermore, by physical intuition it is evident that this is surely the case when the linear momentum is nonzero; in other words, if the end-effector is kept at a desired location while the base position drifts, then the arm surely outstretches, and thus converges to workspace limit. The statement was validated

via hardware experiments (see Chapter 8). On the other hand, in the case of nonzero angular momentum only, it could be possible to force the joints to stay on a singularity-free path [NP11] within the reachable workspace; however, the robot may – and, for conventional joint designs, *will* – still converge to joint limits, due to the unidirectional rotational joint motion induced by the angular momentum; furthermore, the singularity-free path could be unfeasible due to self collisions.
Note that the problem of the nonzero momentum does not have only an academic relevance, but it also results in severe practical limitations. Even a small contact on the end-effector transfers a momentum which may induce workspace limit within seconds, thus potentially compromising the grasping operation, as shown in the experimental investigation in Chapter 8. The only way to solve the above-mentioned limitation is to resort to an actuated-base strategy, one in which $\boldsymbol{\mathcal{F}}_b \neq \mathbf{0}$, to introduce an additional control action that extracts the momentum from the system, and thus stops the drift of the joints.

3.2. The Free-Flying Approach

As mentioned in Section 1.1, a free-flying strategy is commonly adopted as alternative to the free-floating one. In a free-flying strategy the thrusters are used with the aim of enforcing different translational and rotational requirements on the spacecraft. For instance, let us consider the free-flying controller [PD91a], which coordinately actuates the thrusters and the joint torques to regulate the poses of the spacecraft and of the end-effector. The strategy was formulated for the control of an orbital robot with a nonredundant arm; in the following, the strategy is reformulated for the case of orbital robot with a redundant arm

3.2.1. Transformation of the dynamics

To control the pose of the spacecraft and of the end-effector, the dynamics is transformed to an allocation space based on the velocities of the base, $\boldsymbol{\nu}_b \in \mathbb{R}^6$, and of the end-effector, $\boldsymbol{\nu}_e \in \mathbb{R}^6$. By using (2.16c), (2.18c), such velocities can be expressed as a function of the generalized velocity of the system, as

$$\boldsymbol{\nu}_b = \boldsymbol{J}_b \boldsymbol{\upsilon}, \tag{3.19}$$

$$\boldsymbol{\nu}_e = \boldsymbol{J}_e(\boldsymbol{q}_m) \boldsymbol{\upsilon}, \tag{3.20}$$

where[3] $\boldsymbol{J}_b \in \mathbb{R}^{6\times(6+n_m)}$ and $\boldsymbol{J}_e(\boldsymbol{q}_m) \in \mathbb{R}^{6\times(6+n_m)}$. The base and end-effector velocities are six-dimensional vectors, and together form a twelve-dimensional motion. For a redundant arm it is $n_m > 6$; thus an additional motion of dimension $r = n_m - 6$ is required to construct an allocation space of dimension $6 + n_m$. By denoting $\boldsymbol{\upsilon}_n \in \mathbb{R}^r$ such an additional motion, it can be expressed as

$$\boldsymbol{\upsilon}_n = \boldsymbol{J}_n(\boldsymbol{q}_m) \boldsymbol{\upsilon}, \tag{3.21}$$

where $\boldsymbol{J}_n(\boldsymbol{q}_m) \in \mathbb{R}^{r\times(6+n_m)}$. To limit the interference with the base and the end-effector, one may define $\boldsymbol{\upsilon}_n$ as being a dynamically-consistent null-space velocity of the base and end-effector velocities. This is done by choosing a mapping $\boldsymbol{J}_n(\boldsymbol{q}_m)$ such that the condition

$$\begin{bmatrix} \boldsymbol{J}_b \\ \boldsymbol{J}_e(\boldsymbol{q}_m) \end{bmatrix} \boldsymbol{M}(\boldsymbol{q}_m)^{-1} \boldsymbol{J}_n(\boldsymbol{q}_m)^T = \mathbf{0} \tag{3.22}$$

[3] Remark that for the base it is trivially $\boldsymbol{J}_b = \begin{bmatrix} \boldsymbol{E} & \mathbf{0} \end{bmatrix}$.

holds. Based on the above definitions, the velocities $\boldsymbol{\nu}_b$, $\boldsymbol{\nu}_e$, and $\boldsymbol{\upsilon}_n$ form an allocation space $\boldsymbol{\chi} = \begin{bmatrix}\boldsymbol{\nu}_b^T & \boldsymbol{\nu}_e^T & \boldsymbol{\upsilon}_n{}^T\end{bmatrix}^T$ of dimension $6 + n_m$, which can be expressed as

$$\boldsymbol{\chi} = \begin{bmatrix}\boldsymbol{\nu}_b \\ \boldsymbol{\nu}_e \\ \boldsymbol{\upsilon}_n\end{bmatrix} = \boldsymbol{\Gamma}(\boldsymbol{q}_m)\boldsymbol{\upsilon}, \qquad \text{where} \quad \boldsymbol{\Gamma}(\boldsymbol{q}_m) = \begin{bmatrix}\boldsymbol{J}_b \\ \boldsymbol{J}_e(\boldsymbol{q}_m) \\ \boldsymbol{J}_n(\boldsymbol{q}_m)\end{bmatrix} \in \mathbb{R}^{(6+n_m)\times(6+n_m)}. \tag{3.23}$$

For the computation of $\boldsymbol{J}_n(\boldsymbol{q}_m)$ see the Appendix C.2. In a region $\mathcal{Q}$ where the mapping $\boldsymbol{\Gamma}(\boldsymbol{q}_m)$ is nonsingular (see (2.65)), the inverse of $\boldsymbol{\Gamma}(\boldsymbol{q}_m)$ exists. Thus, considering a contact at the end-effector[4], the dynamics in the allocation space is obtained by applying (2.69) and (2.70), as

$$\boldsymbol{M}_\chi(\boldsymbol{q}_m)\begin{bmatrix}\dot{\boldsymbol{\nu}}_b \\ \dot{\boldsymbol{\nu}}_e \\ \dot{\boldsymbol{\upsilon}}_n\end{bmatrix} + \boldsymbol{C}_\chi(\boldsymbol{q}_m, \boldsymbol{\nu}_b, \boldsymbol{\nu}_e, \boldsymbol{\upsilon}_n)\begin{bmatrix}\boldsymbol{\nu}_b \\ \boldsymbol{\nu}_e \\ \boldsymbol{\upsilon}_n\end{bmatrix} = \begin{bmatrix}\bar{\boldsymbol{\mathcal{F}}}_b \\ \boldsymbol{\mathcal{F}}_e \\ \boldsymbol{\varsigma}_n\end{bmatrix} + \begin{bmatrix}\boldsymbol{0} \\ \boldsymbol{\mathcal{F}}_e^{ext} \\ \boldsymbol{0}\end{bmatrix}, \tag{3.24}$$

where $\bar{\boldsymbol{\mathcal{F}}}_b \in \mathbb{R}^6$, $\boldsymbol{\mathcal{F}}_e \in \mathbb{R}^6$, and $\boldsymbol{\varsigma}_n \in \mathbb{R}^r$ are the virtual actuators associated to $\boldsymbol{\nu}_b$, $\boldsymbol{\nu}_e$, and $\boldsymbol{\upsilon}_n$, respectively. They are related to the actuators by a mapping

$$\begin{bmatrix}\boldsymbol{\mathcal{F}}_b \\ \boldsymbol{\tau}_m\end{bmatrix} = \begin{bmatrix}\boldsymbol{E} & \boldsymbol{A}_{eb}(\boldsymbol{q}_m)^T & \boldsymbol{J}_{nb}(\boldsymbol{q}_m)^T \\ \boldsymbol{0} & \boldsymbol{J}_{em}(\boldsymbol{q}_m)^T & \boldsymbol{J}_{nm}(\boldsymbol{q}_m)^T\end{bmatrix}\begin{bmatrix}\bar{\boldsymbol{\mathcal{F}}}_b \\ \boldsymbol{\mathcal{F}}_e \\ \boldsymbol{\varsigma}_n\end{bmatrix}. \tag{3.25}$$

where the partitionings of $\boldsymbol{J}_b$ and $\boldsymbol{J}_e(\boldsymbol{q}_m)$ resulting from (2.17), (2.19), (2.61b), and the partitioning $\boldsymbol{J}_n(\boldsymbol{q}_m) = \begin{bmatrix}\boldsymbol{J}_{nb}(\boldsymbol{q}_m) & \boldsymbol{J}_{nm}(\boldsymbol{q}_m)\end{bmatrix}$, with $\boldsymbol{J}_{nb}(\boldsymbol{q}_m) \in \mathbb{R}^{r\times 6}$ and $\boldsymbol{J}_{nm}(\boldsymbol{q}_m) \in \mathbb{R}^{r\times n_m}$, are used.

To analyze the couplings in the system, let us rewrite (3.24) by expliciting the inertia and Coriolis/centrifugal matrices in partitioned form, as

$$\underbrace{\begin{bmatrix}\bar{\boldsymbol{M}}_b & \boldsymbol{M}_{be} & \boldsymbol{0} \\ \boldsymbol{M}_{be}^T & \boldsymbol{M}_e & \boldsymbol{0} \\ \boldsymbol{0} & \boldsymbol{0} & \boldsymbol{M}_n\end{bmatrix}}_{\boldsymbol{M}_\chi(\boldsymbol{q}_m)}\begin{bmatrix}\dot{\boldsymbol{\nu}}_b \\ \dot{\boldsymbol{\nu}}_e \\ \dot{\boldsymbol{\upsilon}}_n\end{bmatrix} + \underbrace{\begin{bmatrix}\bar{\boldsymbol{C}}_b & \boldsymbol{C}_{be} & \boldsymbol{C}_{bn} \\ \boldsymbol{C}_{eb} & \boldsymbol{C}_e & \boldsymbol{C}_{en} \\ -\boldsymbol{C}_{bn}^T & -\boldsymbol{C}_{en}^T & \boldsymbol{C}_n\end{bmatrix}}_{\boldsymbol{C}_\chi(\boldsymbol{q}_m, \boldsymbol{\nu}_b, \boldsymbol{\nu}_e, \boldsymbol{\upsilon}_n)}\begin{bmatrix}\boldsymbol{\nu}_b \\ \boldsymbol{\nu}_e \\ \boldsymbol{\upsilon}_n\end{bmatrix} = \begin{bmatrix}\bar{\boldsymbol{\mathcal{F}}}_b \\ \boldsymbol{\mathcal{F}}_e \\ \boldsymbol{\varsigma}_n\end{bmatrix} + \begin{bmatrix}\boldsymbol{0} \\ \boldsymbol{\mathcal{F}}_e^{ext} \\ \boldsymbol{0}\end{bmatrix}. \tag{3.26}$$

Notice in (3.26) that the choice of the dynamically-consistent null-space velocity $\boldsymbol{\upsilon}_n$ leads to a decoupled inertia; however, the base and end-effector systems are still inertially coupled. Furthermore, note that the base, end-effector, and null-space subsystem are fully coupled in the Coriolis/centrifugal matrix.

Lastly, as a consequence of Proposition 2.1, remark that the dynamics matrices in (3.26) satisfy the skew-symmetry property

$$\dot{\boldsymbol{M}}_\chi(\boldsymbol{q}_m) = \boldsymbol{C}_\chi(\boldsymbol{q}_m, \boldsymbol{\nu}_b, \boldsymbol{\nu}_e, \boldsymbol{\upsilon}_n) + \boldsymbol{C}_\chi(\boldsymbol{q}_m, \boldsymbol{\nu}_b, \boldsymbol{\nu}_e, \boldsymbol{\upsilon}_n)^T. \tag{3.27}$$

3.2.2. Design of the controller

The objective of the control is to regulate the poses of the frames $\mathcal{B}$ and $\mathcal{E}$ around desired frames that are fixed in the target frame $\mathcal{T}$. Furthermore, the null-space motion shall be

[4] For contact only at the end-effector, the external wrench term in (2.70) results in $\boldsymbol{\Gamma}(\boldsymbol{R}_b, \boldsymbol{q})^{-T}\sum_{j=0}^{n}\boldsymbol{J}_j(\boldsymbol{q})^T\boldsymbol{\mathcal{F}}_j^{ext} = \boldsymbol{\Gamma}(\boldsymbol{R}_b, \boldsymbol{q})^{-T}\boldsymbol{J}_e(\boldsymbol{q})^T\boldsymbol{\mathcal{F}}_e^{ext} = \begin{bmatrix}\boldsymbol{0} \\ \boldsymbol{\mathcal{F}}_e^{ext} \\ \boldsymbol{0}\end{bmatrix}$.

stopped. Towards this aim, let us consider error coordinates $\tilde{\boldsymbol{x}}_b \in \mathbb{R}^6$ and $\tilde{\boldsymbol{x}}_e \in \mathbb{R}^6$ for the base and the end-effector, respectively, and associated velocity errors $\tilde{\boldsymbol{\nu}}_b \in \mathbb{R}^6$ and $\tilde{\boldsymbol{\nu}}_e \in \mathbb{R}^6$. As a consequence of Assumption 2.2, it is $\tilde{\boldsymbol{\nu}}_b = \boldsymbol{\nu}_b$ and $\tilde{\boldsymbol{\nu}}_e = \boldsymbol{\nu}_e$. The null-space velocity error is $\tilde{\boldsymbol{\upsilon}}_n = \boldsymbol{\upsilon}_n$. The design of the controller is restricted to the contact-free operation:

Assumption 3.1. *There is no contact, i.e.,* $\boldsymbol{\mathcal{F}}_e^{ext} = \boldsymbol{0}$.

The controller is designed as

$$\bar{\boldsymbol{\mathcal{F}}}_b = -\boldsymbol{J}_{\tilde{x}_b}(\tilde{\boldsymbol{x}}_b)^T \boldsymbol{K}_b \tilde{\boldsymbol{x}}_b - \boldsymbol{D}_b \tilde{\boldsymbol{\nu}}_b, \tag{3.28a}$$

$$\boldsymbol{\mathcal{F}}_e = -\boldsymbol{J}_{\tilde{x}_e}(\tilde{\boldsymbol{x}}_e)^T \boldsymbol{K}_e \tilde{\boldsymbol{x}}_e - \boldsymbol{D}_e \tilde{\boldsymbol{\nu}}_e, \tag{3.28b}$$

$$\boldsymbol{\varsigma}_n = -\boldsymbol{D}_n \tilde{\boldsymbol{\upsilon}}_n, \tag{3.28c}$$

where $\boldsymbol{K}_b \in \mathbb{R}^{6\times6}$, $\boldsymbol{K}_e \in \mathbb{R}^{6\times6}$ are symmetric, positive definite stiffness matrices, $\boldsymbol{D}_b \in \mathbb{R}^{6\times6}$, $\boldsymbol{D}_e \in \mathbb{R}^{6\times6}$, and $\boldsymbol{D}_n \in \mathbb{R}^{r\times r}$ are a positive definite damping matrices, and where $\boldsymbol{J}_{\tilde{x}_b}(\tilde{\boldsymbol{x}}_b) \in \mathbb{R}^{6\times6}$ and $\boldsymbol{J}_{\tilde{x}_e}(\tilde{\boldsymbol{x}}_e) \in \mathbb{R}^{6\times6}$ are the coordinates Jacobians for the base and the end-effector, respectively.

3.2.3. Analysis of the closed loop

For the analysis of the stability of the closed loop the following assumption is made:

Assumption 3.2. *The arm is nonredundant, i.e.,* $n_m = 6$.

The analysis of the stability of the redundant case may be addressed similarly as in [Ott08], by adding a null-space stiffness that enforces regulation of the joint angles around an equilibrium point. The closed-loop dynamics and kinematics equations are obtained by inserting (3.28) into (3.26), considering the error kinematics (B.6), and applying Assumption 3.2, as

$$\boldsymbol{M}_{\tilde{\chi}}(\boldsymbol{q})\dot{\tilde{\boldsymbol{\chi}}} + \boldsymbol{C}_{\tilde{\chi}}(\boldsymbol{q}, \tilde{\boldsymbol{\chi}})\tilde{\boldsymbol{\chi}} + \boldsymbol{D}\tilde{\boldsymbol{\chi}} + \boldsymbol{J}(\tilde{\boldsymbol{x}})^T \boldsymbol{K}\tilde{\boldsymbol{x}} = \boldsymbol{0}, \tag{3.29a}$$

$$\dot{\tilde{\boldsymbol{x}}} = \boldsymbol{J}(\tilde{\boldsymbol{x}})\tilde{\boldsymbol{\chi}}, \tag{3.29b}$$

where it is compactly denoted

$$\tilde{\boldsymbol{\chi}} = \begin{bmatrix} \tilde{\boldsymbol{\nu}}_b \\ \tilde{\boldsymbol{\nu}}_e \end{bmatrix} \in \mathbb{R}^{12}, \qquad \tilde{\boldsymbol{x}} = \begin{bmatrix} \tilde{\boldsymbol{x}}_b \\ \tilde{\boldsymbol{x}}_e \end{bmatrix} \in \mathbb{R}^{12} \tag{3.30a}$$

$$\boldsymbol{M}_{\tilde{\chi}}(\boldsymbol{q}_m) = \begin{bmatrix} \bar{\boldsymbol{M}}_b(\boldsymbol{q}_m) & \boldsymbol{M}_{be}(\boldsymbol{q}_m) \\ \boldsymbol{M}_{be}(\boldsymbol{q}_m)^T & \boldsymbol{M}_e(\boldsymbol{q}_m) \end{bmatrix}, \qquad \boldsymbol{C}_{\tilde{\chi}}(\boldsymbol{q}_m, \tilde{\boldsymbol{\chi}}) = \begin{bmatrix} \bar{\boldsymbol{C}}_b(\boldsymbol{q}_m, \tilde{\boldsymbol{\chi}}) & \boldsymbol{C}_{be}(\boldsymbol{q}_m, \tilde{\boldsymbol{\chi}}) \\ \boldsymbol{C}_{eb}(\boldsymbol{q}_m, \tilde{\boldsymbol{\chi}}) & \boldsymbol{C}_e(\boldsymbol{q}_m, \tilde{\boldsymbol{\chi}}) \end{bmatrix}, \tag{3.30b}$$

$$\boldsymbol{K} = \mathrm{blkdiag}(\boldsymbol{K}_b, \boldsymbol{K}_e) \in \mathbb{R}^{12\times12}, \tag{3.30c}$$

$$\boldsymbol{D} = \mathrm{blkdiag}(\boldsymbol{D}_b, \boldsymbol{D}_e) \in \mathbb{R}^{12\times12}, \tag{3.30d}$$

$$\boldsymbol{J}(\tilde{\boldsymbol{x}}) = \mathrm{blkdiag}(\boldsymbol{J}_{\tilde{x}_b}(\tilde{\boldsymbol{x}}_b), \boldsymbol{J}_{\tilde{x}_e}(\tilde{\boldsymbol{x}}_e)) \in \mathbb{R}^{12\times12}. \tag{3.30e}$$

To represent the closed-loop in a state-space form, the joint dependency is removed. In order to do so, let us firstly define a region $\mathcal{Q}_2$ in which the invertibility of the forward kinematics of the arm is ensured, as

$$\mathcal{Q}_2 = \{\boldsymbol{q}_m \in \mathcal{Q} : \ \boldsymbol{H}_{be}(\boldsymbol{q}_m) \ \text{is one-to-one}\}. \tag{3.31}$$

Secondly, the forward kinematics of the arm can be rewritten in terms of the error and desired poses, as

$$\underbrace{\boldsymbol{H}_{be}(\boldsymbol{q}_m)}_{\boldsymbol{g}(\boldsymbol{q}_m)} = \underbrace{\boldsymbol{H}_{b_d b}(\tilde{\boldsymbol{x}}_b)^{-1}\boldsymbol{H}_{tb_d}^{-1}\boldsymbol{H}_{te_d}\boldsymbol{H}_{e_d e}(\tilde{\boldsymbol{x}}_e)}_{\boldsymbol{f}(\tilde{\boldsymbol{x}})}, \tag{3.32}$$

where $\boldsymbol{g}(\boldsymbol{q}_m) : \mathbb{R}^6 \to \mathrm{SE}(3)$ and $\boldsymbol{f}(\tilde{\boldsymbol{x}}) : \mathbb{R}^{12} \to \mathrm{SE}(3)$. Then, a region in the task space is defined as the pre-image through $\boldsymbol{f}(\tilde{\boldsymbol{x}})$ of the image of $\mathcal{Q}_2$ through $\boldsymbol{g}(\boldsymbol{q}_m)$, and is given by

$$\mathcal{X}_2 = \left\{\tilde{\boldsymbol{x}} \in \mathbb{R}^{12} : \ \exists \boldsymbol{q}_m \in \mathcal{Q}_2, \ \ \boldsymbol{g}(\boldsymbol{q}_m) = \boldsymbol{f}(\tilde{\boldsymbol{x}})\right\}. \tag{3.33}$$

Note that this region exists if the desired setpoints $\boldsymbol{H}_{tb_d}$ and $\boldsymbol{H}_{te_d}$ are compatible with the workspace of the arm. In $\mathcal{X}$, the inverse function

$$\boldsymbol{q}_m = \boldsymbol{g}^{-1}(\boldsymbol{f}(\tilde{\boldsymbol{x}})) \tag{3.34}$$

exists, and can be inserted in the closed-loop (3.29), obtaining

$$\boldsymbol{M}_{\tilde{\chi}}(\tilde{\boldsymbol{x}})\dot{\tilde{\boldsymbol{\chi}}} + \boldsymbol{C}_{\tilde{\chi}}(\tilde{\boldsymbol{x}}, \boldsymbol{\chi})\tilde{\boldsymbol{\chi}} + \boldsymbol{D}\tilde{\boldsymbol{\chi}} + \boldsymbol{J}(\tilde{\boldsymbol{x}})^T\boldsymbol{K}\tilde{\boldsymbol{x}} = \boldsymbol{0}, \tag{3.35a}$$

$$\dot{\tilde{\boldsymbol{x}}} = \boldsymbol{J}(\tilde{\boldsymbol{x}})\tilde{\boldsymbol{\chi}}, \tag{3.35b}$$

where with an abuse of notation the same matrix symbols are used after the substitution of the argument. The closed-loop (3.35) represents an autonomous dynamical system having the state-space form

$$\dot{\boldsymbol{z}} = \boldsymbol{f}(\boldsymbol{z}), \qquad \text{with} \quad \boldsymbol{z} = \begin{bmatrix}\tilde{\boldsymbol{x}} \\ \tilde{\boldsymbol{\chi}}\end{bmatrix} \in D_2 = \mathcal{X}_2 \times \mathbb{R}^{12}. \tag{3.36}$$

Proposition 3.1. *The equilibrium point $\boldsymbol{z} = \boldsymbol{0}$ is asymptotically stable.*

Proof. Let us consider the Lyapunov function candidate

$$V(\boldsymbol{z}) = \frac{1}{2}\tilde{\boldsymbol{\chi}}^T\boldsymbol{M}_{\tilde{\chi}}(\tilde{\boldsymbol{x}})\tilde{\boldsymbol{\chi}} + \frac{1}{2}\tilde{\boldsymbol{x}}^T\boldsymbol{K}\tilde{\boldsymbol{x}}, \tag{3.37}$$

which is positive definite. The time derivative along system trajectories is

$$\begin{aligned}\dot{V}(\boldsymbol{z}) &= -\tilde{\boldsymbol{\chi}}^T\left(\boldsymbol{C}_{\tilde{\chi}}(\tilde{\boldsymbol{x}}, \boldsymbol{\chi})\tilde{\boldsymbol{\chi}} + \boldsymbol{D}\tilde{\boldsymbol{\chi}} + \boldsymbol{J}(\tilde{\boldsymbol{x}})^T\boldsymbol{K}\tilde{\boldsymbol{x}}\right) + \frac{1}{2}\tilde{\boldsymbol{\chi}}^T\dot{\boldsymbol{M}}_{\tilde{\chi}}(\tilde{\boldsymbol{x}})\tilde{\boldsymbol{\chi}} + \tilde{\boldsymbol{\chi}}^T\boldsymbol{J}_{\tilde{x}}(\tilde{\boldsymbol{x}})^T\boldsymbol{K}\tilde{\boldsymbol{x}} \\ &= -\tilde{\boldsymbol{\chi}}^T\boldsymbol{D}\tilde{\boldsymbol{\chi}},\end{aligned} \tag{3.38}$$

where (3.35) and (3.27) are applied. The function $\dot{V}(\boldsymbol{z})$ is a negative semi-definite function, then stability is concluded. By invoking LaSalle's theorem, $\tilde{\boldsymbol{\chi}} = \boldsymbol{0} \Rightarrow \tilde{\boldsymbol{x}} = \boldsymbol{0}$, thus the asymptotic stability of the equilibrium point is proven. □

3.2.4. Limitations of a free-flying strategy

The controller coordinates the actuators in such a way that the thrusters are always active during end-effector motions; this leads to overuse of the thrusters and causes thrusters-related limitations such as excessive fuel consumption, thrusters saturation, and limitation of the control bandwidth[5] (as discussed in the introductory Section 1.1). Mathematically, the overuse of the thrusters is related to the structure of the couplings in the actuation matrix in (3.25):

[5]The terminology "bandwidth" is normally employed for linear systems, and shall be understood *cum grano salis* for nonlinear systems; herein, it is adopted to carry over the useful insight of "responsiveness" of a control loop.

Direct coupling The term $\boldsymbol{A}_{eb}(\boldsymbol{q}_m)^T\boldsymbol{\mathcal{F}}_e$ in (3.25) directly couples the motion of the end-effector, i.e., the terms $\tilde{\boldsymbol{x}}_e$ and $\boldsymbol{\nu}_e$ in (3.28b), into the thrusters command $\boldsymbol{\mathcal{F}}_b$. Similarly, the term $\boldsymbol{J}_{nb}(\boldsymbol{q}_m)^T\boldsymbol{\varsigma}_n$ in (3.25) directly couples the motion of the null space, i.e., the velocity $\boldsymbol{\upsilon}_n$ in (3.28c), into the thrusters $\boldsymbol{\mathcal{F}}_b$.

Indirect coupling The motion of the base is dynamically coupled with the motion of the end-effector through the inertial coupling $\boldsymbol{M}_{be}(\boldsymbol{q}_m)\dot{\boldsymbol{\nu}}_e$ and the Coriolis/centrifugal coupling $\boldsymbol{C}_{be}(\boldsymbol{q}_m, \boldsymbol{\nu}_b, \boldsymbol{\nu}_e, \boldsymbol{\upsilon}_n)\boldsymbol{\nu}_e$ in (3.26). Similarly, the motion of the base is dynamically coupled with the motion of the null space through the Coriolis/centrifugal coupling $\boldsymbol{C}_{bn}(\boldsymbol{q}_m, \boldsymbol{\nu}_b, \boldsymbol{\nu}_e, \boldsymbol{\upsilon}_n)\boldsymbol{\upsilon}_n$ Therefore, the base task in (3.28a) and the null-space task in (3.28c) indirectly couple the end-effector and null-space motions into the thrusters $\boldsymbol{\mathcal{F}}_b$ via the term $\bar{\boldsymbol{\mathcal{F}}}_b$ in (3.25).

Both the couplings degrade the fuel consumption. Furthermore, they may induce saturation of the thrusters and, in turn, a limitation of the maneuvering speed of the end-effector. This can happen especially for arms of moderate lengths, because their lever arm would result in a high moment commanded to the thrusters. The direct coupling may further limit the responsiveness and the accuracy of the end-effector task when a multi-rate implementation is adopted. In such implementation the command rate of the thrusters $\boldsymbol{\mathcal{F}}_b$ is order of magnitudes smaller than the sampling rate of the end-effector signals $\tilde{\boldsymbol{x}}_e$ and $\boldsymbol{\nu}_e$; because of the coupling the maximum end-effector gains $\boldsymbol{K}_e$ and $\boldsymbol{D}_e$ may be limited by the low command rate of the thrusters, thus affecting the responsiveness and the accuracy of the end-effector.
To overcome the above-mentioned limitations, one or both couplings may be removed by the following solutions:

1. to remove the direct coupling, adopt a **thrusters-decoupled actuation** mapping, i.e., one which is decoupled in $\boldsymbol{\mathcal{F}}_b$,

2. to remove the indirect coupling, replace the base task in (3.28a) with an **invariant task**, i.e., a task which is invariant during motions of the manipulator. The problem boils down to finding a task whose dynamics has no inertial and Coriolis/centrifugal couplings with the end-effector – in other words, whose dynamics is decoupled.

The exact mathematical definition of thrusters-decoupled actuation, invariant task, and decoupled dynamics, is one of the main results of the thesis, and is the subject of Chapter 4.

3.3. Summary

In this chapter the common free-floating and free-flying strategies were discussed. Two commonly adopted free-floating and free-flying controllers were reported and extended, and the underlying equations were derived based on the unified notation and methodology for the dynamics transformation presented in Chapter 2.

A task-space dynamics of a free-floating robot was derived for the the case of nonzero linear and angular momenta, and redundant arm. Then, the transposed-Jacobian free-floating controller [MMA89b] was extended to the case of nonzero momentum by additional compensation of the momentum-induced disturbance on the end-effector. The drifting behavior of a free-floating system with nonzero momenta was described, and it was pointed out how this drift causes convergence to singularity, or to workspace or joint limits. This

behavior represents the main limitation of a free-floating strategy, and represents a safety issue particularly during the post-contact phase.

The base and end-effector task space dynamics of a representative free-flying controller robot was derived considering a nonredundant arm. Then, the transposed-Jacobian free-flying controller [PD91a] was extended to the case of redundant arm, and a stability proof was reported. The limitations of the approach were analyzed and linked to the direct and indirect couplings induced by the actuation decomposition adopted by the method, and by the control requirements enforced therein on the spacecraft.

Finally, it was pointed out how these drawbacks can be overcome by adoption of a thrusters-decoupled actuation, and by replacement of the spacecraft control task with an invariant task. The detailed description and mathematical formulation of these two ideas is the subject of the next chapter.

CHAPTER 4

Framework for Whole-Body Control Design

In this chapter, an approach is derived to overcome the limitations of the free-floating and free-flying strategies; the key elements of the whole-body control are described.

First, the two core ideas of thrusters-decoupled actuation and invariant task are mathematically formulated. Then, two classes of allocation spaces are defined, which leverage on these ideas, and form the basis for the derivation of the subsequent whole-body controllers.

4.1. Decoupled decompositions of the allocation space

4.1.1. Thrusters-decoupled actuation

Let us partition the allocation space and its dual space as

$$\underbrace{\begin{bmatrix}\boldsymbol{\chi}_1\\ \boldsymbol{\chi}_2\end{bmatrix}}_{\boldsymbol{\chi}} = \underbrace{\begin{bmatrix}\boldsymbol{\Gamma}_{11} & \boldsymbol{\Gamma}_{12} & \dots & \boldsymbol{\Gamma}_{1l}\\ \boldsymbol{\Gamma}_{21} & \boldsymbol{\Gamma}_{22} & \dots & \boldsymbol{\Gamma}_{2l}\end{bmatrix}}_{\boldsymbol{\Gamma}(\boldsymbol{R}_b,\boldsymbol{q})} \underbrace{\begin{bmatrix}\boldsymbol{v}_1\\ \boldsymbol{v}_2\\ \vdots\\ \boldsymbol{v}_l\end{bmatrix}}_{\boldsymbol{v}}, \qquad \underbrace{\begin{bmatrix}\boldsymbol{\varsigma}_1\\ \boldsymbol{\varsigma}_2\\ \vdots\\ \boldsymbol{\varsigma}_l\end{bmatrix}}_{\boldsymbol{\varsigma}} = \underbrace{\begin{bmatrix}\boldsymbol{\Gamma}_{11} & \boldsymbol{\Gamma}_{21}^T\\ \boldsymbol{\Gamma}_{12}^T & \boldsymbol{\Gamma}_{22}^T\\ \vdots & \vdots\\ \boldsymbol{\Gamma}_{1l}^T & \boldsymbol{\Gamma}_{2l}^T\end{bmatrix}}_{\boldsymbol{\Gamma}(\boldsymbol{R}_b,\boldsymbol{q})^T} \underbrace{\begin{bmatrix}\boldsymbol{\Upsilon}_1\\ \boldsymbol{\Upsilon}_2\end{bmatrix}}_{\boldsymbol{\Upsilon}}, \tag{4.1}$$

where $\boldsymbol{\chi}_1, \boldsymbol{\Upsilon}_1 \in \mathbb{R}^{a_1}$, $\boldsymbol{\chi}_2, \boldsymbol{\Upsilon}_2 \in \mathbb{R}^{6+n-a_1}$, and $a_1 \in \mathbb{N}$. The quantities $\boldsymbol{v}_i$, $\boldsymbol{\varsigma}_i \in \mathbb{R}^{b_i}$, with $i = 1, \dots, l$, are the i^{th} generalized velocity and i^{th} generalized force – also referred to as i^{th} *actuator* –, respectively, are of dimension $b_i \in \mathbb{N}$, and are $l \in \mathbb{N}$ in total.
Let us say that the actuation mapping is $\boldsymbol{\Gamma}(\boldsymbol{R}_b, \boldsymbol{q})^T$ is **decoupled in the $\boldsymbol{i^{*th}}$ actuator** if[1]

$$\boldsymbol{\Gamma}_{2i}(\boldsymbol{R}_b, \boldsymbol{q})^T = \boldsymbol{0}, \qquad i = i^*. \tag{4.2}$$

To overcome the direct coupling mentioned in Section 3.2.4, one would like to define an allocation space $\boldsymbol{\chi}$ having a virtual actuator $\boldsymbol{\Upsilon}_1$ that is only actuated by thrusters, and not by the other actuators. Then, the problem boils down in finding an actuation mapping

[1] In (4.2) the row index two is a convention, the same definition can be formulated using a row index one. Note that there is no loss of generality in the definition, because the ordering of the partitioning of $\boldsymbol{\chi}$ is freely chosen.

which is decoupled in the base force, moment, or both. Such an actuation mapping is referred to as **thrusters-decoupled actuation** mapping.
For defining a completely thrusters-decoupled actuation, i.e., an actuation which is decoupled in the entire base wrench, the following form is to be seeked at

$$\begin{bmatrix}\boldsymbol{\chi}_1\\ \boldsymbol{\chi}_2\end{bmatrix} = \begin{bmatrix}\boldsymbol{\Gamma}_{11} & \boldsymbol{\Gamma}_{12}\\ \mathbf{0} & \boldsymbol{\Gamma}_{22}\end{bmatrix}\begin{bmatrix}\boldsymbol{\nu}_b\\ \dot{\boldsymbol{q}}\end{bmatrix}, \qquad \begin{bmatrix}\boldsymbol{\mathcal{F}}_b\\ \boldsymbol{\tau}\end{bmatrix} = \begin{bmatrix}\boldsymbol{\Gamma}_{11}^T & \mathbf{0}\\ \boldsymbol{\Gamma}_{12}^T & \boldsymbol{\Gamma}_{22}^T\end{bmatrix}\begin{bmatrix}\boldsymbol{\Upsilon}_1\\ \boldsymbol{\Upsilon}_2\end{bmatrix}, \tag{4.3a}$$

$$\boldsymbol{\Gamma}_{21}(\boldsymbol{R}_b, \boldsymbol{q}) = \mathbf{0}, \tag{4.3b}$$

where it is $a_1 = 6$, $\boldsymbol{\Gamma}_{11}(\boldsymbol{R}_b, \boldsymbol{q}) \in \mathbb{R}^{6\times 6}$, $\boldsymbol{\Gamma}_{12}(\boldsymbol{R}_b, \boldsymbol{q}) \in \mathbb{R}^{6\times n}$, $\boldsymbol{\Gamma}_{21}(\boldsymbol{R}_b, \boldsymbol{q}) \in \mathbb{R}^{n\times 6}$, and $\boldsymbol{\Gamma}_{22}(\boldsymbol{R}_b, \boldsymbol{q}) \in \mathbb{R}^{n\times n}$. For defining partially thrusters-decoupled actuation, one may, for instance, decouple only the base force or only the base moment. For decoupling the base force, the following form is to be seeked at

$$\begin{bmatrix}\boldsymbol{\chi}_1\\ \boldsymbol{\chi}_2\end{bmatrix} = \begin{bmatrix}\boldsymbol{\Gamma}_{11} & \boldsymbol{\Gamma}_{12} & \boldsymbol{\Gamma}_{13}\\ \mathbf{0} & \boldsymbol{\Gamma}_{22} & \boldsymbol{\Gamma}_{23}\end{bmatrix}\begin{bmatrix}\boldsymbol{v}_b\\ \boldsymbol{\omega}_b\\ \dot{\boldsymbol{q}}\end{bmatrix}, \qquad \begin{bmatrix}\boldsymbol{f}_b\\ \boldsymbol{m}_b\\ \boldsymbol{\tau}\end{bmatrix} = \begin{bmatrix}\boldsymbol{\Gamma}_{11}^T & \mathbf{0}\\ \boldsymbol{\Gamma}_{12}^T & \boldsymbol{\Gamma}_{22}^T\\ \boldsymbol{\Gamma}_{13}^T & \boldsymbol{\Gamma}_{23}^T\end{bmatrix}\begin{bmatrix}\boldsymbol{\Upsilon}_1\\ \boldsymbol{\Upsilon}_2\end{bmatrix}, \tag{4.4a}$$

$$\boldsymbol{\Gamma}_{21}(\boldsymbol{R}_b, \boldsymbol{q}) = \mathbf{0}, \tag{4.4b}$$

whereas, for decoupling the base moment, the following form is to be seeked at

$$\begin{bmatrix}\boldsymbol{\chi}_1\\ \boldsymbol{\chi}_2\end{bmatrix} = \begin{bmatrix}\boldsymbol{\Gamma}_{11} & \boldsymbol{\Gamma}_{12} & \boldsymbol{\Gamma}_{13}\\ \boldsymbol{\Gamma}_{21} & \mathbf{0} & \boldsymbol{\Gamma}_{23}\end{bmatrix}\begin{bmatrix}\boldsymbol{v}_b\\ \boldsymbol{\omega}_b\\ \dot{\boldsymbol{q}}\end{bmatrix}, \qquad \begin{bmatrix}\boldsymbol{f}_b\\ \boldsymbol{m}_b\\ \boldsymbol{\tau}\end{bmatrix} = \begin{bmatrix}\boldsymbol{\Gamma}_{11}^T & \boldsymbol{\Gamma}_{21}^T\\ \boldsymbol{\Gamma}_{12}^T & \mathbf{0}\\ \boldsymbol{\Gamma}_{13}^T & \boldsymbol{\Gamma}_{23}^T\end{bmatrix}\begin{bmatrix}\boldsymbol{\Upsilon}_1\\ \boldsymbol{\Upsilon}_2\end{bmatrix}, \tag{4.5a}$$

$$\boldsymbol{\Gamma}_{22}(\boldsymbol{R}_b, \boldsymbol{q}) = \mathbf{0}. \tag{4.5b}$$

In the equations (4.4a) and (4.5a) it is $a_1 = 3$, $\boldsymbol{\Gamma}_{11}(\boldsymbol{R}_b, \boldsymbol{q}) \in \mathbb{R}^{3\times 3}$, $\boldsymbol{\Gamma}_{12}(\boldsymbol{R}_b, \boldsymbol{q}) \in \mathbb{R}^{3\times 3}$, $\boldsymbol{\Gamma}_{13}(\boldsymbol{R}_b, \boldsymbol{q}) \in \mathbb{R}^{3\times n}$, $\boldsymbol{\Gamma}_{21}(\boldsymbol{R}_b, \boldsymbol{q}) \in \mathbb{R}^{(3+n)\times 3}$, $\boldsymbol{\Gamma}_{22}(\boldsymbol{R}_b, \boldsymbol{q}) \in \mathbb{R}^{(3+n)\times 3}$, and $\boldsymbol{\Gamma}_{23}(\boldsymbol{R}_b, \boldsymbol{q}) \in \mathbb{R}^{(3+n)\times n}$.
A form (4.3a) is provided by means of a so-called **external/internal** allocation space, which is analyzed in Sect. 4.2. A form (4.4a) is provided by means of a so-called **centroidal/circumcentroidal** allocation space, which is analyzed in Sect. 4.3. The form (4.5b) is not investigated in the present work.

4.1.2. Decoupled dynamics and invariant task

Let us consider the dynamics equations associated to the partitioned allocation space (4.1). They are written as

$$\underbrace{\begin{bmatrix}\boldsymbol{M}_{11} & \boldsymbol{M}_{12}\\ \boldsymbol{M}_{12}^T & \boldsymbol{M}_{22}\end{bmatrix}}_{\boldsymbol{M}_\chi(\boldsymbol{R}_b, \boldsymbol{q})}\begin{bmatrix}\dot{\boldsymbol{\chi}}_1\\ \dot{\boldsymbol{\chi}}_2\end{bmatrix} + \underbrace{\begin{bmatrix}\boldsymbol{C}_{11} & \boldsymbol{C}_{12}\\ \boldsymbol{C}_{21} & \boldsymbol{C}_{22}\end{bmatrix}}_{\boldsymbol{C}_\chi(\boldsymbol{R}_b, \boldsymbol{q}, \boldsymbol{\chi})}\underbrace{\begin{bmatrix}\boldsymbol{\chi}_1\\ \boldsymbol{\chi}_2\end{bmatrix}}_{\boldsymbol{\chi}} = \begin{bmatrix}\boldsymbol{\Upsilon}_1\\ \boldsymbol{\Upsilon}_2\end{bmatrix} + \boldsymbol{\Gamma}(\boldsymbol{R}_b, \boldsymbol{q})^{-T}\sum_{j=0}^{n}\boldsymbol{J}_j(\boldsymbol{q})^T\boldsymbol{\mathcal{F}}_j^{ext}. \tag{4.6}$$

It is said that the dynamics (4.6) is **decoupled in** $\boldsymbol{\chi}_1$ if $\forall \boldsymbol{R}_b \in \mathrm{SO}(3), \boldsymbol{q} \in \mathcal{Q}, \boldsymbol{\chi} \in \mathbb{R}^{6+n}$ the following conditions hold

$$\boldsymbol{M}_{12}(\boldsymbol{R}_b, \boldsymbol{q}) = \mathbf{0}, \tag{4.7a}$$

$$\begin{bmatrix}\boldsymbol{C}_{11}(\boldsymbol{R}_b, \boldsymbol{q}, \boldsymbol{\chi}) & \boldsymbol{C}_{12}(\boldsymbol{R}_b, \boldsymbol{q}, \boldsymbol{\chi})\end{bmatrix}\boldsymbol{\chi} = \mathbf{0}. \tag{4.7b}$$

In this case, the dynamics of $\boldsymbol{\chi}_1$ is not affected by the motion of the rest of the system when there is no external wrench. Then the task $\boldsymbol{\Upsilon}_1$ can be defined as

$$\boldsymbol{\Upsilon}_1 = \boldsymbol{g}(\boldsymbol{R}_b, \boldsymbol{q}, \boldsymbol{\chi}_1, \tilde{\boldsymbol{x}}_1), \tag{4.8}$$

where $\tilde{\boldsymbol{x}}_1 \in \mathbb{R}^{a_1^x}$ is a coordinate that is uniquely associated to the motion $\boldsymbol{\chi}_1$, i.e., its time derivative can be written in the form

$$\dot{\tilde{\boldsymbol{x}}}_1 = \boldsymbol{J}_{\tilde{x}_1}(\tilde{\boldsymbol{x}}_1)\boldsymbol{\chi}_1, \tag{4.9}$$

where $\boldsymbol{J}_{\tilde{x}_1}(\tilde{\boldsymbol{x}}_1) \in \mathbb{R}^{a_1^x \times a_1}$ is the mapping of $\boldsymbol{\chi}_1$ to $\dot{\tilde{\boldsymbol{x}}}_1$. When the conditions (4.7) hold, it is said that the task $\boldsymbol{\Upsilon}_1$ is **invariant during the motion** $\boldsymbol{\chi}_2$.

Remark 1. *The task position error is not strictly required in the definition of* (4.8)*, i.e., the task may also have the form* $\boldsymbol{\Upsilon}_1 = \boldsymbol{g}(\boldsymbol{R}_b, \boldsymbol{q}, \boldsymbol{\chi}_1)$.

Remark 2. *The positive-definiteness property* (2.71a) *and the skew-symmetry property* (2.71b) *hold also for the principal submatrices of* $\boldsymbol{M}_\chi(\boldsymbol{R}_b, \boldsymbol{q})$ *and* $\boldsymbol{C}_\chi(\boldsymbol{R}_b, \boldsymbol{q}, \boldsymbol{\chi})$*, i.e., for* $\boldsymbol{M}_{22}(\boldsymbol{R}_b, \boldsymbol{q})$ *and* $\boldsymbol{C}_{22}(\boldsymbol{R}_b, \boldsymbol{q}, \boldsymbol{\chi})$ *it hold*

$$\boldsymbol{M}_{22}(\boldsymbol{R}_b, \boldsymbol{q}) = \boldsymbol{M}_{22}(\boldsymbol{R}_b, \boldsymbol{q})^T, \quad \boldsymbol{y}^T \boldsymbol{M}_{22}(\boldsymbol{R}_b, \boldsymbol{q})\boldsymbol{y} > 0 \qquad \forall \boldsymbol{y} \neq \boldsymbol{0} \in \mathbb{R}^{6+n}, \tag{4.10a}$$

$$\dot{\boldsymbol{M}}_{22}(\boldsymbol{R}_b, \boldsymbol{q}) = \boldsymbol{C}_{22}(\boldsymbol{R}_b, \boldsymbol{q}, \boldsymbol{\chi}) + \boldsymbol{C}_{22}(\boldsymbol{R}_b, \boldsymbol{q}, \boldsymbol{\chi})^T, \qquad \forall \boldsymbol{\chi} \in \mathbb{R}^{6+n}, \tag{4.10b}$$

and similar relations hold for $\boldsymbol{M}_{11}(\boldsymbol{R}_b, \boldsymbol{q})$ *and* $\boldsymbol{C}_{11}(\boldsymbol{R}_b, \boldsymbol{q}, \boldsymbol{\chi})$.

The derivation of dynamics equations that are decoupled in $\boldsymbol{\chi}_1$ is analyzed in the Sections 4.2 and 4.3.

4.2. External/internal allocation space

In this section, an allocation space is derived which has simultaneously a decoupled actuation structure in the base wrench $\boldsymbol{\mathcal{F}}_b$, i.e., it holds (4.3a), and a decoupled dynamics[2], i.e., the conditions in (4.7) hold.
Towards this aim, let us define an **internal motion** $\boldsymbol{v}^{int} \in \mathbb{R}^s$ as a motion taking place in the dynamically-consistent null space of the momentum, as

$$\boldsymbol{v}^{int} := \boldsymbol{J}^{int}(\boldsymbol{q})\boldsymbol{v}, \tag{4.11}$$

where $\boldsymbol{J}^{int}(\boldsymbol{q}) \in \mathbb{R}^{s \times (6+n)}$ is a mapping having the property

$$\boldsymbol{L}(\boldsymbol{R}_b, \boldsymbol{q})\boldsymbol{M}(\boldsymbol{q})^{-1}\boldsymbol{J}^{int}(\boldsymbol{q})^T = \boldsymbol{0}, \tag{4.12}$$

with $\boldsymbol{L}(\boldsymbol{R}_b, \boldsymbol{q})$ being the momentum map defined in (2.43b).
Because of its well-known conserving properties, a natural candidate for finding a decoupled dynamics is the momentum of the system. Therefore, one may then choose as first allocation-space motion the momentum, i.e.,

$$\boldsymbol{\chi}_1 = \boldsymbol{h}_c = \boldsymbol{L}(\boldsymbol{R}_b, \boldsymbol{q})\boldsymbol{v}, \tag{4.13a}$$

[2]Note that the two features are not intrinsically linked; as a matter of fact, $\boldsymbol{\chi} = \begin{bmatrix} \boldsymbol{\nu}_b \\ \boldsymbol{\nu}_{be} \end{bmatrix}$ and $\boldsymbol{\chi} = \begin{bmatrix} \boldsymbol{\nu}_e \\ \boldsymbol{\nu}_{be} \end{bmatrix}$ are allocation spaces having a thrusters-decoupled actuation, but not a decoupled dynamics.

and call $\boldsymbol{\chi}_1 \in \mathbb{R}^6$ as **external motion of the system**. Then, one may choose the second motion to be an internal motion of dimension n, as

$$\boldsymbol{\chi}_2 = \boldsymbol{\chi}^{int} = \bar{\boldsymbol{J}}^{int}(\boldsymbol{q})\boldsymbol{\upsilon}, \tag{4.13b}$$

and call $\boldsymbol{\chi}^{int} \in \mathbb{R}^n$ as **internal motion of the system**. The map $\bar{\boldsymbol{J}}^{int}(\boldsymbol{q}) \in \mathbb{R}^{n\times(n+6)}$ can be constructed based on the specific control application[3]. As shown in the next sections, such a construction yields an allocation space which has simultaneously a decoupled actuation in the thrusters wrench $\boldsymbol{\mathcal{F}}_b$, and a the decoupled dynamics. It is stressed that, to construct such a space, it is not sufficient to use the momentum and a general (possibly non-internal) motion, but is important to use the momentum together with an internal motion.
The concept of external-internal actuation decomposition was first derived in [GGAS17] for the end-effector motion of a arm-equipped body without reaction wheels. In [GDOA20] the same concept was extended to the motion of the end-effector and base frames of an arm-equipped body with reaction wheels. Herein, the concept is presented for the case of general motions[4] of general open chain robots.

4.2.1. Example of internal motion

An example of internal motion is now provided to make the concept more concrete. Let us consider the frame of the general j^{th} body of the multibody system; its velocity $\boldsymbol{\nu}_j$ is expressed by the relation (2.16c) using the mapping $\boldsymbol{J}_j(\boldsymbol{q}) = \begin{bmatrix}\boldsymbol{A}_{jb}(\boldsymbol{q}) & \boldsymbol{J}_{jq}(\boldsymbol{q})\end{bmatrix}$ defined in (2.17). Then, one may define the mapping

$$\boldsymbol{J}_j^{int}(\boldsymbol{q}) = \boldsymbol{J}_j(\boldsymbol{q})\boldsymbol{N}_h(\boldsymbol{q}) \in \mathbb{R}^{6\times(6+n)}, \tag{4.14}$$

where $\boldsymbol{N}_h(\boldsymbol{q}) \in \mathbb{R}^{(6+n)\times(6+n)}$ is the projector into the dynamically-consistent momentum null space[5]

$$\boldsymbol{N}_h(\boldsymbol{q}) = \boldsymbol{E} - \boldsymbol{L}(\boldsymbol{R}_b, \boldsymbol{q})^{\#}\boldsymbol{L}(\boldsymbol{R}_b, \boldsymbol{q}), \tag{4.15}$$

and where $\boldsymbol{L}(\boldsymbol{R}_b, \boldsymbol{q})^{\#} \in \mathbb{R}^{(6+n)\times 6}$ is the dynamically-consistent pseudoinverse [Kha87] of $\boldsymbol{L}(\boldsymbol{R}_b, \boldsymbol{q})$, defined as

$$\boldsymbol{L}(\boldsymbol{R}_b, \boldsymbol{q})^{\#} = \boldsymbol{M}(\boldsymbol{q})^{-1}\boldsymbol{L}(\boldsymbol{R}_b, \boldsymbol{q})^T\left(\boldsymbol{L}(\boldsymbol{R}_b, \boldsymbol{q})\boldsymbol{M}(\boldsymbol{q})^{-1}\boldsymbol{L}(\boldsymbol{R}_b, \boldsymbol{q})^T\right)^{-1}. \tag{4.16}$$

It is interesting to notice that $\boldsymbol{N}_h(\boldsymbol{q})$ depends only on the joints and not on the base rotation, notwithstanding $\boldsymbol{L}(\boldsymbol{R}_b, \boldsymbol{q})$ depends on it (see Appendix A.1).
Based on the definitions above, an internal motion $\boldsymbol{\nu}_j^{int} \in \mathbb{R}^6$ is defined as

$$\boldsymbol{\nu}_j^{int} = \boldsymbol{J}_j^{int}(\boldsymbol{q})\boldsymbol{\upsilon}, \tag{4.17}$$

and is referred to as **internal velocity of the j^{th} body**. It can be shown (see Appendix A.1) that (4.17) simplifies to

$$\boldsymbol{\nu}_j^{int} = \boldsymbol{J}_{jq}^{int}(\boldsymbol{q})\dot{\boldsymbol{q}}, \tag{4.18}$$

[3] The construction of $\bar{\boldsymbol{J}}^{int}(\boldsymbol{q})$ will be detailed in Chapters 5 and 6.

[4] With "general motion" is meant that $\boldsymbol{\upsilon}^{int}$ in (4.39) shall not necessarily be the velocity of a frame, but may be arbitrarily constructed. This concept is clarified in Section 4.2.1.

[5] A preliminary link between the pseudoinverse of the momentum map and the generalized Jacobian appeared in [GHEO15] for the end-effector Jacobian considering zero momentum.

where $\boldsymbol{J}_{jq}^{int}(\boldsymbol{q}) = \boldsymbol{J}_{jq}(\boldsymbol{q}) - \boldsymbol{A}_{jb}(\boldsymbol{q})\boldsymbol{M}_b(\boldsymbol{q})^{-1}\boldsymbol{M}_{bq}(\boldsymbol{q})$ is the internal joint mapping of the $\boldsymbol{j}^{th}$ body, which is equivalent to the generalized Jacobian[6] of the j^{th} body.
An interpretation of $\boldsymbol{\nu}_j^{int}$ is now provided in terms of superposition of motions. By eliminating the base motion $\boldsymbol{\nu}_b$ from (2.18b) and (2.43b), and by inserting (4.18) into the resulting equation, the velocity $\boldsymbol{\nu}_j$ can be rewritten as

$$\boldsymbol{\nu}_j = \boldsymbol{A}_{jc}(\boldsymbol{R}_b, \boldsymbol{q})\boldsymbol{M}_c(\boldsymbol{R}_b, \boldsymbol{q})^{-1}\boldsymbol{h}_c + \boldsymbol{\nu}_j^{int}, \tag{4.19}$$

where $\boldsymbol{M}_c(\boldsymbol{R}_b, \boldsymbol{q}) = \boldsymbol{A}_{cb}(\boldsymbol{R}_b, \boldsymbol{q})^{-T}\boldsymbol{M}_b(\boldsymbol{q})\boldsymbol{A}_{cb}(\boldsymbol{R}_b, \boldsymbol{q})^{-1} \in \mathbb{R}^{6\times 6}$ is the inertia of the whole robot around the CoM. The decomposition (4.19) gives the intuition that the velocity of the j^{th} body of the multibody system is the superposition of its internal velocity and a velocity induced by the external motion.

4.2.2. Decoupled actuation of the external/internal space

Herein it is now shown how (4.13) yield an actuation mapping with a decoupled structure (4.3a).

Lemma 1. *Considering a partitioning* $\boldsymbol{\upsilon} = \begin{bmatrix}\boldsymbol{\nu}_b^T & \dot{\boldsymbol{q}}^T\end{bmatrix}^T$ *and* $\bar{\boldsymbol{J}}^{int}(\boldsymbol{q}) = \begin{bmatrix}\bar{\boldsymbol{J}}_b^{int}(\boldsymbol{q}) & \bar{\boldsymbol{J}}_q^{int}(\boldsymbol{q})\end{bmatrix}$, *then* $\bar{\boldsymbol{J}}_b^{int}(\boldsymbol{q}) = \boldsymbol{0}$ *holds.*

Proof. Condition (4.12) can be rewritten as

$$\boldsymbol{L}(\boldsymbol{R}_b, \boldsymbol{q})\boldsymbol{M}(\boldsymbol{q})^{-1}\begin{bmatrix}\bar{\boldsymbol{J}}_b^{int}(\boldsymbol{q})^T \\ \bar{\boldsymbol{J}}_q^{int}(\boldsymbol{q})^T\end{bmatrix} = \boldsymbol{0}. \tag{4.20}$$

By using the expression of the inverted inertia (2.49), it results

$$\boldsymbol{L}(\boldsymbol{R}_b, \boldsymbol{q})\boldsymbol{M}(\boldsymbol{q})^{-1} = \begin{bmatrix}\boldsymbol{A}_{cb}(\boldsymbol{R}_b, \boldsymbol{q})^{-T} & \boldsymbol{0}\end{bmatrix}, \tag{4.21}$$

and then (4.20) reduces to

$$\boldsymbol{A}_{cb}(\boldsymbol{R}_b, \boldsymbol{q})^{-T}\bar{\boldsymbol{J}}_b^{int}(\boldsymbol{q})^T = \boldsymbol{0}. \tag{4.22}$$

In turn, it follows that $\bar{\boldsymbol{J}}_b^{int}(\boldsymbol{q}) = \boldsymbol{0}$, and this proves the Lemma. □

Note that, as a consequence of Lemma 1, it results that any internal velocity depends only on the velocity of the joints, and not on the velocity of the base. Furthermore, the decoupling condition (4.3b) for the actuation is met, and the transformations of the allocation space have the form

$$\begin{bmatrix}\boldsymbol{h}_c \\ \boldsymbol{\chi}^{int}\end{bmatrix} = \underbrace{\begin{bmatrix}\boldsymbol{A}_{cb}(\boldsymbol{R}_b, \boldsymbol{q})^{-T}\boldsymbol{M}_b(\boldsymbol{q}) & \boldsymbol{A}_{cb}(\boldsymbol{R}_b, \boldsymbol{q})^{-T}\boldsymbol{M}_{bq}(\boldsymbol{q}) \\ \boldsymbol{0} & \bar{\boldsymbol{J}}_q^{int}(\boldsymbol{q})\end{bmatrix}}_{\boldsymbol{\Gamma}(\boldsymbol{R}_b, \boldsymbol{q})}\begin{bmatrix}\boldsymbol{\nu}_b \\ \dot{\boldsymbol{q}}\end{bmatrix}, \tag{4.23a}$$

$$\begin{bmatrix}\boldsymbol{\mathcal{F}}_b \\ \boldsymbol{\tau}\end{bmatrix} = \underbrace{\begin{bmatrix}\boldsymbol{M}_b(\boldsymbol{q})\boldsymbol{A}_{cb}(\boldsymbol{R}_b, \boldsymbol{q})^{-1} & \boldsymbol{0} \\ \boldsymbol{M}_{bq}(\boldsymbol{q})^T\boldsymbol{A}_{cb}(\boldsymbol{R}_b, \boldsymbol{q})^{-1} & \bar{\boldsymbol{J}}_q^{int}(\boldsymbol{q})^T\end{bmatrix}}_{\boldsymbol{\Gamma}(\boldsymbol{R}_b, \boldsymbol{q})^T}\begin{bmatrix}\boldsymbol{\alpha}_c \\ \boldsymbol{\varsigma}^{int}\end{bmatrix}, \tag{4.23b}$$

[6]Equation (4.18) suggests that the generalized Jacobian maps more generally $\dot{\boldsymbol{q}}$ to $\boldsymbol{\nu}_j^{int}$, rather than $\dot{\boldsymbol{q}}$ to $\boldsymbol{\nu}_j$. As discussed in Sect.3.1.3, the generalized Jacobian was classically adopted to map $\dot{\boldsymbol{q}}$ to $\boldsymbol{\nu}_j$ under the assumption of zero momentum [MMA89a, UY89], i.e., $\boldsymbol{h}_c = \boldsymbol{0}$; in contrast, the definition (4.18) does not require any assumption of zero momentum, i.e., it holds also for $\boldsymbol{h}_c \neq \boldsymbol{0}$; therefore (4.18) is more general.

where $\boldsymbol{\alpha}_c \in \mathbb{R}^6$ is the virtual actuator associated to the momentum, and $\boldsymbol{\varsigma}^{int} \in \mathbb{R}^n$ is the virtual actuator associated to the internal motion. The transformation of the generalized velocity is called **external-internal motion decomposition**, whereas the transformation of the generalized forces is called **external-internal actuation decomposition**. Note that the external-internal actuation decomposition in (4.23b) is in the block-decoupled form (4.3a), so it provides a mean of decoupling the actuation in the base wrench $\boldsymbol{\mathcal{F}}_b$ – as it was seeked at. Furthermore, note that (4.23) is general in the sense that any internal motion – not only the joint motion as done in [GHEO15] – can be used to decouple the system. This generality turns out to be useful in many applications, as will be shown in the derivation of the controllers in Chapter 5 and Chapter 6.

As a last step, let us replace the virtual actuator $\boldsymbol{\alpha}_c$, dual to the momentum $\boldsymbol{h}_c$, with one which is dual to a velocity. The **control wrench around the CoM** is defined as

$$\boldsymbol{\mathcal{F}}_c := \boldsymbol{M}_c(\boldsymbol{R}_b, \boldsymbol{q})\boldsymbol{\alpha}_c \in \mathbb{R}^6. \tag{4.24}$$

Based on this, the external-internal actuation decomposition is written in the alternative form

$$\begin{bmatrix} \boldsymbol{\mathcal{F}}_b \\ \boldsymbol{\tau} \end{bmatrix} = \begin{bmatrix} \boldsymbol{A}_{cb}(\boldsymbol{R}_b, \boldsymbol{q})^T & \boldsymbol{0} \\ \boldsymbol{M}_{bq}(\boldsymbol{q})^T \boldsymbol{M}_b(\boldsymbol{q})^{-1} \boldsymbol{A}_{cb}(\boldsymbol{R}_b, \boldsymbol{q})^T & \bar{\boldsymbol{J}}_q^{int}(\boldsymbol{q})^T \end{bmatrix} \begin{bmatrix} \boldsymbol{\mathcal{F}}_c \\ \boldsymbol{\varsigma}^{int} \end{bmatrix}, \tag{4.25}$$

which gives a somewhat better intuition of how the generalized forces are mapped.

4.2.3. Decoupled dynamics of the external/internal space

It is now shown how (4.13) yield a dynamics with a decoupled structure satisfying the conditions (4.7). To prove the inertia decoupling (4.7a), let us consider the inverse inertia $\boldsymbol{M}_\chi(\boldsymbol{R}_b, \boldsymbol{q})^{-1}$. It can be computed by inverting (2.69a), as

$$\boldsymbol{M}_\chi(\boldsymbol{R}_b, \boldsymbol{q})^{-1} = \boldsymbol{\Gamma}(\boldsymbol{R}_b, \boldsymbol{q}) \boldsymbol{M}(\boldsymbol{q})^{-1} \boldsymbol{\Gamma}(\boldsymbol{R}_b, \boldsymbol{q})^T. \tag{4.26}$$

Based on the definitions (4.13), $\boldsymbol{\Gamma}(\boldsymbol{R}_b, \boldsymbol{q})$ has the form

$$\boldsymbol{\Gamma}(\boldsymbol{R}_b, \boldsymbol{q}) = \begin{bmatrix} \boldsymbol{L}(\boldsymbol{R}_b, \boldsymbol{q}) \\ \bar{\boldsymbol{J}}^{int}(\boldsymbol{q}) \end{bmatrix}, \tag{4.27}$$

and thus $\boldsymbol{M}_\chi(\boldsymbol{R}_b, \boldsymbol{q})^{-1}$ takes the form

$$\boldsymbol{M}_\chi(\boldsymbol{R}_b, \boldsymbol{q})^{-1} = \begin{bmatrix} \boldsymbol{L}(\boldsymbol{R}_b, \boldsymbol{q}) \boldsymbol{M}(\boldsymbol{q})^{-1} \boldsymbol{L}(\boldsymbol{R}_b, \boldsymbol{q})^T & \boldsymbol{L}(\boldsymbol{R}_b, \boldsymbol{q}) \boldsymbol{M}(\boldsymbol{q})^{-1} \bar{\boldsymbol{J}}^{int}(\boldsymbol{q})^T \\ \bar{\boldsymbol{J}}^{int}(\boldsymbol{q}) \boldsymbol{M}(\boldsymbol{q})^{-1} \boldsymbol{L}(\boldsymbol{R}_b, \boldsymbol{q})^T & \bar{\boldsymbol{J}}^{int}(\boldsymbol{q}) \boldsymbol{M}(\boldsymbol{q})^{-1} \bar{\boldsymbol{J}}^{int}(\boldsymbol{q})^T \end{bmatrix} \tag{4.28}$$

$$= \begin{bmatrix} \boldsymbol{M}_c(\boldsymbol{R}_b, \boldsymbol{q}) & \boldsymbol{0} \\ \boldsymbol{0} & \bar{\boldsymbol{J}}_q^{int}(\boldsymbol{q}) \boldsymbol{M}_q^*(\boldsymbol{q})^{-1} \bar{\boldsymbol{J}}_q^{int}(\boldsymbol{q})^T \end{bmatrix}, \tag{4.29}$$

where (4.21) and the property (4.12) of the dynamically-consistent nullspace are used. Let us now analyze the singularity-free region $\mathcal{Q}$ of the external-internal allocation space. Based on the triangular form (4.23a), $\boldsymbol{\Gamma}(\boldsymbol{R}_b, \boldsymbol{q})$ is singular when

$$\det \boldsymbol{A}_{cb}(\boldsymbol{R}_b, \boldsymbol{q})^{-T} \det \boldsymbol{M}_b(\boldsymbol{q}) \det \bar{\boldsymbol{J}}_q^{int}(\boldsymbol{q}) = \boldsymbol{0} \quad \Rightarrow \quad \det \bar{\boldsymbol{J}}_q^{int}(\boldsymbol{q}) = \boldsymbol{0}, \tag{4.30}$$

which says that the singularity of $\boldsymbol{\Gamma}(\boldsymbol{R}_b, \boldsymbol{q})$ depends only on the singularity of the internal mapping $\bar{\boldsymbol{J}}_q^{int}(\boldsymbol{q})$, and, in turn, that it depends only on the joints. Thus, the region $\mathcal{Q}$ reduces to

$$\mathcal{Q}^* = \left\{ \boldsymbol{q} \in \mathbb{R}^n : \min_{i=1,\dots,6+n} \sigma_i \left(\bar{\boldsymbol{J}}_q^{int}(\boldsymbol{q}) \right) \geq \sigma_{J_q^{int}, min} \right\}, \tag{4.31}$$

for some $\sigma_{J_q^{int},min} \in \mathbb{R}_+$. In $\mathcal{Q}^*$, the inverse of (4.29) can then be written, and it takes the form

$$\boldsymbol{M}_\chi(\boldsymbol{R}_b, \boldsymbol{q}) = \begin{bmatrix} \boldsymbol{M}_c(\boldsymbol{R}_b, \boldsymbol{q})^{-1} & \boldsymbol{0} \\ \boldsymbol{0} & \left(\bar{\boldsymbol{J}}_q^{int}(\boldsymbol{q}) \boldsymbol{M}_q^*(\boldsymbol{q})^{-1} \bar{\boldsymbol{J}}_q^{int}(\boldsymbol{q})^T\right)^{-1} \end{bmatrix}. \tag{4.32}$$

Then, the inertia is decoupled, meaning that the decoupling condition (4.7a) for the inertia holds.

Let us now analyze the decoupling condition (4.7b) for the Coriolis/centrifugal terms. Based on the transformation (2.69b), the Coriolis/centrifugal terms in (4.6) are given by

$$\begin{aligned} \boldsymbol{C}_\chi \boldsymbol{\chi} &= \boldsymbol{\Gamma}^{-T} \left(\boldsymbol{C} - \boldsymbol{M} \boldsymbol{\Gamma}^{-1} \dot{\boldsymbol{\Gamma}} \right) \boldsymbol{\Gamma}^{-1} \boldsymbol{\chi} \\ &= \boldsymbol{\Gamma}^{-T} \boldsymbol{M} \boldsymbol{\Gamma}^{-1} \left(\boldsymbol{\Gamma} \boldsymbol{M}^{-1} \boldsymbol{C} - \dot{\boldsymbol{\Gamma}} \right) \boldsymbol{v} \\ &= \boldsymbol{M}_\chi \left(\boldsymbol{\Gamma} \boldsymbol{M}^{-1} \boldsymbol{C} - \dot{\boldsymbol{\Gamma}} \right) \boldsymbol{v} \\ &= \begin{bmatrix} \boldsymbol{M}_c^{-1} & \boldsymbol{0} \\ \boldsymbol{0} & \left(\bar{\boldsymbol{J}}_q^{int} \boldsymbol{M}_q^{*-1} \bar{\boldsymbol{J}}_q^{int\ T} \right)^{-1} \end{bmatrix} \begin{bmatrix} \boldsymbol{L} \boldsymbol{M}^{-1} \boldsymbol{C} - \dot{\boldsymbol{L}} \\ \boldsymbol{J}^{int} \boldsymbol{M}^{-1} \boldsymbol{C} - \dot{\boldsymbol{J}}^{int} \end{bmatrix} \boldsymbol{v}, \end{aligned} \tag{4.33}$$

where (4.27) and (4.32) are used, and where the functional dependencies are omitted for brevity. Then, the first row results in

$$\begin{bmatrix} \boldsymbol{C}_{11} & \boldsymbol{C}_{12} \end{bmatrix} \boldsymbol{\chi} = \boldsymbol{M}_c^{-1} \underbrace{\left(\boldsymbol{L} \boldsymbol{M}^{-1} \boldsymbol{C} - \dot{\boldsymbol{L}} \right) \boldsymbol{v}}_{\boldsymbol{0}} = \boldsymbol{0}, \tag{4.34}$$

where the conservation structure, i.e., Property 2.4, is applied. This proves the decoupling condition (4.7b) for the Coriolis/centrifugal terms. Finally, let us compute the expression of the external interaction term in (2.70). By straightforwardly computing the inverse of the block-triangular actuation mapping in (4.54), and by using the expression of $\boldsymbol{J}_j(\boldsymbol{q})$ in (2.17), the contribution of the uncontrolled external wrenches is expressed as

$$\boldsymbol{\Gamma}(\boldsymbol{R}_b, \boldsymbol{q})^{-T} \sum_{j=0}^{n} \boldsymbol{J}_j(\boldsymbol{q})^T \boldsymbol{\mathcal{F}}_j^{ext} = \sum_{j=0}^{n} \begin{bmatrix} \boldsymbol{M}_c(\boldsymbol{R}_b, \boldsymbol{q})^{-1} \boldsymbol{A}_{jc}(\boldsymbol{R}_b, \boldsymbol{q})^T \\ \bar{\boldsymbol{J}}_q^{int}(\boldsymbol{q})^{-T} \boldsymbol{J}_{jq}^{int}(\boldsymbol{q})^T \end{bmatrix} \boldsymbol{\mathcal{F}}_j^{ext}. \tag{4.35}$$

Based on (4.32), (4.34), and (4.35), the dynamics has the form

$$\boldsymbol{M}_c(\boldsymbol{R}_b, \boldsymbol{q})^{-1} \dot{\boldsymbol{h}}_c = \boldsymbol{\alpha}_c + \boldsymbol{\alpha}_c^{ext}, \tag{4.36a}$$

$$\boldsymbol{M}_\chi^{int}(\boldsymbol{q}) \dot{\boldsymbol{\chi}}^{int} + \boldsymbol{C}_{\chi^{int}}(\boldsymbol{R}_b, \boldsymbol{q}, \boldsymbol{h}_c, \boldsymbol{\chi}^{int}) \boldsymbol{\chi}^{int} + \boldsymbol{C}_{\chi^{int}h}(\boldsymbol{R}_b, \boldsymbol{q}, \boldsymbol{h}_c, \boldsymbol{\chi}^{int}) \boldsymbol{h}_c = \boldsymbol{\varsigma}^{int} + \boldsymbol{\varsigma}^{int,ext}, \tag{4.36b}$$

where $\boldsymbol{M}_\chi^{int}(\boldsymbol{q}) = \left(\bar{\boldsymbol{J}}_q^{int}(\boldsymbol{q}) \boldsymbol{M}_q^*(\boldsymbol{q})^{-1} \bar{\boldsymbol{J}}_q^{int}(\boldsymbol{q})^T \right)^{-1} \in \mathbb{R}^{n \times n}$ is referred to as **generalized inertia of the internal motion**, for which the skew-symmetric property holds[7]:

$$\dot{\boldsymbol{M}}_\chi^{int}(\boldsymbol{q}) = \boldsymbol{C}_{\chi^{int}}(\boldsymbol{R}_b, \boldsymbol{q}, \boldsymbol{h}_c, \boldsymbol{\chi}^{int}) + \boldsymbol{C}_{\chi^{int}}(\boldsymbol{R}_b, \boldsymbol{q}, \boldsymbol{h}_c, \boldsymbol{\chi}^{int})^T. \tag{4.37}$$

The terms $\boldsymbol{\alpha}_c^{ext} \in \mathbb{R}^6$ and $\boldsymbol{\varsigma}^{int,ext} \in \mathbb{R}^6$ are the projections[8] of the uncontrolled external wrenches into the momentum and internal dynamics, respectively. Lastly, by inserting the

[7] This is a consequence of (4.10).

[8] Based on (4.35), they are $\boldsymbol{\alpha}_c^{ext} = \boldsymbol{M}_c(\boldsymbol{R}_b, \boldsymbol{q})^{-1} \boldsymbol{\mathcal{F}}_c^{ext}$, and $\boldsymbol{\varsigma}^{int,ext} = \sum_{j=0}^{n} \boldsymbol{J}_q^{int}(\boldsymbol{q})^{-T} \boldsymbol{J}_{jq}^{int}(\boldsymbol{q})^T \boldsymbol{\mathcal{F}}_j^{ext}$, where $\boldsymbol{\mathcal{F}}_c^{ext} = \sum_{j=0}^{n} \boldsymbol{A}_{jc}(\boldsymbol{R}_b, \boldsymbol{q})^T \boldsymbol{\mathcal{F}}_j^{ext}$.

virtual actuator (4.24) in (4.36), the dynamics (4.36) is rewritten as

$$\dot{\boldsymbol{h}}_c = \boldsymbol{\mathcal{F}}_c + \boldsymbol{\mathcal{F}}_c^{ext}, \tag{4.38a}$$

$$\boldsymbol{M}_{\chi}^{int}(\boldsymbol{q})\dot{\boldsymbol{\chi}}^{int} + \boldsymbol{C}_{\chi^{int}}(\boldsymbol{R}_b, \boldsymbol{q}, \boldsymbol{h}_c, \boldsymbol{\chi}^{int})\boldsymbol{\chi}^{int} + \boldsymbol{C}_{\chi^{int}h}(\boldsymbol{R}_b, \boldsymbol{q}, \boldsymbol{h}_c, \boldsymbol{\chi}^{int})\boldsymbol{h}_c = \boldsymbol{\varsigma}^{int} + \boldsymbol{\varsigma}^{int,ext}. \tag{4.38b}$$

where $\boldsymbol{\mathcal{F}}_c^{ext} \in \mathbb{R}^6$ is the resultant of all uncontrolled external wrenches around the CoM. Notice that the dynamics in (4.38) is decoupled[9] in $\boldsymbol{h}_c$ – as it was seeked at. The momentum is decoupled from the internal motion, however, note that the internal motion is coupled with the momentum via the Coriolis/centrifugal terms.

4.3. Centroid/circumcentroidal allocation space

In this section, an allocation space is derived which has simultaneously a decoupled actuation in the base force $\boldsymbol{f}_b$, i.e., it holds (4.4a), and a decoupled dynamics, i.e., the conditions in (4.7) hold.
Towards this aim, let us define a general **circumcentroidal motion** $\boldsymbol{\upsilon}^{\oplus} \in \mathbb{R}^s$ as a motion in the dynamically-consistent nullspace of the velocity of the CoM. It can be defined as

$$\boldsymbol{\upsilon}^{\oplus} := \boldsymbol{J}^{\oplus}(\boldsymbol{q})\boldsymbol{\upsilon}, \tag{4.39}$$

where $\boldsymbol{J}^{\oplus}(\boldsymbol{q}) \in \mathbb{R}^{s\times(6+n)}$ is a mapping having the property

$$\boldsymbol{L}_v(\boldsymbol{R}_b, \boldsymbol{q})\boldsymbol{M}(\boldsymbol{q})^{-1}\boldsymbol{J}^{\oplus}(\boldsymbol{q})^T = \boldsymbol{0}, \tag{4.40}$$

with $\boldsymbol{L}_v(\boldsymbol{R}_b, \boldsymbol{q})$ being the mapping of the CoM velocity defined in (2.43c).
To construct an allocation space which simultaneously verifies the decoupled actuation condition (4.4b) and the decoupled dynamics condition (4.7), one may choose as first motion the velocity of the CoM, i.e.,

$$\boldsymbol{\chi}_1 = \boldsymbol{v}_c = \boldsymbol{L}_v(\boldsymbol{R}_b, \boldsymbol{q})\boldsymbol{\upsilon}, \tag{4.41a}$$

and call $\boldsymbol{\chi}_1 \in \mathbb{R}^3$ as **centroid motion of the system**. Then, by defining a transformation $\bar{\boldsymbol{J}}^{\oplus}(\boldsymbol{q}) \in \mathbb{R}^{(n+3)\times(n+6)}$, one may choose the second motion to be a circumcentroidal motion of dimension $n+3$, as

$$\boldsymbol{\chi}_2 = \boldsymbol{\chi}^{\oplus} = \bar{\boldsymbol{J}}^{\oplus}(\boldsymbol{q})\boldsymbol{\upsilon}, \tag{4.41b}$$

and call $\boldsymbol{\chi}^{\oplus} \in \mathbb{R}^{n+3}$ as **circumcentroidal motion of the system**. The circumcentroidal transformation $\bar{\boldsymbol{J}}^{\oplus}(\boldsymbol{q}) \in \mathbb{R}^{n\times(n+6)}$ can be constructed based on the specific control application[10].
The concept of centroid-circumcentroidal actuation decomposition was first derived in [GOA19] for the end-effector motion of an arm-equipped body without reaction wheels. Herein, the concept is presented for the case of general motions of general open chain robots.

[9] The momentum equation (4.38a) is a well-known feature of a multibody system, and shall come at no surprise; that being said, note that the rationale of the external-internal motion decomposition is to endow this feature into the coordination of all actuators to remove the couplings in the thrusters wrench and simultaneously maintain the useful property (4.37) .

[10] The construction of $\bar{\boldsymbol{J}}^{\oplus}(\boldsymbol{q})$ will be detailed in Chapter 5.

4.3.1. Example of circumcentroidal motion

An example of circumcentroidal motion is now provided to make the concept more concrete. Let us consider the frame of the general j^{th} body; its velocity $\boldsymbol{\nu}_j$ is expressed by the relation (2.16c) using a mapping $\boldsymbol{J}_j \in \mathbb{R}^{6\times(6+n)}$. Then, one may define the mapping

$$\boldsymbol{J}_j^{\oplus}(\boldsymbol{q}) = \boldsymbol{J}_j(\boldsymbol{q})\boldsymbol{N}_v(\boldsymbol{q}) \in \mathbb{R}^{6\times(6+n)}, \tag{4.42}$$

where $\boldsymbol{N}_v(\boldsymbol{q}) \in \mathbb{R}^{(6+n)\times(6+n)}$ is the projector into the dynamically-consistent nullspace of the CoM velocity

$$\boldsymbol{N}_v(\boldsymbol{q}) = \boldsymbol{E} - \boldsymbol{L}_v(\boldsymbol{R}_b, \boldsymbol{q})^{\#}\boldsymbol{L}_v(\boldsymbol{R}_b, \boldsymbol{q}), \tag{4.43}$$

and where $\boldsymbol{L}_v(\boldsymbol{R}_b, \boldsymbol{q})^{\#} \in \mathbb{R}^{(6+n)\times 6}$ is the dynamically-consistent pseudo-inverse [Kha87] of $\boldsymbol{L}_v(\boldsymbol{R}_b, \boldsymbol{q})$, defined as

$$\boldsymbol{L}_v(\boldsymbol{R}_b, \boldsymbol{q})^{\#} = \boldsymbol{M}(\boldsymbol{q})^{-1}\boldsymbol{L}_v(\boldsymbol{R}_b, \boldsymbol{q})^T \left(\boldsymbol{L}_v(\boldsymbol{R}_b, \boldsymbol{q})\boldsymbol{M}(\boldsymbol{q})^{-1}\boldsymbol{L}_v(\boldsymbol{R}_b, \boldsymbol{q})^T\right)^{-1}. \tag{4.44}$$

Based on this, a circumcentroidal motion $\boldsymbol{\nu}_j^{\oplus} \in \mathbb{R}^6$ is defined as

$$\boldsymbol{\nu}_j^{\oplus} = \boldsymbol{J}_j^{\oplus}(\boldsymbol{q})\boldsymbol{\upsilon}, \tag{4.45}$$

and is referred to as **circumcentroidal velocity of the j^{th} body**. It can be shown (see Appendix A.2) that $\boldsymbol{J}_j^{\oplus}(\boldsymbol{q}) = \begin{bmatrix}\boldsymbol{0} & \boldsymbol{J}_{j\omega}^{\oplus}(\boldsymbol{q}) & \boldsymbol{J}_{jq}^{\oplus}(\boldsymbol{q})\end{bmatrix}$ and thus (4.45) simplifies to

$$\boldsymbol{\nu}_j^{\oplus} = \boldsymbol{J}_{j\omega}^{\oplus}(\boldsymbol{q})\boldsymbol{\omega}_b + \boldsymbol{J}_{jq}^{\oplus}(\boldsymbol{q})\dot{\boldsymbol{q}}, \tag{4.46}$$

where

$$\boldsymbol{J}_{j\omega}^{\oplus}(\boldsymbol{q}) = \begin{bmatrix}[\boldsymbol{o}_{jc}(\boldsymbol{q})]^{\wedge}\boldsymbol{R}_{jb}(\boldsymbol{q}) \\ \boldsymbol{R}_{jb}(\boldsymbol{q})\end{bmatrix} \in \mathbb{R}^{6\times 3}, \quad \boldsymbol{J}_{jq}^{\oplus}(\boldsymbol{q}) = \boldsymbol{J}_{jq}(\boldsymbol{q}) - \frac{1}{m}\begin{bmatrix}\boldsymbol{R}_{jb}(\boldsymbol{q}) \\ \boldsymbol{0}\end{bmatrix}\boldsymbol{M}_{vq}(\boldsymbol{q}) \in \mathbb{R}^{6\times n}. \tag{4.47}$$

It is interesting to observe that, by computing and comparing the translational and rotational parts of the velocities (4.18) and (4.46), the linear part of circumcentroidal velocity is not equivalent to the linear part of the internal velocity of the j^{th} body, i.e., it is $\boldsymbol{v}_j^{\oplus} \neq \boldsymbol{v}_j^{int}$; on the other hand, the angular part of circumcentroidal velocity is also not equivalent to the angular part of the internal velocity, but it is equivalent to the angular velocity of the j^{th} body, i.e., it is $\boldsymbol{\omega}_j^{\oplus} = \boldsymbol{\omega}_j$.

An interpretation of $\boldsymbol{\nu}_j^{\oplus}$ is now provided in terms of superposition of motions. Let us partition expressions of the velocities $\boldsymbol{v}_c$ and $\boldsymbol{\nu}_j$ in translation and rotation components, as

$$\boldsymbol{v}_c = \boldsymbol{R}_b\boldsymbol{v}_b - \boldsymbol{R}_b\left[\boldsymbol{p}_{bc}(\boldsymbol{q})\right]^{\wedge}\boldsymbol{\omega}_b + \boldsymbol{R}_b\frac{1}{m}\boldsymbol{M}_{vq}(\boldsymbol{q})\dot{\boldsymbol{q}}, \tag{4.48}$$

$$\boldsymbol{\nu}_j = \begin{bmatrix}\boldsymbol{R}_{jb}(\boldsymbol{q}) \\ \boldsymbol{0}\end{bmatrix}\boldsymbol{v}_b + \begin{bmatrix}[\boldsymbol{o}_{jb}(\boldsymbol{q})]^{\wedge}\boldsymbol{R}_{jb}(\boldsymbol{q}) \\ \boldsymbol{R}_{jb}(\boldsymbol{q})\end{bmatrix}\boldsymbol{\omega}_b + \boldsymbol{J}_{jq}(\boldsymbol{q})\dot{\boldsymbol{q}}, \tag{4.49}$$

where (2.43c),(2.44c), (2.16b), and (2.8) are used. By eliminating the base translational motion $\boldsymbol{v}_b$ from (4.48) and (4.49), and by inserting (4.46) into the resulting equation, the velocity $\boldsymbol{\nu}_j$ can be rewritten as

$$\boldsymbol{\nu}_j = \begin{bmatrix}\boldsymbol{R}_{jc}(\boldsymbol{R}_b, \boldsymbol{q}) \\ \boldsymbol{0}\end{bmatrix}\boldsymbol{v}_c + \boldsymbol{\nu}_j^{\oplus}, \tag{4.50}$$

Equation (4.50) gives the intuition that the velocity of the general j^{th} body is the superposition of its internal velocity and a velocity induced by the centroid motion.

4.3.2. Decoupled actuation of the centroid/circumcentroidal space

Let us preliminary derive the following Lemma.

Lemma 2. *Considering a partitioning* $\boldsymbol{\upsilon} = \begin{bmatrix}\boldsymbol{v}_b^T & \boldsymbol{\omega}_b^T & \dot{\boldsymbol{q}}^T\end{bmatrix}^T$ *and* $\bar{\boldsymbol{J}}^{\oplus}(\boldsymbol{q}) = \begin{bmatrix}\bar{\boldsymbol{J}}_v^{\oplus}(\boldsymbol{q}) & \bar{\boldsymbol{J}}_\omega^{\oplus}(\boldsymbol{q}) & \bar{\boldsymbol{J}}_q^{\oplus}(\boldsymbol{q})\end{bmatrix}$, *it is* $\bar{\boldsymbol{J}}_v^{\oplus}(\boldsymbol{q}) \equiv \boldsymbol{0}$.

Proof. Condition (4.40) can be rewritten as

$$\boldsymbol{L}_v(\boldsymbol{R}_b, \boldsymbol{q})\boldsymbol{M}(\boldsymbol{q})^{-1} \begin{bmatrix}\bar{\boldsymbol{J}}_v^{\oplus}(\boldsymbol{q})^T \\ \bar{\boldsymbol{J}}_\omega^{\oplus}(\boldsymbol{q})^T \\ \bar{\boldsymbol{J}}_q^{\oplus}(\boldsymbol{q})^T\end{bmatrix} = \boldsymbol{0}. \tag{4.51}$$

By considering the relation $\boldsymbol{L}_v(\boldsymbol{R}_b, \boldsymbol{q}) = \frac{1}{m}\boldsymbol{S}_v\boldsymbol{L}(\boldsymbol{R}_b, \boldsymbol{q})$ in (2.44b), and applying (4.21), it results

$$\boldsymbol{L}_v(\boldsymbol{R}_b, \boldsymbol{q})\boldsymbol{M}(\boldsymbol{q})^{-1} = \frac{1}{m}\boldsymbol{S}_v\boldsymbol{L}(\boldsymbol{R}_b, \boldsymbol{q})\boldsymbol{M}(\boldsymbol{q})^{-1} = \frac{1}{m}\boldsymbol{S}_v \begin{bmatrix}\boldsymbol{A}_{cb}(\boldsymbol{R}_b, \boldsymbol{q})^{-T} & \boldsymbol{0}\end{bmatrix} = \begin{bmatrix}\boldsymbol{R}_b\frac{1}{m} & \boldsymbol{0} & \boldsymbol{0}\end{bmatrix}, \tag{4.52}$$

and then (4.51) reduces to

$$\frac{1}{m}\boldsymbol{R}_b\bar{\boldsymbol{J}}_v^{\oplus}(\boldsymbol{q})^T = \boldsymbol{0}. \tag{4.53}$$

In turn, it follows that $\bar{\boldsymbol{J}}_v^{\oplus}(\boldsymbol{q}) = \boldsymbol{0}$, and this proves the Lemma. □

Note that, as a consequence of Lemma 2, it results that any circumcentroidal velocity depends only on the velocity of the joints and on the angular velocity of the base, it does not depend on the linear velocity of the base. Furthermore, the decoupling condition (4.4b) for the actuation is met, and the transformations of the allocation space have the form

$$\begin{bmatrix}\boldsymbol{v}_c \\ \boldsymbol{\chi}^{\oplus}\end{bmatrix} = \underbrace{\begin{bmatrix}\boldsymbol{R}_b & \frac{1}{m}\boldsymbol{R}_b\boldsymbol{M}_{v\omega}(\boldsymbol{q}) & \frac{1}{m}\boldsymbol{R}_b\boldsymbol{M}_{vq}(\boldsymbol{q}) \\ \boldsymbol{0} & \bar{\boldsymbol{J}}_\omega^{\oplus}(\boldsymbol{q}) & \bar{\boldsymbol{J}}_q^{\oplus}(\boldsymbol{q})\end{bmatrix}}_{\boldsymbol{\Gamma}(\boldsymbol{R}_b, \boldsymbol{q})}\begin{bmatrix}\boldsymbol{v}_b \\ \boldsymbol{\omega}_b \\ \dot{\boldsymbol{q}}\end{bmatrix}, \quad \begin{bmatrix}\boldsymbol{f}_b \\ \boldsymbol{m}_b \\ \boldsymbol{\tau}\end{bmatrix} = \underbrace{\begin{bmatrix}\boldsymbol{R}_b^T & \boldsymbol{0} \\ \frac{1}{m}\boldsymbol{M}_{v\omega}(\boldsymbol{q})^T\boldsymbol{R}_b^T & \bar{\boldsymbol{J}}_\omega^{\oplus}(\boldsymbol{q})^T \\ \frac{1}{m}\boldsymbol{M}_{vq}(\boldsymbol{q})^T\boldsymbol{R}_b^T & \bar{\boldsymbol{J}}_q^{\oplus}(\boldsymbol{q})^T\end{bmatrix}}_{\boldsymbol{\Gamma}(\boldsymbol{R}_b, \boldsymbol{q})^T}\begin{bmatrix}\boldsymbol{f}_c \\ \boldsymbol{\varsigma}^{\oplus}\end{bmatrix}, \tag{4.54}$$

where $\boldsymbol{f}_c \in \mathbb{R}^3$ is the virtual actuator associated to the velocity of the CoM , and $\boldsymbol{\varsigma}^{\oplus} \in \mathbb{R}^{n+3}$ is the virtual actuator associated to the circumcentroidal motion. The transformation of the generalized velocity in (4.54) is called **centroid-circumcentroidal motion decomposition**, whereas the transformation of the generalized velocities, is called **centroid-circumcentroidal actuation decomposition**. Note that the actuation decomposition is in the block-decoupled form (4.4a), so it provides a mean of decoupling the actuation in the base force $\boldsymbol{f}_b$ – as it was seeked at.

4.3.3. Decoupled dynamics of the centroid/circumcentroidal space

Herein it is now shown how the allocation space defined by (4.41) has a dynamics with a decoupled structure satisfying the conditions (4.7). Based on the definitions (4.41), $\boldsymbol{\Gamma}(\boldsymbol{R}_b, \boldsymbol{q})$ has the form

$$\boldsymbol{\Gamma}(\boldsymbol{R}_b, \boldsymbol{q}) = \begin{bmatrix}\boldsymbol{L}_v(\boldsymbol{R}_b, \boldsymbol{q}) \\ \bar{\boldsymbol{J}}^{\oplus}(\boldsymbol{q})\end{bmatrix}. \tag{4.55}$$

Hence, the inverse inertia $\boldsymbol{M}_\chi(\boldsymbol{R}_b,\boldsymbol{q})^{-1} = \boldsymbol{\Gamma}(\boldsymbol{R}_b,\boldsymbol{q})\boldsymbol{M}(\boldsymbol{q})^{-1}\boldsymbol{\Gamma}(\boldsymbol{R}_b,\boldsymbol{q})^T$ takes the form

$$\boldsymbol{M}_\chi(\boldsymbol{R}_b,\boldsymbol{q})^{-1} = \begin{bmatrix} \boldsymbol{L}_v(\boldsymbol{R}_b,\boldsymbol{q})\boldsymbol{M}(\boldsymbol{q})^{-1}\boldsymbol{L}_v(\boldsymbol{R}_b,\boldsymbol{q})^T & \boldsymbol{L}_v(\boldsymbol{R}_b,\boldsymbol{q})\boldsymbol{M}(\boldsymbol{q})^{-1}\bar{\boldsymbol{J}}^{\oplus}(\boldsymbol{q})^T \\ \bar{\boldsymbol{J}}^{\oplus}(\boldsymbol{q})\boldsymbol{M}(\boldsymbol{q})^{-1}\boldsymbol{L}_v(\boldsymbol{R}_b,\boldsymbol{q})^T & \bar{\boldsymbol{J}}^{\oplus}(\boldsymbol{q})\boldsymbol{M}(\boldsymbol{q})^{-1}\bar{\boldsymbol{J}}^{\oplus}(\boldsymbol{q})^T \end{bmatrix} \tag{4.56}$$

$$= \begin{bmatrix} \frac{1}{m}\boldsymbol{E} & \boldsymbol{0} \\ \boldsymbol{0} & \bar{\boldsymbol{J}}^{\oplus}(\boldsymbol{q})\boldsymbol{M}(\boldsymbol{q})^{-1}\bar{\boldsymbol{J}}^{\oplus}(\boldsymbol{q})^T \end{bmatrix}, \tag{4.57}$$

where (4.52) and (2.35) are applied to simplify $\boldsymbol{L}_v(\boldsymbol{R}_b,\boldsymbol{q})\boldsymbol{M}(\boldsymbol{q})^{-1}\boldsymbol{L}_v(\boldsymbol{R}_b,\boldsymbol{q})^T$, and where the property (4.40) of the dynamically-consistent nullspace is used to nullify the couplings. Let us now analyze the singularity-free region $\mathcal{Q}$ of the centroid-circumcentroidal space. Based on the triangular form (4.54), $\boldsymbol{\Gamma}(\boldsymbol{R}_b,\boldsymbol{q})$ is singular when

$$\det \boldsymbol{R}_b \det \begin{bmatrix} \bar{\boldsymbol{J}}^{\oplus}_{\omega}(\boldsymbol{q}) & \bar{\boldsymbol{J}}^{\oplus}_{q}(\boldsymbol{q}) \end{bmatrix} = \boldsymbol{0} \quad \Rightarrow \quad \det \begin{bmatrix} \bar{\boldsymbol{J}}^{\oplus}_{\omega}(\boldsymbol{q}) & \bar{\boldsymbol{J}}^{\oplus}_{q}(\boldsymbol{q}) \end{bmatrix} = \boldsymbol{0}, \tag{4.58}$$

which says that the singularity of $\boldsymbol{\Gamma}(\boldsymbol{R}_b,\boldsymbol{q})$ depends only on the singularity of the circumcentroidal mapping $\begin{bmatrix} \bar{\boldsymbol{J}}^{\oplus}_{\omega}(\boldsymbol{q}) & \bar{\boldsymbol{J}}^{\oplus}_{q}(\boldsymbol{q}) \end{bmatrix}$, and, in turn, that it depends only on the joints. Thus, the region $\mathcal{Q}$ reduces to

$$\mathcal{Q}^{\oplus} = \left\{ \boldsymbol{q} \in \mathbb{R}^n : \min_{i=1,\dots,6+n} \sigma_i \left(\begin{bmatrix} \bar{\boldsymbol{J}}^{\oplus}_{\omega}(\boldsymbol{q}) & \bar{\boldsymbol{J}}^{\oplus}_{q}(\boldsymbol{q}) \end{bmatrix} \right) \geq \sigma_{J^{\oplus},min} \right\}, \tag{4.59}$$

for some $\sigma_{J^{\oplus},min} \in \mathbb{R}_+$. In $\mathcal{Q}^{\oplus}$, the inverse of (4.57) can then be written, and it takes the form

$$\boldsymbol{M}_\chi(\boldsymbol{R}_b,\boldsymbol{q}) = \begin{bmatrix} m\boldsymbol{E} & \boldsymbol{0} \\ \boldsymbol{0} & \left(\bar{\boldsymbol{J}}^{\oplus}(\boldsymbol{q})\boldsymbol{M}(\boldsymbol{q})^{-1}\bar{\boldsymbol{J}}^{\oplus}(\boldsymbol{q})^T\right)^{-1} \end{bmatrix}. \tag{4.60}$$

Then, it is straightforward to see that the decoupling condition for the inertia, i.e., equation (4.7a), holds.

Let us now analyze the decoupling condition (4.7b) for the Coriolis/centrifugal terms. Based on the transformation (2.69b), the Coriolis/centrifugal terms in (4.6) are given by

$$\begin{aligned} \boldsymbol{C}_\chi\boldsymbol{\chi} &= \boldsymbol{\Gamma}^{-T}\left(\boldsymbol{C} - \boldsymbol{M}\boldsymbol{\Gamma}^{-1}\dot{\boldsymbol{\Gamma}}\right)\boldsymbol{\Gamma}^{-1}\boldsymbol{\chi} \\ &= \boldsymbol{\Gamma}^{-T}\boldsymbol{M}\boldsymbol{\Gamma}^{-1}\left(\boldsymbol{\Gamma}\boldsymbol{M}^{-1}\boldsymbol{C} - \dot{\boldsymbol{\Gamma}}\right)\boldsymbol{v} \\ &= \boldsymbol{M}_\chi\left(\boldsymbol{\Gamma}\boldsymbol{M}^{-1}\boldsymbol{C} - \dot{\boldsymbol{\Gamma}}\right)\boldsymbol{v} \\ &= \begin{bmatrix} m\boldsymbol{E} & \boldsymbol{0} \\ \boldsymbol{0} & \left(\bar{\boldsymbol{J}}^{\oplus}\boldsymbol{M}^{-1}\bar{\boldsymbol{J}}^{\oplus\ T}\right)^{-1} \end{bmatrix} \begin{bmatrix} \boldsymbol{L}_v\boldsymbol{M}^{-1}\boldsymbol{C} - \dot{\boldsymbol{L}}_v \\ \bar{\boldsymbol{J}}^{\oplus}\boldsymbol{M}^{-1}\boldsymbol{C} - \dot{\bar{\boldsymbol{J}}}^{\oplus} \end{bmatrix} \boldsymbol{v}, \end{aligned} \tag{4.61}$$

where (4.55) and (4.60) are used, and where the functional dependencies are omitted for brevity Then, the first row results in

$$\begin{bmatrix} \boldsymbol{C}_{11} & \boldsymbol{C}_{12} \end{bmatrix}\boldsymbol{\chi} = m\underbrace{\left(\boldsymbol{L}_v\boldsymbol{M}^{-1}\boldsymbol{C} - \dot{\boldsymbol{L}}_v\right)\boldsymbol{v}}_{\boldsymbol{0}} = \boldsymbol{0}, \tag{4.62}$$

where the symmetry of the CoM velocity, i.e., Property 2.4, is applied. This proves the decoupling condition (4.7b). Finally, let us compute the expression of the term related to the uncontrolled external wrenches in (2.70). By straightforwardly computing the inverse of the block-triangular matrix actuation mapping in (4.54), the term results in

$$\boldsymbol{\Gamma}(\boldsymbol{R}_b,\boldsymbol{q})^{-T}\sum_{j=0}^{n}\boldsymbol{J}_j(\boldsymbol{q})^T\boldsymbol{\mathcal{F}}_j^{ext} = \sum_{j=0}^{n}\begin{bmatrix} \boldsymbol{R}_{jc}(\boldsymbol{R}_b,\boldsymbol{q})^T\boldsymbol{f}_j^{ext} \\ \begin{bmatrix} \bar{\boldsymbol{J}}^{\oplus}_{\omega}(\boldsymbol{q}) & \bar{\boldsymbol{J}}^{\oplus}_{q}(\boldsymbol{q}) \end{bmatrix}^{-T}\begin{bmatrix} \boldsymbol{J}^{\oplus}_{j\omega}(\boldsymbol{q})^T \\ \boldsymbol{J}^{\oplus}_{jq}(\boldsymbol{q})^T \end{bmatrix}\boldsymbol{\mathcal{F}}_j^{ext} \end{bmatrix}. \tag{4.63}$$

Based on (4.60), (4.62), and (4.63), the centroid-circumcentroidal dynamics has the form

$$m\dot{\boldsymbol{v}}_c = \boldsymbol{f}_c + \boldsymbol{f}_c^{ext} \tag{4.64a}$$

$$\boldsymbol{M}_{\chi}^{\oplus}(\boldsymbol{q})\dot{\boldsymbol{\chi}}^{\oplus} + \boldsymbol{C}_{\chi^{\oplus}}(\boldsymbol{R}_b, \boldsymbol{q}, \boldsymbol{v}_c, \boldsymbol{\chi}^{\oplus})\boldsymbol{\chi}^{\oplus} + \boldsymbol{C}_{\chi^{\oplus}v}(\boldsymbol{R}_b, \boldsymbol{q}, \boldsymbol{v}_c, \boldsymbol{\chi}^{\oplus})\boldsymbol{v}_c = \boldsymbol{\varsigma}^{\oplus} + \boldsymbol{\varsigma}^{\oplus ext}, \tag{4.64b}$$

where $\boldsymbol{M}_{\chi}^{\oplus}(\boldsymbol{q}) = \left(\bar{\boldsymbol{J}}^{\oplus}(\boldsymbol{q})\boldsymbol{M}(\boldsymbol{q})^{-1}\bar{\boldsymbol{J}}^{\oplus}(\boldsymbol{q})^T\right)^{-1} \in \mathbb{R}^{(n+3)\times(n+3)}$ is referred to as **generalized inertia of the circumcentroidal motion**, and where $\boldsymbol{f}_c^{ext} \in \mathbb{R}^3$ and $\boldsymbol{\varsigma}^{\oplus ext} \in \mathbb{R}^6$ are the projections[11] of the external wrenches into the centroid and circumcentroidal space, respectively. For the dynamics matrices in (4.64b) it holds the skew-symmetry property:

$$\dot{\boldsymbol{M}}_{\chi}^{\oplus}(\boldsymbol{q}) = \boldsymbol{C}_{\chi^{\oplus}}(\boldsymbol{R}_b, \boldsymbol{q}, \boldsymbol{v}_c, \boldsymbol{\chi}^{\oplus}) + \boldsymbol{C}_{\chi^{\oplus}}(\boldsymbol{R}_b, \boldsymbol{q}, \boldsymbol{v}_c, \boldsymbol{\chi}^{\oplus})^T. \tag{4.65}$$

Notice that the left-hand side of (4.64) has a decoupled structure[12] – as it was seeked at –, wherein $\boldsymbol{C}_{\chi^{\oplus}v}(\boldsymbol{R}_b, \boldsymbol{q}, \boldsymbol{v}_c, \boldsymbol{\chi}^{\oplus})\boldsymbol{v}_c$ represents the perturbation of the CoM system into the circumcentroidal system.

4.4. Summary

In this chapter, the concept of thrusters-decoupled actuation was mathematically formulated; furthermore, the concept of invariant task was mathematically formulated based on a decoupled form of the dynamics in the allocation space.
It was analyzed that a complete or partial thrusters-decoupled actuation removes, completely or partially, respectively, the direct coupling of the free-flying strategy; furthermore, the adoption of an invariant task instead of a base control task removes the indirect coupling of the same strategy. By means of the framework derived in the chapter, the limitations of the free-flying strategy can be thus completely or partially solved. Two decompositions of the dynamics were presented, which simultaneously own a thrusters-decoupled actuation and a decoupled dynamics suitable for the definition of an invariant task; they are used as a framework for the derivation of Whole-Body controllers in the next chapters. In the first decomposition, i.e., the external-internal decomposition, the system dynamics was decomposed based on the momentum of the whole robot, and on internal velocities. The internal velocities were defined as general motions in the inertia-weighted null space of the momentum; the internal velocity of a body of the multi-body chain was derived as a particular case of internal velocity, and it was linked to the generalized Jacobian. In the second decomposition, i.e., the centroid-circumcentroidal decomposition, the system was decomposed based on the velocity of the CoM of the whole robot, and on circumcentroidal velocities. The circumcentroidal velocities were defined as general motions in the inertia-weighted null space of the velocity of the CoM (or, equivalently, of the linear momentum); the circumcentroidal velocity of a body of the multi-body chain was derived as a particular case of circumcentroidal velocity.

In the next chapter, the framework is applied for deriving controllers of an orbital robot, which satisfy the whole-body requirements envisioned in Section 1.2 while overcoming or reducing the limitations of the free-floating and free-flying strategies.

[11] They are given by $\boldsymbol{f}_c^{ext} = \sum_{j=0}^{n} \boldsymbol{R}_{jc}(\boldsymbol{R}_b, \boldsymbol{q})^T \boldsymbol{f}_j^{ext}$ and $\boldsymbol{\varsigma}^{\oplus ext} = \sum_{j=0}^{n} \begin{bmatrix}\bar{\boldsymbol{J}}_{\omega}^{\oplus}(\boldsymbol{q}) & \bar{\boldsymbol{J}}_{q}^{\oplus}(\boldsymbol{q})\end{bmatrix}^{-T} \begin{bmatrix}\boldsymbol{J}_{j\omega}^{\oplus}(\boldsymbol{q})^T \\ \boldsymbol{J}_{jq}^{\oplus}(\boldsymbol{q})^T\end{bmatrix} \boldsymbol{\mathcal{F}}_j^{ext}$. The term $\boldsymbol{f}_c^{ext}$ is obviously the resultant of all uncontrolled external forces

[12] The CoM equation (4.64a) is a well-known feature of a multibody system, and shall come at no surprise; that being said, note that the rationale of the centroid-circumcentroidal motion decomposition is to endow this feature into the coordination of all actuators so to remove the couplings in the actuation and simultaneously maintain the useful property (4.65).

CHAPTER 5

Whole-Body Control for robots with thrusters

In this chapter, whole-body controllers for orbital robots equipped with one arm and a set of spacecraft-mounted thrusters are presented. Throughout the chapter it is therefore intended that the used dynamics and kinematics matrices are those of a robot without reaction wheels (see Section 2.4).
The controllers developed herein allow enforcing some of the whole-body requirements listed in Section 1.2, thus providing a more general control approach than the free-floating and free-flying strategies. In particular, two controllers are presented:

(C3) Whole-Body Control with no requirements on the base (robot without RWs),

(C4) Whole-Body Control with requirements on the attitude of the base (robot without RWs).

Controller (C3) is designed to satisfy the whole-body requirements (R1), (R2), and (R3) listed in Section 1.2; to implement the desired feature of reducing the use of the thrusters, the controller employs a **complete decoupling** of the thrusters and of the dynamics. Controller (C4) is designed to satisfy the same requirements of Controller (C3), and to additionally enforce the requirement (R4) for the particular case of control of the attitude of the base. To enforce this additional requirement in a system with thrusters only – i.e., without further actuation devices, such as momentum exchange devices –, and to endow the controller with the desired feature of reducing the use of the thrusters, a **partial decoupling** of the thrusters and of the dynamics is employed. Doing so results in a control approach which lies in between of a purely whole-body one and a free-flying one, and can be used as an intermediate solution to at least endow a floating-base behavior in translation in those systems with attitude-control requirements.

The requirements are enforced by assigning the following tasks: regulation of the pose of the end-effector in order to force requirement (R1); stabilization of any residual joint motion in the system in order to enforce requirement (R2); regulation of the position of the CoM in order to enforce (R3); regulation of the orientation of the base in order to enforce (R4) for the particular base body.

The controllers (C3) and (C4) are presented in Sections 5.1 and 5.2, respectively. Finally, a summary is drawn up in Section 5.3.

5.1. Whole-Body Control with no requirements on the base

The control method developed herein is based on the external-internal motion decomposition described in Section 4.2, and on the **momentum dumping** and **CoM control** invariant tasks, firstly introduced in [GGAS17] and [GCAS18], respectively.
The method was developed in [GGAS17] and [GCAS18] for a nonredundant arm; in the following, the extended method for application with a redundant arm is presented.

5.1.1. Transformation of the dynamics

In the following, the transformation of the system into an external-internal form is addressed. For a robot without reaction wheels, the internal motion of the external-internal decomposition shall have dimension n_m; the construction of the internal motion is described in the following. Let us consider the internal velocity $\boldsymbol{\nu}_e^{int} \in \mathbb{R}^6$ of the end-effector. According to the general expression (4.17), $\boldsymbol{\nu}_e^{int}$ is given by

$$\boldsymbol{\nu}_e^{int} = \boldsymbol{J}_e^{int}(\boldsymbol{q}_m)\boldsymbol{\upsilon}, \tag{5.1}$$

where $\boldsymbol{J}_e^{int}(\boldsymbol{q}_m) \in \mathbb{R}^{6\times(6+n_m)}$. The internal velocity of the end-effector is a six-dimensional motion. For a redundant arm it is $n_m > 6$; thus, an additional internal motion of dimension $r = n_m - 6$ is required to construct an internal motion of dimension n_m; $r \in \mathbb{N}$ denotes the degree of redundancy of the arm. By denoting $\boldsymbol{\upsilon}_n^{int} \in \mathbb{R}^r$ such an additional internal motion, it can be expressed as

$$\boldsymbol{\upsilon}_n^{int} = \boldsymbol{J}_n^{int}(\boldsymbol{q}_m)\boldsymbol{\upsilon}, \tag{5.2}$$

where $\boldsymbol{J}_n^{int}(\boldsymbol{q}_m) \in \mathbb{R}^{r\times(6+n_m)}$. To limit the interference with the end-effector, one may define $\boldsymbol{\upsilon}_n^{int}$ as being a dynamically-consistent null-space velocity of the end-effector internal velocity. This is done by choosing a mapping $\boldsymbol{J}_n^{int}(\boldsymbol{q}_m)$ satisfying the condition

$$\boldsymbol{J}_e^{int}(\boldsymbol{q}_m)\boldsymbol{M}(\boldsymbol{q}_m)^{-1}\boldsymbol{J}_n^{int}(\boldsymbol{q}_m)^T = \boldsymbol{0}. \tag{5.3}$$

The expressions of $\boldsymbol{J}_e^{int}(\boldsymbol{q}_m)$ and $\boldsymbol{J}_n^{int}(\boldsymbol{q}_m)$, as well as their sub-blocks, are provided in the Appendix C.3.

Based on the above definitions, $\boldsymbol{\nu}_e^{int}$ and $\boldsymbol{\upsilon}_n^{int}$ form an internal motion $\boldsymbol{\chi}^{int} = \begin{bmatrix}\boldsymbol{\nu}_e^{int}\\ \boldsymbol{\upsilon}_n^{int}\end{bmatrix}$ of dimension n_m, which can be expressed as

$$\boldsymbol{\chi}^{int} = \begin{bmatrix}\boldsymbol{\nu}_e^{int}\\ \boldsymbol{\upsilon}_n^{int}\end{bmatrix} = \bar{\boldsymbol{J}}^{int}(\boldsymbol{q}_m)\boldsymbol{\upsilon}, \qquad \text{where} \quad \bar{\boldsymbol{J}}^{int}(\boldsymbol{q}_m) = \begin{bmatrix}\boldsymbol{J}_e^{int}(\boldsymbol{q}_m)\\ \boldsymbol{J}_n^{int}(\boldsymbol{q}_m)\end{bmatrix} \in \mathbb{R}^{n_m\times(6+n_m)}. \tag{5.4}$$

Hence, in the singularity-free region $\mathcal{Q}^{int}$ (see (4.31)) the dynamics in the allocation space can be transformed to the decoupled external-internal form (4.38). Considering only contact at the end-effector[1], the dynamics has the form

$$\dot{\boldsymbol{h}}_c = \boldsymbol{\mathcal{F}}_c + \boldsymbol{A}_{ec}(\boldsymbol{R}_b, \boldsymbol{q}_m)^T\boldsymbol{\mathcal{F}}_e^{ext}, \tag{5.5a}$$

$$\boldsymbol{M}_\chi^{int}(\boldsymbol{q}_m)\begin{bmatrix}\dot{\boldsymbol{\nu}}_e^{int}\\ \dot{\boldsymbol{\upsilon}}_n^{int}\end{bmatrix} + \boldsymbol{C}_{\chi^{int}}(\boldsymbol{R}_b, \boldsymbol{q}_m, \boldsymbol{h}_c, \boldsymbol{\chi}^{int})\begin{bmatrix}\boldsymbol{\nu}_e^{int}\\ \boldsymbol{\upsilon}_n^{int}\end{bmatrix} + \boldsymbol{C}_{\chi^{int}h}(\boldsymbol{R}_b, \boldsymbol{q}_m, \boldsymbol{h}_c, \boldsymbol{\chi}^{int})\boldsymbol{h}_c = \begin{bmatrix}\boldsymbol{\mathcal{F}}_e^{int}\\ \boldsymbol{\varsigma}_n^{int}\end{bmatrix} + \begin{bmatrix}\boldsymbol{\mathcal{F}}_e^{ext}\\ \boldsymbol{0}\end{bmatrix}, \tag{5.5b}$$

[1] In this case, the terms $\boldsymbol{\mathcal{F}}_c^{ext}$ and $\boldsymbol{\varsigma}^{int,ext}$ in (4.38) are $\boldsymbol{\mathcal{F}}_c^{ext} = \boldsymbol{A}_{ec}(\boldsymbol{R}_b, \boldsymbol{q})^T\boldsymbol{\mathcal{F}}_e^{ext}$ and $\boldsymbol{\varsigma}^{int,ext} = \begin{bmatrix}\boldsymbol{\mathcal{F}}_e^{ext}\\ \boldsymbol{0}\end{bmatrix}$.

where $\boldsymbol{\mathcal{F}}_e^{int} \in \mathbb{R}^6$ and $\boldsymbol{\varsigma}_n^{int} \in \mathbb{R}^r$ are the virtual actuators associated to $\boldsymbol{\nu}_e^{int}$ and $\boldsymbol{\upsilon}_n^{int}$, respectively, and where $\boldsymbol{\mathcal{F}}_e^{ext} \in \mathbb{R}^6$ is the contact force at the end-effector. The virtual actuators are related to the actuators by an actuation mapping decoupled in $\boldsymbol{\mathcal{F}}_b$. By using (2.61c), (4.25), and (C.11) the actuation mapping is expressed as

$$\begin{bmatrix} \boldsymbol{\mathcal{F}}_b \\ \boldsymbol{\tau}_m \end{bmatrix} = \begin{bmatrix} \boldsymbol{A}_{cb}(\boldsymbol{R}_b, \boldsymbol{q}_m)^T & \boldsymbol{0} & \boldsymbol{0} \\ \boldsymbol{M}_{bm}(\boldsymbol{q}_m)^T \boldsymbol{M}_b(\boldsymbol{q}_m)^{-1} \boldsymbol{A}_{cb}(\boldsymbol{R}_b, \boldsymbol{q}_m)^T & \boldsymbol{J}_{em}^{int}(\boldsymbol{q}_m)^T & \boldsymbol{J}_{nm}^{int}(\boldsymbol{q}_m)^T \end{bmatrix} \begin{bmatrix} \boldsymbol{\mathcal{F}}_c \\ \boldsymbol{\mathcal{F}}_e^{int} \\ \boldsymbol{\varsigma}_n^{int} \end{bmatrix} \tag{5.6}$$

where $\boldsymbol{J}_{em}^{int}(\boldsymbol{q}_m) \in \mathbb{R}^{6 \times n_m}$ and $\boldsymbol{J}_{nm}^{int}(\boldsymbol{q}_m) \in \mathbb{R}^{r \times n_m}$ are the sub-blocks of $\boldsymbol{J}_e^{int}(\boldsymbol{q}_m)$ and $\boldsymbol{J}_n^{int}(\boldsymbol{q}_m)$, respectively, associated to the manipulator motion; note that $\boldsymbol{J}_{em}^{int}(\boldsymbol{q}_m) = \boldsymbol{J}_{em}^{*}(\boldsymbol{q}_m)$, i.e., $\boldsymbol{J}_{em}^{int}(\boldsymbol{q}_m)$ is the generalized Jacobian (3.1).
Let us mention that the choice of the dynamically-consistent null space of the end-effector leads to a decoupled internal inertia

$$\boldsymbol{M}_{\chi}^{int}(\boldsymbol{q}_m) = \begin{bmatrix} \left(\boldsymbol{J}_{em}^{int}(\boldsymbol{q}_m) \boldsymbol{M}_m^{*}(\boldsymbol{q}_m)^{-1} \boldsymbol{J}_{em}^{int}(\boldsymbol{q}_m)^T\right)^{-1} & \boldsymbol{0} \\ \boldsymbol{0} & \boldsymbol{Z}_m(\boldsymbol{q}_m) \boldsymbol{M}_m^{*}(\boldsymbol{q}_m) \boldsymbol{Z}_m(\boldsymbol{q}_m)^T \end{bmatrix}, \tag{5.7}$$

where $\boldsymbol{Z}_m \in \mathbb{R}^{r \times n_m}$ is a null-space base matrix (see Appendix C.3). However, the internal Coriolis/centrifugal matrix $\boldsymbol{C}_{\chi^{int}}(\boldsymbol{R}_b, \boldsymbol{q}_m, \boldsymbol{h}_c, \boldsymbol{\nu}_e^{int}, \boldsymbol{\upsilon}_n^{int})$ is still fully coupled. Therefore, the end-effector and null-space subsystems in (5.5b) are coupled.
Two considerations are now germane to the argumentation. First, note that by exploiting the decoupled structure of the dynamics (5.5), it is possible to design controllers in a cascade fashion, using $\boldsymbol{\mathcal{F}}_c$ to control the global motion, and using $\boldsymbol{\mathcal{F}}_e^{int}$ and $\boldsymbol{\varsigma}_n^{int}$ to control the coupled end-effector and the null-space motion. From this it follows that if one assigns an invariant task to the virtual actuator $\boldsymbol{\mathcal{F}}_c$, then any indirect coupling[2] of the arm tasks, i.e., the end-effector and null-space tasks, into the thrusters would be avoided. Secondly, note that the actuation mapping (5.6) is decoupled in $\boldsymbol{\mathcal{F}}_b$, therefore any direct coupling of the arm tasks into the thrusters is avoided.

5.1.2. Design of the controller

The objective of the control is to regulate the pose of the end-effector frame $\mathcal{E}$ and the position of CoM around desired locations that are fixed in the target frame $\mathcal{T}$. Furthermore, the momentum shall be dumped and the null-space motion shall be stopped in order to avoid any joint drift after the above-mentioned tasks have converged. Towards this aim, let us consider error coordinates $\tilde{\boldsymbol{x}}_c \in \mathbb{R}^3$ and $\tilde{\boldsymbol{x}}_e \in \mathbb{R}^6$ for the CoM and the end-effector respectively; let us further define the errors $\tilde{\boldsymbol{\nu}}_e \in \mathbb{R}^6$, $\tilde{\boldsymbol{h}}_c \in \mathbb{R}^6$ and $\tilde{\boldsymbol{\upsilon}}_n^{int} \in \mathbb{R}^r$ for the end-effector velocity, the momentum, and the null-space velocity, respectively. As a consequence of Assumption 2.2, it is $\tilde{\boldsymbol{\nu}}_e = \boldsymbol{\nu}_e$, $\tilde{\boldsymbol{h}}_c = \boldsymbol{h}_c$, and $\tilde{\boldsymbol{\upsilon}}_n^{int} = \boldsymbol{\upsilon}_n^{int}$. The design of the controller is restricted to the contact-free operation:

Assumption 5.1. *There is no contact, i.e.,* $\boldsymbol{\mathcal{F}}_e^{ext} = \boldsymbol{0}$.

The controller is designed as follows. The invariant task is designed as

$$\boldsymbol{\mathcal{F}}_c = -\boldsymbol{S}_v^T \boldsymbol{K}_c \tilde{\boldsymbol{x}}_c - \boldsymbol{D}_h \tilde{\boldsymbol{h}}_c, \tag{5.8a}$$

where $\boldsymbol{K}_c \in \mathbb{R}^{3 \times 3}$ is a symmetric, positive definite stiffness matrix, and $\boldsymbol{D}_h \in \mathbb{R}^{6 \times 6}$ is a positive definite momentum gain matrix. The task (5.8a) imposes the requirement that

[2] As discussed in Section 3.2.4.

the CoM be controlled around a desired position and, additionally, that any residual momentum be extracted from the system. Notice in (5.5) that the dynamics associated to a CoM and momentum task is decoupled from the motion of the end-effector and the null space, i.e., it verifies the task-invariancy conditions (4.7), (4.8).
The end-effector and null-space tasks are designed as

$$\boldsymbol{\mathcal{F}}_e^{int} = -\boldsymbol{J}_{\tilde{x}_e}(\tilde{\boldsymbol{x}}_e)^T \boldsymbol{K}_e \tilde{\boldsymbol{x}}_e - \boldsymbol{D}_e \tilde{\boldsymbol{\nu}}_e, \tag{5.8b}$$

$$\boldsymbol{\varsigma}_n^{int} = -\boldsymbol{D}_n \tilde{\boldsymbol{v}}_n^{int}, \tag{5.8c}$$

where $\boldsymbol{D}_n \in \mathbb{R}^{r\times r}$ is a positive definite damping matrix for the null space.

5.1.3. Analysis of the closed loop

To derive the closed-loop dynamics, the task-space velocity error $\tilde{\boldsymbol{\nu}}_e$ used in (5.8b) is first preliminarily written in terms of the momentum $\boldsymbol{h}_c$ and of the internal end-effector velocity $\boldsymbol{\nu}_e^{int}$ used in the allocation-space dynamics (5.5); by using (4.19), the end-effector error is written as

$$\tilde{\boldsymbol{\nu}}_e = \boldsymbol{\nu}_e^{int} + \boldsymbol{A}_{ec}(\boldsymbol{R}_b, \boldsymbol{q}_m)\boldsymbol{M}_c(\boldsymbol{R}_b, \boldsymbol{q}_m)^{-1}\boldsymbol{h}_c. \tag{5.9}$$

The closed-loop dynamics and kinematics equations are obtained by inserting (5.8) into (5.5), by considering the error kinematics equations (B.2) and (B.6b) together with (5.9), and by inverting[3] (5.1) to get $\dot{\boldsymbol{q}}_m$, obtaining

$$\dot{\boldsymbol{h}}_c + \boldsymbol{D}_h \boldsymbol{h}_c + \boldsymbol{S}_v^T \boldsymbol{K}_c \tilde{\boldsymbol{x}}_c = \boldsymbol{0}, \tag{5.10a}$$

$$\dot{\tilde{\boldsymbol{x}}}_c = \frac{1}{m}\boldsymbol{S}_v \boldsymbol{h}_c, \tag{5.10b}$$

$$\begin{aligned}\boldsymbol{M}^{int}(\boldsymbol{q}_m)\dot{\boldsymbol{\chi}}^{int} + \boldsymbol{C}_{\chi^{int}}(\boldsymbol{R}_b, \boldsymbol{q}_m, \boldsymbol{h}_c, \boldsymbol{\chi}^{int})\boldsymbol{\chi}^{int} + \boldsymbol{D}_e\boldsymbol{\nu}_e^{int} + \boldsymbol{S}_e^T \boldsymbol{J}_{\tilde{x}_e}(\tilde{\boldsymbol{x}}_e)^T \boldsymbol{K}_e \tilde{\boldsymbol{x}}_e \\ = \boldsymbol{\gamma}(\boldsymbol{R}_b, \boldsymbol{q}_m, \boldsymbol{h}_c, \boldsymbol{\chi}^{int})\boldsymbol{h}_c,\end{aligned} \tag{5.10c}$$

$$\dot{\tilde{\boldsymbol{x}}}_e = \boldsymbol{J}_{\tilde{x}_e}(\tilde{\boldsymbol{x}}_e)\boldsymbol{S}_e\boldsymbol{\chi}^{int} + \boldsymbol{J}_{\tilde{x}_e}(\tilde{\boldsymbol{x}}_e)\boldsymbol{S}_e\boldsymbol{A}_{ec}(\boldsymbol{R}_b, \boldsymbol{q}_m)\boldsymbol{M}_c(\boldsymbol{R}_b, \boldsymbol{q}_m)^{-1}\boldsymbol{h}_c, \tag{5.10d}$$

$$\dot{\boldsymbol{q}}_m = \boldsymbol{J}_{em}^{int}(\boldsymbol{q}_m)^{-1}\boldsymbol{S}_e\boldsymbol{\chi}^{int}, \tag{5.10e}$$

where

$$\boldsymbol{S}_e = \begin{bmatrix}\boldsymbol{E} & \boldsymbol{0}\end{bmatrix} \in \mathbb{R}^{6\times n_m}, \tag{5.11}$$

$$\boldsymbol{\gamma}(\boldsymbol{R}_b, \boldsymbol{q}_m, \boldsymbol{h}_c, \boldsymbol{\chi}^{int}) = \begin{bmatrix}-\boldsymbol{D}_e\boldsymbol{A}_{ec}(\boldsymbol{R}_b, \boldsymbol{q}_m)\boldsymbol{M}_c(\boldsymbol{R}_b, \boldsymbol{q}_m)^{-1} \\ \boldsymbol{0}\end{bmatrix} - \boldsymbol{C}_{\chi^{int}h}(\boldsymbol{R}_b, \boldsymbol{q}_m, \boldsymbol{h}_c, \boldsymbol{\chi}^{int}) \in \mathbb{R}^{n_m\times 6}. \tag{5.12}$$

The system (5.10) is function of the attitude $\boldsymbol{R}_b$; it can be replaced with the error $\tilde{\boldsymbol{x}}_e$ and the joint angles $\boldsymbol{q}_m$ by using the following relation

$$\boldsymbol{R}_b = \boldsymbol{R}_t \boldsymbol{R}_{te_d} \boldsymbol{R}_{e_de}(\tilde{\boldsymbol{x}}_e)\boldsymbol{R}_{eb}(\boldsymbol{q}_m), \tag{5.13}$$

where $\boldsymbol{R}_t$ is constant because of Assumption 2.2, and where $\boldsymbol{R}_{te_d}$ specifies the (constant) end-effector rotational setpoint w.r.t. $\mathcal{T}$. With the representation (5.10) and (5.13), the

[3] Note that the inverse of (5.1) exists in the singularity-free region (4.31).

closed loop is described as an autonomous system

$$\dot{\boldsymbol{z}} = \boldsymbol{f}(\boldsymbol{z}), \qquad \text{with} \quad \boldsymbol{z} = \begin{bmatrix} \boldsymbol{h}_c \\ \tilde{\boldsymbol{x}}_c \\ \boldsymbol{\chi}^{int} \\ \tilde{\boldsymbol{x}}_e \\ \boldsymbol{q}_m \end{bmatrix} \in D_3 = \mathbb{R}^{15\times 2n_m}.$$

Note that, by partitioning the state $\boldsymbol{z}$ as

$$\boldsymbol{z} = \begin{bmatrix} \boldsymbol{z}_{whole} \\ \boldsymbol{z}_{arm} \end{bmatrix}, \quad \text{with} \quad \boldsymbol{z}_{whole} = \begin{bmatrix} \boldsymbol{h}_c \\ \tilde{\boldsymbol{x}}_c \end{bmatrix} \in \mathbb{R}^9,\ \boldsymbol{z}_{arm} = \begin{bmatrix} \boldsymbol{\chi}^{int} \\ \tilde{\boldsymbol{x}}_e \\ \boldsymbol{q}_m \end{bmatrix} \in \mathbb{R}^{6+2n}, \tag{5.14}$$

the closed-loop equations (5.10) and (5.13) are in the triangular form

$$\dot{\boldsymbol{z}}_{whole} = \boldsymbol{g}_{whole}\left(\boldsymbol{z}_{whole}\right), \tag{5.15a}$$

$$\dot{\boldsymbol{z}}_{arm} = \boldsymbol{g}_{arm}\left(\boldsymbol{z}_{whole}, \boldsymbol{z}_{arm}\right), \tag{5.15b}$$

where $\boldsymbol{g}_{whole}$ is given by (5.10a) and (5.10b), and $\boldsymbol{g}_{arm}$ is given by (5.10c), (5.10d), and (5.10e). Notice that the dynamics of $\boldsymbol{z}_{whole}$ is totally decoupled from $\boldsymbol{z}_{arm}$ and, furthermore, is linear. The equilibrium of the equations (5.10) is the set

$$\boldsymbol{z}_0 = \left\{\boldsymbol{z} \in D_3 : \boldsymbol{h}_c = \boldsymbol{0},\ \tilde{\boldsymbol{x}}_c = \boldsymbol{0},\ \boldsymbol{\chi}^{int} = \boldsymbol{0},\ \tilde{\boldsymbol{x}}_e = \boldsymbol{0}\right\}. \tag{5.16}$$

5.1.4. Discussion of the controller

As a consequence of the adopted external-internal motion decomposition, the actuation mapping (5.6) has a decoupled structure in the thrusters wrench $\boldsymbol{\mathcal{F}}_b$: the thrusters wrench is only used to actuate the centroidal wrench $\boldsymbol{\mathcal{F}}_c$; on the other hand, the joint torques are used to actuate the end-effector wrench $\boldsymbol{\mathcal{F}}_e^{int}$, the null-space generalized force $\boldsymbol{\varsigma}_n^{int}$, and to further counteract the effect of the centroidal wrench $\boldsymbol{\mathcal{F}}_c$ in the joints. Based on this, the controller has no direct coupling of the robot tasks into the thrusters wrench. Furthermore, the centroidal wrench in (5.8a) is only used to actuate an invariant task – thanks to the triangular structure of the closed-loop dynamics (5.10), the end-effector and null-space motions do not excite the momentum –; therefore, the controller has also no indirect coupling and no thrusters at all are fired during end-effector and null-space motions. Hence, it is concluded that the controller performs a **complete decoupling** of the thrusters from the control action, and it is not affected by the limitations of the free-flying strategy discussed in Section 3.2.4.

Another important feature of the proposed controller is concluded as follows. After CoM and momentum transients – this may be for example the case of a contact, or a workspace relocation maneuver –, the system converges to a stationary situation in which the CoM remains fixed in the inertial space and the momentum remains zero. Therefore, during the entire time of robot maneuvers that do not involve momentum transients, it will remain $\tilde{\boldsymbol{x}}_c = \boldsymbol{0}$ and $\boldsymbol{h}_c = \boldsymbol{0}$. In this nominal situation, it remains $\boldsymbol{\mathcal{F}}_c = \boldsymbol{0}$, and the actuator commands given by the equations (5.6) reduce to

$$\boldsymbol{\mathcal{F}}_b = \boldsymbol{0}, \tag{5.17a}$$

$$\boldsymbol{\tau}_m = \boldsymbol{J}_{em}^{int}(\boldsymbol{q}_m)^T \boldsymbol{\mathcal{F}}_e^{int} + \boldsymbol{J}_{nm}^{int}(\boldsymbol{q}_m)^T \boldsymbol{\varsigma}_n^{int}, \tag{5.17b}$$

which are equivalent to the free-floating actuator commands (3.9b), meaning that the controller automatically reduces to the free-floating controller once the momentum is dumped. In conclusion, with the proposed controller, all robotic operations require no thrusters when no CoM or momentum transients are involved, and are performed in a free-floating fashion. They are turned on only when contact occurs and their use is limited to extracting the accumulated momentum and to restoring the desired CoM location.

5.2. Whole-Body Control with requirements on the attitude of the base

The control method developed herein is based on the centroid-circumcentroidal motion decomposition described in Section 4.3, and on a CoM control invariant task. Differently than Whole-Body Control in Section 5.1, the momentum dumping invariant task is replaced with an attitude control task.
The method was developed in [GOA19] for a nonredundant arm; in the following, the extended method for application with a redundant arm is presented.

5.2.1. Transformation of the dynamics

In the following, the transformation of the system into an centroid-circumcentroidal form is addressed. For a robot without reaction wheels, the circumcentroidal motion of the centroid-circumcentroidal decomposition shall have dimension $n_m + 3$; the construction of the circumcentroidal motion is described in the following.
Let us consider the circumcentroidal velocities $\boldsymbol{\nu}_e^{\oplus} \in \mathbb{R}^6$ and $\boldsymbol{\nu}_b^{\oplus} \in \mathbb{R}^6$ of the end-effector and of the base, respectively. By using general expression (4.45) for the base and end-effector frames, they are given by

$$\boldsymbol{\nu}_e^{\oplus} = \boldsymbol{J}_e^{\oplus}(\boldsymbol{q}_m)\boldsymbol{\upsilon}, \tag{5.18}$$

$$\boldsymbol{\nu}_b^{\oplus} = \boldsymbol{J}_b^{\oplus}(\boldsymbol{q}_m)\boldsymbol{\upsilon}, \tag{5.19}$$

where $\boldsymbol{J}_e^{\oplus}(\boldsymbol{q}_m) \in \mathbb{R}^{6\times(6+n_m)}$ and $\boldsymbol{J}_b^{\oplus}(\boldsymbol{q}_m) \in \mathbb{R}^{6\times(6+n_m)}$. With the aim of implementing a control of the rotation of the base, only the angular part $\boldsymbol{\omega}_b^{\oplus} \in \mathbb{R}^3$ of (5.19) is of interest. It can be expressed as

$$\boldsymbol{\omega}_b^{\oplus} = \boldsymbol{J}_{\omega_b}^{\oplus}\boldsymbol{\upsilon}, \tag{5.20}$$

where $\boldsymbol{J}_{\omega_b}^{\oplus} \in \mathbb{R}^{3\times(6+n_m)}$. The circumcentroidal velocities (5.18) and (5.20) are six- and three-dimensional vectors, respectively, which complessively form a nine-dimensional circumcentroidal motion. For a redundant arm it is $n_m > 6$; thus an additional circumcentroidal motion of dimension $r = n_m - 6$ is required to construct a circumcentroidal motion of dimension $n_m + 3$. By denoting $\boldsymbol{\upsilon}_n^{\oplus} \in \mathbb{R}^r$ such an additional circumcentroidal motion, it can be expressed as

$$\boldsymbol{\upsilon}_n^{\oplus} = \boldsymbol{J}_n^{\oplus}(\boldsymbol{q}_m)\boldsymbol{\upsilon}, \tag{5.21}$$

where $\boldsymbol{J}_n^{\oplus}(\boldsymbol{q}_m) \in \mathbb{R}^{r\times(6+n_m)}$. To limit the interference with the base rotation and the end-effector, one may define $\boldsymbol{\upsilon}_n^{\oplus}$ as being a dynamically-consistent null-space velocity of both the base circumcentroidal angular velocity and the end-effector circumcentroidal velocity. This is done by choosing mappings $\boldsymbol{J}_{n\omega}^{\oplus}(\boldsymbol{q}_m)$ and $\boldsymbol{J}_{nm}^{\oplus}(\boldsymbol{q}_m)$ satisfying the condition

$$\begin{bmatrix} \boldsymbol{J}_{\omega_b}^{\oplus} \\ \boldsymbol{J}_e^{\oplus}(\boldsymbol{q}_m) \end{bmatrix} \boldsymbol{M}(\boldsymbol{q}_m)^{-1} \boldsymbol{J}_n^{\oplus}(\boldsymbol{q}_m)^T = \boldsymbol{0}. \tag{5.22}$$

The expressions of $\boldsymbol{J}_e^{\oplus}(\boldsymbol{q}_m)$, $\boldsymbol{J}_b^{\oplus}(\boldsymbol{q}_m)$, and $\boldsymbol{J}_n^{\oplus}(\boldsymbol{q}_m)$, as well as their sub-blocks, are provided in the Appendix C.4.
Based on the above definitions, $\boldsymbol{\omega}_b^{\oplus}$, $\boldsymbol{\nu}_e^{\oplus}$, and $\boldsymbol{v}_n^{\oplus}$ complessively form a circumcentroidal motion $\boldsymbol{\chi}^{\oplus} = \begin{bmatrix}\boldsymbol{\omega}_b^{\oplus T} & \boldsymbol{\nu}_e^{\oplus T} & \boldsymbol{v}_n^{\oplus T}\end{bmatrix}^T$ of dimension $n_m + 3$, which can be expressed as

$$\boldsymbol{\chi}^{\oplus} = \begin{bmatrix}\boldsymbol{\omega}_b^{\oplus} \\ \boldsymbol{\nu}_e^{\oplus} \\ \boldsymbol{v}_n^{\oplus}\end{bmatrix} = \bar{\boldsymbol{J}}^{\oplus}(\boldsymbol{q}_m)\boldsymbol{v}, \qquad \text{where} \quad \bar{\boldsymbol{J}}^{\oplus}(\boldsymbol{q}_m) = \begin{bmatrix}\boldsymbol{J}_{\omega_b}^{\oplus} \\ \boldsymbol{J}_e^{\oplus}(\boldsymbol{q}_m) \\ \boldsymbol{J}_n^{\oplus}(\boldsymbol{q}_m)\end{bmatrix} \in \mathbb{R}^{(n_m+3)\times(6+n_m)}. \tag{5.23}$$

Hence, in the singularity-free region $\mathcal{Q}^{\oplus}$ (see (4.59)) the dynamics in the allocation space can be transformed to the decoupled centroid-circumcentroidal form (4.64). Considering only contact at the end-effector[4], the dynamics has the form

$$m\dot{\boldsymbol{v}}_c = \boldsymbol{f}_c + \boldsymbol{R}_{ec}(\boldsymbol{R}_b, \boldsymbol{q})^T \boldsymbol{f}_e^{ext}, \tag{5.24a}$$

$$\boldsymbol{M}_{\chi}^{\oplus}(\boldsymbol{q}_m)\begin{bmatrix}\dot{\boldsymbol{\omega}}_b^{\oplus} \\ \dot{\boldsymbol{\nu}}_e^{\oplus} \\ \dot{\boldsymbol{v}}_n^{\oplus}\end{bmatrix} + \boldsymbol{C}_{\chi^{\oplus}}(\boldsymbol{R}_b, \boldsymbol{q}_m, \boldsymbol{v}_c, \boldsymbol{\chi}^{\oplus})\begin{bmatrix}\boldsymbol{\omega}_b^{\oplus} \\ \boldsymbol{\nu}_e^{\oplus} \\ \boldsymbol{v}_n^{\oplus}\end{bmatrix} + \boldsymbol{C}_{\chi^{\oplus}v}(\boldsymbol{R}_b, \boldsymbol{q}_m, \boldsymbol{v}_c, \boldsymbol{\chi}^{\oplus})\boldsymbol{v}_c = \begin{bmatrix}\boldsymbol{m}_b^{\oplus} \\ \boldsymbol{\mathcal{F}}_e^{\oplus} \\ \boldsymbol{\varsigma}_n^{\oplus}\end{bmatrix} + \begin{bmatrix}\boldsymbol{0} \\ \boldsymbol{\mathcal{F}}_e^{ext} \\ \boldsymbol{0}\end{bmatrix}, \tag{5.24b}$$

where $\boldsymbol{m}_b^{\oplus} \in \mathbb{R}^3$, $\boldsymbol{\mathcal{F}}_e^{\oplus} \in \mathbb{R}^6$ and $\boldsymbol{\varsigma}_n^{\oplus} \in \mathbb{R}^r$ are the virtual actuators, which are associated to $\boldsymbol{\omega}_b^{\oplus}$, $\boldsymbol{\nu}_e^{\oplus}$, and $\boldsymbol{v}_n^{\oplus}$, respectively, and where $\boldsymbol{f}_e^{ext} \in \mathbb{R}^3$ is the linear part of $\boldsymbol{\mathcal{F}}_e^{ext} \in \mathbb{R}^6$. The virtual actuators are related to the actuators by an actuation mapping decoupled in $\boldsymbol{f}_b$, which, by using (4.54), (2.61e), and (C.24), is expressed as

$$\begin{bmatrix}\boldsymbol{f}_b \\ \boldsymbol{m}_b \\ \boldsymbol{\tau}_m\end{bmatrix} = \begin{bmatrix}\boldsymbol{R}_b^T & \boldsymbol{0} & \boldsymbol{0} & \boldsymbol{0} \\ \frac{1}{m}\boldsymbol{M}_{v\omega}(\boldsymbol{q}_m)^T\boldsymbol{R}_b^T & \boldsymbol{E} & \boldsymbol{J}_{e\omega}^{\oplus}(\boldsymbol{q}_m)^T & \boldsymbol{J}_{n\omega}^{\oplus}(\boldsymbol{q}_m)^T \\ \frac{1}{m}\boldsymbol{M}_{vm}(\boldsymbol{q}_m)^T\boldsymbol{R}_b^T & \boldsymbol{0} & \boldsymbol{J}_{em}^{\oplus}(\boldsymbol{q}_m)^T & \boldsymbol{J}_{nm}^{\oplus}(\boldsymbol{q}_m)^T\end{bmatrix}\begin{bmatrix}\boldsymbol{f}_c \\ \boldsymbol{m}_b^{\oplus} \\ \boldsymbol{\mathcal{F}}_e^{\oplus} \\ \boldsymbol{\varsigma}_n^{\oplus}\end{bmatrix}, \tag{5.25}$$

where $\boldsymbol{J}_{e\omega}^{\oplus}(\boldsymbol{q}_m) \in \mathbb{R}^{6\times 3}$ and $\boldsymbol{J}_{em}^{\oplus}(\boldsymbol{q}_m) \in \mathbb{R}^{6\times n_m}$ are the attitude and manipulator sub-blocks, respectively, of the map $\boldsymbol{J}_e^{\oplus}(\boldsymbol{q}_m)$, and where $\boldsymbol{J}_{n\omega}^{\oplus}(\boldsymbol{q}_m) \in \mathbb{R}^{r\times 3}$ and $\boldsymbol{J}_{nm}^{\oplus}(\boldsymbol{q}_m) \in \mathbb{R}^{r\times n_m}$ are the rotation and manipulator sub-blocks, respectively, of the map $\boldsymbol{J}_n^{\oplus}(\boldsymbol{q}_m)$ (see Appendix C.4).
Let us mention that the choice of the dynamically-consistent null space of the base and the end-effector leads to a decoupled circumcentroidal inertia

$$\boldsymbol{M}_{\chi}^{\oplus}(\boldsymbol{q}_m) = \begin{bmatrix}\boldsymbol{M}_{\omega}^{\oplus}(\boldsymbol{q}_m) & \boldsymbol{M}_{\omega e}^{\oplus}(\boldsymbol{q}_m) & \boldsymbol{0} \\ \boldsymbol{M}_{\omega e}^{\oplus}(\boldsymbol{q}_m)^T & \boldsymbol{M}_{e}^{\oplus}(\boldsymbol{q}_m) & \boldsymbol{0} \\ \boldsymbol{0} & \boldsymbol{0} & \boldsymbol{Z}(\boldsymbol{q}_m)\boldsymbol{M}(\boldsymbol{q}_m)\boldsymbol{Z}(\boldsymbol{q}_m)^T\end{bmatrix}. \tag{5.26}$$

where $\boldsymbol{M}_{\omega}^{\oplus}(\boldsymbol{q}_m) \in \mathbb{R}^{3\times 3}$, $\boldsymbol{M}_{\omega e}^{\oplus}(\boldsymbol{q}_m) \in \mathbb{R}^{3\times 6}$, and $\boldsymbol{M}_{e}^{\oplus}(\boldsymbol{q}_m) \in \mathbb{R}^{6\times 6}$, and where $\boldsymbol{Z} \in \mathbb{R}^{r\times(6+n_m)}$ is the base matrix of the chosen null space (see (C.22)). However, the base and end-effector circumcentroidal subblock of the inertia is still coupled, as well as the entire circumcentroidal Coriolis/centrifugal matrix $\boldsymbol{C}_{\chi^{\oplus}}(\boldsymbol{R}_b, \boldsymbol{q}_m, \boldsymbol{v}_c, \boldsymbol{\omega}_b^{\oplus}, \boldsymbol{\nu}_e^{\oplus}, \boldsymbol{v}_n^{\oplus})$. Therefore, the base and end-effector subsystem in (5.24b) is coupled.

[4] In this case, the terms $\boldsymbol{f}_c^{ext}$ and $\boldsymbol{\varsigma}^{\oplus ext}$ in (4.64b) result in $\boldsymbol{f}_c^{ext} = \boldsymbol{R}_{ec}(\boldsymbol{R}_b, \boldsymbol{q})^T\boldsymbol{f}_e^{ext}$ and $\boldsymbol{\varsigma}^{\oplus ext} = \begin{bmatrix}\boldsymbol{0} \\ \boldsymbol{\mathcal{F}}_e^{ext} \\ \boldsymbol{0}\end{bmatrix}$.

Similarly to the controller in Section 5.1, note that by exploiting the decoupled structure of the dynamics (5.24), it is possible to design controllers in a cascade fashion, using $\boldsymbol{f}_c$ to control the CoM, and using $\boldsymbol{m}_b^{\oplus}$, $\boldsymbol{\mathcal{F}}_e^{\oplus}$, and $\boldsymbol{\varsigma}_n^{\oplus}$ to control the coupled base, end-effector, and null-space motion. From this it follows that, if one assigns an invariant task to the virtual actuator $\boldsymbol{f}_c$, then any indirect coupling of the base, end-effector, and null-space tasks, into the thrusters force would be avoided. Secondly, note that the actuation mapping (5.25) is decoupled in $\boldsymbol{f}_b$, therefore any direct coupling of the arm tasks into the thrusters is avoided.

5.2.2. Design of the controller

The objective of the control is to regulate the pose of the end-effector frame $\mathcal{E}$, the orientation[5] of the base frame $\mathcal{B}$, and the position of CoM, around desired locations that are fixed in the target frame $\mathcal{T}$. Furthermore, the null-space motion shall be stopped to avoid any joint drift after the above-mentioned tasks have converged. Towards this aim, let us consider error coordinates $\tilde{\boldsymbol{x}}_c \in \mathbb{R}^3$, $\tilde{\boldsymbol{x}}_{b,rot} \in \mathbb{R}^3$, and $\tilde{\boldsymbol{x}}_e \in \mathbb{R}^6$ for the CoM, base, and the end-effector, respectively, as well as velocity errors $\tilde{\boldsymbol{v}}_c \in \mathbb{R}^3$, $\tilde{\boldsymbol{\omega}}_b \in \mathbb{R}^3$, $\tilde{\boldsymbol{\nu}}_e \in \mathbb{R}^6$, and $\tilde{\boldsymbol{v}}_n^{\oplus} \in \mathbb{R}^r$. As a consequence of Assumption 2.2, it is $\tilde{\boldsymbol{v}}_c = \boldsymbol{v}_c$, $\tilde{\boldsymbol{\omega}}_b = \boldsymbol{\omega}_b$, $\tilde{\boldsymbol{\nu}}_e = \boldsymbol{\nu}_e$, and $\tilde{\boldsymbol{v}}_n^{\oplus} = \boldsymbol{v}_n^{\oplus}$. The derivation of the controller is restricted to the contact-free operation:

Assumption 5.2. *There is no contact, i.e.,* $\boldsymbol{\mathcal{F}}_e^{ext} = \boldsymbol{0}$.

The controller is designed as follows. The invariant task is designed as

$$\boldsymbol{f}_c = -\boldsymbol{K}_c\tilde{\boldsymbol{x}}_c - \boldsymbol{D}_c\tilde{\boldsymbol{v}}_c, \tag{5.27a}$$

where $\boldsymbol{D}_c \in \mathbb{R}^{3\times3}$ is a positive definite CoM damping matrix. The task (5.27a) imposes the requirement that the CoM be controlled around a desired position. Notice in (5.24) that the task is decoupled from the motion of the base, the end-effector, and the nullspace, i.e., it verifies the task-invariancy conditions (4.7), (4.8).
The base, end-effector, and null-space tasks are designed as

$$\boldsymbol{m}_b^{\oplus} = -\boldsymbol{J}_{\tilde{x}_{b,rot}}(\tilde{\boldsymbol{x}}_{b,rot})^T\boldsymbol{K}_{b,rot}\tilde{\boldsymbol{x}}_{b,rot} - \boldsymbol{D}_{b,rot}\tilde{\boldsymbol{\omega}}_b, \tag{5.27b}$$

$$\boldsymbol{\mathcal{F}}_e^{\oplus} = -\boldsymbol{J}_{\tilde{x}_e}(\tilde{\boldsymbol{x}}_e)^T\boldsymbol{K}_e\tilde{\boldsymbol{x}}_e - \boldsymbol{D}_e\tilde{\boldsymbol{\nu}}_e, \tag{5.27c}$$

$$\boldsymbol{\varsigma}_n^{\oplus} = -\boldsymbol{D}_n\tilde{\boldsymbol{v}}_n^{int}, \tag{5.27d}$$

where $\boldsymbol{K}_{b,rot} \in \mathbb{R}^{3\times3}$ is a symmetric, positive definite stiffness matrix and $\boldsymbol{D}_{b,rot} \in \mathbb{R}^{3\times3}$ is a positive definite damping matrix.

5.2.3. Analysis of the closed loop

For the analysis of the stability of the closed loop the following assumption is made:

Assumption 5.3. *The arm is nonredundant, i.e.,* $n_m = 6$.

To derive the closed-loop dynamics, the task-space velocity errors $\tilde{\boldsymbol{\omega}}_b$ and $\tilde{\boldsymbol{\nu}}_e$ used in (5.27b) and (5.27b) are first preliminarily written in terms of the centroidal and circumcentroidal velocities $\boldsymbol{v}_c$, $\boldsymbol{\omega}_b^{\oplus}$, and $\boldsymbol{\nu}_e^{\oplus}$ used in the allocation-space dynamics (5.24); by using

[5] Note that no dumping of the angular momentum is necessary in this controller because this is indirectly achieved by the thrusters allocated for the orientation control of $\mathcal{B}$.

(4.50), they are related by

$$\tilde{\boldsymbol{\omega}}_b = \boldsymbol{\omega}_b^{\oplus}, \tag{5.28a}$$

$$\tilde{\boldsymbol{\nu}}_e = \begin{bmatrix} \boldsymbol{R}_e(\boldsymbol{R}_b, \boldsymbol{q}_m)^T \\ \boldsymbol{0} \end{bmatrix} \boldsymbol{v}_c + \boldsymbol{\nu}_e^{\oplus}. \tag{5.28b}$$

The closed-loop dynamics and kinematics equations are obtained by inserting (5.27) into (5.24), considering the error kinematics equations (B.2), (B.4) and (B.6b) together with (5.28), and considering that the null-space velocity and the null-space equation are identically zero because of Assumption 5.3, obtaining

$$m\ddot{\tilde{\boldsymbol{x}}}_c + \boldsymbol{D}_c\dot{\tilde{\boldsymbol{x}}}_c + \boldsymbol{K}_c\tilde{\boldsymbol{x}}_c = \boldsymbol{0}, \tag{5.29a}$$

$$\boldsymbol{M}_{\chi}^{\oplus}(\boldsymbol{q}_m)\dot{\boldsymbol{\chi}}^{\oplus} + \boldsymbol{C}_{\chi}^{\oplus}(\boldsymbol{R}_b, \boldsymbol{q}_m, \boldsymbol{\chi}^{\oplus}, \dot{\tilde{\boldsymbol{x}}}_c)\boldsymbol{\chi}^{\oplus} + \boldsymbol{D}\boldsymbol{\chi}^{\oplus} + \boldsymbol{J}_{\tilde{x}}(\tilde{\boldsymbol{x}})^T\boldsymbol{K}\tilde{\boldsymbol{x}} = \boldsymbol{\gamma}(\boldsymbol{R}_b, \boldsymbol{q}_m, \boldsymbol{\chi}^{\oplus}, \dot{\tilde{\boldsymbol{x}}}_c)\dot{\tilde{\boldsymbol{x}}}_c, \tag{5.29b}$$

$$\dot{\tilde{\boldsymbol{x}}} = \boldsymbol{J}_{\tilde{x}}(\tilde{\boldsymbol{x}})\boldsymbol{\chi}^{\oplus} + \boldsymbol{J}_{\tilde{x}}(\tilde{\boldsymbol{x}})\boldsymbol{G}_{v_c}(\boldsymbol{R}_b, \boldsymbol{q}_m)\dot{\tilde{\boldsymbol{x}}}_c, \tag{5.29c}$$

where it is compactly denoted

$$\tilde{\boldsymbol{x}} = \begin{bmatrix} \tilde{\boldsymbol{x}}_{b,rot} \\ \tilde{\boldsymbol{x}}_e \end{bmatrix} \in \mathbb{R}^9, \tag{5.30a}$$

$$\boldsymbol{K} = \text{blkdiag}(\boldsymbol{K}_{b,rot}, \boldsymbol{K}_e) \in \mathbb{R}^{9\times 9}, \tag{5.30b}$$

$$\boldsymbol{D} = \text{blkdiag}(\boldsymbol{D}_{b,rot}, \boldsymbol{D}_e) \in \mathbb{R}^{9\times 9}, \tag{5.30c}$$

$$\boldsymbol{J}_{\tilde{x}}(\tilde{\boldsymbol{x}}) = \text{blkdiag}(\boldsymbol{J}_{\tilde{x}_{b,rot}}(\tilde{\boldsymbol{x}}_{b,rot}), \boldsymbol{J}_{\tilde{x}_e}(\tilde{\boldsymbol{x}}_e)) \in \mathbb{R}^{9\times 9}, \tag{5.30d}$$

and where it is

$$\boldsymbol{\gamma}(\boldsymbol{R}_b, \boldsymbol{q}_m, \boldsymbol{\chi}^{\oplus}, \dot{\tilde{\boldsymbol{x}}}_c) = -\boldsymbol{C}_{\chi^{\oplus}v}(\boldsymbol{R}_b, \boldsymbol{q}_m, \boldsymbol{\chi}^{\oplus}, \dot{\tilde{\boldsymbol{x}}}_c) + \boldsymbol{D}\boldsymbol{G}_{v_c}(\tilde{\boldsymbol{x}}_e) \in \mathbb{R}^{9\times 3}, \tag{5.31}$$

$$\boldsymbol{G}_{v_c}(\boldsymbol{R}_b, \boldsymbol{q}_m) = \begin{bmatrix} \boldsymbol{0} \\ \boldsymbol{R}_e(\boldsymbol{R}_b, \boldsymbol{q}_m)^T \\ \boldsymbol{0} \end{bmatrix} \in \mathbb{R}^{9\times 3}. \tag{5.32}$$

With a slight abuse of notation the same symbols have been used for denoting the nonredundant matrices and vectors

$$\boldsymbol{\chi}^{\oplus} = \begin{bmatrix} \boldsymbol{\omega}_b^{\oplus} \\ \boldsymbol{\nu}_e^{\oplus} \end{bmatrix} \in \mathbb{R}^9, \qquad \boldsymbol{M}_{\chi}^{\oplus}(\boldsymbol{q}_m) = \begin{bmatrix} \boldsymbol{M}_{\omega}^{\oplus}(\boldsymbol{q}_m) & \boldsymbol{M}_{\omega e}^{\oplus}(\boldsymbol{q}_m) \\ \boldsymbol{M}_{\omega e}^{\oplus}(\boldsymbol{q}_m)^T & \boldsymbol{M}_{e}^{\oplus}(\boldsymbol{q}_m) \end{bmatrix}, \tag{5.33a}$$

$$\boldsymbol{C}_{\chi}^{\oplus}(\boldsymbol{R}_b, \boldsymbol{q}_m, \boldsymbol{\chi}^{\oplus}, \dot{\tilde{\boldsymbol{x}}}_c) = \begin{bmatrix} \boldsymbol{C}_{\omega}^{\oplus}(\boldsymbol{R}_b, \boldsymbol{q}_m, \boldsymbol{\chi}^{\oplus}, \dot{\tilde{\boldsymbol{x}}}_c) & \boldsymbol{C}_{\omega e}^{\oplus}(\boldsymbol{R}_b, \boldsymbol{q}_m, \boldsymbol{\chi}^{\oplus}, \dot{\tilde{\boldsymbol{x}}}_c) \\ \boldsymbol{C}_{e\omega}^{\oplus}(\boldsymbol{R}_b, \boldsymbol{q}_m, \boldsymbol{\chi}^{\oplus}, \dot{\tilde{\boldsymbol{x}}}_c) & \boldsymbol{C}_{e}^{\oplus}(\boldsymbol{R}_b, \boldsymbol{q}_m, \boldsymbol{\chi}^{\oplus}, \dot{\tilde{\boldsymbol{x}}}_c) \end{bmatrix}. \tag{5.33b}$$

The closed-loop equations (5.29) are function of $\boldsymbol{R}_b$ and $\boldsymbol{q}_m$; next, to represent the system in a state-space form, these dependencies are replaced with the errors $\tilde{\boldsymbol{x}}$ and $\tilde{\boldsymbol{x}}_c$. The dependency on $\boldsymbol{R}_b$ is trivially removed by considering that

$$\boldsymbol{R}_b = \boldsymbol{R}_b(\tilde{\boldsymbol{x}}_{b,rot}). \tag{5.34}$$

In order to remove the dependency on $\boldsymbol{q}_m$, let us firstly define a frame $\mathcal{C}'$ placed on the CoM of the multibody system, and with axes always aligned with the axes of the base frame $\mathcal{B}$. A CoM-based kinematics[6] of the end-effector is defined as the homogeneous

[6] In the classical literature, this kinematics is well-known as "virtual manipulator" [VD90].

transformation matrix $\boldsymbol{H}_{c'e}(\boldsymbol{q}_m)$; note that it is only function of the joints[7]. Secondly, a region $\mathcal{Q}_4 \subset \mathcal{Q}^{\oplus}$ is defined , in which the invertibility of the CoM-based kinematics of the end-effector is ensured, as

$$\mathcal{Q}_4 = \left\{ \boldsymbol{q}_m \in \mathcal{Q}^{\oplus} : \ \boldsymbol{H}_{c'e}(\boldsymbol{q}_m) \ \text{is one-to-one} \right\}. \tag{5.35}$$

The forward kinematics of the arm can be rewritten in terms of the error and desired poses, as

$$\underbrace{\boldsymbol{H}_{c'e}(\boldsymbol{q}_m)}_{\boldsymbol{g}(\boldsymbol{q}_m)} = \underbrace{\boldsymbol{H}_{c'c'_d}(\tilde{\boldsymbol{x}}_c, \tilde{\boldsymbol{x}}_{b,rot}) \boldsymbol{H}_{tc'_d}^{-1} \boldsymbol{H}_{te_d} \boldsymbol{H}_{e_de}(\tilde{\boldsymbol{x}}_e)}_{\boldsymbol{f}(\tilde{\boldsymbol{x}}, \tilde{\boldsymbol{x}}_c)} \tag{5.36}$$

where $\boldsymbol{g}(\boldsymbol{q}_m) : \mathbb{R}^6 \to \mathrm{SE}(3)$ and $\boldsymbol{f}(\tilde{\boldsymbol{x}}, \tilde{\boldsymbol{x}}_c) : \mathbb{R}^{12} \to \mathrm{SE}(3)$, and $\boldsymbol{H}_{tc'_d}$, $\boldsymbol{H}_{te_d}$ are[8] the constant homogeneous matrices that specify the setpoints of the controller. Then, a region in the task space is defined as the pre-image through $\boldsymbol{f}(\tilde{\boldsymbol{x}}, \tilde{\boldsymbol{x}}_c)$ of the image of $\bar{\mathcal{Q}}$ through $\boldsymbol{g}(\boldsymbol{q}_m)$, and is given by

$$\mathcal{X}_4 = \left\{ \tilde{\boldsymbol{x}} \in \mathbb{R}^9, \boldsymbol{x}_c \in \mathbb{R}^3 : \ \exists \boldsymbol{q}_m \in \mathcal{Q}_4, \ \ \boldsymbol{g}(\boldsymbol{q}_m) = \boldsymbol{f}(\tilde{\boldsymbol{x}}, \tilde{\boldsymbol{x}}_c) \right\}. \tag{5.37}$$

Note that this region exists if the desired setpoints $\boldsymbol{H}_{tc'_d}$ and $\boldsymbol{H}_{te_d}$ are compatible with the workspace of the arm. In $\mathcal{X}_4$, the inverse function

$$\boldsymbol{q}_m = \boldsymbol{g}^{-1}(\boldsymbol{f}(\tilde{\boldsymbol{x}}, \tilde{\boldsymbol{x}}_c)) \tag{5.38}$$

exists, and can be substituted together with (5.34) in the closed-loop (5.29), obtaining

$$m\ddot{\tilde{\boldsymbol{x}}}_c + \boldsymbol{D}_c\dot{\tilde{\boldsymbol{x}}}_c + \boldsymbol{K}_c\tilde{\boldsymbol{x}}_c = \boldsymbol{0} \tag{5.39a}$$

$$\bar{\boldsymbol{M}}_{\chi}^{\oplus}(\tilde{\boldsymbol{x}}, \tilde{\boldsymbol{x}}_c)\dot{\boldsymbol{\chi}}^{\oplus} + \bar{\boldsymbol{C}}_{\chi}^{\oplus}(\tilde{\boldsymbol{x}}, \tilde{\boldsymbol{x}}_c, \boldsymbol{\chi}^{\oplus}, \dot{\tilde{\boldsymbol{x}}}_c)\boldsymbol{\chi}^{\oplus} + \boldsymbol{D}\boldsymbol{\chi}^{\oplus} + \boldsymbol{J}_{\tilde{x}}(\tilde{\boldsymbol{x}})^T\boldsymbol{K}\tilde{\boldsymbol{x}} = \bar{\boldsymbol{\gamma}}(\tilde{\boldsymbol{x}}, \tilde{\boldsymbol{x}}_c, \boldsymbol{\chi}^{\oplus}, \dot{\tilde{\boldsymbol{x}}}_c)\dot{\tilde{\boldsymbol{x}}}_c, \tag{5.39b}$$

$$\dot{\tilde{\boldsymbol{x}}} = \boldsymbol{J}_{\tilde{x}}(\tilde{\boldsymbol{x}})\boldsymbol{\chi}^{\oplus} + \boldsymbol{J}_{\tilde{x}}(\tilde{\boldsymbol{x}})\boldsymbol{G}_{v_c}(\tilde{\boldsymbol{x}}_e)\dot{\tilde{\boldsymbol{x}}}_c, \tag{5.39c}$$

where the symbols $\bar{\boldsymbol{M}}_{\chi}^{\oplus}(\tilde{\boldsymbol{x}}, \tilde{\boldsymbol{x}}_c) \in \mathbb{R}^{(n+3)\times(n+3)}$, $\bar{\boldsymbol{C}}_{\chi}^{\oplus}(\tilde{\boldsymbol{x}}, \tilde{\boldsymbol{x}}_c, \boldsymbol{\chi}^{\oplus}, \dot{\tilde{\boldsymbol{x}}}_c) \in \mathbb{R}^{(n+3)\times(n+3)}$, and $\bar{\boldsymbol{\gamma}}(\tilde{\boldsymbol{x}}, \tilde{\boldsymbol{x}}_c, \boldsymbol{\chi}^{\oplus}, \dot{\tilde{\boldsymbol{x}}}_c) \in \mathbb{R}^{(n+3)\times 3}$ denote the matrices after the substitution. With the representation (5.39), the closed-loop system is described in the state-space form

$$\dot{\boldsymbol{z}} = \boldsymbol{f}(\boldsymbol{z}), \qquad \text{with} \quad \boldsymbol{z} = \begin{bmatrix} \tilde{\boldsymbol{x}}_c \\ \dot{\tilde{\boldsymbol{x}}}_c \\ \boldsymbol{\chi}^{\oplus} \\ \tilde{\boldsymbol{x}} \end{bmatrix} \in D_4 = \mathbb{R}^{6+n_m} \times \mathcal{X}_4.$$

Note that, by partitioning the state $\boldsymbol{z}$ as

$$\boldsymbol{z} = \begin{bmatrix} \boldsymbol{z}_{com} \\ \boldsymbol{z}_{sys} \end{bmatrix}, \quad \text{with} \quad \boldsymbol{z}_{com} = \begin{bmatrix} \tilde{\boldsymbol{x}}_c \\ \dot{\tilde{\boldsymbol{x}}}_c \end{bmatrix}, \boldsymbol{z}_{sys} = \begin{bmatrix} \boldsymbol{\chi}^{\oplus} \\ \tilde{\boldsymbol{x}} \end{bmatrix}, \tag{5.40}$$

the dynamics (5.39) results having the triangular state-space form

$$\dot{\boldsymbol{z}}_{com} = \boldsymbol{g}_{com}\left(\boldsymbol{z}_{com}\right), \tag{5.41a}$$

$$\dot{\boldsymbol{z}}_{sys} = \boldsymbol{g}_{sys}\left(\boldsymbol{z}_{com}, \boldsymbol{z}_{sys}\right), \tag{5.41b}$$

[7] This can be seen as follows: applying (2.37) , it is $\boldsymbol{H}_{bc'} = \begin{bmatrix} \boldsymbol{E} & [\boldsymbol{o}_{bc'}]^{\wedge} \\ \boldsymbol{0} & \boldsymbol{E} \end{bmatrix} = \begin{bmatrix} \boldsymbol{E} & [\boldsymbol{o}_{bc}(\boldsymbol{q}_m)]^{\wedge} \\ \boldsymbol{0} & \boldsymbol{E} \end{bmatrix} = \boldsymbol{H}_{bc'}(\boldsymbol{q}_m)$, then it results $\boldsymbol{H}_{c'e}(\boldsymbol{q}_m) = \boldsymbol{H}_{bc'}(\boldsymbol{q}_m)^{-1}\boldsymbol{H}_{be}(\boldsymbol{q}_m)$.

[8] Note that $\boldsymbol{H}_{tc'_d}$ specifies both the desired position of the CoM and the desired attitude of the base.

where $\boldsymbol{g}_{com}$ is given by (5.39a), and $\boldsymbol{g}_{sys}$ is given by (5.39b), (5.39c). Notice that the dynamics of $\boldsymbol{z}_{com}$ is totally decoupled from the rest of the system and, furthermore, it is linear.

Proposition 5.1. *The equilibrium point $\boldsymbol{z} = \boldsymbol{0}$ is asymptotically stable.*

Proof. The proof is done in a cascade fashion, proving first the asymptotic stability of the subsystem (5.41a), and then the asymptotic stability of the subsystem (5.41b) under the constraint $\boldsymbol{z}_{com} = \boldsymbol{0}$.

1. The system (5.39a) is asymptotically stable, having chosen $\boldsymbol{K}_c$ symmetric, positive definite, and $\boldsymbol{D}_c$ positive definite. Therefore the subsystem $\dot{\boldsymbol{z}}_{com} = \boldsymbol{g}_{com}(\boldsymbol{z}_{com})$ is asymptotically stable.

2. The stability of the subsystem $\dot{\boldsymbol{z}}_{sys} = \boldsymbol{g}_2(\boldsymbol{0}, \boldsymbol{z}_{sys})$ is addressed using the Lyapunov function
$$V = \frac{1}{2}\boldsymbol{\chi}^{\oplus T}\bar{\boldsymbol{M}}_{\chi}^{\oplus}(\tilde{\boldsymbol{x}})\boldsymbol{\chi}^{\oplus} + \frac{1}{2}\tilde{\boldsymbol{x}}^T\boldsymbol{K}\tilde{\boldsymbol{x}} > 0, \quad \forall \boldsymbol{z}_{sys} \neq \boldsymbol{0}, \tag{5.42}$$
which is always defined and positive definite for $\boldsymbol{z} \in D_4$. The time derivative along the system trajectories is
$$\dot{V} = \boldsymbol{\chi}^{\oplus T}\bar{\boldsymbol{M}}_{\chi}^{\oplus}(\tilde{\boldsymbol{x}}, \tilde{\boldsymbol{x}}_c)\dot{\boldsymbol{\chi}}^{\oplus} + \frac{1}{2}\boldsymbol{\chi}^{\oplus T}\dot{\bar{\boldsymbol{M}}}_{\chi}^{\oplus}(\tilde{\boldsymbol{x}})\boldsymbol{\chi}^{\oplus} + \dot{\tilde{\boldsymbol{x}}}^T\boldsymbol{K}\tilde{\boldsymbol{x}} = \frac{1}{2}\boldsymbol{\chi}^{\oplus T}\left(\dot{\bar{\boldsymbol{M}}}_{\chi}^{\oplus}(\tilde{\boldsymbol{x}}) - 2\bar{\boldsymbol{C}}_{\chi}^{\oplus}(\tilde{\boldsymbol{x}}, \boldsymbol{\chi}^{\oplus}, \dot{\tilde{\boldsymbol{x}}}_c)\right)\boldsymbol{\chi}^{\oplus} - \boldsymbol{\chi}^{\oplus T}\boldsymbol{D}\boldsymbol{\chi}^{\oplus} = -\boldsymbol{\chi}^{\oplus T}\boldsymbol{D}\boldsymbol{\chi}^{\oplus} \leq 0, \tag{5.43}$$
where (5.39b) and (5.39c) were used together with the constraint $\tilde{\boldsymbol{x}}_c = \dot{\tilde{\boldsymbol{x}}}_c = \boldsymbol{0}$, and where the property (4.65) was exploited. Applying LaSalle to (5.39b), $\boldsymbol{\chi}^{\oplus} \equiv \boldsymbol{0}$ implies $\tilde{\boldsymbol{x}} = \boldsymbol{0}$ and the asymptotic stability of $\dot{\boldsymbol{z}}_{sys} = \boldsymbol{g}_2(\boldsymbol{0}, \boldsymbol{z}_{sys})$ is thus proven.

From 1) and 2) it follows the asymptotic stability of the closed-loop (5.41). □

5.2.4. Discussion of the controller

As a consequence of the adopted centroid-circumcentroidal motion decomposition, the actuation mapping (5.25) has a decoupled structure in the thrusters force $\boldsymbol{f}_b$: the thrusters force is only used to actuate the centroidal force $\boldsymbol{f}_c$; on the other hand, the thrusters moment $\boldsymbol{m}_b$ and the joint torques $\boldsymbol{\tau}_m$ are employed to actuated the other tasks. In particular, the thrusters moment and the joint torques are used to actuate the end-effector wrench $\boldsymbol{\mathcal{F}}_e^{\oplus}$, the null-space generalized force $\boldsymbol{\varsigma}_n^{\oplus}$, and to counteract the effects of the centroidal force $\boldsymbol{f}_c$ in the base rotation and in the joints, respectively; additionally, the thrusters torque is employed to actuate the base attitude-control task $\boldsymbol{m}_b^{\oplus}$. Based on this, it is concluded that the controller has no direct coupling of the arm tasks into the thrusters force, but it has a direct coupling of the arm tasks into the thrusters torque. Furthermore, the centroidal force in (5.27a) is only used to actuate an invariant task – thanks to the triangular structure of the dynamics (5.24), end-effector and null-space motions do not excite the CoM dynamics –; therefore, the controller has also no indirect couplings of the arm motion into the thrusters force; on the other hand, it has an indirect coupling of the arm motion into the thrusters torque, because of the coupling between the end-effector and null-space subsystem and the rotation subsystem in (5.24). Thus, it is concluded that the controller performs a **partial decoupling** of the thrusters: in translation, it is not

affected by the limitations of the free-flying strategy discussed in Section 3.2.4; in rotation, it is affected by similar limitations as the free-flying strategy.
It is interesting to point out that, based on the special conserving properties of the CoM task, after a CoM transient vanishes, the system converges to a stationary situation in which the CoM remains fixed in the inertial space. Therefore, during the entire time of robot maneuvers that do not involve contact or CoM relocation, it will remain $\tilde{\boldsymbol{x}}_c = \boldsymbol{v}_c = \mathbf{0}$ and in turn $\boldsymbol{f}_b = \mathbf{0}$. Hence, with the proposed controller, all operations that do not involve contact will require no base force. The base force will be activated only when contact occurs, and its use will be limited to restoring the CoM location for the workspace need. The resulting controller represents an intermediate solution to endow a floating-base behavior in translation, and saves at least partially fuel and thrusters effort in the missions which explicitly require attitude pointing.

5.3. Summary

In this chapter, two Whole-Body controllers were derived based on the framework presented in Chapter 4.

One controller satisfying the whole-body requirements (R1)-(R3) was derived based on an external-internal dynamics decomposition. The external-internal form of the dynamics was obtained by using the momentum of the whole system, the internal velocity of the end-effector, and an internal velocity quantifying the residual null-space motion resulting from the arm redundancy. The controller was designed by adopting the invariant task of controlling the momentum and the CoM of the whole robot, instead of the task of controlling the position or orientation of the spacecraft, which is proper of a free-flying strategy. It was shown that, thanks to the external-internal decomposition and to the invariant task, the controller avoids direct and indirect couplings in the thrusters, and thus solves the limitation of the free-flying controller; furthermore, thanks to the momentum and CoM task, it allows satisfying the requirements (R1) and (R2), which are not satisfied by a free-floating controller. Finally, it was pointed out that after momentum transient – this may be for example the case of a post-contact situation, or a workspace relocation maneuver –, the controller automatically reduces to the transposed-Jacobian free-floating controller. Based on the above-mentioned aspects, the controller may be interpreted as a *free-floating-like* Whole-Body strategy which merges the floating-base behavior of the free-floating strategy into a fully-actuated one.

One controller satisfying the whole-body requirements (R1)-(R3), and the additional requirement (R4) for the specific case of attitude pointing of the base, was derived. The controller was derived based on a centroid-circumcentroidal dynamics decomposition. The centroid-circumcentroidal form of the dynamics was obtained by using the velocity of the CoM of the whole system, the circumcentroidal velocity of the end-effector, and a circumcentroidal velocity quantifying the residual null-space motion resulting from the arm redundancy. The controller was designed by adopting the invariant task of controlling the CoM of the whole robot instead of the task of controlling the position of the spacecraft, which is proper of a free-flying strategy. It was shown that, thanks to centroid-circumcentroidal decomposition and to the invariant task, the direct and indirect couplings in the thrusters are removed in translation, thereby obtaining a partially thrusters-decoupled structure. Based on this, the controller may be interpreted as an intermediate Whole-Body approach which endows floating-base behavior in translation, but works like a free-flying controller in rotation.

In the next chapter, a Whole-Body controller is derived which applies the same concepts in a robot equipped with thrusters and, additionally, reaction wheels.

CHAPTER 6

Whole-Body Control for robots with thrusters and reaction wheels

In this chapter, a whole-body controller for orbital robots equipped with one arm, a set of spacecraft-mounted thrusters, and an additional set of spacecraft-mounted reaction wheels is presented. Throughout the chapter it is therefore intended that the used dynamics and kinematics matrices are those of a robot with reaction wheels (see Section 2.3).
Similarly as the controllers (C3) and (C4), the controller developed herein allows enforcing some of the whole-body requirements listed in Section 1.2 – namely, the requirements (R1), (R2), (R3), (R4) for the particular case of control of the attitude of the base –, as well as implementing the desired feature of reducing the use of the thrusters, thus providing a more general control approach than the free-floating and free-flying strategies. The following controller is presented:

(C5) Whole-Body Control with requirements on the attitude of the base (robot with RWs).

Differently from controller (C3), controller (C5) additionally implements the task of the control of the attitude of the base. Differently from controller (C4), controller (C5) implements the attitude-control task by using reaction wheels instead of thrusters, and this allows using a completely thrusters-decoupled actuation, instead of the partially thrusters-decoupled one adopted by the controller (C4). Doing so results in a controller which realizes the requirements (R1)-(R4) with minimum use of thrusters.
The controller (C5) is presented in Section 6.1. Then, a summary is drawn up in Section 6.2.

6.1. Whole-Body Control with requirements on the attitude of the base

The control method developed herein is based on the external-internal motion decomposition described in Section 4.2, and on the **momentum dumping** and **CoM control** invariant tasks, similarly as the controller (C3) presented in Section 5.1.
The additional DOFs provided by the reaction wheels allow allocating additional internal actuators; this enables the endowment of an additional attitude control task into an

external-internal actuation strategy. These additional DOFs are exploited in controller (C5) to implement a completely thrusters-decoupled actuation – in turn, resulting in no thrusters use during contact-free robot operations –, *even for the case of an attitude-controlled base.*
The method was developed in [GDOA20] for a nonredundant arm and a nonredundant set of reaction wheels; in the following, the extended method for application with redundant arm and wheels is presented.

6.1.1. Transformation of the dynamics

An external-internal motion decomposition is employed herein to simultaneously yield a decoupled actuation in $\boldsymbol{\mathcal{F}}_b$ and a decoupled dynamics. Based on this, an allocation space is defined as the composition of the momentum and an internal motion of dimension $n = n_m + n_w$. The internal motion is constructed as follows.
Let us consider the internal velocities $\boldsymbol{\nu}_e^{int} \in \mathbb{R}^6$ and $\boldsymbol{\nu}_b^{int} \in \mathbb{R}^6$ of the end-effector and of the base, respectively. By using the general expression (4.17) for the end-effector and base frames, they are given by

$$\boldsymbol{\nu}_e^{int} = \boldsymbol{J}_e^{int}(\boldsymbol{q}_m)\boldsymbol{\upsilon}, \tag{6.1}$$

$$\boldsymbol{\nu}_b^{int} = \boldsymbol{J}_b^{int}(\boldsymbol{q}_m)\boldsymbol{\upsilon}, \tag{6.2}$$

where $\boldsymbol{J}_e^{int}(\boldsymbol{q}_m), \boldsymbol{J}_b^{int}(\boldsymbol{q}_m) \in \mathbb{R}^{6\times(6+n_w+n_m)}$. With the aim of implementing a control of the rotation of the base, only the angular part $\boldsymbol{\omega}_b^{int} \in \mathbb{R}^3$ of (6.2) is of interest. It can be expressed as

$$\boldsymbol{\omega}_b^{int} = \boldsymbol{J}_{\omega_b}^{int}(\boldsymbol{q}_m)\boldsymbol{\upsilon}, \tag{6.3}$$

where $\boldsymbol{J}_{\omega_b}^{int}(\boldsymbol{q}_m) = \boldsymbol{S}_\omega \boldsymbol{J}_b^{int}(\boldsymbol{q}_m) \in \mathbb{R}^{3\times(6+n_w+n_m)}$ and $\boldsymbol{S}_\omega = \begin{bmatrix}\boldsymbol{0} & \boldsymbol{E}\end{bmatrix}$. One may directly build upon the internal velocities $\boldsymbol{\nu}_e^{int}$ and $\boldsymbol{\omega}_b^{int}$ for the construction of the allocation space. However, the internal velocities would be inertially coupled in the transformed dynamics, and simulative tests reveal that the inertial coupling considerably affects the response of the end-effector. To avoid such interference of the base system into the end-effector, a different internal velocity $\breve{\boldsymbol{\omega}}_b^{int} \in \mathbb{R}^3$ is adopted for the base. It is defined as

$$\breve{\boldsymbol{\omega}}_b^{int} = \boldsymbol{J}_{\breve{\omega}_b}^{int}(\boldsymbol{q}_m)\boldsymbol{\upsilon}, \qquad \text{with} \quad \boldsymbol{J}_{\breve{\omega}_b}^{int}(\boldsymbol{q}_m) = \boldsymbol{J}_{\omega_b}^{int}(\boldsymbol{q}_m)\boldsymbol{N}_e^{int}(\boldsymbol{q}_m) \in \mathbb{R}^{3\times(6+n_w+n_m)}, \tag{6.4}$$

where $\boldsymbol{N}_e^{int}(\boldsymbol{q}_m) \in \mathbb{R}^{(6+n_w+n_m)\times(6+n_w+n_m)}$ is the dynamically-consistent projector of $\boldsymbol{\omega}_b^{int}$ into the null space of $\boldsymbol{\nu}_e^{int}$. The choice (6.4) ensures that the dynamics of $\boldsymbol{\nu}_e^{int}$ and $\breve{\boldsymbol{\omega}}_b^{int}$ is inertially decoupled.
The internal velocities $\boldsymbol{\nu}_e^{int}$ and $\breve{\boldsymbol{\omega}}_b^{int}$ are six- and three-dimensional vectors, respectively, and complessively form a nine-dimensional internal motion. For a redundant arm it is $n_m > 6$, for a redundant set of wheels it is $n_m > 3$, thus an additional internal motion of dimension $r = n_m + n_w - 9$ is required to construct an internal motion of dimension $n_m + n_w$. By denoting $\boldsymbol{\upsilon}_n^{int} \in \mathbb{R}^r$ such an additional internal motion, it can be expressed as

$$\boldsymbol{\upsilon}_n^{int} = \boldsymbol{J}_n^{int}(\boldsymbol{q}_m)\boldsymbol{\upsilon}, \tag{6.5}$$

where $\boldsymbol{J}_n^{int}(\boldsymbol{q}_m) \in \mathbb{R}^{r\times(6+n_w+n_m)}$. To limit the interference with the base rotation and the end-effector, one may define $\boldsymbol{\upsilon}_n^{int}$ as being a dynamically-consistent null-space velocity

of both the base circumcentroidal angular velocity and the end-effector circumcentroidal velocity. This is done by choosing a mapping $\boldsymbol{J}_n^{int}(\boldsymbol{q}_m)$ such that the condition

$$\begin{bmatrix} \boldsymbol{J}_{\breve{\omega}_b}^{int}(\boldsymbol{q}_m) \\ \boldsymbol{J}_e^{int}(\boldsymbol{q}_m) \end{bmatrix} \boldsymbol{M}(\boldsymbol{q}_m)^{-1} \boldsymbol{J}_n^{int}(\boldsymbol{q}_m)^T = \boldsymbol{0} \tag{6.6}$$

holds. The expression of the mappings $\boldsymbol{J}_e^{int}(\boldsymbol{q}_m)$, $\boldsymbol{J}_b^{int}(\boldsymbol{q}_m)$, $\boldsymbol{J}_{\omega_b}^{int}(\boldsymbol{q}_m)$, $\boldsymbol{N}_e^{int}(\boldsymbol{q}_m)$, and $\boldsymbol{J}_n^{int}(\boldsymbol{q}_m)$ can be found in the Appendix C.5.
Based on the previous definitions, $\breve{\boldsymbol{\omega}}_b^{int}$, $\boldsymbol{\nu}_e^{int}$, and $\boldsymbol{\upsilon}_n^{int}$ complessively form an internal motion $\boldsymbol{\chi}^{int} = \begin{bmatrix} \breve{\boldsymbol{\omega}}_b^{int T} & \boldsymbol{\nu}_e^{int T} & \boldsymbol{\upsilon}_n^{int T} \end{bmatrix}^T$ of dimension $n_w + n_m$, which can be expressed as

$$\boldsymbol{\chi}^{int} = \begin{bmatrix} \breve{\boldsymbol{\omega}}_b^{int} \\ \boldsymbol{\nu}_e^{int} \\ \boldsymbol{\upsilon}_n^{int} \end{bmatrix} = \bar{\boldsymbol{J}}^{int}(\boldsymbol{q}_m)\boldsymbol{\upsilon}, \qquad \text{where} \quad \bar{\boldsymbol{J}}^{int}(\boldsymbol{q}_m) = \begin{bmatrix} \boldsymbol{J}_{\breve{\omega}_b}^{int}(\boldsymbol{q}_m) \\ \boldsymbol{J}_e^{int}(\boldsymbol{q}_m) \\ \boldsymbol{J}_n^{int}(\boldsymbol{q}_m) \end{bmatrix} \in \mathbb{R}^{(n_w+n_m)\times(6+n_w+n_m)}. \tag{6.7}$$

Hence, in the singularity-free region $\mathcal{Q}^{int}$ (see (4.31)) the dynamics in the allocation space can be transformed to the decoupled external-internal form (4.38). Considering only contact at the end-effector[1], the dynamics has the form

$$\dot{\boldsymbol{h}}_c = \boldsymbol{\mathcal{F}}_c + \boldsymbol{A}_{ec}(\boldsymbol{R}_b, \boldsymbol{q}_m)^T \boldsymbol{\mathcal{F}}_e^{ext}, \tag{6.8a}$$

$$\boldsymbol{M}_\chi^{int}(\boldsymbol{q}_m) \begin{bmatrix} \dot{\breve{\boldsymbol{\omega}}}_b^{int} \\ \dot{\boldsymbol{\nu}}_e^{int} \\ \dot{\boldsymbol{\upsilon}}_n^{int} \end{bmatrix} + \boldsymbol{C}_{\chi^{int}}(\boldsymbol{R}_b, \boldsymbol{q}_m, \boldsymbol{h}_c, \boldsymbol{\chi}^{int}) \begin{bmatrix} \breve{\boldsymbol{\omega}}_b^{int} \\ \boldsymbol{\nu}_e^{int} \\ \boldsymbol{\upsilon}_n^{int} \end{bmatrix} + \boldsymbol{C}_{\chi^{int}h}(\boldsymbol{R}_b, \boldsymbol{q}_m, \boldsymbol{h}_c, \boldsymbol{\chi}^{int}) \boldsymbol{h}_c = \begin{bmatrix} \breve{\boldsymbol{m}}_b^{int} \\ \boldsymbol{\mathcal{F}}_e^{int} \\ \boldsymbol{\varsigma}_n^{int} \end{bmatrix} + \begin{bmatrix} \boldsymbol{0} \\ \boldsymbol{\mathcal{F}}_e^{ext} \\ \boldsymbol{0} \end{bmatrix}, \tag{6.8b}$$

where $\breve{\boldsymbol{m}}_b^{int} \in \mathbb{R}^3$, $\boldsymbol{\mathcal{F}}_e^{int} \in \mathbb{R}^6$ and $\boldsymbol{\varsigma}_n^{int} \in \mathbb{R}^r$ are virtual actuators, which are associated to $\breve{\boldsymbol{\omega}}_b^{int}$, $\boldsymbol{\nu}_e^{int}$, and $\boldsymbol{\upsilon}_n^{int}$, respectively. They are related to the actuators by an actuation mapping decoupled in $\boldsymbol{\mathcal{F}}_b$. By using (4.25), (2.55a), and (C.35), the actuation mapping is expressed as

$$\begin{bmatrix} \boldsymbol{\mathcal{F}}_b \\ \boldsymbol{\tau}_w \\ \boldsymbol{\tau}_m \end{bmatrix} = \begin{bmatrix} \boldsymbol{A}_{cb}(\boldsymbol{R}_b, \boldsymbol{q}_m)^T & \boldsymbol{0} & \boldsymbol{0} & \boldsymbol{0} \\ \boldsymbol{M}_{bw}(\boldsymbol{q}_m)^T \boldsymbol{M}_b(\boldsymbol{q}_m)^{-1} \boldsymbol{A}_{cb}(\boldsymbol{R}_b, \boldsymbol{q}_m)^T & \boldsymbol{J}_{\breve{\omega}_b w}^{int}(\boldsymbol{q}_w)^T & \boldsymbol{J}_{ew}^{int}(\boldsymbol{q}_m)^T & \boldsymbol{J}_{nw}^{int}(\boldsymbol{q}_m)^T \\ \boldsymbol{M}_{bm}(\boldsymbol{q}_m)^T \boldsymbol{M}_b(\boldsymbol{q}_m)^{-1} \boldsymbol{A}_{cb}(\boldsymbol{R}_b, \boldsymbol{q}_m)^T & \boldsymbol{J}_{\breve{\omega}_b m}^{int}(\boldsymbol{q}_m)^T & \boldsymbol{J}_{em}^{int}(\boldsymbol{q}_m)^T & \boldsymbol{J}_{nm}^{int}(\boldsymbol{q}_m)^T \end{bmatrix} \begin{bmatrix} \boldsymbol{\mathcal{F}}_c \\ \breve{\boldsymbol{m}}_b^{int} \\ \boldsymbol{\mathcal{F}}_e^{int} \\ \boldsymbol{\varsigma}_n^{int} \end{bmatrix}, \tag{6.9}$$

where $\boldsymbol{J}_{\breve{\omega}_b w}^{int}(\boldsymbol{q}_m) \in \mathbb{R}^{3\times n_w}$, $\boldsymbol{J}_{\breve{\omega}_b m}^{int}(\boldsymbol{q}_m) \in \mathbb{R}^{3\times n_m}$, $\boldsymbol{J}_{ew}^{int}(\boldsymbol{q}_m) \in \mathbb{R}^{6\times n_w}$, $\boldsymbol{J}_{em}^{int}(\boldsymbol{q}_m) \in \mathbb{R}^{6\times n_m}$, $\boldsymbol{J}_{nw}^{int}(\boldsymbol{q}_m) \in \mathbb{R}^{r\times n_w}$, and $\boldsymbol{J}_{nm}^{int}(\boldsymbol{q}_m) \in \mathbb{R}^{r\times n_m}$ are the sub-blocks of $\boldsymbol{J}_e^{int}(\boldsymbol{q}_m)$, $\breve{\boldsymbol{J}}_{\omega_b}^{int}(\boldsymbol{q}_m)$, and $\boldsymbol{J}_n^{int}(\boldsymbol{q}_m)$, associated to the reaction wheels and the arm (see Appendix C.5). Let us mention that in (6.8) the inertia matrix of the internal motion has the block-decoupled form

$$\boldsymbol{M}_\chi^{int}(\boldsymbol{q}_m) = \begin{bmatrix} \boldsymbol{M}_{\breve{\omega}_b}^{int}(\boldsymbol{q}_m) & \boldsymbol{0} & \boldsymbol{0} \\ \boldsymbol{0} & \boldsymbol{M}_e^{int}(\boldsymbol{q}_m) & \boldsymbol{0} \\ \boldsymbol{0} & \boldsymbol{0} & \boldsymbol{M}_n^{int}(\boldsymbol{q}_m) \end{bmatrix}, \tag{6.10}$$

[1] In this case, the terms $\boldsymbol{\mathcal{F}}_c^{ext}$ and $\boldsymbol{\varsigma}^{int,ext}$ in (4.38) are $\boldsymbol{\mathcal{F}}_c^{ext} = \boldsymbol{A}_{ec}(\boldsymbol{R}_b, \boldsymbol{q})^T \boldsymbol{\mathcal{F}}_e^{ext}$ and $\boldsymbol{\varsigma}^{int,ext} = \begin{bmatrix} \boldsymbol{0} \\ \boldsymbol{\mathcal{F}}_e^{ext} \\ \boldsymbol{0} \end{bmatrix}$.

The decoupled form is a consequence of defining $\breve{\boldsymbol{\omega}}_b^{int}$ in the dynamically-consistent null space of the $\boldsymbol{\nu}_e^{int}$, and defining $\boldsymbol{v}_n^{int}$ in the dynamically-consistent null space of both $\breve{\boldsymbol{\omega}}_b^{int}$ and $\boldsymbol{\nu}_e^{int}$. Nevertheless, the Coriolis/centrifugal matrix $\boldsymbol{C}_{\chi^{int}}(\boldsymbol{R}_b, \boldsymbol{q}_m, \boldsymbol{h}_c, \breve{\boldsymbol{\omega}}_b^{int}, \boldsymbol{\nu}_e^{int}, \boldsymbol{v}_n^{int})$ is still fully coupled, i.e.,

$$\boldsymbol{C}_{\chi^{int}}(\boldsymbol{R}_b, \boldsymbol{q}_m, \boldsymbol{\chi}^{int}) = \begin{bmatrix} \boldsymbol{C}^{int}_{\breve{\omega}_b}(\boldsymbol{R}_b, \boldsymbol{q}_m, \boldsymbol{\chi}^{int}) & \boldsymbol{C}^{int}_{\breve{\omega}_b e}(\boldsymbol{R}_b, \boldsymbol{q}_m, \boldsymbol{\chi}^{int}) & \boldsymbol{C}^{int}_{\breve{\omega}_b n}(\boldsymbol{R}_b, \boldsymbol{q}_m, \boldsymbol{\chi}^{int}) \\ -\boldsymbol{C}^{int}_{\breve{\omega}_b e}(\boldsymbol{R}_b, \boldsymbol{q}_m, \boldsymbol{\chi}^{int})^T & \boldsymbol{C}^{int}_{e}(\boldsymbol{R}_b, \boldsymbol{q}_m, \boldsymbol{\chi}^{int}) & \boldsymbol{C}^{int}_{en}(\boldsymbol{R}_b, \boldsymbol{q}_m, \boldsymbol{\chi}^{int}) \\ -\boldsymbol{C}^{int}_{\breve{\omega}_b n}(\boldsymbol{R}_b, \boldsymbol{q}_m, \boldsymbol{\chi}^{int})^T & -\boldsymbol{C}^{int}_{en}(\boldsymbol{R}_b, \boldsymbol{q}_m, \boldsymbol{\chi}^{int})^T & \boldsymbol{C}^{int}_{n}(\boldsymbol{R}_b, \boldsymbol{q}_m, \boldsymbol{\chi}^{int}) \end{bmatrix}, \tag{6.11}$$

therefore the internal subsystem in (6.8b) is coupled. Note that the property (4.37) holds also for the sub-blocks of inertia and Coriolis-centrifugal matrix, i.e.,

$$\dot{\boldsymbol{M}}^{int}_{\breve{\omega}_b}(\boldsymbol{q}_m) = \boldsymbol{C}^{int}_{\breve{\omega}_b}(\boldsymbol{R}_b, \boldsymbol{q}_m, \boldsymbol{\chi}^{int}) + \boldsymbol{C}^{int}_{\breve{\omega}_b}(\boldsymbol{R}_b, \boldsymbol{q}_m, \boldsymbol{\chi}^{int})^T, \tag{6.12a}$$

$$\dot{\boldsymbol{M}}^{int}_{e}(\boldsymbol{q}_m) = \boldsymbol{C}^{int}_{e}(\boldsymbol{R}_b, \boldsymbol{q}_m, \boldsymbol{\chi}^{int}) + \boldsymbol{C}^{int}_{e}(\boldsymbol{R}_b, \boldsymbol{q}_m, \boldsymbol{\chi}^{int})^T, \tag{6.12b}$$

$$\dot{\boldsymbol{M}}^{int}_{n}(\boldsymbol{q}_m) = \boldsymbol{C}^{int}_{n}(\boldsymbol{R}_b, \boldsymbol{q}_m, \boldsymbol{\chi}^{int}) + \boldsymbol{C}^{int}_{n}(\boldsymbol{R}_b, \boldsymbol{q}_m, \boldsymbol{\chi}^{int})^T. \tag{6.12c}$$

For later reference, the Coriolis-centrifugal momentum coupling matrix is also reported in partitioned form, as

$$\boldsymbol{C}_{\chi^{int}h}(\boldsymbol{R}_b, \boldsymbol{q}_m, \boldsymbol{\chi}^{int}) = \begin{bmatrix} \boldsymbol{C}^{int}_{\breve{\omega}_b h}(\boldsymbol{R}_b, \boldsymbol{q}_m, \boldsymbol{\chi}^{int}) \\ \boldsymbol{C}^{int}_{eh}(\boldsymbol{R}_b, \boldsymbol{q}_m, \boldsymbol{\chi}^{int}) \\ \boldsymbol{C}^{int}_{nh}(\boldsymbol{R}_b, \boldsymbol{q}_m, \boldsymbol{\chi}^{int}) \end{bmatrix}. \tag{6.13}$$

Similarly to the previous controllers, note that by exploiting the decoupled structure of the dynamics (6.8), it is possible to design controllers in a cascade fashion, using $\boldsymbol{\mathcal{F}}_c$ to control the global motion, and using $\breve{\boldsymbol{m}}_b^{int}$, $\boldsymbol{\mathcal{F}}_e^{int}$, and $\boldsymbol{\varsigma}_n^{int}$ to control the coupled base, end-effector, and null-space motion. From this it follows that, if one assigns an invariant task to the virtual actuator $\boldsymbol{\mathcal{F}}_c$, then any indirect coupling of the base, end-effector, and null-space tasks, into the thrusters wrench would be avoided. Secondly, note that the actuation mapping (6.9) is decoupled in $\boldsymbol{\mathcal{F}}_b$, therefore any direct coupling of the arm tasks into the thrusters is avoided.

6.1.2. Design of the controller

The objective of the control is to regulate the pose of the end-effector frame $\mathcal{E}$, the orientation of the base frame $\mathcal{B}$, and the position of CoM, around desired locations that are fixed in the target frame $\mathcal{T}$. Furthermore, the angular momentum shall be dumped, to avoid early saturation of the reaction wheels' velocity, and the null-space motion shall be stopped, to avoid any joint drift after the above-mentioned tasks have converged. Towards this aim, let us consider error coordinates $\tilde{\boldsymbol{x}}_c \in \mathbb{R}^3$, $\tilde{\boldsymbol{x}}_{b,rot} \in \mathbb{R}^3$, and $\tilde{\boldsymbol{x}}_e \in \mathbb{R}^6$ for the CoM, base, and the end-effector, respectively, as well as momentum and velocity errors $\tilde{\boldsymbol{h}}_c \in \mathbb{R}^6$, $\tilde{\boldsymbol{\omega}}_b \in \mathbb{R}^3$, $\tilde{\boldsymbol{\nu}}_e \in \mathbb{R}^6$, and $\tilde{\boldsymbol{v}}_n^{int} \in \mathbb{R}^r$. As a consequence of Assumption 2.2, it is $\tilde{\boldsymbol{h}}_c = \boldsymbol{h}_c$, $\tilde{\boldsymbol{\omega}}_b = \boldsymbol{\omega}_b$, $\tilde{\boldsymbol{\nu}}_e = \boldsymbol{\nu}_e$, and $\tilde{\boldsymbol{v}}_n^{int} = \boldsymbol{v}_n^{int}$. The derivation of the controller is restricted to the contact-free operation:

Assumption 6.1. *There is no contact, i.e.,* $\boldsymbol{\mathcal{F}}_e^{ext} = \boldsymbol{0}$.

The controller is designed as follows. The invariant task is designed as

$$\boldsymbol{\mathcal{F}}_c = -\boldsymbol{S}_v^T \boldsymbol{K}_c \tilde{\boldsymbol{x}}_c - \boldsymbol{D}_h \tilde{\boldsymbol{h}}_c, \tag{6.14a}$$

which is the same of one of the controller (5.8a) for a robot without reaction wheels; it imposes the requirement that the CoM be controlled around a desired position and, additionally, that any residual momentum be extracted from the system.
The base, end-effector, and null-space tasks are designed as

$$\breve{\boldsymbol{m}}_b^{int} = -\boldsymbol{J}_{\tilde{x}_{b,rot}}(\tilde{\boldsymbol{x}}_{b,rot})^T \boldsymbol{K}_{b,rot}\tilde{\boldsymbol{x}}_{b,rot} - \boldsymbol{D}_{b,rot}\tilde{\boldsymbol{\omega}}_b, \tag{6.14b}$$

$$\boldsymbol{\mathcal{F}}_e^{int} = -\boldsymbol{J}_{\tilde{x}_e}(\tilde{\boldsymbol{x}}_e)^T \boldsymbol{K}_e\tilde{\boldsymbol{x}}_e - \boldsymbol{D}_e\tilde{\boldsymbol{\nu}}_e - \boldsymbol{C}_{\breve{\omega}_b e}^{int}(\boldsymbol{R}_b, \boldsymbol{q}_m, \boldsymbol{\chi}^{int})^T \breve{\boldsymbol{\omega}}_b^{int}, \tag{6.14c}$$

$$\boldsymbol{\varsigma}_n^{int} = -\boldsymbol{D}_n\tilde{\boldsymbol{v}}_n^{int}. \tag{6.14d}$$

The controllers (6.14b), (6.14c), (6.14d) include a PD-like term, whereas (6.14c) includes an additional term for compensating the Coriolis and centrifugal coupling of the base into the end-effector. This term is necessary for the proof of stability shown in Sect. 6.1.3.

6.1.3. Analysis of the closed loop

For the analysis of the stability of the closed loop the following assumptions are made:

Assumption 6.2. *The set of reaction wheels is nonredundant, i.e., $n_w = 3$, and nonsingular.*

Assumption 6.3. *The arm is nonredundant, i.e., $n_m = 6$.*

To derive the closed-loop dynamics, the task-space velocity errors $\tilde{\boldsymbol{\omega}}_b$ and $\tilde{\boldsymbol{\nu}}_e$ used in (6.14b) and (6.14c) are first preliminarily written in terms of the momentum and internal velocities velocities $\boldsymbol{h}_c$, $\breve{\boldsymbol{\omega}}_b^{int}$, and $\boldsymbol{\nu}_e^{int}$ used in the allocation-space dynamics (6.8); by using (4.19), the end-effector error is written as

$$\tilde{\boldsymbol{\nu}}_e = \boldsymbol{\nu}_e^{int} + \boldsymbol{A}_{ec}(\boldsymbol{R}_b, \boldsymbol{q}_m)\boldsymbol{M}_c(\boldsymbol{R}_b, \boldsymbol{q}_m)^{-1}\boldsymbol{h}_c. \tag{6.15a}$$

It can be shown (see Appendix C.5) that the base angular velocity error results in

$$\tilde{\boldsymbol{\omega}}_b = \breve{\boldsymbol{\omega}}_b^{int} + \boldsymbol{J}_{\omega_b}^{int}(\boldsymbol{q}_m)\boldsymbol{J}_{eq}{}^{int}(\boldsymbol{q}_m)^{\#}\boldsymbol{\nu}_e^{int} + \boldsymbol{S}_\omega\boldsymbol{A}_{bc}(\boldsymbol{R}_b, \boldsymbol{q}_m)\boldsymbol{M}_c(\boldsymbol{R}_b, \boldsymbol{q}_m)^{-1}\boldsymbol{h}_c. \tag{6.15b}$$

The closed-loop dynamics and kinematics equations are obtained by inserting (6.14) into (6.8), considering the error kinematics equations (B.2), (B.4) and (B.6b) together with (6.15), and considering that the null-space velocity and the null-space equation are identically zero because of Assumption 6.2 and Assumption 6.3, obtaining

$$\dot{\boldsymbol{h}}_c + \boldsymbol{D}_h\boldsymbol{h}_c + \boldsymbol{S}_v^T\boldsymbol{K}_c\tilde{\boldsymbol{x}}_c = \boldsymbol{0}, \tag{6.16a}$$

$$\dot{\tilde{\boldsymbol{x}}}_c = \frac{1}{m}\boldsymbol{S}_v\boldsymbol{h}_c, \tag{6.16b}$$

$$\boldsymbol{M}_e^{int}\dot{\boldsymbol{\nu}}_e^{int} + \boldsymbol{C}_e^{int}\boldsymbol{\nu}_e^{int} + \boldsymbol{D}_e\boldsymbol{\nu}_e^{int} + \boldsymbol{J}_{\tilde{x}_e}^T\boldsymbol{K}_e\tilde{\boldsymbol{x}}_e = \left(-\boldsymbol{D}_e\boldsymbol{A}_{ec}\boldsymbol{M}_c^{-1} + \boldsymbol{C}_{eh}^{int}\right)\boldsymbol{h}_c, \tag{6.16c}$$

$$\dot{\tilde{\boldsymbol{x}}}_e = \boldsymbol{J}_{\tilde{x}_e}\boldsymbol{\nu}_e^{int} + \boldsymbol{J}_{\tilde{x}_e}\boldsymbol{A}_{ec}\boldsymbol{M}_c^{-1}\boldsymbol{h}_c, \tag{6.16d}$$

$$\begin{aligned}\boldsymbol{M}_{\breve{\omega}_b}^{int}\dot{\breve{\boldsymbol{\omega}}}_b^{int} + \boldsymbol{C}_{\breve{\omega}_b}^{int}\breve{\boldsymbol{\omega}}_b^{int} + \boldsymbol{D}_b\breve{\boldsymbol{\omega}}_b^{int} + \boldsymbol{J}_{\tilde{x}_{b,rot}}^T\boldsymbol{K}_{b,rot}\tilde{\boldsymbol{x}}_{b,rot} = \\ = \left(-\boldsymbol{C}_{be}^*\boldsymbol{\nu}_e^{int} - \boldsymbol{D}_b\boldsymbol{J}_{\omega_b}^{int}\boldsymbol{J}_{eq}{}^{int\#}\right)\boldsymbol{\nu}_e^{int} + \left(-\boldsymbol{D}_b\boldsymbol{S}_\omega\boldsymbol{A}_{bc}\boldsymbol{M}_c^{-1} + \boldsymbol{C}_{\breve{\omega}_b h}^{int}\right)\boldsymbol{h}_c,\end{aligned} \tag{6.16e}$$

$$\dot{\tilde{\boldsymbol{x}}}_b = \boldsymbol{J}_{\tilde{x}_{b,rot}}\breve{\boldsymbol{\omega}}_b^{int} + \boldsymbol{J}_{\tilde{x}_{b,rot}}\boldsymbol{J}_{\omega_b}^{int}\boldsymbol{J}_{eq}{}^{int\#}\boldsymbol{\nu}_e^{int} + \boldsymbol{J}_{\tilde{x}_{b,rot}}\boldsymbol{S}_\omega\boldsymbol{A}_{bc}\boldsymbol{M}_c^{-1}\boldsymbol{h}_c, \tag{6.16f}$$

where the functional dependence of the matrices is omitted for brevity; complessively, they are depending on the configuration variables $\boldsymbol{R}_b$, $\boldsymbol{q}_m$. To represent the closed-loop in a

state-space form, those two dependencies are replaced in terms of the errors $\tilde{\boldsymbol{x}}_c$, $\tilde{\boldsymbol{x}}_{b,rot}$, and $\tilde{\boldsymbol{x}}_e$. The dependence on $\boldsymbol{R}_b$ is replaced considering that is

$$\boldsymbol{R}_b = \boldsymbol{R}_b(\tilde{\boldsymbol{x}}_{b,rot}). \tag{6.17}$$

To replace the joint dependency, let us consider the CoM-based kinematics $\boldsymbol{H}_{c'e}(\boldsymbol{q}_m)$ defined in Section 5.2.3[2]. A region $\mathcal{Q}_5 \subset \mathcal{Q}^{\oplus}$ is defined , in which the invertibility of the CoM-based kinematics of the end-effector is ensured, as

$$\mathcal{Q}_5 = \left\{ \boldsymbol{q}_m \in \mathcal{Q}^{int} : \ \boldsymbol{H}_{c'e}(\boldsymbol{q}_m) \text{ is one-to-one} \right\}. \tag{6.18}$$

Similarly as done in Section 5.2.3, the forward kinematics of the arm can be rewritten in terms of the error and desired poses, as

$$\underbrace{\boldsymbol{H}_{c'e}(\boldsymbol{q}_m)}_{\boldsymbol{g}(\boldsymbol{q}_m)} = \underbrace{\boldsymbol{H}_{c'c'_d}(\tilde{\boldsymbol{x}}_c, \tilde{\boldsymbol{x}}_{b,rot}) \boldsymbol{H}_{tc'_d}^{-1} \boldsymbol{H}_{te_d} \boldsymbol{H}_{e_de}(\tilde{\boldsymbol{x}}_e)}_{\boldsymbol{f}(\tilde{\boldsymbol{x}}_c, \tilde{\boldsymbol{x}}_{b,rot}, \tilde{\boldsymbol{x}}_e)}, \tag{6.19}$$

where $\boldsymbol{g}(\boldsymbol{q}_m) : \mathbb{R}^6 \to \mathrm{SE}(3)$ and $\boldsymbol{f}(\tilde{\boldsymbol{x}}_c, \tilde{\boldsymbol{x}}_{b,rot}, \tilde{\boldsymbol{x}}_e) : \mathbb{R}^{12} \to \mathrm{SE}(3)$, and $\boldsymbol{H}_{tc'_d}$, $\boldsymbol{H}_{te_d}$ are the constant homogeneous matrices that specify the setpoints of the controller. Then, a region in the task space is defined as the pre-image through $\boldsymbol{f}(\tilde{\boldsymbol{x}}_c, \tilde{\boldsymbol{x}}_{b,rot}, \tilde{\boldsymbol{x}}_e)$ of the image of $\bar{\mathcal{Q}}$ through $\boldsymbol{g}(\boldsymbol{q}_m)$, and is given by

$$\mathcal{X}_5 = \left\{ \tilde{\boldsymbol{x}}_c, \tilde{\boldsymbol{x}}_{b,rot}, \tilde{\boldsymbol{x}}_e \in \mathbb{R}^{12} : \ \exists \boldsymbol{q}_m \in \mathcal{Q}_5, \ \boldsymbol{g}(\boldsymbol{q}_m) = \boldsymbol{f}(\tilde{\boldsymbol{x}}_c, \tilde{\boldsymbol{x}}_{b,rot}, \tilde{\boldsymbol{x}}_e) \right\}. \tag{6.20}$$

Note that this region exists if the desired setpoints $\boldsymbol{H}_{tc'_d}$ and $\boldsymbol{H}_{te_d}$ are compatible with the workspace of the arm. In $\mathcal{X}_5$, the inverse function

$$\boldsymbol{q}_m = \boldsymbol{g}^{-1}(\boldsymbol{f}(\tilde{\boldsymbol{x}}_c, \tilde{\boldsymbol{x}}_{b,rot}, \tilde{\boldsymbol{x}}_e)) \tag{6.21}$$

exists, and can be substituted in the closed-loop (6.16). Then, the closed-loop dynamics results in the state-space form

$$\dot{\boldsymbol{z}} = \boldsymbol{f}(\boldsymbol{z}), \qquad \boldsymbol{z} = \begin{bmatrix} \boldsymbol{h}_c \\ \tilde{\boldsymbol{x}}_c \\ \boldsymbol{\nu}_e^{int} \\ \tilde{\boldsymbol{x}}_e \\ \breve{\boldsymbol{\omega}}_b^{int} \\ \tilde{\boldsymbol{x}}_{b,rot} \end{bmatrix} \in D_5 = \mathbb{R}^{15} \times \mathcal{X}_5 \tag{6.22}$$

The proof is based on the application of conditional stability theory [RS97, p.45]. The formulation in [GO17] is used herein, whose main result is reported here for the subcase of stability of equilibrium points:

Theorem 6.1 (Conditional stability [GO17])**.** *Let $\boldsymbol{z}_0$ be an equilibrium point of a system $\dot{\boldsymbol{z}} = \boldsymbol{f}(\boldsymbol{z})$, and let $V(\boldsymbol{z})$ be a C^1 function such that $V(\boldsymbol{z}) \geq 0$, $V(\boldsymbol{z}_0) = 0$ and $\dot{V}(\boldsymbol{z}) \leq 0$. If $\boldsymbol{z}_0$ is asymptotically stable conditionally to the largest positively invariant set $\mathcal{A}$ within $\left\{ \boldsymbol{z} : \dot{V}(\boldsymbol{z}) = 0 \right\}$, then $\boldsymbol{z}_0$ is asymptotically stable.*

[2]Note that $\boldsymbol{H}_{c'e}(\boldsymbol{q}_m)$ is a function of only the joint angles of the arm also for a robot with reaction wheels, as a consequence of Assumption 2.6.

The proof of stability of (6.22) is conducted on a hierarchical basis, proving the successive convergence of nested subsets [ODAS15] by recursively applying Theorem 6.1. The following subsets are defined:

$$\mathcal{A}_1 = \{\boldsymbol{z} \in D_5 : \boldsymbol{h}_c = \boldsymbol{0}, \tilde{\boldsymbol{x}}_c = \boldsymbol{0}\}, \tag{6.23}$$

$$\mathcal{A}_2 = \left\{\boldsymbol{z} \in D_5 : \boldsymbol{h}_c = \boldsymbol{0}, \tilde{\boldsymbol{x}}_c = \boldsymbol{0}, \boldsymbol{\nu}_e^{int} = \tilde{\boldsymbol{x}}_e = \boldsymbol{0}\right\}. \tag{6.24}$$

Note that $\boldsymbol{0} \in \mathcal{A}_2 \subset \mathcal{A}_1 \subset D_5$. The main stability result can be now stated:

Proposition 6.1. *Consider the system* (6.22)*. Under the Assumptions 2.6, 6.2, and 6.3, the equilibrium point* $\boldsymbol{z}_0 = \boldsymbol{0}$ *is asymptotically stable.*

Proof. The proof is performed in three steps, proving first the asymptotic stability conditionally to $\mathcal{A}_2$, then the asymptotic stability conditionally to $\mathcal{A}_1$ and, lastly, the asymptotic stability of the equilibrium point without any restrictions.

Step 1. Asymptotic stability of $\boldsymbol{z}_0$ conditionally to $\mathcal{A}_2$

In $\mathcal{A}_2$ the conditions $\boldsymbol{h}_c \equiv \boldsymbol{0}$ and $\boldsymbol{\nu}_e^{int} \equiv \boldsymbol{0}$ are applied to (6.22). Let us consider the Lyapunov function candidate

$$V_b(\boldsymbol{z}) = \frac{1}{2}\breve{\boldsymbol{\omega}}_b^{int\,T}\boldsymbol{M}_{\breve{\omega}_b}^{int}\breve{\boldsymbol{\omega}}_b^{int} + \frac{1}{2}\tilde{\boldsymbol{x}}_{b,rot}^T\boldsymbol{K}_{b,rot}\tilde{\boldsymbol{x}}_{b,rot}, > 0,\ \forall \boldsymbol{z} \in \mathcal{A}_2 : \boldsymbol{z} \neq \boldsymbol{z}_0, \tag{6.25}$$

which satisfies $V_b(\boldsymbol{z}_0) = 0$. Its time derivative is

$$\begin{aligned}\dot{V}_b(\boldsymbol{z}) = \breve{\boldsymbol{\omega}}_b^{int\,T}\boldsymbol{M}_{\breve{\omega}_b}^{int}\dot{\breve{\boldsymbol{\omega}}}_b^{int} + \frac{1}{2}\breve{\boldsymbol{\omega}}_b^{int\,T}\dot{\boldsymbol{M}}_{\breve{\omega}_b}^{int}\breve{\boldsymbol{\omega}}_b^{int} + \dot{\tilde{\boldsymbol{x}}}_{b,rot}^T\boldsymbol{K}_{b,rot}\tilde{\boldsymbol{x}}_{b,rot} = \breve{\boldsymbol{\omega}}_b^{int\,T}\big(-\boldsymbol{C}_{\breve{\omega}_b}^{int}\breve{\boldsymbol{\omega}}_b^{int} - \boldsymbol{D}_b\breve{\boldsymbol{\omega}}_b^{int} + \\ - \boldsymbol{J}_{\tilde{x}_{b,rot}}^T\boldsymbol{K}_{b,rot}\tilde{\boldsymbol{x}}_{b,rot}\big) + \frac{1}{2}\breve{\boldsymbol{\omega}}_b^{int\,T}\dot{\boldsymbol{M}}_{\breve{\omega}_b}^{int}\breve{\boldsymbol{\omega}}_b^{int} + \breve{\boldsymbol{\omega}}_b^{int\,T}\boldsymbol{J}_{\tilde{x}_{b,rot}}^T\boldsymbol{K}_{b,rot}\tilde{\boldsymbol{x}}_{b,rot} = -\breve{\boldsymbol{\omega}}_b^{int\,T}\boldsymbol{D}_b\breve{\boldsymbol{\omega}}_b^{int} \leq 0, \\ \forall \boldsymbol{z} \in \mathcal{A}_2,\end{aligned} \tag{6.26}$$

wherein (6.16e), (6.16f), and (6.12a) are used. Then, $\dot{V}_b(\boldsymbol{z})$ is negative semi-definite, and the stability conditionally to $\mathcal{A}_2$ is proven. To prove convergence, LaSalle's invariance principle is applied. It can be seen in (6.16e) that in $\mathcal{A}_2$ the condition $\breve{\boldsymbol{\omega}}_b^{int} \equiv \boldsymbol{0}$ implies $\tilde{\boldsymbol{x}}_{b,rot} \equiv \boldsymbol{0}$, so $\boldsymbol{z}_0$ is asymptotically stable conditionally to $\mathcal{A}_2$.

Step 2. Asymptotic stability of $\boldsymbol{z}_0$ conditionally to $\mathcal{A}_1$

In $\mathcal{A}_1$ the condition $\boldsymbol{h}_c \equiv \boldsymbol{0}$ is applied to (6.22). Theorem 6.1 is applied considering $\mathcal{A} = \mathcal{A}_2$ and restricting all the statements to the subset $\mathcal{A}_1$. Let us then consider the function

$$V_e(\boldsymbol{z}) = \frac{1}{2}\boldsymbol{\nu}_e^{int\,T}\boldsymbol{M}_e^{int}\boldsymbol{\nu}_e^{int} + \frac{1}{2}\tilde{\boldsymbol{x}}_e^T\boldsymbol{K}_e\tilde{\boldsymbol{x}}_e \geq 0, \quad \forall \boldsymbol{z} \in \mathcal{A}_1, \tag{6.27}$$

which satisfies $V_e(\boldsymbol{z}_0) = 0$. Its time derivative is

$$\begin{aligned}\dot{V}_e(\boldsymbol{z}) = \boldsymbol{\nu}_e^{int\,T}\boldsymbol{M}_e^{int}\dot{\boldsymbol{\nu}}_e^{int} + \frac{1}{2}\boldsymbol{\nu}_e^{int\,T}\dot{\boldsymbol{M}}_e^{int}\boldsymbol{\nu}_e^{int} + \dot{\tilde{\boldsymbol{x}}}_e\boldsymbol{K}_e\boldsymbol{\nu}_e^{int} = \boldsymbol{\nu}_e^{int\,T}\big(-\boldsymbol{C}_e^{int}\boldsymbol{\nu}_e^{int} - \boldsymbol{D}_e\boldsymbol{\nu}_e^{int} - \boldsymbol{J}_{\tilde{x}_e}^T\boldsymbol{K}_e\tilde{\boldsymbol{x}}_e\big) + \\ + \frac{1}{2}\boldsymbol{\nu}_e^{int\,T}\dot{\boldsymbol{M}}_e^{int}\boldsymbol{\nu}_e^{int} + \boldsymbol{\nu}_e^{int\,T}\boldsymbol{J}_{\tilde{x}_e}^T\boldsymbol{K}_e\boldsymbol{\nu}_e^{int} = -\boldsymbol{\nu}_e^{int\,T}\boldsymbol{D}_e\boldsymbol{\nu}_e^{int} \leq 0, \quad \forall \boldsymbol{z} \in \mathcal{A}_1,\end{aligned} \tag{6.28}$$

wherein (6.16c), (6.16d), and (6.12b) are used. Then, $V_e(\boldsymbol{z})$ satisfies the conditions of Theorem 6.1. By inserting $\boldsymbol{h}_c = \boldsymbol{0}$ and $\boldsymbol{\nu}_e^{int} = \boldsymbol{0}$ in (6.16c), it can be seen that $\mathcal{A}_2$ is the largest invariant set such that $\dot{V}_e(\boldsymbol{z}) = 0$. Then, the further requirement of asymptotic stability of $\boldsymbol{z}_0$ conditionally to $\mathcal{A} = \mathcal{A}_2$ is guaranteed by Step 1. By application of Theorem 6.1, it follows that $\boldsymbol{z}_0$ is asymptotically stable conditionally to $\mathcal{A}_1$.

Step 3. Asymptotic stability of $\boldsymbol{z}_0$

The asymptotic stability is proven by application of Theorem 6.1, considering $\mathcal{A} = \mathcal{A}_1$. Let us consider the function

$$V_h(\boldsymbol{z}) = \frac{1}{2}\boldsymbol{h}_c^T\boldsymbol{h}_c + \frac{1}{2}m\tilde{\boldsymbol{x}}_c^T\boldsymbol{K}_c\tilde{\boldsymbol{x}}_c \geq 0, \quad \forall \boldsymbol{z} \in D_5, \tag{6.29}$$

which satisfies $V_h(\boldsymbol{z}_0) = 0$. Its time derivative is

$$\begin{aligned}\dot{V}_h(\boldsymbol{z}) = \boldsymbol{h}_c^T\dot{\boldsymbol{h}}_c + m\dot{\tilde{\boldsymbol{x}}}_c^T\boldsymbol{K}_c\tilde{\boldsymbol{x}}_c = \boldsymbol{h}_c^T\left(-\boldsymbol{D}_h\boldsymbol{h}_c - \boldsymbol{S}_v^T\boldsymbol{K}_c\tilde{\boldsymbol{x}}_c\right) \\ + \boldsymbol{h}_c^T\boldsymbol{S}_v^T\boldsymbol{K}_c\tilde{\boldsymbol{x}}_c = -\boldsymbol{h}_c^T\boldsymbol{D}_h\boldsymbol{h}_c \leq 0, \qquad \forall \boldsymbol{z} \in D_5,\end{aligned} \tag{6.30}$$

where (6.16a) and (6.16b) are applied. Then, $V_h(\boldsymbol{z})$ satisfies the conditions of Theorem 6.1. By inserting $\boldsymbol{h}_c = \boldsymbol{0}$ in (6.16a), it can be easily seen that $\mathcal{A}_1$ is the largest invariant set such that $\dot{V}_h(\boldsymbol{z}) = 0$. Then, the requirement of asymptotic stability of $\boldsymbol{z}_0$ conditionally to $\mathcal{A} = \mathcal{A}_1$ is guaranteed by Step 2. By applying Theorem 6.1, it follows that $\boldsymbol{z}_0$ is asymptotically stable. □

6.1.4. Discussion of the controller

As a consequence of the adopted external-internal motion decomposition, the actuation mapping (6.9) has a decoupled structure in the thrusters wrench $\boldsymbol{\mathcal{F}}_b$: the thrusters wrench is only used to actuate the centroidal wrench $\boldsymbol{\mathcal{F}}_c$; on the other hand, the torques in the joints and in the reaction wheels are used to actuate the base moment $\check{\boldsymbol{m}}_b^{int}$ the end-effector wrench $\boldsymbol{\mathcal{F}}_e^{int}$, the null-space generalized force $\boldsymbol{\varsigma}_n^{int}$, and to further counteract the effect of the centroidal wrench $\boldsymbol{\mathcal{F}}_c$ in the joints. Based on this, the controller has no direct coupling of the robot tasks into the thrusters wrench. Furthermore, the centroidal wrench in (6.14a) is only used to actuate an invariant task – thanks to the triangular structure of the closed-loop dynamics (6.8), the attitude, end-effector, and null-space internal motions do not excite the momentum –; therefore, the controller has also no indirect coupling and no thrusters at all are fired during attitude, end-effector, and null-space motions. Hence, it is concluded that the controller performs a **complete decoupling** of the actuation in the thrusters, and it is not affected by the limitations of the free-flying strategy discussed in Section 3.2.4.

Another important feature of the proposed controller is concluded as follows. After CoM and momentum transients – this may be for example the case of a contact, or a workspace relocation maneuver –, the system converges to a stationary situation in which the CoM remains fixed in the inertial space and the momentum remains zero. Therefore, during the entire time of robot maneuvers that do not involve momentum transients, it will remain $\tilde{\boldsymbol{x}}_c = \boldsymbol{0}$ and $\boldsymbol{h}_c = \boldsymbol{0}$. In this nominal situation, it remains $\boldsymbol{\mathcal{F}}_c = \boldsymbol{0}$, and in turn $\boldsymbol{\mathcal{F}}_b = \boldsymbol{0}$. Thus, with the proposed controller, all robotic operations require no thrusters when no CoM or momentum transients are involved, and are performed in a free-floating fashion; they are turned on only when contact occurs and their use is limited to extracting the accumulated momentum and to restoring the desired CoM location. This feature is similar as the one observed for the controller (C3) in Section 5.1.4; however, with the present controller the attitude of the base is additionally regulated by means of the reaction wheels.

6.2. Summary

In this chapter, one Whole-Body controller was derived, based on the framework presented in Chapter 4, for a robot equipped with thrusters and a set of spacecraft-mounted reaction wheels.

The controller was designed to satisfy the whole-body requirements (R1)-(R3) and, similarly as done for the Whole-Body controller (C4), the additional requirement (R4) for the specific case of attitude pointing of the base, which is required by certain missions. Thanks to the additional redundancy provided by the reaction wheels, an external-internal dynamics decomposition was employed instead of a centroid-circumcentroidal one; in this way, the requirement (R4) could be enforced without the use of thrusters. The external-internal form of the dynamics was obtained by using the momentum of the whole system, the internal velocity of the end-effector, an internal velocity of the attitude of the base which is in the null space of the end-effector velocity, and an internal velocity quantifying the residual null-space motion resulting from the arm's and wheels' redundancy. The controller was designed by adopting the invariant task of controlling the momentum and the CoM of the whole robot, instead of the task of controlling the position or orientation of the spacecraft, which is proper of a free-flying strategy. It was shown that, thanks to the external-internal decomposition and to the invariant task, the controller avoids direct and indirect couplings in the thrusters, and thus solves the limitation of the free-flying controller (C2); secondly, thanks to the momentum and CoM task, it allows satisfying the requirements (R1) and (R2), which are not satisfied by the free-floating controller (C1); thirdly, thanks to the additional redundancy provided by the reaction wheels, a completely thrusters-decoupled actuation is used by the controller, instead of the partially thrusters-decoupled actuation used by the whole-body controller (C4). Finally, it was pointed out that after momentum transient the controller automatically reduces to a free-floating controller with attitude control.

Based on the above-mentioned aspects, the controller may be interpreted as a *free-floating-like* Whole-Body strategy which merges the floating-base behavior of the free-floating strategy into a fully-actuated one, and allows reducing the use of the thrusters to the minimum needed also for missions which need the attitude control of the spacecraft.

In the next two chapters, the numerical and experimental verification of the controllers derived in this thesis is reported.

CHAPTER 7

Validation via numerical simulation

In this chapter, the controllers developed throughout the thesis are validated via numerical simulation; they are listed in the following:

(C1) Free-Floating Control: equations (3.9b) and (3.14),

(C2) Free-Flying control with requirements on the pose of the base: equations (3.25) and (3.28),

(C3) Whole-body Control with no requirements on the base: equations (5.6) and (5.8),

(C4) Whole-Body Control with requirements on the attitude of the base: equations (5.25) and (5.27),

(C5) Whole-Body Control with requirements on the attitude of the base (robot with RWs): equations (6.9) and (6.14).

The controllers (C1)-(C5) are compared in simulation in terms of functional behavior and thrusters effort. The simulated scenario is depicted in Fig. 2.1. The dynamics model used is the same for online dynamics computation and for simulation. The simulated arm is a KUKA KR4+ lightweight robot which has an outstretched length of 1.2 m and, including the gripper, weights approximately 17 kg. The dynamics parameters for the spacecraft are:

$$m^{(b)} = 300\,\text{kg}, \qquad {}_b\boldsymbol{o}_{bc_b} = \begin{bmatrix}0 & 0 & 0\end{bmatrix}\text{m}, \qquad \boldsymbol{I}_b^{(b)} = \begin{bmatrix}43.67 & -4.5 & -2.4\\ -4.5 & 29.92 & -1.2\\ -2.4 & -1.2 & 37.75\end{bmatrix}\text{kgm}^2.$$

Three reaction wheels are modeled; they are oriented around the x,y,z axes of the spacecraft, and their dynamic parameters are

$$m^{(j)} = 4.7\,\text{kg}, \qquad {}_j\boldsymbol{o}_{jc_j} = \begin{bmatrix}0 & 0 & 0\end{bmatrix}\text{m}, \qquad \boldsymbol{I}_j^{(j)} = \begin{bmatrix}0.0252 & 0 & 0\\ 0 & 0.0252 & 0\\ 0 & 0 & 0.0425\end{bmatrix}\text{kgm}^2, \quad j \in j_w.$$

In order to compare the controllers with and without reaction wheels under the same model, when simulating the controllers without reaction wheels, i.e., controllers (C1)-(C4), the reaction wheels are locked so to yield the same numerical values of the overall inertia used for the simulation of the controllers with reaction wheels.

The stiffness gains for each controller are listed in 7.1. The damping gains for the CoM, base, and end-effector are designed such that the quasi-static closed-loop dynamics of each controller[1] has a damping ratio $\zeta = 1$. The gains are designed by using the double-diagonalization method [AOFH03] based on the inertia matrix at the initial time of the simulation. The angular momentum gain and the nullspace damping gain are empirically tuned. The momentum gain and nullspace damping gain are listed in 7.2.

Controller	$\boldsymbol{K}_c$ $\mathrm{N\,m^{-1}}$	$\boldsymbol{K}_{b,tras}$ $\mathrm{N\,m^{-1}}$	$\boldsymbol{K}_{b,rot}$ $\mathrm{N\,m\,rad^{-1}}$	$\boldsymbol{K}_{e,tras}$ $\mathrm{N\,m^{-1}}$	$\boldsymbol{K}_{e,rot}$ $\mathrm{N\,m\,rad^{-1}}$
Free-Floating (C1)	n.a[a]	n.a.	n.a.	$1000\,\boldsymbol{E}$	$70\,\boldsymbol{E}$
Free-Flying (C2)[b]	n.a.	$128\,\boldsymbol{E}$	blkdiag(18,15,15)	$1000\,\boldsymbol{E}$	$70\,\boldsymbol{E}$
Whole-Body (C3)	$128\,\boldsymbol{E}$	n.a.	n.a.	$1000\,\boldsymbol{E}$	$70\,\boldsymbol{E}$
Whole-Body (C4)	$128\,\boldsymbol{E}$	n.a.	blkdiag(18,15,15)	$1000\,\boldsymbol{E}$	$70\,\boldsymbol{E}$
Whole-Body (C5)	$128\,\boldsymbol{E}$	n.a.	blkdiag(9000,3350,3350)	$1000\,\boldsymbol{E}$	$70\,\boldsymbol{E}$

[a] Not applicable.
[b] For (C2) it is $\boldsymbol{K}_b = \mathrm{blkdiag}(\boldsymbol{K}_{b,tras}, \boldsymbol{K}_{b,rot})$; for all controllers it is $\boldsymbol{K}_e = \mathrm{blkdiag}(\boldsymbol{K}_{e,tras}, \boldsymbol{K}_{e,rot})$.

Table 7.1.: Stiffness gains used during numerical simulation.

Controller	$\boldsymbol{D}_h$ $\mathrm{s^{-1}}$	$\boldsymbol{D}_n$ $\mathrm{N\,m\,rad\,s^{-1}}$
Free-Floating (C1)	n.a.	0.001
Free-Flying (C2)[a]	n.a.	0.0001
Whole-Body (C3)	blkdiag($1.24\,\boldsymbol{E}$,$1\,\boldsymbol{E}$)	0.001
Whole-Body (C4)	n.a	0.002
Whole-Body (C5)	blkdiag($1.24\,\boldsymbol{E}$,$1\,\boldsymbol{E}$)	0.15

Table 7.2.: Momentum and nullspace gains used during numerical simulation.

7.1. Comparison of behavior with ideal model

To outline the differences between the functional behavior of the controllers, a simulative comparison is carried out considering ideal models for the rigid-body dynamics, the measurements, and the actuators. A simplified model is used to quantify the effort of the thrusters; it is given by

$$c_{tras} = \int_0^{t_f} ||\boldsymbol{f}_b||_1 \mathrm{d}t, \qquad c_{rot} = \int_0^{t_f} ||\boldsymbol{\tau}_b||_1 \mathrm{d}t, \tag{7.1}$$

[1] In the controllers (C2) and (C4) the inertia couplings (see (3.26) and (5.26), respectively) between the base and the end-effector have been neglected for the design of the damping matrices.

where $c_{tras} \in \mathbb{R}$ and $c_{rot} \in \mathbb{R}$ quantify the usage of the thrusters in translation and in rotation, respectively. The total thrusters effort is $c_{tot} = c_{tras} + c_{rot}$.
A representative scenario is considered, in which the end-effector is commanded to reach a desired location w. r. t. the target object, and accidental or voluntary contact happens. The scenario may be divided in the following phases:

pre-contact force; the end-effector is steered towards the target location in absence of external

contact a contact force acts on the space robot and transfers momentum to it;

post-contact the contact has terminated and the space robot is subject to the effects of the momentum induced by the contact.

The scope of the analysis is to analyze the behavior of the controllers during the pre- and post-contact phases. Two sets of simulations are performed:

1. the end-effector is maneuvered in absence of contact, to compare the behavior of the controllers during the pre-contact phase;

2. the end-effector is commanded to stay in place and a short contact is simulated, to compare the behavior of the controllers during the post-contact phases.

In both simulations, the system starts from rest. In the first simulation, the end-effector's pose is commanded to follow a desired trajectory w.r.t. the target, while the rest of the system is commanded according to the different requirements of the controllers. The end-effector's trajectory is generated using a smooth 5th order interpolator between the initial pose and a final one which is displaced ${}_t\boldsymbol{o}_{ee_f} = [18,\ -16, -18]$ cm in translation and $\boldsymbol{\phi}_{ee_f} = [-2, -2,\ 9]$ deg in rotation (roll, pitch, and yaw angles). The base translation, the base rotation, and the CoM translation are stabilized around the initial position; the angular momentum is stabilized around zero.
In the second simulation, both the end-effector and the rest of the system are regulated around their initial position. The contact consists in a constant external force $\boldsymbol{f}_{e,ext} = \begin{bmatrix}8 & 0 & 2\end{bmatrix}^T$ N applied at the end-effector, which lasts 0.3 s. Remark that, in agreement with Assumption 2.2, during the contact the effects of the acceleration of the target object are neglected. The main focus of the post-contact simulation is to analyze the different functional behavior of the controllers under the effect of the momentum induced by the contact *on the space robot*; thus, for this analysis the acceleration of the target is not of primary importance.

7.1.1. Results for the pre-contact phase

Fig. 7.1 shows the position of end-effector, the position and attitude of the base, and the position of the overall CoM w. r. t. their initial locations at the beginning of the end-effector maneuver. Furthermore, it shows the angular momentum, and commanded the forces and torques acting on the base. Fig. 7.2 shows the effort of the thrusters. Note that, Fig. 7.1 the results of the Free-Floating controller and the Whole-Body controller (C3) are overlapped because, in absence of linear and angular momenta, the two controllers result being identical (see Section 5.1.4).
In Fig. 7.1, the main functional differences among all controllers in terms of translation and rotation of the base are observed. During simulation, the position of the base was

kept in place for the Free-Flying controller but changed and converged to new final values for the Free-Floating and Whole-Body controllers. Meanwhile, the position of the CoM stayed in place for the Free-Floating and Whole-Body controllers, but changed for the Free-Flying controller. This indicates that the Free-Flying controller displaces the overall CoM during end-effector maneuvering even if no contact is involved, resulting in inefficient behavior. On the other hand, for the Free-Floating and Whole-Body controllers the CoM is not displaced, and this comes at no effort as the CoM automatically conserves due to the natural decoupling of the CoM dynamics. This is confirmed by the fact that for the Free-Floating and Whole-Body controllers no force on the base was commanded, as shown in Fig. 7.1, whereas for the Free-Flying controller a nonzero force on the base was commanded.
The rotation of the base was correctly restored to the desired values for the Free-Flying control and for the Whole-Body controllers (C4) and (C5), but changed and converged to new values for the Free-Floating controller and for the Whole-Body controller (C3). Note that the angular momentum remained zero for the Free-Floating controller and for the Whole-Body controllers (C3) and (C5), whereas it changed for the Free-Flying controller and for the Whole-Body controller (C4). Remark that the Whole-Body controllers (C3) and (C5) implement a complete decoupling of the thrusters, whereas the Whole-Body controller (C4) implements only a partial decoupling of the thrusters. This indicates that completely thrusters-coupled and partially thrusters-decoupled strategies – e.g. the Free-Flying controller (C2) and the Whole-Body controller (C4), respectively – vary the total angular momentum during end-effector maneuvering, and this results in inefficient behavior. On the other hand, with completely thrusters-decoupled strategies – e.g. the Whole-Body controllers (C3) and (C5) –, the angular momentum stays at zero, and this comes at no effort as the angular momentum automatically conserves due to the natural decoupling of the angular momentum dynamics. This is confirmed by the fact that for the Whole-Body controllers (C3) and (C5), no base torque was commanded, as shown in Fig. 7.1, whereas for the Free-Flying controller and for the Whole-Body controller (C4) a nonzero force on the base was commanded.
The expected results regarding the efficiency w. r. t. the thruster effort are confirmed in Fig. 7.2. Therein, it is shown that the thrusters effort of the Free-Flying controller was all the time bigger than that of Whole-Body controllers. Similarly, the thrusters effort of the partially thrusters-decoupled Whole-Body controller (C4) was all the time bigger than that of the completely thrusters-decoupled Whole-Body controllers (C3) and (C5), which is exactly zero. The cumulated amount of thrusters effort for the entire maneuver is represented in further detail in the bar plot in Fig. 7.2b, wherein the differences of the effort in rotation and translation are highlighted. In the plot it is possible to observe that the total effort was reduced when the position-control requirement on the base – enforced by the Free-Flying controller – was replaced with a position-control requirement on the overall CoM – enforced by the Whole-Body controllers –, resulting in zero translational effort. Furthermore, the rotational effort was reduced to zero when the attitude-control requirement on the base was replaced by a angular momentum dumping requirement, as realized in the Whole-Body controller (C3), or when it was actuated by reaction wheels, as done in the Whole-Body controller (C5).
In scenarios in which the control of the rotation of the base is mandatory and only thrusters are available, one may use the partially thrusters-decoupled Whole-Body controller (C4) instead of a Free-Flying controller as an intermediate solution to save at least the considerable amount of effort required for translation. The cost to pay is a displacement of the

position of the base after end-effector maneuvers. If the robot is equipped with also reaction wheels, then one may use the completely thrusters-decoupled Whole-Body controller (C5) to achieve zero effort and still be able to control the rotation of the base.

7.1.2. Results for the post-contact phase

Fig. 7.3 shows the external force acting on the end-effector during the simulation of all controllers. Fig. 7.4 shows the position of end-effector, the position and attitude of the base, and the position of the overall CoM w. r. t. their initial locations at the start of the simulation. Furthermore, it shows the angular momentum, the commanded forces and torques acting on the base, and the commanded torques acting in the reaction wheels. The results are shown for the Free-Floating controller and for the Whole-Body controllers. The simulation of the Free-Flying controller yielded similar conclusions as the ones drawn for the Whole-Body controllers; thus, the results are omitted for the sake of brevity.

In Fig. 7.4 it is shown that all controllers were capable of restoring the desired position of the end-effector after contact; however, a consistently different behavior is observed between the Free-Floating controller and the Whole-Body controllers, which shows the main drawback of a Free-Floating controller. After contact, the linear and angular momenta of the system remained constant for the Free-Floating controller, as can be observed in the CoM and angular momentum plots in Fig. 7.4, respectively. This in turn induced an unstoppable drift of the position and rotation of the base, as well as a drift of the overall CoM. Then, a singularity was reached around $t = 13\,s$ and also the end-effector task got compromised. In contrast, for the Whole-Body controllers the linear and angular momenta were dumped by activating the thrusters, and no drift was induced after contact. In turn, the rest of the system was successfully stabilized, and the correct CoM location was restored after contact.
No major differences in the behavior of the Whole-Body controllers during the post-contact phase are observed; the small differences observed are mainly linked to the main functional behavior of the different Whole-Body controllers. Namely, for the Whole-Body controllers (C4) and (C5) the rotation of the base was restored after contact, whereas for the Whole-Body controller (C3) the rotation converged to a new value. Furthermore, a stronger actuation of the torques at the base was requested during contact for the Whole-Body controller (C4). This comes as no surprise: it is a consequence of the direct coupling of the end-effector task into the torques of the base that happens in the (partially thrusters-decoupled) Whole-Body controller (C4) and does not happen for the (completely thrusters-decoupled) Whole-Body controllers (C3) and (C5).

7.2. Validation with realistic actuation and noise models

Numerical simulations were carried out to validate the applicability of the controllers considering realistic actuation and noise models.
A unified scenario involving contact as well as contact-free maneuvering was simulated. A sequence of two end-effector maneuvers lasting 10 s was first commanded, then a contact was simulated. For each maneuver, the end-effector was commanded to reach a desired pose and then to come back; in both maneuvers, a displacement ${}_t\boldsymbol{o}_{ee_f} = \begin{bmatrix}30 & 0 & -25\end{bmatrix}$ cm of the position and $\boldsymbol{\phi}_{ee_f} = \begin{bmatrix}0 & -20 & 0\end{bmatrix}$ deg of the rotation was commanded. The rest of the system was commanded to stay in place according to the different requirements imple-

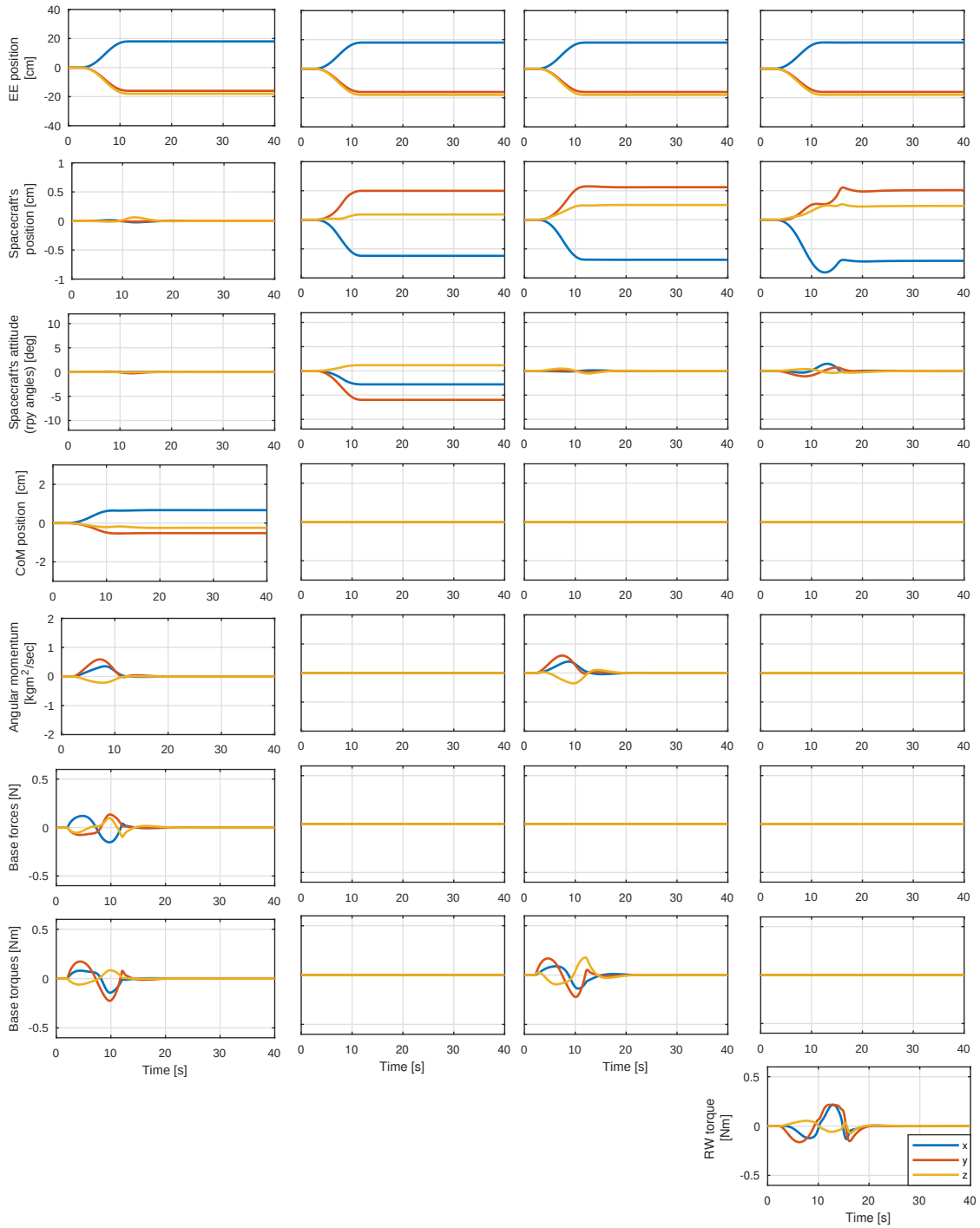

Free-Flying (C2) | Whole-Body (C3) and Free-Floating (C1) | Whole-Body (C4) | Whole-Body (C5)

Figure 7.1.: Response of the controllers during the pre-contact simulation.

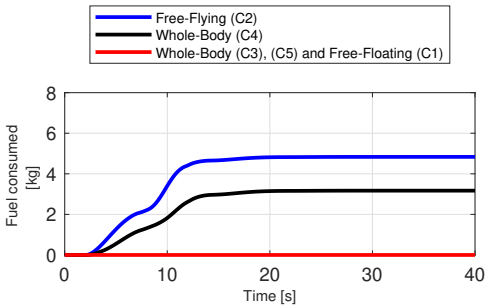

(a) Total thrusters effort. vs time

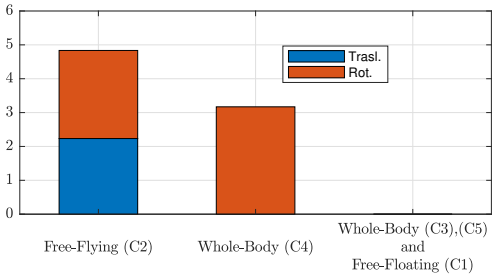

(b) Translational and rotational effort at the end of the maneuver.

Figure 7.2.: Fuel consumption for different control strategies during pre-contact simulation.

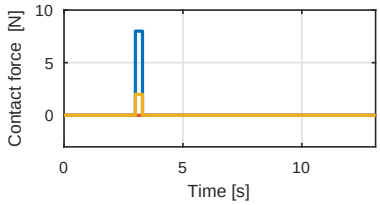

Figure 7.3.: External force acting on EE during post-contact simulation.

mented by the controllers. The contact consisted in a pure force $\boldsymbol{f}_{e,ext} = \begin{bmatrix}-20 & 0 & 0\end{bmatrix}$ N at the end-effector lasting 0.3 s. Initial linear and angular velocities $\boldsymbol{v}_b(t_0) = \begin{bmatrix}2 & 0 & 2\end{bmatrix}$ mm/s and $\boldsymbol{\omega}_b(t_0) = \begin{bmatrix}0 & 0.1 & 0\end{bmatrix}$ deg/s of the base were simulated in order to render the effects of initial nonzero linear and angular momenta present in practical systems at the starting of a proximity maneuver.
The simulation results are shown for the Free-Flying controller (C2) and for the Whole-Body controllers (C3), (C4), (C5); the results of the simulation of the Free-Floating controller (C1) are omitted for brevity, considering its limitations during the post-contact phase.

7.2.1. Actuation models

The thrusters system is composed of a redundant set of $n_t = 24$ thrusters[2] providing full actuation capability on all translational and rotational components. The thrusters are arranged on a cubic geometry (see Fig. 7.5), which is a simplified but still meaningful one for the purpose of investigating the control behavior; the optimization of the thrusters geometry for design purposes is not part of the present study. The cube has an edge length of 2 m, and its center is located on the origin of the frame $\mathcal{B}$ (see Fig. 7.5). On each vertex, three thrusters are mounted, pointing along the x,y,z directions of the frame $\mathcal{B}$.
All thrusters are the same and have the following properties: thrust $u_{max} = 5$ N, Minimum Impulse Bit (MIB) 0.05 Ns, and minimum valve activation time $\Delta t_{min} = 10$ ms. The base control signal $\boldsymbol{\mathcal{F}}_b$ is sampled at a $T_{base} = 300$ ms rate. On the other hand, the joint and RW control signals, $\boldsymbol{\tau}_m$ and $\boldsymbol{\tau}_w$ respectively, are sampled at a $T_{arm} = T_{wheels} = 3$ ms rate. The reaction wheels are simplistically modeled as a saturation of 0.3 Nm.

[2]Note that such level of thrusters' redundancy is not uncommon for space systems (e.g., see [CBS+18]).

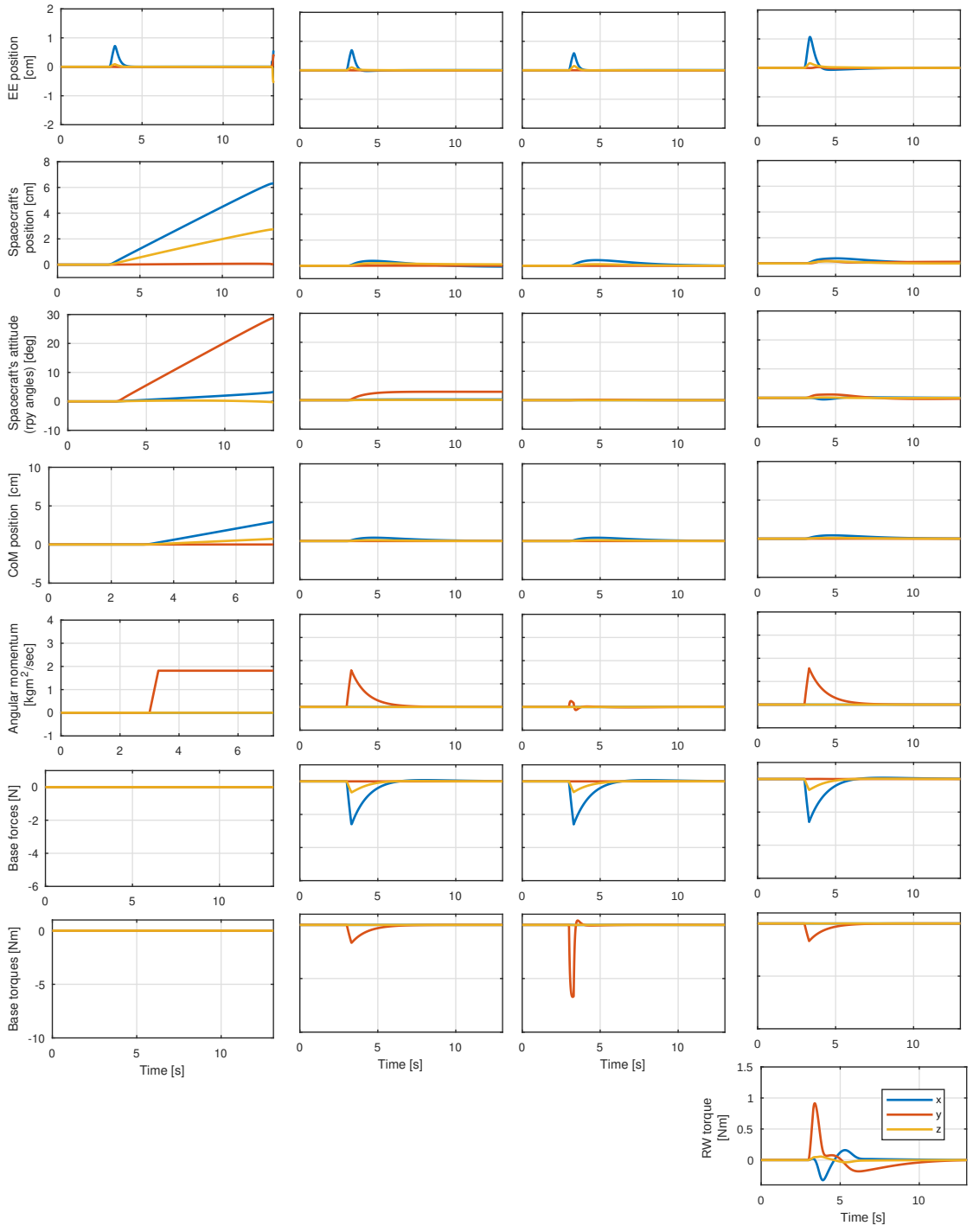

Figure 7.4.: Response of the controllers during the post-contact simulation.

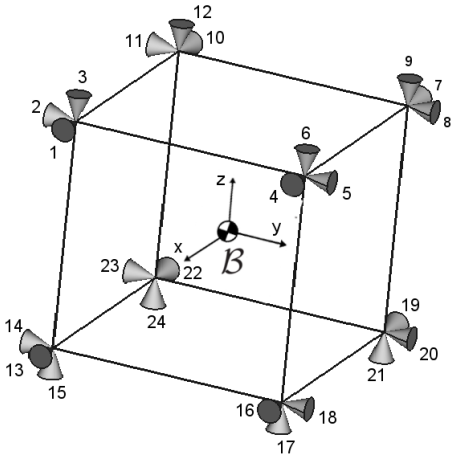

Figure 7.5.: Thrusters system composed of 24 thrusters arranged on a cubic structure.

To resolve the thrusters redundancy, an optimization problem is solved, which takes into account the geometry of the thrusters system, the limitations of the commandable thrust, and a certain optimization criterion. Denoting by $\boldsymbol{u} \in \mathbb{R}^{n_t}$ the stacked vector of the desired thrust levels of all thrusters, the satellite control wrench $\boldsymbol{\mathcal{F}}_b$ can be related to $\boldsymbol{u}$, as

$$\boldsymbol{\mathcal{F}}_b = \boldsymbol{W}\boldsymbol{u}, \tag{7.2a}$$

where $\boldsymbol{W} \in \mathbb{R}^{6\times n_t}$ is the so-called thrust distribution matrix, which is constant and is computed based on the given cubic geometry. No thrusters misalignment are considered in the present work. Equation (7.2a) represents an equality constraint for the optimization problem, and is augmented with the following set of inequality constraints that model the thrust as upper-bounded and positive-only:

$$0 \leq u_i \leq u_{max}, \tag{7.2b}$$

where $u_i \in \mathbb{R}$ denotes the i^{th} component of the vector $\boldsymbol{u}$, i.e., the thrust of the i^{th} thruster. The optimization criterion is the minimization of the consumed fuel; at this purpose, the following cost function is considered:

$$J = \sum_{i=1}^{n_t} u_i. \tag{7.2c}$$

By adopting (7.2c), an optimal solution for $\boldsymbol{u}$ is seeked at that limits conflicting actuation of the thrusters and thus minimizes the fuel consumption. The selection of the thrusters based on the solution of the linear programming problem (7.2), is a classic method in the space engineering practice [Cra, BCTW79] and is solved online by application of the simplex algorithm [Dan63] within the T_{base} sampling interval.

The thrusters are inherently discrete devices that can be operated only in on-off mode. A Pulse-Width-Modulation (PWM) is employed herein to modulate the continuous values u_i, commanded to the i^{th} thruster, to a signal $\bar{u}_i$ that can assume either 0 or u_{max} [BZM92, SWS96, IOK99]. Given the continuous thrust u_i requested over the control interval T_{base}, a rectangular pulse of amplitude u_{max} and variable duration is commanded to the thrusters. The pulse is centered at the middle of the control interval and its duration is computed such to yield an equivalent total impulse of the continuous signal, i.e., such that it holds

Signal		Std. deviation	Sampling rate
joint angles	$\boldsymbol{q}_m$	0.29 deg	1 ms
joint velocities	$\dot{\boldsymbol{q}}_m$	0.35 deg/s	1 ms
reaction wheels' velocities	$\dot{\boldsymbol{q}}_w$	0.15 deg/s	1 ms
position from target to base	$\boldsymbol{o}_{tb}$	3 mm	300 ms
rotation from target to base	$\boldsymbol{R}_{tb}$	0.5 deg	300 ms
linear velocity of base relative to target	$\boldsymbol{v}_{tb}$	1 mm/s	1 ms
angular velocity of base relative to target	$\boldsymbol{\omega}_{tb}$	0.42 deg/s	1 ms
position from target to EE	$\boldsymbol{o}_{te}$	2 mm	90 ms
rotation from target to EE	$\boldsymbol{R}_{te}$	0.2 deg	90 ms
linear velocity of EE relative to target	$\boldsymbol{v}_{te}$	2 mm/s	1 ms
angular velocity of EE relative to target	$\boldsymbol{\omega}_{te}$	0.3 deg/s	1 ms

Table 7.3.: Gaussian noise models for the measurements.

$u_i T_{base} = u_{max} \Delta t_i$; a deadzone is then set on the signal Δt_i to model the minimum valve activation time Δt_{min}. Based on this, the command to the valve of the i^{th} thruster is modeled as

$$\Delta t_i = \begin{cases} \frac{u_i}{u_{max}} T_{base} & \frac{u_i}{u_{max}} T_{base} \geq \Delta t_{min} \\ 0 & \frac{u_i}{u_{max}} T_{base} < \Delta t_{min}. \end{cases} \tag{7.3}$$

The Δt_i signal is discretized with a time step of $T_{pwm} = 3\,\text{ms}$.
The force $\bar{\boldsymbol{f}}_b \in \mathbb{R}^3$ and torque $\bar{\boldsymbol{\tau}}_b \in \mathbb{R}^3$ actuated by the thrusters system are given by

$$\begin{bmatrix} \bar{\boldsymbol{f}}_b \\ \bar{\boldsymbol{m}}_b \end{bmatrix} = \boldsymbol{W} \bar{\boldsymbol{u}}, \tag{7.4}$$

where $\bar{\boldsymbol{u}} \in \mathbb{R}^{n_t}$ denotes the stacked vector of the thrusts $\bar{u}_i$ of the i^{th} thruster, resulting from the PWM modulation. Finally, the fuel consumed by the thrusters is computed as [GPS16]

$$c = \frac{1}{I_{sp} g_0} \int_0^{t_f} \sum_{i=1}^{n_t} \bar{u}_i \mathrm{d}t, \tag{7.5}$$

where I_{sp} is the specific impulse of the thruster and where $g_0 = 9.8\,\text{m}\,\text{s}^{-2}$ is the gravitational acceleration at sea level; herein, it is used $I_{sp} = 70\,\text{s}$.

7.2.2. Measurement models

A white Gaussian noise with zero mean is used to model the uncertainties in the joint, reaction wheels, base, and end-effector measurements; the CoM and momentum states are reconstructed based on the measurements in Table 7.3 and on the inertia model, i.e., by using (2.43). The standard deviation and the sampling rate of the noise models are listed in Table 7.3.

In a real implementation $\boldsymbol{q}_m$ is directly measured by the joints' encoders; $\dot{\boldsymbol{q}}_m$ can be obtained by time differentiation of the joints' encoders; $\dot{\boldsymbol{q}}_w$ can be obtained by the time differentiation of the reaction wheels' encoders. The position and orientation of the base relative to the target, i.e., $\boldsymbol{o}_{tb}$ and $\boldsymbol{R}_{tb}$ are measured by a base-mounted camera or 3D Lidar; the relative linear velocity $\boldsymbol{v}_{tb}$ can be reconstructed by using an observer. The

relative angular velocity $\boldsymbol{\omega}_{tb}$ can be reconstructed as the difference between the absolute angular velocity of the base $\boldsymbol{\omega}_b$, which is directly measured by a base-mounted gyro, and an estimation of the absolute angular velocity of the target $\boldsymbol{\omega}_t$; for the noninertial target considered herein (see Assumption 2.2), $\boldsymbol{\omega}_{tb}$ can be thus directly measured by a base-mounted gyro. An Extended Kalman Filter of the position and the orientation of the base relative to the target, the relative linear velocity, and the absolute angular velocity of the target, was presented in [GMGL19] for the case of no external force; an external force observer for an orbital robot was presented in [CGM19b]; further estimation schemes of the state of the target were developed in [Agh12, Agh13]. The position $\boldsymbol{o}_{te}$ and orientation $\boldsymbol{R}_{te}$ of the end-effector are measured by an EE-mounted camera; the velocities $\boldsymbol{v}_{te}$ and $\boldsymbol{\omega}_{te}$ can be reconstructed based on the forward differential kinematics (2.18b) based on the $\boldsymbol{q}_m$, $\dot{\boldsymbol{q}}_m$, $\boldsymbol{v}_{tb}$, and $\boldsymbol{\omega}_{tb}$ measurements.

A first-order filter is implemented on the control inputs to mitigate the effects of the noise; the cut-off frequency is 15 Hz for the thrusters control signals $\boldsymbol{f}_b$ and $\boldsymbol{m}_b$, whereas it is 50 Hz for the joints and reaction wheels control signals $\boldsymbol{\tau}_m$ and $\boldsymbol{\tau}_w$. A rate-limiter with slope 1 and a saturation of ± 2 Nm, were implemented on the null-space actuator $\boldsymbol{f}_n$ to avoid spikes of the null-space control near singularity. A deadzone of $\pm 2.4\,N$ on $\boldsymbol{f}_b$ and $\pm 0.2\,Nm$ on $\boldsymbol{m}_b$ is implemented to avoid persistent actuation of the thrusters around the zero value, which would lead to excessive fuel consumption.

7.2.3. Results

Fig. 7.6 shows the external force acting on the end-effector during the simulation of all controllers. The response of the system is shown in Fig. 7.7 for the Free-Flying controller, in Fig. 7.8 for the Whole-Body controller C3, Fig. 7.9 for the Whole-Body controller C4, and in Fig. 7.10 for the Whole-Body controller C5. The figures show the time responses of the position and orientation of the end-effector position, of the position and orientation of the base, of the position of the CoM, w. r. t. their initial locations, and of the angular momentum. Furthermore, they show the actuation forces and torques: the torques in the joints and in the reaction wheels, and the force $\bar{\boldsymbol{f}}_b$ and moment $\bar{\boldsymbol{m}}_b$ acted on the base by the thrusters system. A comparison of the consumed fuel of the various controllers is then shown in Fig. 7.11.

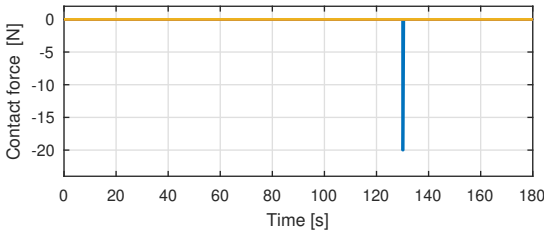

Figure 7.6.: External force acting on EE during simulations with measurement and thrusters models.

In Figs. 7.7 to 7.10 it can be observed that all controllers behaved stably when considering measurements uncertainties, real thursters, and viscous friction in the joints, both during the pre- and post-contact phases. The end-effector maneuvers were successfully accomplished while the remaining requirements were accomplished. More specifically, for the Free-Flying controller, the position and orientation of the base were displaced during the end-effector maneuvers and during contact, but thereafter they were restored to the

desired locations. For the Whole-Body controller C3, the position of the CoM was not affected by end-effector maneuvers; it was affected only by the contact, and it was restored to the desired location afterwards. The angular momentum induced by the contact was successfully dumped. For the Whole-Body controller C4, the position of the CoM was not affected by end-effector maneuvers; it was affected by the contact, and it was restored to the desired location afterwards. The orientation was displaced during the end-effector maneuvers and during contact, but it was successfully restored to the desired locations afterwards. For the Whole-Body controller C5, the position of the CoM was not affected by the end-effector maneuvers; it was affected only by the contact, and it was restored to the desired location afterwards. The orientation was displaced during the end-effector maneuvers and during contact, but it was successfully restored to the desired locations afterwards. The angular momentum induced by the contact was successfully dumped. Note that despite the small size, the reaction wheels successfully accomplished the orientation task, and that the requested torque was, apart from some peaks induced by the noise, mostly within the allowable saturation limits of 0.3 Nm.

Differently than the simulations with ideal measurements and ideal actuation, the control errors of each controller did not converge to zero, but to a bounded region in which they kept varying. This region is a consequence of the discontinuities introduced on $\bar{\boldsymbol{f}}_b$ and $\bar{\boldsymbol{m}}_b$ around zero by the minimum activation time of the valves of the thrusters, and by the deadzone of the controller. More precisely, the discontinuities induced a limit cycle behavior due to the lack of a dissipative action on the *external* dynamics of the robot, – typical of a robot floating in space –, which can dissipate the energy contained within the region. The amount of activity within this region depends on the minimum valve activation time, PWM parameters, thrusters size and geometry, as well as on the noise level, cut-off frequencies of the filters, and gains.
For the Free-Flying controller C2, the limit cycle was induced on the position and orientation of the base, and this in turn induced an excitation of the CoM and of the angular momentum. For the Whole-Body controller C5, the limit cycle was induced on the position of the CoM and on the angular momentum. The limit cycle on the CoM indirectly induced a limit cycle on the position of the base; the limit cycle on the momentum induced a drift on the orientation of the base due to the nonzero angular momentum. However, the residual momentum within the convergence region was considerably smaller then the momentum induced by the contact, therefore the residual drift was considerably improved compared to a purely free-floating strategy. For the Whole-Body controller C4, a limit cycle was induced on the position of the CoM, and on the orientation of the base. The limit cycle on the CoM indirectly induced a limit cycle on the position of the base; the limit cycle on the orientation of the base caused an excitation of the angular momentum. For the Whole-Body controllers C5, a limit cycle was induced on the position of the CoM and on the angular momentum. The limit cycle on the CoM indirectly induced a limit cycle on the position of the base; on the other hand, the limit cycle on the angular momentum did not produce major effects – i.e., neither limit cycles or drifts – on the orientation of the base. This is linked to the beneficial effect of the reaction wheels, which promptly absorbed the residual momentum in the attempt of regulating the orientation of the base.

The pulsed behavior of the PWM is observed in the plots of the base force and base torque shown in Figs. 7.7 to 7.10. From the density of the pulses it is possible to observe therein that the force and torques requested by the (completely thrusters-decoupled) Whole-Body controllers C3 and C5 are considerably smaller than those requested by the (completely thrusters-coupled) Free-Flying controller and by the (partially thrusters-

decoupled) Whole-Body controller C4. From this, a considerable decrease of the consumed fuel is expected.

The consumed fuel and the number of active thrusters at a given instant is shown in Fig. 7.11. Observe therein that the number and density of active thrusters of the (completely thrusters-coupled) Free-Flying controller C2 and the (partially thrusters-decoupled) Whole-Body controller C4 is considerably higher than the (completely thrusters-decoupled) Whole-Body controllers C3 and C5; Accordingly, also the consumed fuel is considerably higher.
During the pre-contact maneuvering phase, the Free-Flying controller C2 consumed fuel in the limit cycle, for restoring the position and orientation of the base after the end-effector maneuvers, and for cooperating in the actuation of the end-effector task; the Whole-Body controller C4 consumed fuel in the limit cycle, for restoring the orientation of the base after the end-effector maneuvers, and for cooperating in the actuation of the end-effector task. In contrast, the Whole-Body controllers C3 and C5 consumed fuel only in the limit cycle.
During the contact-phase, all controllers reacted to stabilize the system, and this caused a visible increase in the consumed fuel; the number of active thrusters during contact is the highest for the Free-Flying controller C2, then for the Whole-Body controller C4, and finally for the Whole-Body controllers C3 and C5.
During the post-contact phase, the Free-Flying controller C2 consumed fuel in the limit cycle, for restoring the position and orientation of the base after contact, and for (indirectly) dumping the momentum induced by the contact; the Whole-Body controller C4 consumed fuel in the limit cycle, for restoring the orientation of the base after contact, and for (indirectly) dumping the momentum induced by the contact. In contrast, the Whole-Body controller C3 and C5 consumed fuel only in the limit cycle and for dumping the momentum induced by the contact.
All in all, the plot of the consumed fuel shows that the Whole-Body controllers C3, C4, C5 employed less fuel than the Free-Flying controller C2 – as it was seeked at in the development of this thesis. Furthermore, it shows that the (partially thrusters-decoupled) Whole-Body controller C4 employed more fuel than the (completely thrusters-decoupled) Whole-Body controllers C3 and C5.

7.2.4. Discussion of results

The simulation results confirmed that the Free-Flying controller C2 and the Whole-Body controllers C3, C4, C5 are applicable considering measurement uncertainties, a representative thrusters system, actuator saturation, and joint friction. The results showed that the PWM modulation strategy [BZM92, SWS96, IOK99] – originally conceived for satellites – can be applied on a multi-body orbital robot. The main effect of the on-off thrusters and of the noise was the appearance of a limit cycle due to the minimum activation time of the valve of the thrusters, and to the control deadzone introduced for the mitigation of the noise. These are tipically known effects from satellite control, and are unavoidable considering the above-mentioned properties of practical thrusters and measurements. The tuning of the magnitude and activity of the limit cycle is a common problem in the engineering practice [Sid97, Kro05], and could be addressed by varying the control gains, the cut-off frequencies of the filters, the deadzone, and the sampling rates of the control and the PWM, based on a trade-off between accuracy and consumed fuel. The main qualitative effect of the limit cycle is that, during the pre-contact phase, the consumed fuel of the Whole-Body controllers C3 and C5 is not exactly zero – as it was established in the

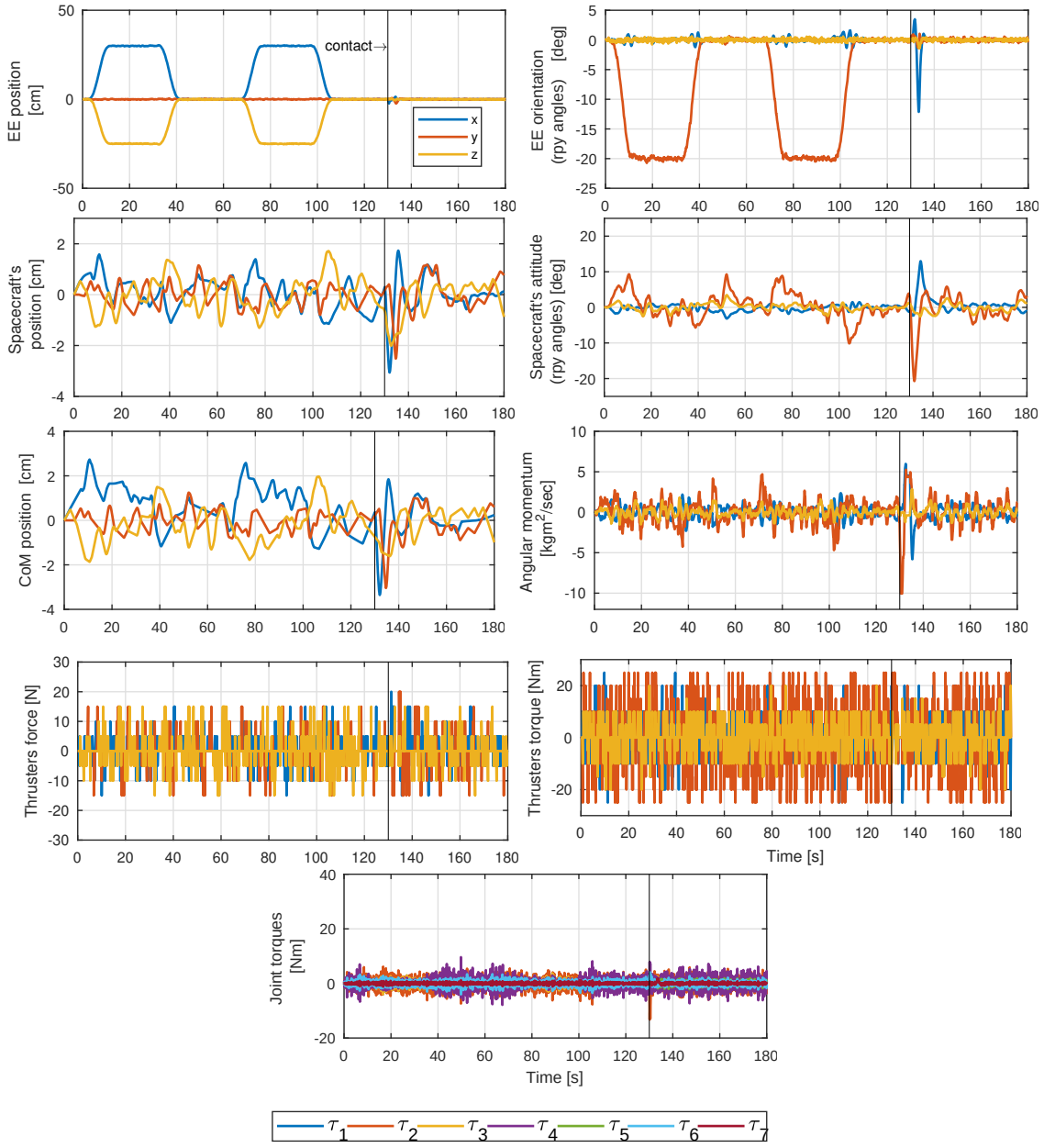

Figure 7.7.: Performance of Free-Flying controller with measurement and real thrusters models.

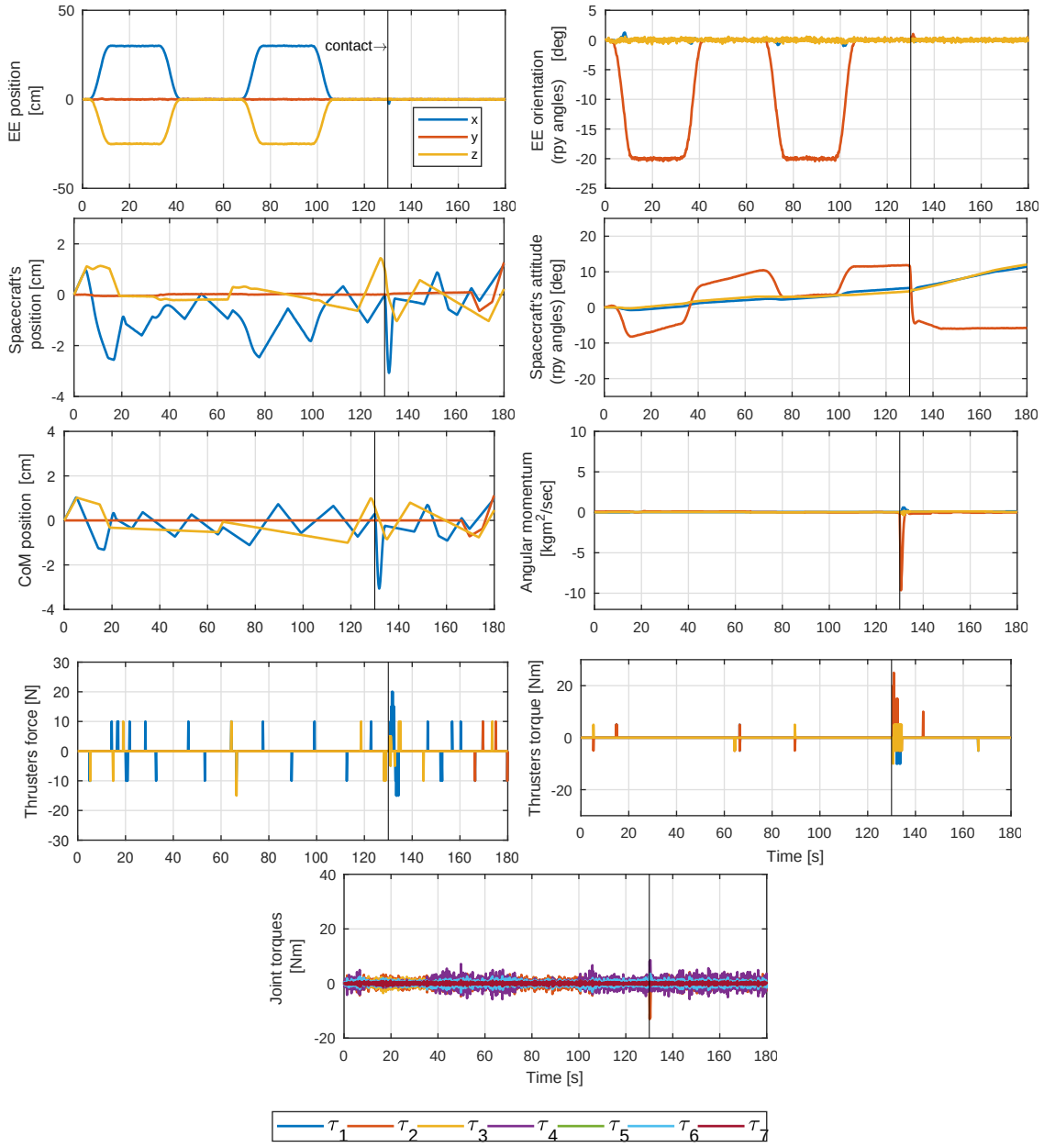

Figure 7.8.: Performance of controller C3 with measurement and real thrusters models.

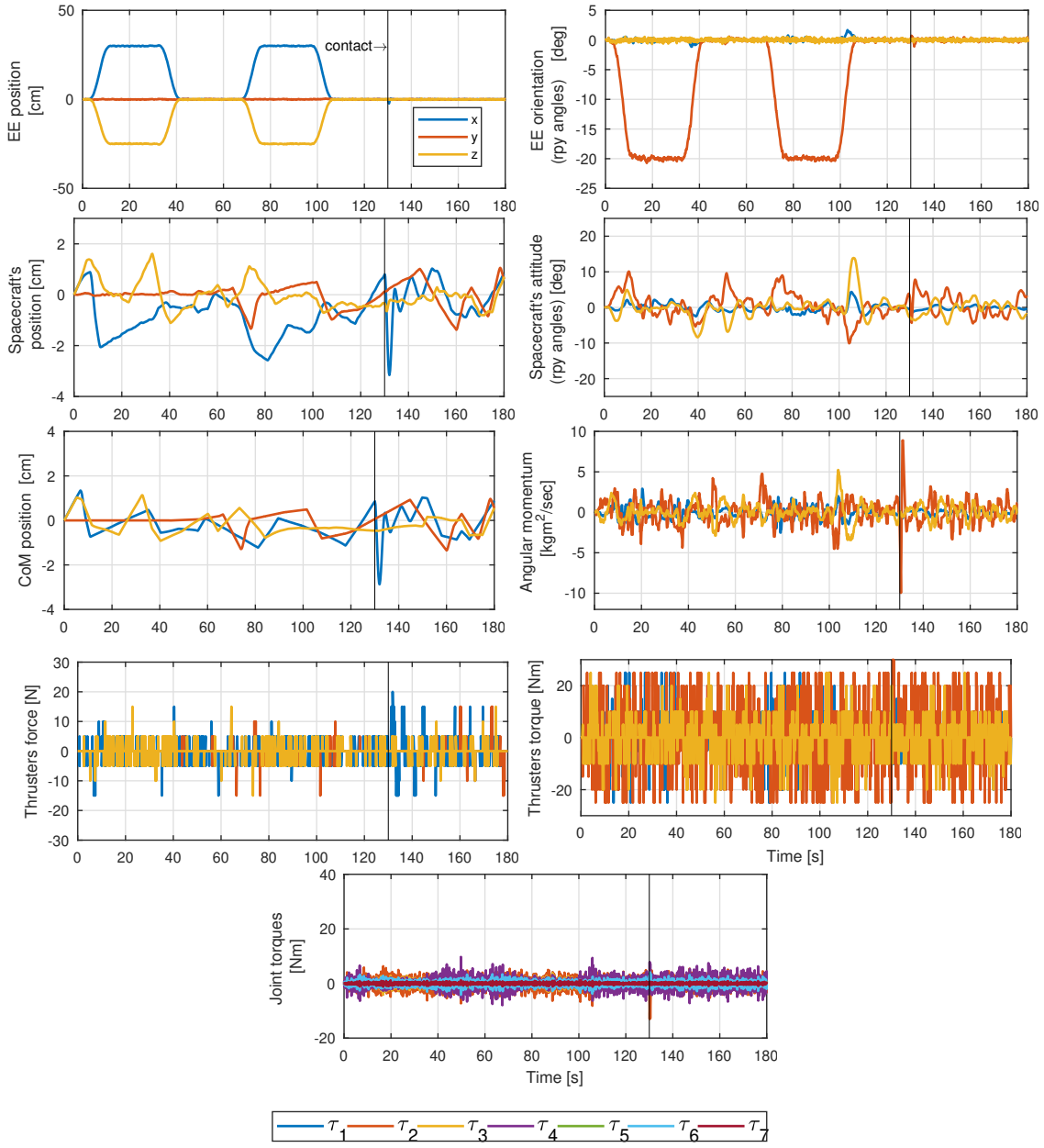

Figure 7.9.: Performance of controller C4 with measurement and real thrusters models.

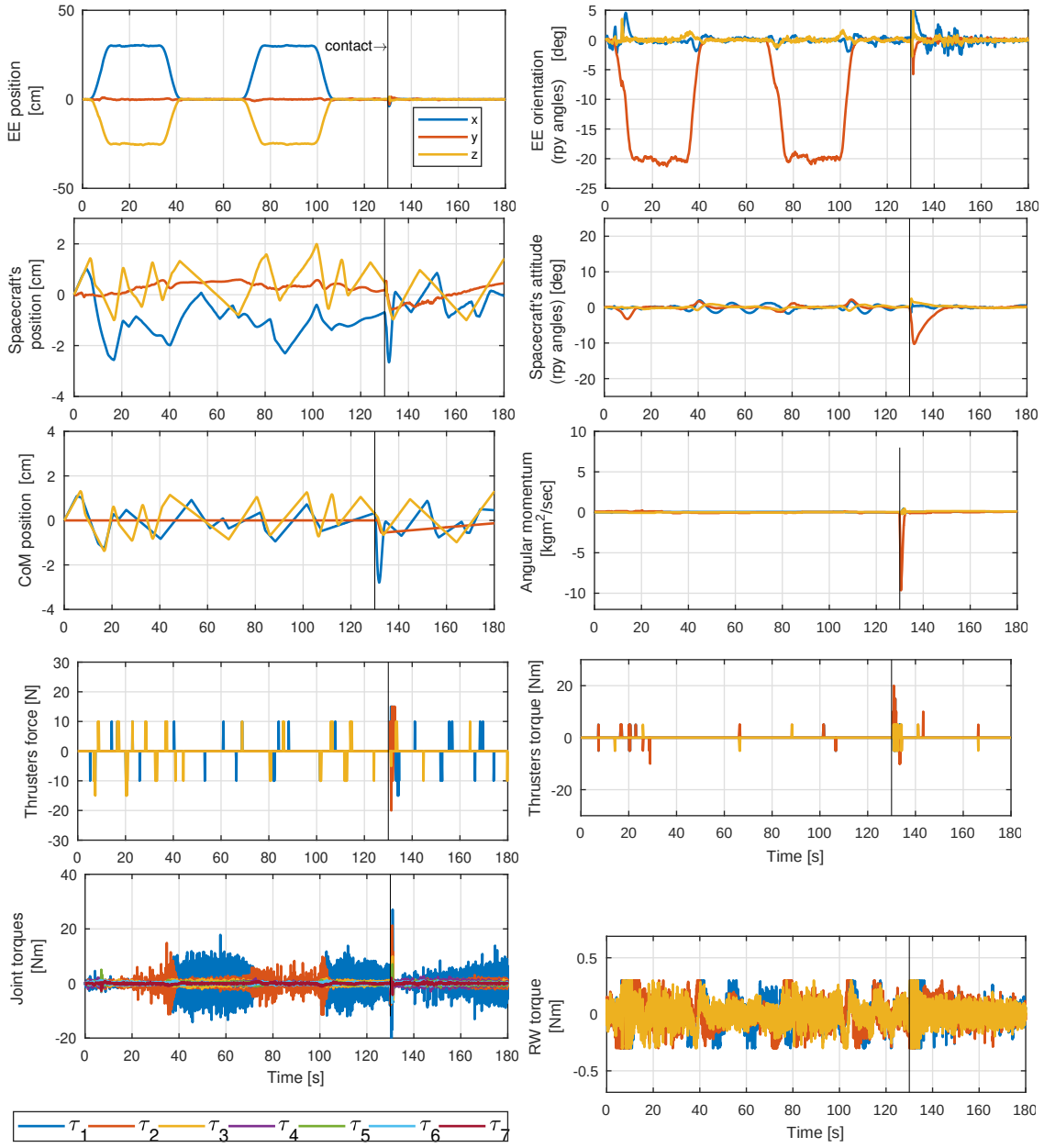

Figure 7.10.: Performance of controller C5 with measurement and real thrusters models.

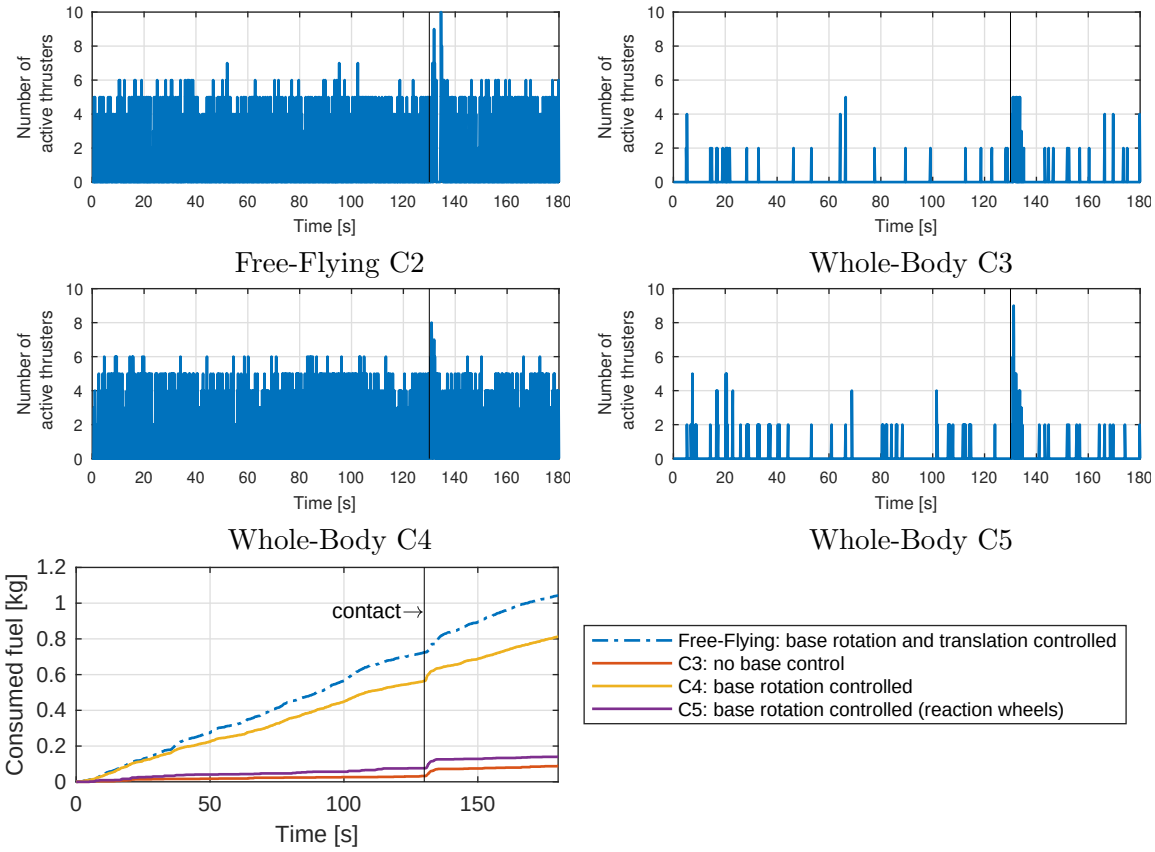

Figure 7.11.: Comparison of the thrusters usage and the consumed fuel for the controller C3, C4, C5, and FreeFlying.

ideal simulation – but a small amount of fuel is employed. However, this does not alter the main conclusions regarding the comparison of the fuel consumption of the controllers, which still remains considerably less for the Whole-Body controllers C3 and C5.
Thus, the conclusions regarding the consumed fuel drawn during the ideal simulation of the pre-contact phase (see Section 7.1.1) were confirmed in the case of measurement models and representative thrusters system. Namely, the Whole-Body control approach reduces the fuel consumption compared to a Free-Flying one (e.g., the Free-Flying controller C2). Remark that, in turn, the reduced fuel consumption translates into reducing the fuel consumption and the effects of plume impingement. Similarly, the conclusions regarding the momentum drift drawn during the ideal simulation of the post-contact phase (see Section 7.1.1) were confirmed in the case of real thrusters and measurement models: the Whole-Body control approach allows solving the problem of the fast drift of a Free-Floating one (e.g., the Free-Floating controller C1) after contact. For the Whole-Body controller C3 a residual drift still happens but is considerably smaller than a free-floating strategy. Note that, to ensure safety, the controller could be still extended with a box-type virtual fixture on the attitude.

As last conclusive remarks, note that the translational ($\boldsymbol{K}_c$ and $\boldsymbol{K}_{b,tras}$) gains in Table 7.1 associated to the control of the position of the CoM and of the base, were the same for the simulation of all controllers. The same holds for the end-effector gains ($\boldsymbol{K}_{e,tras}$ and $\boldsymbol{K}_{e,rot}$). It should be mentioned that for a more detailed investigation of the performance, different gains for each controller shall be used because the inertia of the allocation space is different for the different controllers. However, by numerical investigation it was revealed that the translational sub-block and the end-effector sub-block of the inertia associated to all controllers are similar; therefore, using same gains for the comparison is a realistic approximation. The same consideration applies for the rotational inertia $\boldsymbol{K}_{b,rot}$ of the Free-Flying controller C2 and the Whole-Body controller C4, whereas the rotational inertia of the Whole-Body controller C5 is considerably higher than the others; for this reason a higher rotational gain is necessary for the Whole-Body controller C5. Note that the torque commanded to the reaction wheels is well within the saturation limits; therefore the higher gain used is realistic. Furthermore, varying $\boldsymbol{K}_{b,rot}$ does not affect the fuel consumption of the Whole-Body controller C5, as the task is realized by the coordinated action of joints and reaction wheels – which require only electrical power –, and not by the thrusters.

Finally, it was observed during simulation that the Whole-Body controller C5 is more prone to singularity than the other controllers. This is linked to the chosen decomposition of the internal space, which involves the use of an internal base angular velocity which is in the nullspace of the end-effector internal velocity (see (6.4) and (C.25)). A different decomposition of the internal space with better singularity distribution might be possible, and is devoted to future work.

7.3. Summary

In this chapter, an extensive investigation and validation of the controllers (C1)-(C5) reported in the thesis was performed.

First, a comparison of the controllers was carried out considering a simplified simulation with ideal actuators and measurements. The aim of this simulation was to investigate the different functional behavior of the controllers, and to point out the advantages of the Whole-Body controllers compared to the Free-Floating and Free-Flying controllers. Then,

a validation was carried out by means of a numerical simulation modeling a realistic system of thrusters, realistic measurements models, and joint friction. By means of this simulation, it was validated that whole-body controllers can be applied considering realistic uncertainties of the measurements and of the spacecraft actuation, and that they reduce the use of the thrusters and the fuel consumption compared to the Free-Flying strategy (C2).

In the next chapter, a hardware validation is carried out to validate the controllers considering a real manipulator.

CHAPTER 8

Validation via hardware experiments

In this chapter, the Whole-Body controllers are validated via hardware experiments. To get the most insight about the overall rationale of the Whole-Body control approach, the experimental results are shown in an incremental way which builds up onto the different aspects involved. The aim of the experiments is to

- show the limitation of a purely free-floating strategy during a post-contact phase,
- analyze the benefits of the momentum dumping and CoM control tasks during a post-contact phase;
- analyze the features of the partial thrusters-decoupled actuation during a pre-contact phase;
- validate the applicability of the Whole-Body control approach with a real arm during pre- and post-contact phases,

In Section 8.1, the hardware facility is described. The experimental results for the Whole-Body controller C3, C4, and C5 are shown in Section 8.2, Section 8.3, and Section 8.4, respectively.

8.1. Description of experimental facility

The experiments were conducted on the On-Orbit Servicing Simulator (OOS-Sim) experimental facility [ADSR$^+$15] at the DLR Robotics and Mechatronics Center.

The OOS-Sim is a Hardware-in-The-Loop (HIL) simulator, which enables the testing of control algorithms for orbital robots on ground before their actual employment in orbit. Fig. 8.1 shows a general view of the OOS-SIM facility. The system consists of four main actors: the servicer simulation manipulator, the test manipulator, the target simulation manipulator, and an on-ground control station; the test manipulator is mounted on the servicer simulation manipulator.

A system overview with the main hardware elements and their respective interfaces is shown in Fig. 8.2. The figure highlights the elements that compose the simulation facility and the mission-representative hardware elements. Based on this scheme, the on-ground

Figure 8.1.: The On-Orbit Servicing Simulator at DLR Robotics and Mechatronics Center.

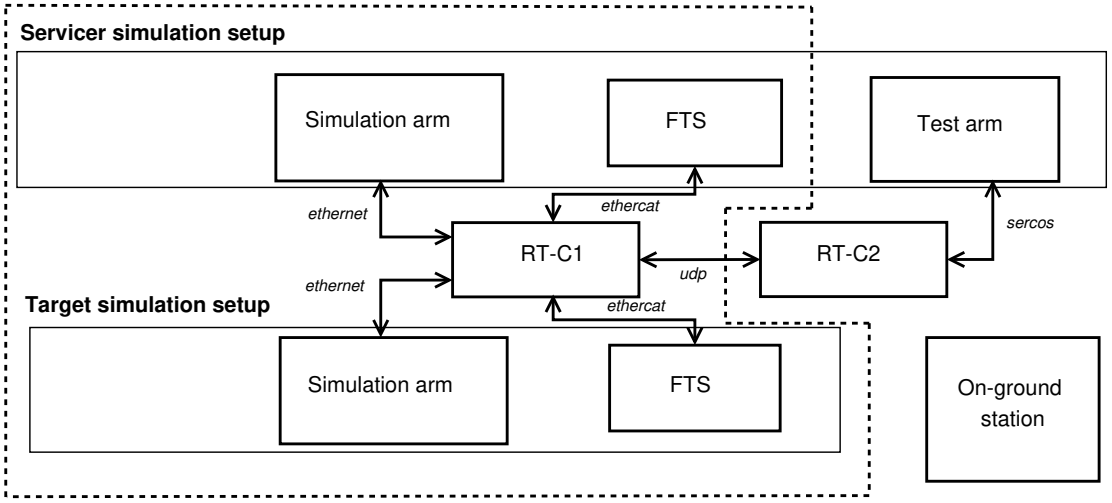

Figure 8.2.: System overview. The dotted line divides simulation- and mission-related elements.

	Name	DOF	Interface	Sampling time
Servicer simulation arm	KUKA KR120	6	Ethernet	4 ms
Target simulation arm	KUKA KR120	6	Ethernet	4 ms
Test arm	LWR 4+	7	Sercos	1 ms
Gripper	Robotic 3f	4+8	Ethercat	1 ms

Table 8.1.: Description of the robotic elements used in the OOS-SIM.

station, the test arm, and the main control CPU (RT-C2) are regarded as mission-related hardware.

A Force Torque Sensor (FTS) is mounted both on the servicer and on the target simulation arms; the FTSs are used for the simulation of the physical interaction between the robots. The RT-C1 is a real-time computer running at 4ms. It computes the simulated servicer and target motion whose outputs (position and orientation signals in the Cartesian space) are commanded to simulation manipulators; the real time integration of the later defined dynamics (8.2) and (8.3) takes place in this computer. The RT-C2 is a real-time computer running at 1ms; this computer is the actual robot control CPU of the test arm. Table 8.1 provides details of the robots involved in the facility.

The orbital microgravity conditions in the test arm are replicated by actively compensating the gravity torques in the joints of the test arm based on an gravity model. The servicer and target simulation manipulators reproduce the motion of the servicer and target spacecrafts based on the real-time integration of a model. With this system, the dynamics is simulated taking into account real sensor noise, time delay, control discretization, model uncertainties and modeled dynamics of the test manipulator. On the other hand, the base dynamics is based on a model, whose parameters can be adapted depending on the specific scenario.

The test arm is commanded via a joint impedance interface; the joint torques commanded to the test arm consist in the joint torques commanded by the controller of the orbital robot, plus the online model-based gravity torques acting in the test arm in the on-ground facility; namely, by denoting $\boldsymbol{\tau}_m^{og} \in \mathbb{R}^7$ the joint torques commanded to the test arm in the on ground facility, they are given by

$$\boldsymbol{\tau}_m^{og} = \boldsymbol{\tau}_m + \boldsymbol{g}(\hat{\boldsymbol{q}}_m), \tag{8.1}$$

where $\boldsymbol{g}(\hat{\boldsymbol{q}}_m) \in \mathbb{R}^7$ are the model-based gravity torques computed based on the current joint measurements.

The scope of the present thesis is the development of coordinated controllers with a specific focus on the coordination of the actuators of the orbital robot. Thus, the main aim of the validation is the applicability of the controllers on an orbital robot *alone*; for this reason, only the servicer integration was activated during the experimental validation, and the target is at rest.

The servicer manipulator is commanded via a joint admittance interface; the joint angles commanded to the servicer arm are computed based on the integration of the model of the orbital robot under investigation. For the validation of controllers that do not employ reaction wheels, the integration is performed based on the dynamics model (2.62), with the addition of a contact wrench at the end-effector. In particular, given measurements of the joint angles $\hat{\boldsymbol{q}}_m$, and their time-derivatives $\dot{\hat{\boldsymbol{q}}}_m$ and $\ddot{\hat{\boldsymbol{q}}}_m$, the motion of the base of the orbital robot is obtained by integration of the first row of (2.62), as

$$\dot{\boldsymbol{\nu}}_b = \boldsymbol{M}_b(\hat{\boldsymbol{q}}_m)^{-1}\Big(-\boldsymbol{M}_{bm}(\hat{\boldsymbol{q}}_m)\ddot{\hat{\boldsymbol{q}}}_m - \boldsymbol{C}_b(\hat{\boldsymbol{q}}_m, \boldsymbol{\nu}_b, \dot{\hat{\boldsymbol{q}}}_m)\boldsymbol{\nu}_b - \boldsymbol{C}_{bm}(\hat{\boldsymbol{q}}_m, \boldsymbol{\nu}_b, \dot{\hat{\boldsymbol{q}}}_m)\dot{\hat{\boldsymbol{q}}}_m + \boldsymbol{\mathcal{F}}_b + \boldsymbol{A}_{eb}(\hat{\boldsymbol{q}}_m)^T\hat{\boldsymbol{\mathcal{F}}}_e^{ext}\Big), \tag{8.2}$$

where $\hat{\boldsymbol{\mathcal{F}}}_e^{ext} \in \mathbb{R}^6$ is the measured contact wrench at the end-effector. For the validation of controllers that employ reaction wheels, the integration is performed based on the dynamics model (2.58), with the addition of a contact wrench at the end-effector. In particular, given measurements of the joint angles $\hat{\boldsymbol{q}}_m$, and their time-derivatives $\dot{\hat{\boldsymbol{q}}}_m$ and

$\ddot{\hat{\boldsymbol{q}}}_m$, the motion of the base and the reaction wheels is obtained by integration of the first two rows of (2.58), as

$$\begin{bmatrix}\dot{\boldsymbol{\nu}}_b\\ \ddot{\boldsymbol{q}}_w\end{bmatrix}=\begin{bmatrix}\boldsymbol{M}_b(\hat{\boldsymbol{q}}_m) & \boldsymbol{M}_{bw}\\ \boldsymbol{M}_{bw}^T & \boldsymbol{M}_w\end{bmatrix}^{-1}\Big(-\begin{bmatrix}\boldsymbol{M}_{bm}(\hat{\boldsymbol{q}}_m)\\ \boldsymbol{0}\end{bmatrix}\ddot{\hat{\boldsymbol{q}}}_m-\begin{bmatrix}\boldsymbol{C}_b(\hat{\boldsymbol{q}}_m,\boldsymbol{\nu}_b,\dot{\boldsymbol{q}}_w,\dot{\hat{\boldsymbol{q}}}_m) & \boldsymbol{C}_{bw}(\hat{\boldsymbol{q}}_m,\boldsymbol{\nu}_b,\dot{\boldsymbol{q}}_w,\dot{\hat{\boldsymbol{q}}}_m)\\ \boldsymbol{C}_{wb}(\hat{\boldsymbol{q}}_m,\boldsymbol{\nu}_b,\dot{\boldsymbol{q}}_w,\dot{\hat{\boldsymbol{q}}}_m) & \boldsymbol{C}_w(\hat{\boldsymbol{q}}_m,\boldsymbol{\nu}_b,\dot{\boldsymbol{q}}_w,\dot{\hat{\boldsymbol{q}}}_m)\end{bmatrix}\begin{bmatrix}\boldsymbol{\nu}_b\\ \dot{\boldsymbol{q}}_w\end{bmatrix}$$
$$-\begin{bmatrix}\boldsymbol{C}_{bm}(\hat{\boldsymbol{q}}_m,\boldsymbol{\nu}_b,\dot{\boldsymbol{q}}_w,\dot{\hat{\boldsymbol{q}}}_m)\\ \boldsymbol{C}_{wm}(\hat{\boldsymbol{q}}_m,\boldsymbol{\nu}_b,\dot{\boldsymbol{q}}_w,\dot{\hat{\boldsymbol{q}}}_m)\end{bmatrix}\dot{\hat{\boldsymbol{q}}}_m+\begin{bmatrix}\boldsymbol{\mathcal{F}}_b\\ \boldsymbol{\tau}_w\end{bmatrix}+\begin{bmatrix}\boldsymbol{A}_{eb}(\hat{\boldsymbol{q}}_m)^T\\ \boldsymbol{0}\end{bmatrix}\hat{\boldsymbol{\mathcal{F}}}_e^{ext}\Big). \quad (8.3)$$

The pose resulting from the integration of $\boldsymbol{\nu}_b$ in (8.2) or (8.3) is then commanded to the end-effector of the servicer manipulator via an inverse-kinematics control.
In the experimental facility, $\hat{\boldsymbol{\mathcal{F}}}_e^{ext}$ can be measured by using the target-mounted FTS, in case of contact of the end-effector with the target, or can be approximately reconstructed by using the measurements of the torques and the angles in the joints of the test arm, in case of contact on the end-effector with objects different than the target. In the experimental campaign performed herein, the second strategy was used in order to more easily give contacts manually by using a rod. The external wrench on the end-effector is approximately reconstructed as

$$\hat{\boldsymbol{\mathcal{F}}}_e^{ext}\approx\boldsymbol{J}_{em}(\hat{\boldsymbol{q}}_m)^{\#T}\left(\hat{\boldsymbol{\tau}}_m^{og}-\boldsymbol{\tau}_m^{og}\right), \quad (8.4)$$

where $\hat{\boldsymbol{\tau}}_m^{og}\in\mathbb{R}^7$ denotes the torque measured in the joints of the test arm. Note that, in the present work, the external wrench is used here only as a mean to inject momentum into the system for the validation of the controllers during the post-contact phase, and *not* to validate the controllers during the contact phase; furthermore, note that all controllers derived herein do not require any external force measurement. Thus, no exact reconstruction is needed for the validation, and an approximate reconstruction fulfills the purposes of the present thesis.

The states used by the controllers are reconstructed based on servicer and test arms: the base and the end-effector poses are obtained from the forward kinematics of the simulator and test arms, and the associated velocities are obtained by time differentiation; the CoM and angular momentum states are obtained based on the measurements of the base state and the joints, and on the inertia model, i.e., by using (2.43).

In the experiments reported in the following, the dynamics parameters in the model-based simulation and in the on-board model of the controllers of the base were:

$$m^{(b)}=150\,\mathrm{kg},\quad {}_b\boldsymbol{o}_{bc_b}=\begin{bmatrix}0 & 0 & 0\end{bmatrix}\mathrm{m},\quad \boldsymbol{I}_b^{(b)}=\begin{bmatrix}21.84 & -2.25 & -1.2\\ -2.25 & 14.96 & -0.6\\ -1.2 & -0.6 & 18.88\end{bmatrix}\mathrm{kgm}^2.$$

Three reaction wheels are modeled; they are oriented around the x,y,z axes of the spacecraft, and their dynamic parameters were

$$m^{(j)}=4.7\,\mathrm{kg},\quad {}_j\boldsymbol{o}_{jc_j}=\begin{bmatrix}0 & 0 & 0\end{bmatrix}\mathrm{m},\quad \boldsymbol{I}_j^{(j)}=\begin{bmatrix}0.0252 & 0 & 0\\ 0 & 0.0252 & 0\\ 0 & 0 & 0.0425\end{bmatrix}\mathrm{kgm}^2,\quad j\in j_w.$$

The parameters of the test arm used in the model-based simulation of the base, in the on-ground gravity compensation, and in the on-board model of the controllers, were obtained by an identification of the test arm performed with its base fixed.

8.2. Experimental investigation of the Whole-Body controller C3

To analyze the benefits of the momentum dumping and CoM control tasks during a post-contact phase, experiments are conducted in which the end effector is commanded in presence of an accumulated momentum.
In the experiments, the momentum is induced in the system by an external contact on the end effector. The contact is provided manually by using a rod. It shall be clear that the contact is given only as a convenient mean to excite the momentum of the system to study the post-contact behavior,and *not* to analyze the behavior of the system during contact.
The experiments show first the limitation of a free-floating strategy during a post-contact situation; second, they incrementally show the benefits of the momentum dumping and the CoM control tasks; finally, they provide evidence of the applicability of the Whole-Body controller C3 with a real arm. The following experiments were conducted

1. Single-contact experiment with a transposed-Jacobian Free-Floating controller, to show the drift limitation of the free-floating control strategy;

2. Single-contact experiment with a Whole-Body controller implementing only a momentum-dumping task, to show the effectiveness of a momentum-dumping task in solving the drift limitation of the free-floating control strategy;

3. Multiple-contacts experiment with a Whole-Body controller implementing only a momentum dumping task, to show the workspace limitation of a momentum-dumping task alone;

4. Multiple-contacts experiment with the Whole-Body controller C3, to show the benefits of a simultaneous momentum dumping and CoM control task, and thus to achieve a strategy which solves both the drift and the workspace limitation.

In all hardware experiments, the nonredundant versions of the controllers were validated, which are obtained by setting the null-space tasks, e.g. $\boldsymbol{\varsigma}_n$, $\boldsymbol{\varsigma}_n^{\oplus}$, $\boldsymbol{\varsigma}_n^{int}$, to zero. The transposed-Jacobian Free-Floating controller executed in the first experiment is a subcase of the nonredundant Free-Floating controller C1 (see equations (3.9b) and (3.14)) when the compensation of the momentum disturbance at the end-effector is deactivated. It is given by the equations

$$\boldsymbol{\mathcal{F}}_b = \mathbf{0}, \tag{8.5a}$$

$$\boldsymbol{\tau}_m = \boldsymbol{J}_{em}^{*}(\hat{\boldsymbol{q}}_m)^T \left(-\boldsymbol{J}_{\tilde{x}_e}(\tilde{\boldsymbol{x}}_e)^T \boldsymbol{K}_e \tilde{\boldsymbol{x}}_e - \boldsymbol{D}_e \tilde{\boldsymbol{\nu}}_e\right). \tag{8.5b}$$

The Whole-Body controller executed in the second and third experiments is a subcase of the nonredundant Whole-Body controller C3 (see (5.6) and (5.8)) when the CoM control task is deactivated. It is given by the equations

$$\boldsymbol{\mathcal{F}}_b = -\boldsymbol{A}_{cb}(\boldsymbol{R}_b, \boldsymbol{q}_m)^T \boldsymbol{D}_h \tilde{\boldsymbol{h}}_c, \tag{8.6a}$$

$$\boldsymbol{\tau}_m = \boldsymbol{J}_{em}^{int}(\hat{\boldsymbol{q}}_m)^T \left(-\boldsymbol{J}_{\tilde{x}_e}(\tilde{\boldsymbol{x}}_e)^T \boldsymbol{K}_e \tilde{\boldsymbol{x}}_e - \boldsymbol{D}_e \tilde{\boldsymbol{\nu}}_e\right). \tag{8.6b}$$

The Whole-Body controller executed in the fourth experiment is the nonredundant Whole-Body controller C3. It is given by the equations

$$\boldsymbol{\mathcal{F}}_b = \boldsymbol{A}_{cb}(\boldsymbol{R}_b, \boldsymbol{q}_m)^T \left(-\boldsymbol{S}_v^T \boldsymbol{K}_c \tilde{\boldsymbol{x}}_c - \boldsymbol{D}_h \tilde{\boldsymbol{h}}_c\right), \tag{8.7a}$$

$$\boldsymbol{\tau}_m = \boldsymbol{J}_{em}^{int}(\hat{\boldsymbol{q}}_m)^T \left(-\boldsymbol{J}_{\tilde{x}_e}(\tilde{\boldsymbol{x}}_e)^T \boldsymbol{K}_e \tilde{\boldsymbol{x}}_e - \boldsymbol{D}_e \tilde{\boldsymbol{\nu}}_e\right). \tag{8.7b}$$

The stiffness gains used were $\boldsymbol{K}_e = \text{blkdiag}(\boldsymbol{K}_{e,tras}, \boldsymbol{K}_{e,rot})$ for the end-effector, where $\boldsymbol{K}_{e,tras} = 1000\boldsymbol{E}\,\text{N}\,\text{m}^{-1}$, $\boldsymbol{K}_{e,rot} = 70\,\boldsymbol{E}\,\text{N}\,\text{m}\,\text{rad}^{-1}$, and $\boldsymbol{K}_c = 700\boldsymbol{E}\,\text{N}\,\text{m}^{-1}$ for the CoM. The end-effector gains were designed using the method in [Ott08, p.36] based on the inertia in the initial configuration. The momentum gain was $\boldsymbol{D}_h = \text{blkdiag}(\boldsymbol{D}_p, \boldsymbol{D}_l)$, where the angular momentum gain was $\boldsymbol{D}_l = 16\boldsymbol{E}\,\text{s}^{-1}$, the linear momentum gain was $\boldsymbol{D}_p = 20.28\boldsymbol{E}\,\text{s}^{-1}$ in the second and third experiments, and it was $\boldsymbol{D}_p = 6.47\boldsymbol{E}\,\text{s}^{-1}$ in the fourth experiment to yield a critical damping of the CoM response.

8.2.1. Experimental results: single contact with free-floating control

In the first experiment, a single contact was given on the end-effector, and the behavior of the Free-Floating controller during the post-contact phase was analyzed.
A snapshot sequence of the first experiment is shown in Fig. 8.3. The time responses of the linear and angular momenta, the position of the end-effector, the position and attitude of the spacecraft, and the joint angles, are shown in Fig. 8.4.

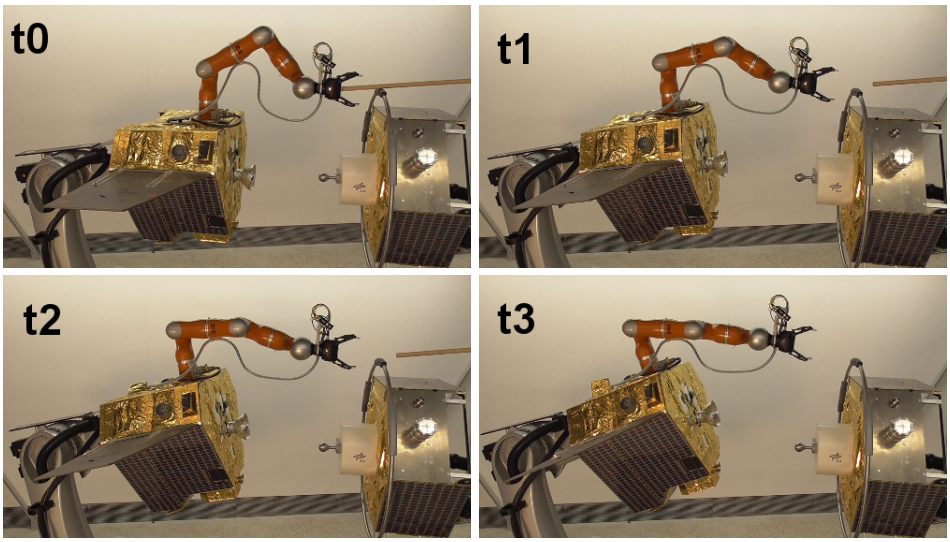

Figure 8.3.: Experiment 1: snapshot sequence of a free-floating robot in response to an accidental contact. The base starts to drift, the robot reaches a singular configuration and the capture operation is compromised.

At $t_0 = 11\,\text{s}$ a contact was given at the end-effector. It can be observed in Fig. 8.3 that, after contact, nonzero linear and angular momenta were induced in the system, and that they remained constant during the post-contact phase because no thrusters were used by the free-floating strategy. Accordingly, the nonzero momenta caused an unstoppable drift of the system in the inertial space; more specifically, a drift of the spacecraft position and attitude, as well as the joint angles, is observed in Fig. 8.3. In particular, the joint angles drifted between t_0 and t_2; at $t_2 = 19\,\text{s}$ they stopped in an almost outstretched configuration, as a consequence of the low manipulability and of the static friction in the joints; then, at $t_3 = 21\,\text{s}$ the arm completely outstretched; finally, after t_3 the system kept drifting in an outstretched configuration.
Observe also how this led to a failure of the end-effector task within few seconds. In Fig. 8.3 it can be observed that between t_0 and t_2, the controller succeeded in keeping the end-effector around the desired position with acceptable error; however, after the

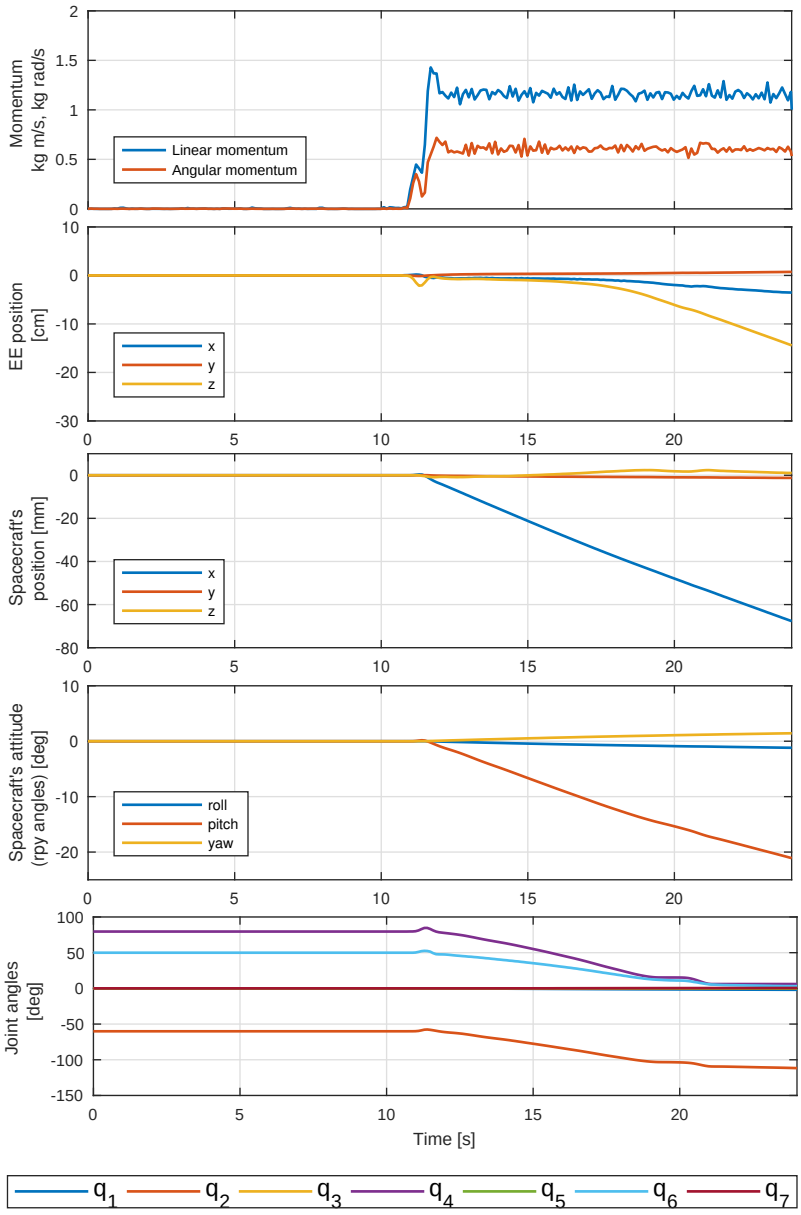

Figure 8.4.: Experiment 1: time response for free-floating control during a post-contact phase.

arm got stuck at t_2, the end-effector started to drift considerably, thus compromising the end-effector task.

8.2.2. Experimental results: single contact with momentum dumping task

To solve the drift of the free-floating strategy, a momentum dumping task was employed and the same single-contact experiment was repeated. A snapshot sequence of the first experiment is shown in Fig. 8.5, wherein $t_0 = 6.2\,\text{s}$, $t_1 = 7.5\,\text{s}$, $t_2 = 9\,\text{s}$, and $t_3 = 12\,\text{s}$. The time responses of the linear and angular momenta, the position of the end-effector, the position and attitude of the spacecraft, and the joint angles, are shown in Fig. 8.6. The commanded thrusters force and torque are shown in Fig. 8.7.

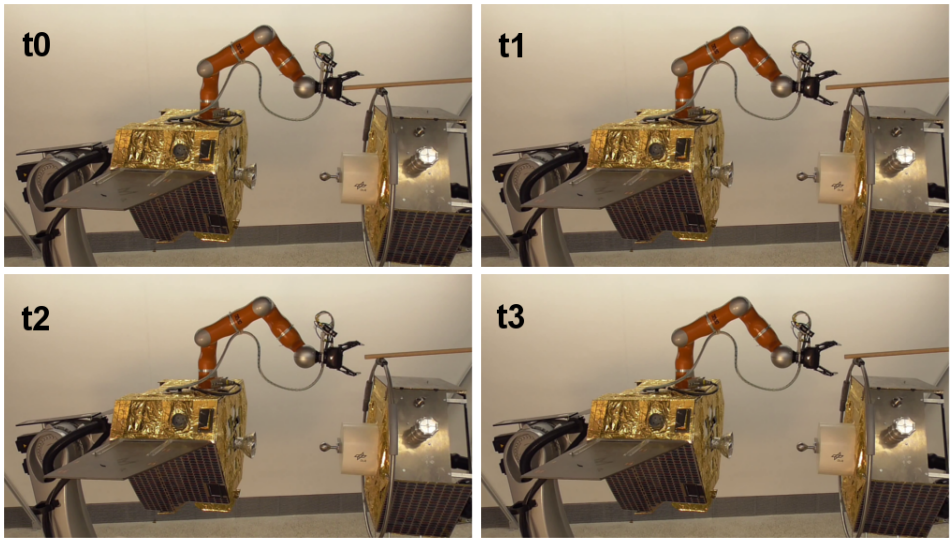

Figure 8.5.: Experiment 2: snapshot sequence of a robot implementing a momentum dumping task in response to an accidental contact. The base does not drift after contact, and it reaches a rest position; the arm remains in a favorable configuration and the capture operation can continue.

Fig. 8.5 shows that the momentum induced by the contact was successfully extracted from the system by the momentum dumping task. Accordingly, the drifts of the position and rotation of the base, as well as of the joint angles, were promptly stopped. The base position and base angle converged to new locations[1], whose values were ≈ 3 mm along x in position, and $\approx -1.5\,\text{deg}$ around y in rotation, respectively. For a 7DOF redundant arm without null-space control, the momentum dumping task alone is in theory not enough to entirely stabilize the joint motion, due to the remaining uncontrolled degree of freedom of the null space; however, in Fig. 8.6 it is possible to observe that, in practice, the drift of the joint angles was successfully stabilized by the joint action of the momentum dumping task and the natural viscous friction in the joints.
Regarding the end-effector, in Fig. 8.6 it is shown that after contact the desired position was restored, and the end-effector was kept in place during the entire time of the post-contact phase. This means that with the momentum dumping task, the system is not affected by the drift, and the end-effector operation can be continued without risk for an indefinite time.

[1] In Fig. 8.6 the same scale as in Fig. 8.4 is used to make a contrast with the big drift of free-floating.

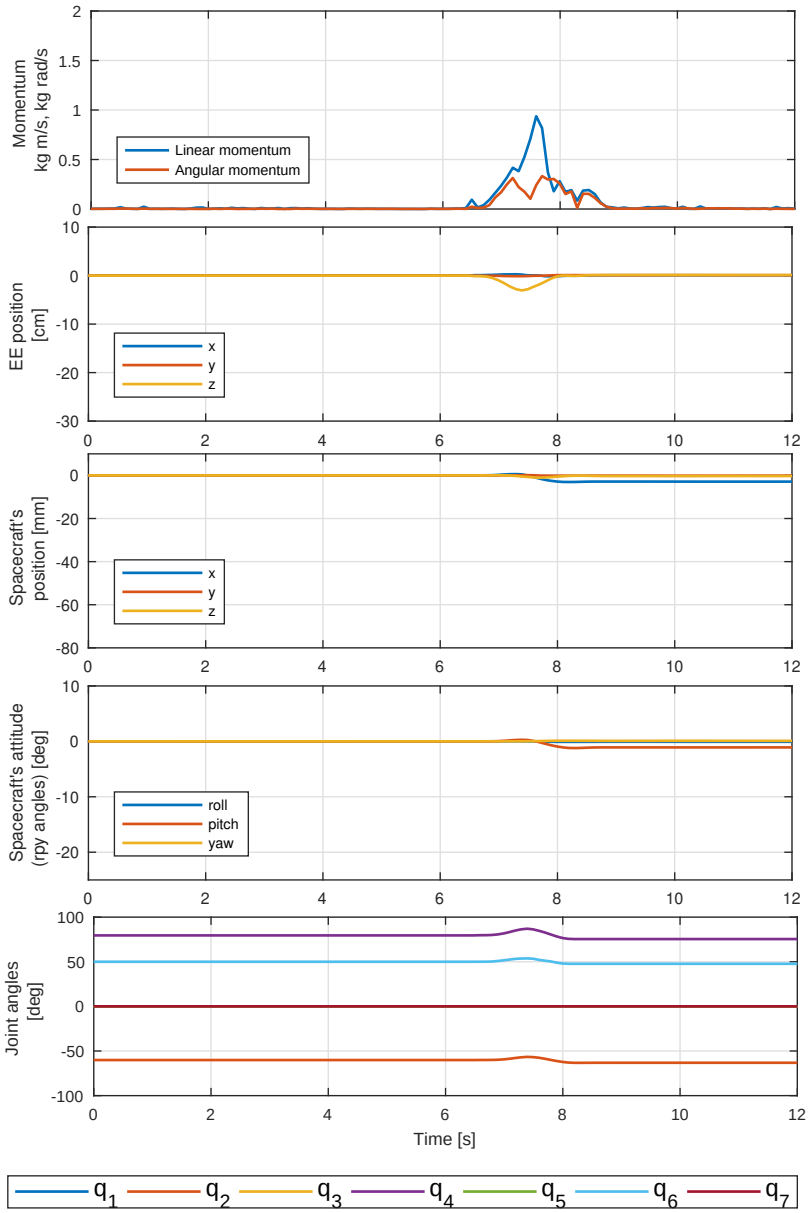

Figure 8.6.: Experiment 2: time response of a robot controller implementing a momentum-dumping task, during a post-contact phase.

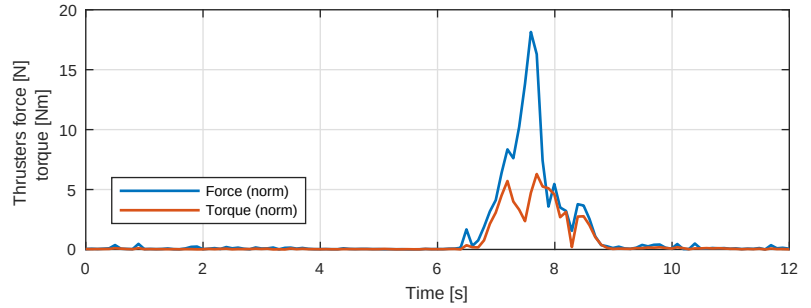

Figure 8.7.: Experiment 2: thrusters force and torque commanded by the momentum-dumping task, during a post-contact phase.

The satellite commanded forces and torques are shown in Fig. 8.7. The plot shows that the momentum-dumping was automatically activated as soon as the the momentum was excited by the contact. The command signal was relatively noisy, due to the momentum computation. However, the noise was filtered out by the low-pass nature of the satellite dynamics and no relevant noise oscillation of the attitude of the spacecraft happened.
For further information, notice in Fig. 8.6 that the momentum converged to zero in a first-order fashion after the contact was released. The speed of the convergence can be adapted by tuning the gain $\boldsymbol{D}_h$, taking into account the the saturation limits of the thrusters' system.

In conclusion, the experiments confirmed the effectiveness of the momentum dumping task in solving the drift limitation of the free-floating control.

8.2.3. Experimental results: multiple contacts with momentum dumping task

A momentum dumping task alone does not implement any restoring action of the global position of the system after the drift has been stopped. Such a situation may represent a limitation because, in case of repeated contact, the workspace may be found shifted in a unfavorable location. The aim of the experiment presented in this section is to investigate the above-mentioned workspace shift.

To portray the situation in which the robot accidentally or voluntarily collides with a heavy target satellite, a series of impulses is given manually to its end-effector by using a rod. In the experiment, the end-effector pose is regulated around a desired position w.r.t. the target object, while the linear and angular momenta are dumped from the system using the same controller of the previous section. The deterioration of the manipulation capability due to workspace shift is quantified by means of the following manipulability measure [UY01]:

$$\text{manipulability} = \sqrt{\det\left(\boldsymbol{J}_{em}^{int}(\hat{\boldsymbol{q}}_m)\boldsymbol{J}_{em}^{int}(\hat{\boldsymbol{q}}_m)^T\right)} \tag{8.8}$$

Fig. 8.8 shows the reconstructed external force at the end-effector, the position of the CoM, and the manipulability measure, respectively, after repeated impulses on the end-effector. Fig. 8.9 shows the position of the end-effector, and the linear and angular momenta.

In Fig. 8.9 it is shown that the momentum was successfully extracted from the system after each impulse. At the same time, the impulses induced a displacement in the CoM position, as seen in Fig. 8.8. Thanks to the dumping of the accumulated momentum in the system, the CoM position converged to new stationary positions. However, after each contact the CoM was displaced farther from the initial location. Accordingly, the manipulator was in a more stretched position, in an attempt to maintain the desired position. The displacements of the CoM after each impulse led to a deterioration of the workspace conditions. In particular, in Fig. 8.8 it is observed that the manipulability was reduced after each contact, resulting in a practically singular configuration around $t_{sing} = 140$ sec. As a matter of fact, Fig. 8.9 further shows that at t_{sing} the end-effector steady state error increased after every impulse due to the low manipulability. This is explained by the fact that the low commanded torques near the singularity were counterbalanced by the static friction in the joints. In this situation, the end-effector control was lost.
To better visualize the workspace displacement, a series of snapshots of the experiment at $t_0 = 0\,\text{sec}, t_1 = 110\,\text{sec}, t_2 = 170\,\text{sec}, t_3 = 220\,\text{sec}$ is shown in Fig. 8.10b. Additionally, in Fig. 8.10a a workspace rendering at the same instants is done based on the experimental

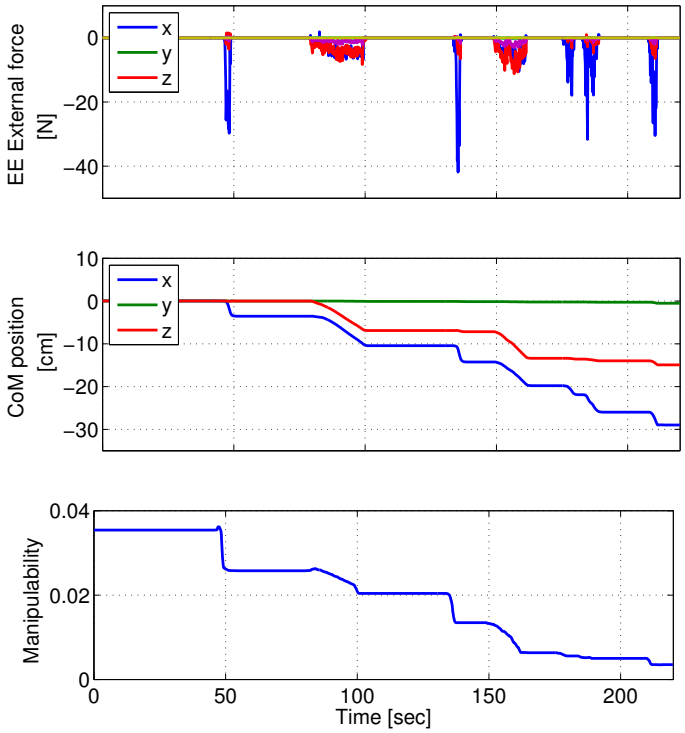

Figure 8.8.: Momentum Dumping Control - Workspace shift due to external contacts.

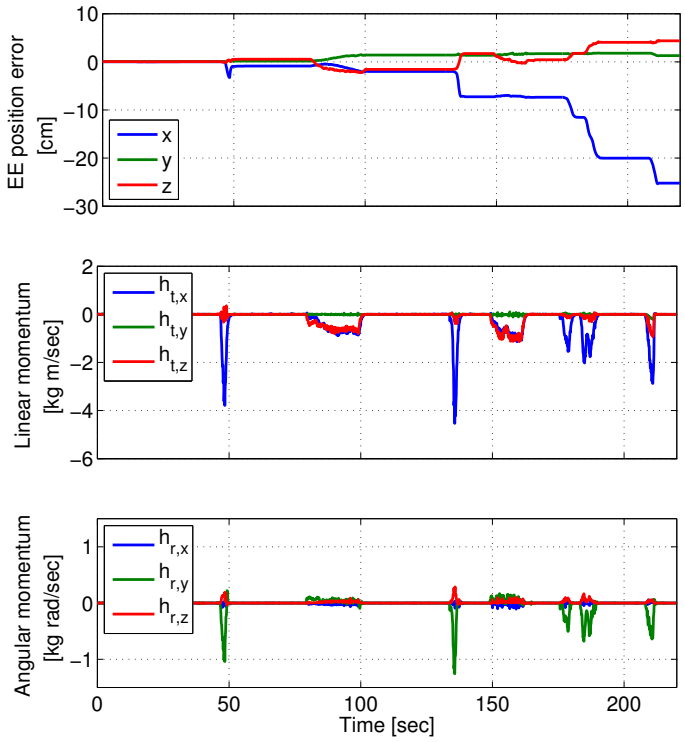

Figure 8.9.: Momentum Dumping Control - End effector position and momenta.

measurements of the pose of the spacecraft and the joint angles. The workspace shown therein is the Maximum Reachable Workspace [UY01] of the robot manipulator.

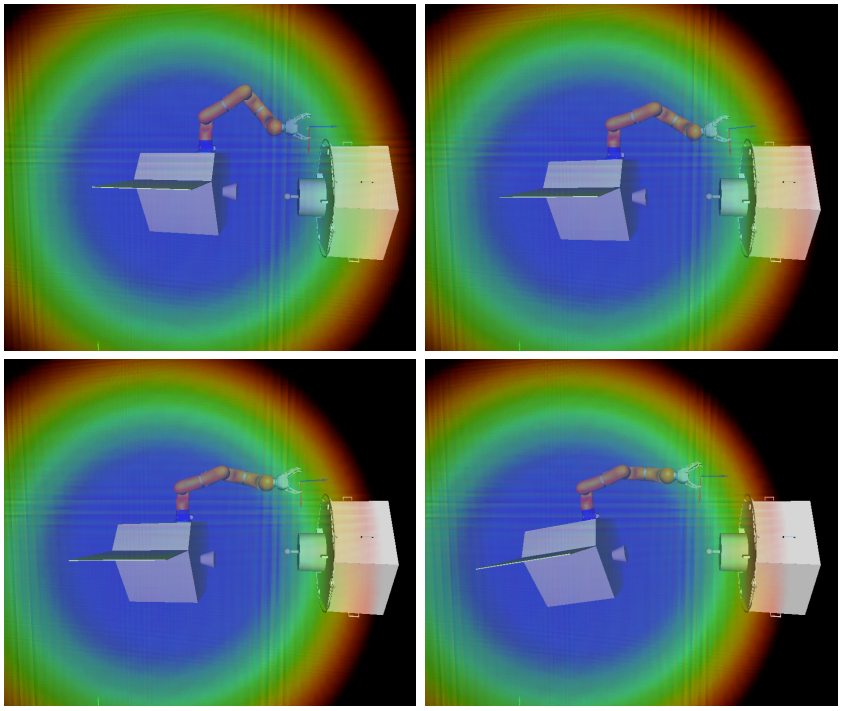

(a) Rendered workspace.

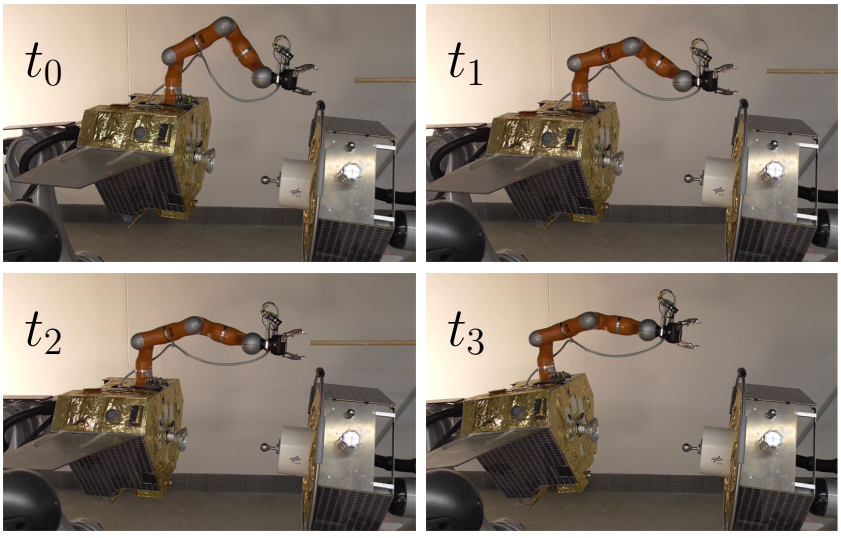

(b) Snapshots of the experiment

Figure 8.10.: Experiment 2: snapshot sequence of the response to repeated contact of a robot implementing a momentum dumping task.

Fig. 8.10 shows that after some contacts, the target satellite exited the reachable

workspace; in a practical scenario, a repositioning maneuver of the whole system would be needed to restore the favorable workspace location and recover the end-effector task. The correct workspace location is needed to accomplish a successful end-effector operation during the post-contact phase in case of repeated contact; in conclusion, the above-illustrated workspace shift is the main limitation of a momentum dumping strategy alone, and motivates the need of a further control action of the CoM of the whole-body that keeps the workspace in a favorable location;

8.2.4. Experimental results: multiple contacts with momentum dumping and CoM control tasks

An experiment is reported herein, which shows how a CoM control task, in additional to a momentum dumping task, allows solving the workspace shift in case of multiple contact. The experiment has the further purpose of confirming that the Whole-Body controller C3 can be applied on real hardware.
A similar series of impulses as in the previous experiment is manually given at the end-effector by using a rod; in addition to the previous experiment, contacts were given also along the y direction for more generality. Fig. 8.11 shows the reconstructed external force at the end-effector, the position of the CoM, and the manipulability measure, when the robot is controlled with the Whole-Body controller C3.

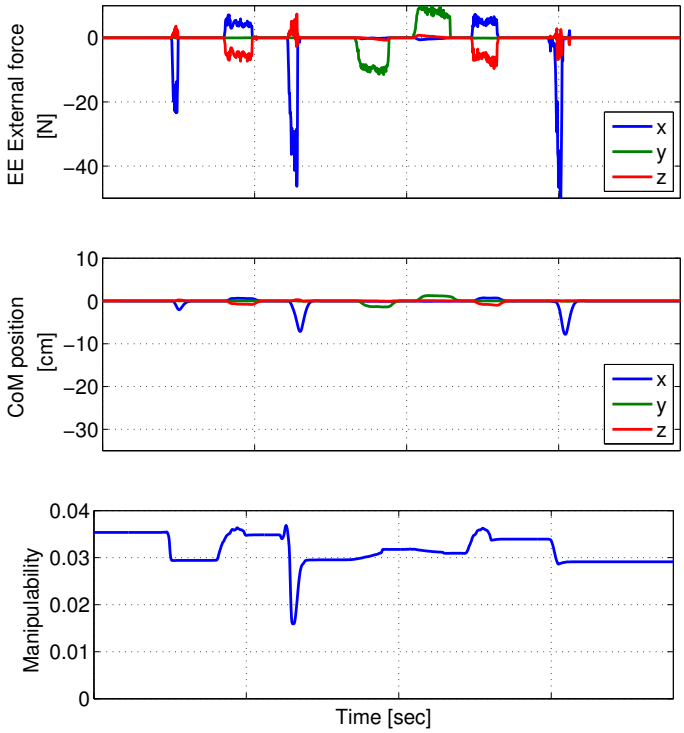

Figure 8.11.: CoM Control - Workspace restore after external contacts.

First, observe in Fig. 8.11 that after each contact the correct CoM location was restored to the initial value, as it was seeked at. Accordingly, the manipulability measure in Fig. 8.11 did not drop to zero, but remained around a favorable value thanks to the restored correct CoM-target location. Second, observe the end-effector position error in

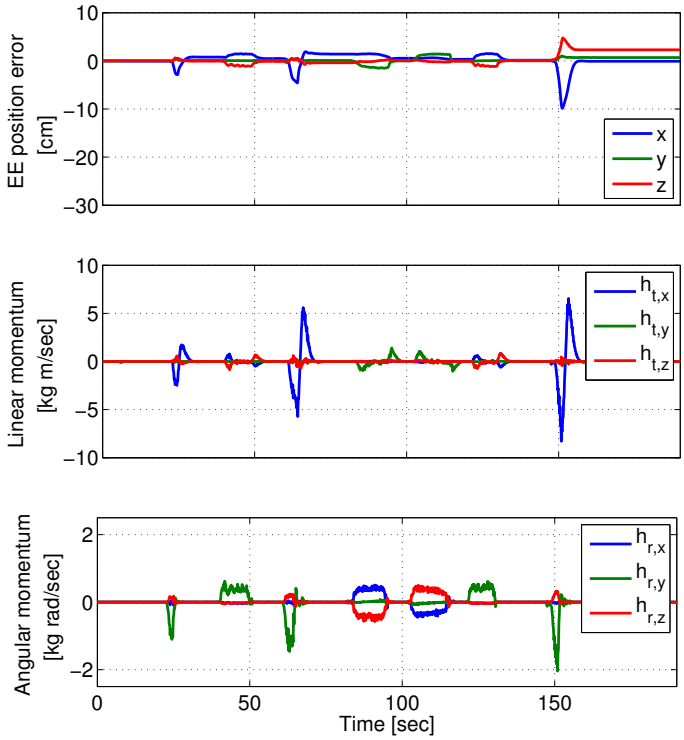

Figure 8.12.: CoM Control - End effector position and momenta.

Fig. 8.12. It can be seen that, during the contacts, the end-effector was displaced; when the contacts ended, the end-effector error converged to zero up to a precision of 1.5 cm due to the static friction in the joints. Note that the end-effector position was restored after every contact, because no singularity was reached. Finally, note that the angular momentum in Fig. 8.12 was properly dumped and any rotational drift of the system was stopped.

The base actuator forces and torques are conclusively shown in Fig. 8.13. Note that the satellite forces acted in reaction to the external force in Fig. 8.11. In particular, as soon as one CoM displacement was generated along a direction, the satellite forces reacted in the same direction but opposite sign. For the sake of completeness, the base attitude is reported in Fig. 8.14. Therein it is seen that the attitude was not controlled. After each impulse, it converged to new values, which were not known in advance. In this sense, the Whole-Body controller C3 leaves the base attitude free, in a similar way as in a free-floating strategy, while solving the drift limitation.

The results confirmed that a simultaneous momentum dumping and CoM task solves both the inertial drift limitation of the free-floating control, and the workspace shift limitation of a momentum dumping task alone, during a post-contact phase. Furthermore, the results confirmed the applicability of the Whole-Body controller C3 with a real manipulator.

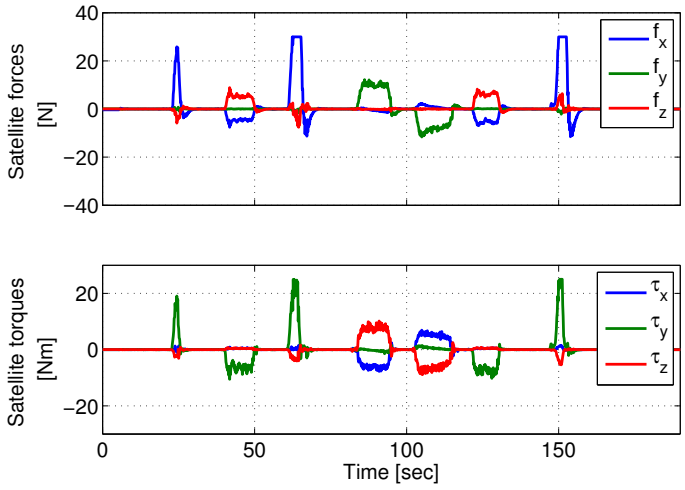

Figure 8.13.: CoM Control - Satellite commanded forces and torques.

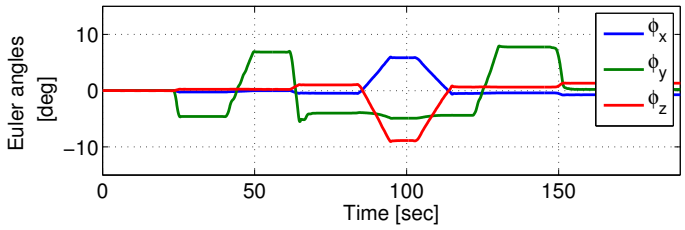

Figure 8.14.: CoM Control - Satellite attitude.

8.3. Experimental investigation of the Whole-Body controller C4

The aim of the experiments reported herein is to validate the applicability of the Whole-Body controller C4 considering a real arm, and to further analyze the advantages of the partially thrusters-decoupled actuation of the Whole-Body controller C4.
The feature of the partially thrusters-decoupled structure employed by the Whole-Body controller C4, i.e., the actuation mapping (5.25), is that the base force actuator is not used to realize the end-effector task, but only to realize the task that cannot be actuated by internal actuators, i.e., controlling the inertial location of the CoM. For a nonredundant arm, the actuation mapping has the form

$$\begin{bmatrix} \boldsymbol{f}_b \\ \boldsymbol{m}_b \\ \boldsymbol{\tau}_m \end{bmatrix} = \begin{bmatrix} \boldsymbol{R}_b^T & \boldsymbol{0} & \boldsymbol{0} \\ \frac{1}{m}\boldsymbol{M}_{v\omega}(\hat{\boldsymbol{q}}_m)^T\boldsymbol{R}_b^T & \boldsymbol{E} & \boldsymbol{J}_{e\omega}^{\oplus}(\hat{\boldsymbol{q}}_m)^T \\ \frac{1}{m}\boldsymbol{M}_{vm}(\hat{\boldsymbol{q}}_m)^T\boldsymbol{R}_b^T & \boldsymbol{0} & \boldsymbol{J}_{em}^{\oplus}(\hat{\boldsymbol{q}}_m)^T \end{bmatrix} \begin{bmatrix} \boldsymbol{f}_c \\ \boldsymbol{m}_b^{\oplus} \\ \boldsymbol{\mathcal{F}}_e^{\oplus} \end{bmatrix}. \tag{8.9}$$

This structure is a property of the circumcentroidal velocity $\boldsymbol{\nu}_e^{\oplus}$ and does not hold when using the absolute velocity $\boldsymbol{\nu}_e$ for defining the allocation space. In fact, in the latter case, the actuation mapping would use the base force actuator to realize the end-effector task, i.e., it would result in

$$\begin{bmatrix} \boldsymbol{f}_b \\ \boldsymbol{m}_b \\ \boldsymbol{\tau}_m \end{bmatrix} = \begin{bmatrix} \boldsymbol{R}_b^T & \boldsymbol{0} & \boldsymbol{J}_{ev}(\hat{\boldsymbol{q}}_m)^T \\ \frac{1}{m}\boldsymbol{M}_{v\omega}(\hat{\boldsymbol{q}}_m)^T\boldsymbol{R}_b^T & \boldsymbol{E} & \boldsymbol{J}_{e\omega}(\hat{\boldsymbol{q}}_m)^T \\ \frac{1}{m}\boldsymbol{M}_{vm}(\hat{\boldsymbol{q}}_m)^T\boldsymbol{R}_b^T & \boldsymbol{0} & \boldsymbol{J}_{em}(\hat{\boldsymbol{q}}_m)^T \end{bmatrix} \begin{bmatrix} \boldsymbol{f}_c \\ \bar{\boldsymbol{m}}_b \\ \bar{\boldsymbol{\mathcal{F}}}_e \end{bmatrix}, \tag{8.10}$$

where $\boldsymbol{J}_{ev}(\hat{\boldsymbol{q}}_m) = \begin{bmatrix} \boldsymbol{R}_b \\ \boldsymbol{0} \end{bmatrix} \in \mathbb{R}^{6\times 3}$, $\boldsymbol{J}_{e\omega}(\hat{\boldsymbol{q}}_m) = \begin{bmatrix} [\boldsymbol{o}_{eb}(\hat{\boldsymbol{q}}_m)]^\wedge \boldsymbol{R}_b \\ \boldsymbol{R}_b \end{bmatrix} \in \mathbb{R}^{6\times 3}$, and where $\bar{\boldsymbol{m}}_b, \bar{\boldsymbol{\mathcal{F}}}_e \in \mathbb{R}^n$ are control inputs dual to $\boldsymbol{\omega}_b$, $\boldsymbol{\nu}_e$, respectively. In order to validate the advantages of decoupling the actuation, an experiment was performed first with the partially thrusters-decoupled actuation (8.9). Then, the same experiment was repeated with a control that enforces exactly the same CoM, attitude, and end-effector control requirements, but which employs the thrusters-coupled actuation (8.10).
The experiment consisted of a sequence of two representative end-effector maneuvers in the pre-contact phase of a grasping scenario. For each maneuver, the end-effector is commanded to reach a desired pose and then to return to the initial position. In the second maneuver, a lateral motion (y component) of the end-effector was commanded to excite three-dimensional effects more pronouncedly. In both maneuvers, the base attitude and the CoM were commanded to hold desired setpoints. No contact or initial momentum were simulated. The stiffness gains used were $\boldsymbol{K}_e = \text{blkdiag}(\boldsymbol{K}_{e,trasl}, \boldsymbol{K}_{e,rot})$ for the end-effector, where $\boldsymbol{K}_{e,trasl} = 800\boldsymbol{E}\,\text{N}\,\text{m}^{-1}$, and $\boldsymbol{K}_{e,rot} = 56\,\boldsymbol{E}\,\text{N}\,\text{m}\,\text{rad}^{-1}$; the stiffness gains $\boldsymbol{K}_{b,rot} = 672\boldsymbol{E}\,\text{N}\,\text{m}\,\text{rad}^{-1}$, and $\boldsymbol{K}_c = 300\boldsymbol{E}\,\text{N}\,\text{m}^{-1}$ were used for the attitude and the CoM, respectively. The damping gains were designed using the method in [Ott08, p.36] based on the inertia in the initial configuration.

Fig. 8.15a shows the time response of the position of the end-effector, the attitude of the base, and the position of the CoM for the Whole-Body controller C4 employing a partial thrusters-decoupled actuation. In Fig. 8.15a, it can be seen that the end-effector successfully converged to the desired position for both end-effector maneuvers. The base attitude was slightly displaced due to the robot motion, but the control action successfully restored the desired location after the end-effector maneuver ended. The CoM stayed in place[2] and was not affected by the end-effector control. On the other hand, the position of the base freely changed in reaction to the end-effector maneuvering, similarly as what already analyzed in Section 7.1.1 by numerical simulation. The commanded base force and torques are shown in Fig. 8.16a. Therein, the main result of the partially thrusters-decoupled decomposition is evident, namely, the base force was exactly zero, and only the base torque is employed by the control.

In Fig. 8.15b, the results for the thrusters-coupled actuation are shown. Therein it is seen that, similarly to the partially thrusters-decoupled actuation, the end-effector converged to the desired position in both end-effector maneuvers, and the attitude was restored to the correct location after the end-effector maneuvers. However, in contrast to the partially thrusters-decoupled actuation, the CoM did not stay in place, but was excited by the term $\boldsymbol{J}_{ev}(\hat{\boldsymbol{q}}_m)^T$ in (8.10) which couples the end-effector control input $\boldsymbol{\mathcal{F}}_e$ into the base actuator $\boldsymbol{f}_b$. The effect of the coupling can especially be seen in the plot of the commanded base force and torques in Fig. 8.16b; therein, it is observed that the base force was nonzero for the thrusters-coupled actuation, and this in fact led to the excitation of the CoM. In conclusion, given the same requirements, the thrusters-coupled actuation led to an activation of the base force, and, in turn, to an excitation of the CoM during the end-effector maneuver. This says that the CoM control task alone is not sufficient to achieve a reduction of the thrusters usage during end-effector maneuvering, but also a (at least partially) thrusters-decoupled actuation is needed. Both features are endowed in the Whole-Body controller C4. The experiments were repeated three times for further validation:

[2]Small deviations from zero that can be explained as disturbances induced by the hardware simulation facility.

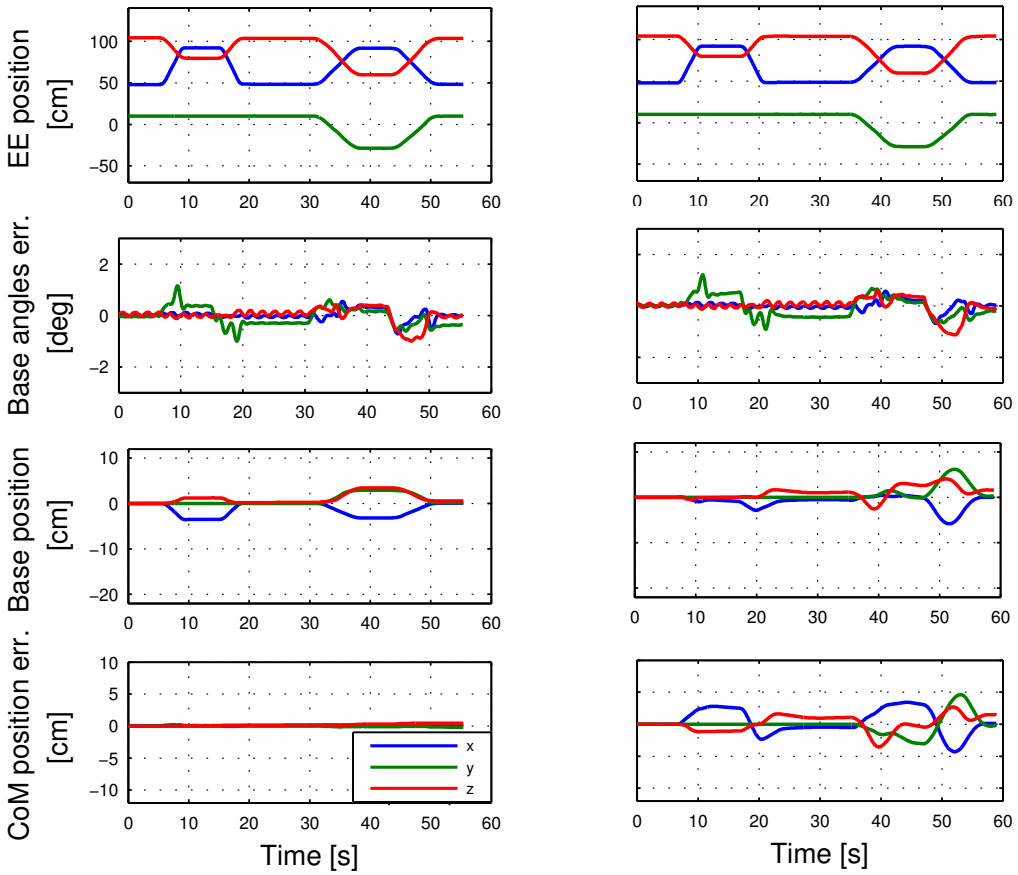

(a) Partially thrusters-decoupled actuation (Whole-Body controller C4)

(b) Completely thrusters-coupled actuation

Figure 8.15.: Performance of the attitude-arm coordinated control.

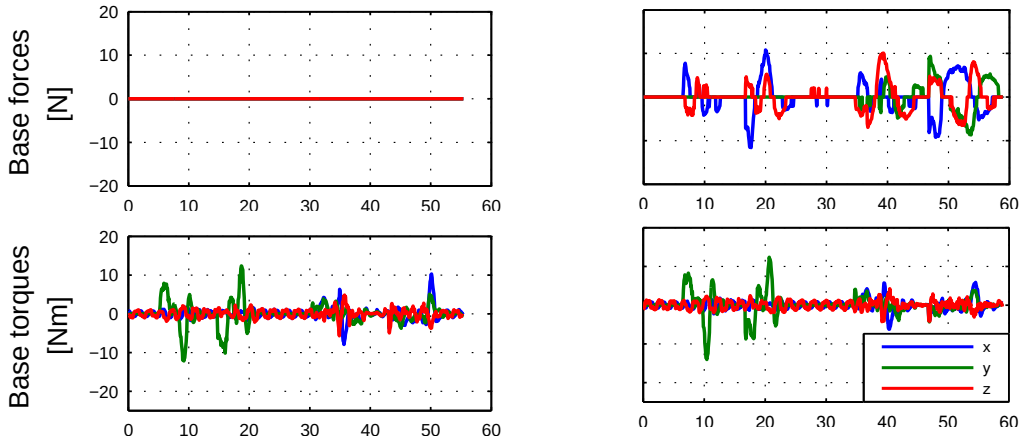

(a) Partially thrusters-decoupled actuation (Whole-Body controller C4)

(b) Completely thrusters-coupled actuation

Figure 8.16.: Commanded base force and base torque.

1. The same trajectories were tested one more time for repeatability. The same results were obtained and are not shown for brevity.

2. The same path with a longer duration was commanded. Similar results were obtained and are not shown.

3. The same trajectory was repeated with an additional deadzone of 2 Nm on the $\boldsymbol{m}_b$ signal. In Fig. 8.17 the base angles and commanded base torques are reported. Therein it is shown that the deadzone avoided the steady oscillation on the base torque observed in Fig. 8.16a without inducing stability issues. Other plots showed no significant difference and are not reported.

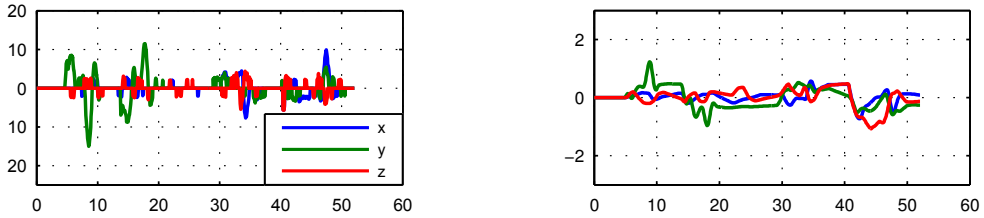

Figure 8.17.: Test with deadzone on $\boldsymbol{\tau}_b$ with Whole-Body controller C4 (partially thrusters-decoupled actuation).

Based on the experimental results, it is concluded that the Whole-Body controller C4 can be applied on real hardware, and that it successfully implements the decoupling feature of the base force which was seeked at.

8.4. Experimental investigation of the Whole-Body controller C5

The aim of the following experiments is to validate the Whole-Body controller C4 during representative pre-contact and post-contact phases. Two sets of experiments were performed:

1. a series of contact-free end-effector maneuvers, to validate the controller in a representative pre-contact situation;

2. a series of experiments in which the end-effector keeps its current position while accumulated momentum is dumped by the thrusters, to validate the behavior in a representative post-contact situation.

In both experiments, the nonredundant version of the Whole-Body controller C5 was validated; it is obtained by setting the null-space task in (6.9) and (6.14) to zero, i.e., $\boldsymbol{\varsigma}_n^{int}$, and is given by

$$\boldsymbol{\mathcal{F}}_b = \boldsymbol{A}_{cb}(\boldsymbol{R}_b, \boldsymbol{q}_m)^T \left(-\boldsymbol{S}_v^T \boldsymbol{K}_c \tilde{\boldsymbol{x}}_c - \boldsymbol{D}_h \tilde{\boldsymbol{h}}_c\right), \tag{8.11a}$$

$$\boldsymbol{\tau}_w = \boldsymbol{J}^{int}_{\tilde{\omega}_b w}(\hat{\boldsymbol{q}}_m)^T \left(-\boldsymbol{J}_{\tilde{x}_{b,rot}}(\tilde{\boldsymbol{x}}_{b,rot})^T \boldsymbol{K}_b \tilde{\boldsymbol{x}}_{b,rot} - \boldsymbol{D}_{b,rot} \tilde{\boldsymbol{\omega}}_b\right) + \boldsymbol{J}^{int}_{ew}(\hat{\boldsymbol{q}}_m)^T \left(-\boldsymbol{J}_{\tilde{x}_e}(\tilde{\boldsymbol{x}}_e)^T \boldsymbol{K}_e \tilde{\boldsymbol{x}}_e - \boldsymbol{D}_e \tilde{\boldsymbol{\nu}}_e\right), \tag{8.11b}$$

$$\boldsymbol{\tau}_m = \boldsymbol{J}^{int}_{\tilde{\omega}_b m}(\hat{\boldsymbol{q}}_m)^T \left(-\boldsymbol{J}_{\tilde{x}_{b,rot}}(\tilde{\boldsymbol{x}}_{b,rot})^T \boldsymbol{K}_b \tilde{\boldsymbol{x}}_{b,rot} - \boldsymbol{D}_{b,rot} \tilde{\boldsymbol{\omega}}_b\right) + \boldsymbol{J}^{int}_{em}(\hat{\boldsymbol{q}}_m)^T \left(-\boldsymbol{J}_{\tilde{x}_e}(\tilde{\boldsymbol{x}}_e)^T \boldsymbol{K}_e \tilde{\boldsymbol{x}}_e - \boldsymbol{D}_e \tilde{\boldsymbol{\nu}}_e\right). \tag{8.11c}$$

8.4.1. Experimental results: pre-contact phase

A sequence of two end-effector maneuvers was tested. For each maneuver, the end-effector was commanded to reach a desired pose and then to come back. In the first maneuver, a displacement ${}_t\boldsymbol{o}_{ee_f} = [35,\ 0, -25]\,\text{cm}$ of the position and $\boldsymbol{\phi}_{ee_f} = [0, -20,\ 0]\,\text{deg}$ of the rotation (roll, pitch, and yaw angles) was commanded to the end-effector. In the second maneuver, a displacement of ${}_t\boldsymbol{o}_{ee_f} = [23.5, -27, -30]\,\text{cm}$ and $\boldsymbol{\phi}_{ee_f} = [-6.7, -6.7, 30]\,\text{deg}$ was commanded. The second maneuver excites three-dimensional effects more pronouncedly. During all maneuvers, the attitude of the spacecraft and the CoM of the whole robot were commanded to hold the initial values. No contact or initial momentum were simulated in the pre-contact experiments. The stiffness gains used were $\boldsymbol{K}_e = \text{blkdiag}(\boldsymbol{K}_{e,trasl}, \boldsymbol{K}_{e,rot})$ for the end-effector, where $\boldsymbol{K}_{e,trasl} = 1000\boldsymbol{E}\,\text{N m}^{-1}$, $\boldsymbol{K}_{e,rot} = 70\,\boldsymbol{E}\,\text{N m rad}^{-1}$, $\boldsymbol{K}_{b,rot} = 3350\boldsymbol{E}\,\text{N m rad}^{-1}$, and $\boldsymbol{K}_c = 700\boldsymbol{E}\,\text{N m}^{-1}$ were used for the attitude and the CoM, respectively. The EE and attitude damping gains were designed using the method in [Ott08, p.36] based on the inertia in the initial configuration. The momentum gain was $\boldsymbol{D}_h = \text{blkdiag}(\boldsymbol{D}_p, \boldsymbol{D}_l)$ where $\boldsymbol{D}_p = 3.93\boldsymbol{E}\,\text{s}^{-1}$ was used for the linear momentum, and $\boldsymbol{D}_l = 16\boldsymbol{E}\,\text{s}^{-1}$ for the angular momentum.

Figure 8.18 shows the results for both maneuvers; the second maneuver starts at $t = t_2$. The figure shows the time responses of the end-effector position, the attitude of the spacecraft, the CoM of the whole robot, and the velocity of the reaction wheels, as well as the forces and torques actuated by the thrusters, the reaction wheels', and the joints' drives. It can be observed that the end-effector successfully converged to the desired position after maneuvering. The attitude of the spacecraft was displaced due to the robot motion, but the joint control action of the reaction wheels and the arm successfully restored it after the maneuver had finished. A longer-lasting oscillation of the attitude of the spacecraft was observed during the lateral maneuver and it was related to the more pronounced excitation of the 1DOF null space of the arm, which was only indirectly damped through the natural friction in the joints. The position of the spacecraft freely moved and was displaced to new locations after each maneuver. On the other hand, the CoM stayed in place and was not affected by the end-effector control. This confirms the effectiveness of the decoupled actuation in also the Whole-Body controller C5. More specifically, thanks to the completely thrusters-decoupled actuation (6.9) adopted by the Whole-Body controller C5, in a nominal starting condition in which the CoM error and the momentum are zero, the thrusters command $\boldsymbol{\mathcal{F}}_b$ does not get activated during end-effector and attitude maneuvering; consequently, the CoM does not get excited by the coordinated controller. Thanks to this property, in the experiment the end-effector maneuvers were accomplished entirely by the joints of the arm and the reaction wheels only, as observed in Fig. 8.18, and exactly zero fuel was consumed.
The steady-state joint torque in Fig. 8.18 was due to the static friction in the joints of the arm. The RW torque was within the allowable limit of 0.3Nm for the considered maneuver, although the maximum robot speed was limited by the low torque capability of the wheels; this proves that the controller is implementable with realistic wheels. Lastly, the RW velocity was low and well below the limits of common devices, e.g. 5000 rpm, and returned to zero after each maneuver ended. Based on this, in accordance with the conservation of the zero initial momentum, the actuation can be interpreted as a mutual exchange of momentum between arm and reaction wheels, with the wheels' momentum returning to zero as soon as the arm comes to rest.

In conclusion, the experiment confirmed the main property of a thrusters-decoupled actuation also for the Whole-Body controller C5, namely, during the pre-contact phase

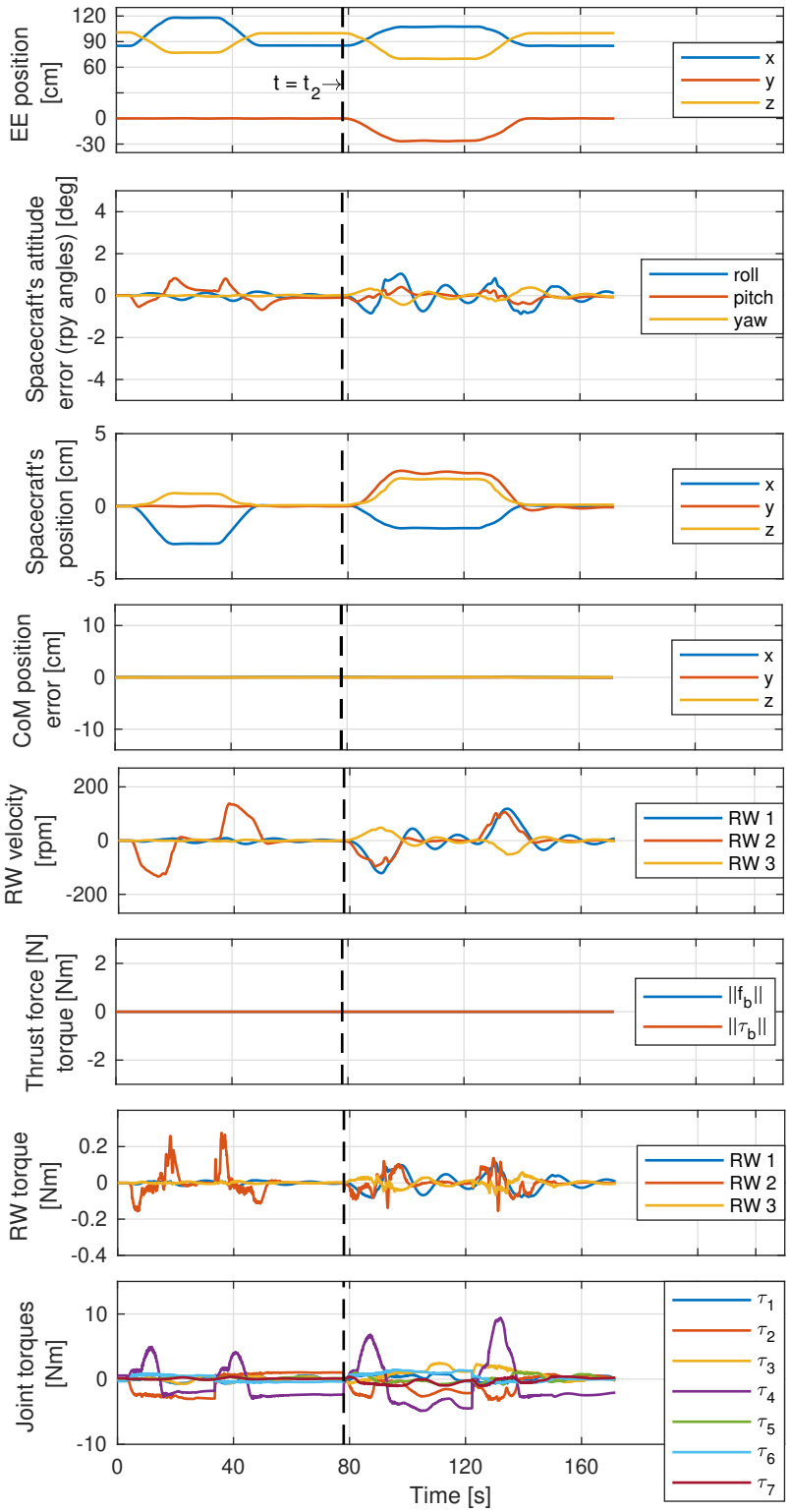

Figure 8.18.: Response during pre-contact phase.

no thrusters are activated; this in turn means that nominally no fuel is consumed by the controller. Furthermore, the experiment confirmed that the Whole-Body controller C5 is applicable during a pre-contact phase considering a real arm, and that the reaction wheels can be successfully employed in the coordinated actuation to restore the attitude.

8.4.2. Experimental results: post-contact phase

An experiment is reported herein, which validates the effectiveness of the Whole-Body controller C5 during a post-contact situation, i.e., one in which the CoM velocity and the angular momentum are nonzero. A series of impulses along different directions was given manually to the end-effector by using a rod. Note that the contact is given only as a mean to excite the momentum of the system and *not* to analyze the behavior of the system during contact. In these experiments, the same gains were used as in the pre-contact experiment, except the ones of the end-effector, which were $\boldsymbol{K}_{e,trasl} = 500\boldsymbol{E}\,\mathrm{N\,m^{-1}}$, $\boldsymbol{K}_{e,rot} = 35\boldsymbol{E}\,\mathrm{N\,m\,rad^{-1}}$.

Figure 8.19 shows the reconstructed applied contact force, the position of the end-effector, the attitude of the base, the position of the CoM, the angular momentum, and the commanded base forces and torques in the inertial $\mathcal{T}$ frame. First, observe in Fig. 8.19 that after each contact the correct CoM location was restored and the momentum was dumped; furthermore, the end-effector and the attitude of the base were successfully kept around the desired values. This means that, when the linear and angular momenta got excited, the controller promptly reacted to stop the drift, thereby guaranteeing the stability of the system and the accomplishment of the envisioned tasks. Second, observe in Fig. 8.19 that the impulses were given along different directions and that the controller behaved properly in every direction. The thrusters automatically fired in reaction to the external force. As soon as a CoM displacement was generated along a direction, the thrusters forces reacted in the same direction, but opposite sign.

In conclusion, the impulse experiments validated the correct behavior of the Whole-Body controller C5 during the post-contact situation.

8.5. Summary

In this chapter, several experiments conducted on the OOS-Sim experimental facility were reported. The experiments have been conducted in an incremental and comparative way, so to point out the main functional features of the derived controllers. The limitation of a purely free-floating strategy during a post-contact phase was shown; then, the benefits of the momentum dumping and CoM control tasks during a post-contact phase were analyzed. The features of a partially thrusters-decoupled approach for the coordinated control of end-effector and base attitude during a pre-contact phase were analyzed, and a comparison with a completely thrusters-coupled approach was done. The feasibility of use of reaction wheels during the pre-contact phase was analyzed.

The experiments provided evidence of the correct behavior of the Whole-Body controllers C3, C4, and C5 during the pre- and post-contact phases, when applied with a real arm.

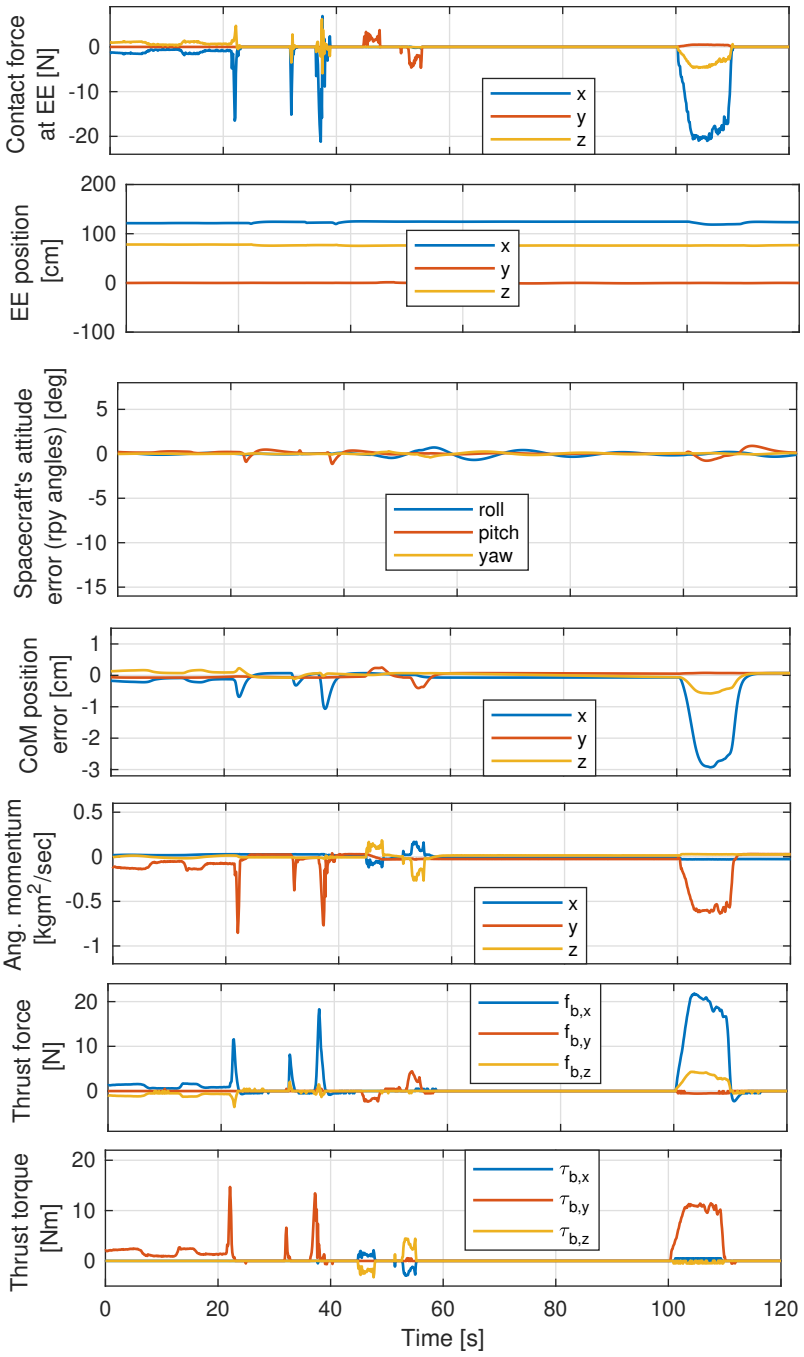

Figure 8.19.: Response during post-contact phase.

CHAPTER 9

Controllers Comparison and Conclusions

In Chapter 3 extended version of common Free-Floating and Free-Flying controllers were presented. In Chapters 5 and 6 three Whole-Body controllers were presented. The controllers were already compared via numerical simulations and hardware experiments. In this Chapter, a final overall comparison of the advantages and the advantages of the controllers is discussed. Table 9.1 summarizes the main properties of the different controllers.

The comparison is in some aspects subjective and therefore some justifications of the ratings are discussed next.

Spacecraft actuators and feedback variables The Free-Floating controller C1 relies on a simpler control architecture that requires less actuators and measurements than the Free-Flying and Whole-Body controllers. This advantage comes at the cost of limitations in terms post-contact drift robustness, workspace control, and attitude pointing.

Post-contact drift robustness Any Free-Floating controller is not robust to contact due to the drift of the system after contact. Thus, the Free-Floating approach cannot be used for prolongated manipulation in presence of momentum without switching to an actuated base strategy.

Workspace control Any Free-Floating controller cannot displace the workspace of the robot in the inertial space, and thus, cannot be used for reaching distant objects.

Attitude pointing The Free-Floating controller C1 cannot guarantee attitude pointing; however, note that other free-floating controllers [NUY92, YDN06, ONY07] can.

Thrusters efficiency Any Free-Floating controller and the Whole-Body controllers C3 and C5 drastically reduce the thrusters usage and, in turn, the fuel consumption. The Free-Flying controller C2 is the most thrusters-inefficient among the presented controllers. The Whole-Body controller C4 is moderately more efficient than the Free-Flying controller C2 thanks to the partially thrusters-decoupled actuation, which induces a floating-base behavior in translation; however, the thrusters usage is still high because the rotational coupling of the arm and the base is dominant compared to the translational decoupling featured by the controller.

	Free-Floating C1	**Free-Flying C2**	**Whole-Body C3**	**Whole-Body C4**	**Whole-Body C5**
Spacecraft actuators	none	thrusters	thrusters	thrusters	thrusters, RWs
Feedback variables	$\boldsymbol{q}_m$, $\boldsymbol{H}_{e_de}, \boldsymbol{\nu}_{e_de}$, $(+\boldsymbol{R}_b)^a$	$\boldsymbol{q}_m$, $\boldsymbol{H}_{e_de}, \boldsymbol{\nu}_{e_de}$, $\boldsymbol{o}_{b_db}, \boldsymbol{v}_{b_db}$ $\boldsymbol{R}_{b_db}, \boldsymbol{\omega}_{b_db}$	$\boldsymbol{q}_m$, $\boldsymbol{H}_{e_de}, \boldsymbol{\nu}_{e_de}$ $\boldsymbol{o}_{c_dc}, \boldsymbol{v}_{c_dc}$, $\boldsymbol{l}_c$	$\boldsymbol{q}_m$, $\boldsymbol{H}_{e_de}, \boldsymbol{\nu}_{e_de}$ $\boldsymbol{o}_{c_dc}, \boldsymbol{v}_{c_dc}$, $\boldsymbol{R}_{b_db}, \boldsymbol{\omega}_{b_db}$	$\boldsymbol{q}_m, \dot{\boldsymbol{q}}_m, \dot{\boldsymbol{q}}_w$, $\boldsymbol{H}_{e_de}, \boldsymbol{\nu}_{e_de}$ $\boldsymbol{o}_{c_dc}, \boldsymbol{v}_{c_dc}$, $\boldsymbol{R}_{b_db}, \boldsymbol{\omega}_{b_db}$ $\boldsymbol{l}_c$
Post-contact drift robustness	-	+	+	+	+
Workspace control	-	+	+	+	+
Attitude pointing	-	+	-	+	+
Thrusters efficiency	+	-	+	0	+

[a] The feedback of the orientation of the spacecraft is required by the angular momentum compensation; it is not required when the angular momentum is zero.

Table 9.1.: Comparison of the controllers.

All in all, it is concluded that the Whole-Body framework represents a general strategy that allows merging the advantages of the Free-Floating and Free-Flying controllers.

9.1. Conclusions and Future Work

In this thesis, a class of Whole-Body controllers was presented, which allows accomplishing the requirements for robotic operation in orbit with a reduced utilization of thrusters. The underlying philosophy is a whole-body-centric perspective of the system, wherein the system is framed in its entirety rather than as a composition of separate spacecraft and manipulator entities. By regulating whole-body objectives and by adopting thrusters-decoupled actuation schemes, natural floating-base behavior was endowed into fully-actuated *Whole-Body* controllers, thereby merging into them the advantages of the classical Free-Floating and Free-Flying strategies, while sorting out their limitations. The main result of doing so is that the mission requirements are satisfied with drastic reduction of the thrusters use, and that a single unified controller can be used during both the pre- and post-contact phases of the robotic operation.

The kinematics and dynamics model of a general orbital robot in orbit was derived for the purpose of onboard utilization and for the validation via simulation. The methodology for the design of multi-objective controllers was derived with a focus on the actuators allocation. The used methodology is similar to the well-known Operational Space Formulation, but it differs in the fact that the virtual actuators may not necessarily be dual to the time-derivative of the task coordinates, but can be general compositions of velocities and momenta.

An extension of the common transposed-Jacobian Free-Floating controller to the case of nonzero momentum, and an extension of the common transposed-Jacobian Free-Flying controller for application with a redundant manipulator, were presented. The limitations of the Free-Floating and Free-Flying controllers were pointed out. It was identified that the main disadvantage of a Free-Floating strategy is the unstoppable drift induced by external interaction on the robot. This drift translates into a severe limitation especially in the post-contact phase following accidental or voluntary contact; in this situation, singularity or workspace limits are reached within short time, and switching to a different strategy is imperative. This limitation is evident in the numerical simulations and the experiments that were carried out in the thesis. On the other hand, the limitations of the analyzed Free-Flying controller were identified being related to the thrusters-coupled actuation, and to the task of controlling the spacecraft position and attitude, which, considering the floating-base nature of an orbital robot, is a unnatural one. The former represents a direct coupling of the manipulator task into the thrusters, whereas the latter represents an indirect coupling due to the coupled spacecraft and end-effector dynamics.

To overcome the limitations, a framework was derived to systematically define allocation spaces that own a thrusters-decoupled actuation and a decoupled dynamics. Two such decoupled allocation spaces — the external-internal and the centroid-circumcentroidal allocation spaces — were derived based on the momentum and the CoM of the whole robot. In the external-internal allocation space, general internal velocities were defined and used in combination with the momentum for the formulation of the allocation space. The formulation features a completely thrusters-decoupled actuation structure, and a decoupled momentum dynamics. In the centroid-circumcentroidal allocation space, general circumcentroidal velocities were defined and used in combination with the CoM for the formulation of the allocation space. The formulation features a partially thrusters-decoupled actuation structure and a decoupled CoM dynamics. The completely thrusters-decoupled actuation avoids the direct coupling, the decoupled momentum dynamics defines an invariant task which avoids the indirect coupling. On the other hand, the partially thrusters-decoupled actuation avoids part of the direct coupling, and the decoupled CoM dynamics defines an invariant tasks that avoids part of the indirect coupling. Based on the above-mentioned framework, three Whole-Body controllers were derived. Two of them use only spacecraft-mounted thrusters, one of them uses spacecraft-mounted thrusters and reaction wheels.

In the first Whole-Body controller, thrusters and manipulator are coordinately actuated, an external-internal decomposition is used, and the invariant task of controlling the angular momentum and the CoM of the whole robot is enforced. The invariant task allows satisfying the requirements of post-contact robustness and workspace control, without necessarily enforcing a control of the position and orientation of the base. It was shown that the controller automatically converges to a free-floating controller once the momentum and CoM momentum transient vanish; therefore, the controller was interpreted as an extension of the free-floating approach to a fully-actuated strategy encapsulating floating-base behavior.

In the second Whole-Body controller, thrusters and manipulator are coordinately actuated, a centroid-circumcentroidal decomposition is used, and the invariant task of controlling the CoM of the whole robot is enforced; additionally, the orientation of the spacecraft is controlled. The centroid-circumcentroidal decomposition is a partially thrusters-decoupled actuation, which avoids thrusters coupling only in translation. The resulting actuation is structurally the same in rotation as in the Free-Flying controller, and is structurally

the same in translation as in the Free-Floating controller. Based on this, and on the enforced CoM-control invariant task, the controller was interpreted as an intermediate Whole-Body approach, which endows floating-base behavior in translation, but works like the Free-Flying controller in rotation. The controller represents a Whole-Body solution for missions explicitly requiring attitude pointing.

In the third Whole-Body controller, thrusters, manipulator, and reaction wheels are coordinately actuated, an external-internal decomposition is used, and the invariant task of controlling the angular momentum and the CoM of the whole robot is enforced; additionally, the orientation of the spacecraft is controlled. The additional task of controlling the orientation of the spacecraft is endowed in an completely thrusters-decoupled external-internal actuation, thanks to the additional redundancy provided by the reaction wheels. By doing so, the maximum benefit of the decoupled actuation framework is exploited, and the attitude pointing requirement is satisfied with minimalistic activation of the thrusters.

To compare and validate the controllers, thorough numerical simulations and hardware experiments were conducted, considering an orbital robot composed of a seven DOFs arm mounted on a six DOFs spacecraft. Simulations based on realistic thrusters and measurements models revealed the applicability of the Whole-Body controllers, and their superior performance in terms of thrusters activation and fuel consumption, when compared to a Free-Floating strategy. The superior performance is an outcome of the reduced thrusters use of the Whole-Body controllers, and confirms the validity of the motivating idea of this thesis. The experimental validation provided evidence of the applicability and effectiveness of the controllers considering a real manipulator. The experiments were conducted on a robotic simulation facility, which allows reproducing the complete three dimensional motion of an orbital robot. These experiments are rather rare in the existing literature, and, in the opinion of the author, provide unique insight.

Certain important aspects were inevitably left out in this thesis, an will be addressed in future works. The Whole-Body strategies shall be extended for application with a noninertial target. Active Debris Removal missions represent one important application domain of orbital robots; these missions are indeed characterized by tumbling targets. Depending on the size of the target, partial synchronization of only the end-effector with the tumbling motion, or also flight synchronization, may be required. To address the partial synchronization, the CoM and the angular momentum tasks shall be specified relative to the orbital frame. The flight synchronization may be instead addressed by specifying the CoM and angular momentum relative to the target frame. In both cases, a disturbance in the closed loop appears, and its compensation may be required.

The controllers shall also be validated with a state estimation algorithm. The controllers require feedback of the end-effector state relative to the grasping point on the target; an end-effector camera can be used to reconstruct this information, but only at low rate. For contact stability, the direct interconnection of a camera is not sufficient, and visual servoing or fusion is necessary for reconstruction of these signals at high rate. The Free-Flying and the Whole-Body controllers additionally require estimation of the velocity of the system relative to the target, for which no direct measurement is available. Existing state estimation algorithms may be used at this purpose, they shall be integrated with the controllers, and the performance of the combined closed-loop shall be validated.

Finally, the framework will be extended for application in the complete pre-contact, contact, and post-contact phase. For this purpose, the momentum dumping task and the theoretical analysis of the controllers will be extended to the case of nonzero contact wrench.

Appendices

APPENDIX A

Expressions of internal and circumcentroidal mappings

A.1. Internal mapping of a body

In the following, it is proved that (4.17) results in (4.18). Let us first compute the expression of the momentum null-space projector. By applying (4.21), the two terms in the pseudoinverse (4.16) have the expression

$$\boldsymbol{M}(\boldsymbol{q})^{-1}\boldsymbol{L}(\boldsymbol{R}_b,\boldsymbol{q})^T = \begin{bmatrix}\boldsymbol{A}_{cb}(\boldsymbol{R}_b,\boldsymbol{q})^{-1}\\ \boldsymbol{0}\end{bmatrix}, \tag{A.1}$$

$$\left(\boldsymbol{L}(\boldsymbol{R}_b,\boldsymbol{q})\boldsymbol{M}(\boldsymbol{q})^{-1}\boldsymbol{L}(\boldsymbol{R}_b,\boldsymbol{q})^T\right)^{-1} = \left(\boldsymbol{A}_{cb}(\boldsymbol{R}_b,\boldsymbol{q})^{-T}\boldsymbol{M}_b(\boldsymbol{q})\boldsymbol{A}_{cb}(\boldsymbol{R}_b,\boldsymbol{q})^{-1}\right)^{-1}. \tag{A.2}$$

Then, the null-space projector (4.15) results having the form[1]

$$\boldsymbol{N}_h(\boldsymbol{q}) = \begin{bmatrix}\boldsymbol{0} & -\boldsymbol{M}_b(\boldsymbol{q})^{-1}\boldsymbol{M}_{bq}(\boldsymbol{q})\\ \boldsymbol{0} & \boldsymbol{E}\end{bmatrix}. \tag{A.3}$$

By considering a partitioning $\boldsymbol{J}_j^{int}(\boldsymbol{q}) = \begin{bmatrix}\boldsymbol{J}_{jb}^{int}(\boldsymbol{q}) & \boldsymbol{J}_{jq}^{int}(\boldsymbol{q})\end{bmatrix}$, and the partitioning of $\boldsymbol{J}_j(\boldsymbol{q})$ defined in (2.17), the internal mapping (4.14) results in

$$\boldsymbol{J}_{jb}^{int}(\boldsymbol{q}) = \boldsymbol{0}, \tag{A.4a}$$

$$\boldsymbol{J}_{jq}^{int}(\boldsymbol{q}) = \boldsymbol{J}_{jq}(\boldsymbol{q}) - \boldsymbol{A}_{jb}(\boldsymbol{q})\boldsymbol{M}_b(\boldsymbol{q})^{-1}\boldsymbol{M}_{bq}(\boldsymbol{q}) \tag{A.4b}$$

and, in turn, (4.17) results in (4.18), as

$$\boldsymbol{\nu}_j^{int} = \boldsymbol{J}_j^{int}(\boldsymbol{q})\boldsymbol{\upsilon} = \begin{bmatrix}\boldsymbol{0} & \boldsymbol{J}_{jq}^{int}(\boldsymbol{q})\end{bmatrix}\begin{bmatrix}\boldsymbol{\nu}_b\\ \dot{\boldsymbol{q}}\end{bmatrix} = \boldsymbol{J}_{jq}^{int}(\boldsymbol{q})\dot{\boldsymbol{q}}. \tag{A.5}$$

[1] Notice in (A.3) that the momentum null-space projector does not depend on $\boldsymbol{A}_{cb}(\boldsymbol{R}_b,\boldsymbol{q})$, so the null-space projector is independent of the frame $\mathcal{C}$ and has the same expression when expressed around any frame. As a further consequence of this, the momentum null-space projector does not depend on the base rotation $\boldsymbol{R}_b$, but only on the joints $\boldsymbol{q}$.

A.2. Circumcentroidal mapping of a body

In the following, it is proved that (4.45) results in (4.46). Let us preliminary rewrite the pseudo-inverse (4.44) as

$$\boldsymbol{L}_v(\boldsymbol{R}_b,\boldsymbol{q})^{\#} = \boldsymbol{M}(\boldsymbol{q})^{-1}\boldsymbol{L}(\boldsymbol{R}_b,\boldsymbol{q})^T\frac{1}{m}\boldsymbol{S}_v^T\left(\frac{1}{m}\boldsymbol{S}_v\boldsymbol{L}(\boldsymbol{R}_b,\boldsymbol{q})\boldsymbol{M}(\boldsymbol{q})^{-1}\boldsymbol{L}(\boldsymbol{R}_b,\boldsymbol{q})^T\frac{1}{m}\boldsymbol{S}_v^T\right)^{-1}, \tag{A.6}$$

where the relation $\boldsymbol{L}_v(\boldsymbol{R}_b,\boldsymbol{q}) = \frac{1}{m}\boldsymbol{S}_v\boldsymbol{L}(\boldsymbol{R}_b,\boldsymbol{q})$ in (2.44b) is applied. Then, by applying (4.21), the two the terms in (A.6) have the form

$$\boldsymbol{M}(\boldsymbol{q})^{-1}\boldsymbol{L}(\boldsymbol{R}_b,\boldsymbol{q})^T\frac{1}{m}\boldsymbol{S}_v^T = \begin{bmatrix}\boldsymbol{R}_b^T\frac{1}{m}\\ \boldsymbol{0}\\ \boldsymbol{0}\end{bmatrix} \tag{A.7a}$$

$$\left(\frac{1}{m}\boldsymbol{S}_v\boldsymbol{L}(\boldsymbol{R}_b,\boldsymbol{q})\boldsymbol{M}(\boldsymbol{q})^{-1}\boldsymbol{L}(\boldsymbol{R}_b,\boldsymbol{q})^T\frac{1}{m}\boldsymbol{S}_v^T\right)^{-1} = m\boldsymbol{E}, \tag{A.7b}$$

where $\boldsymbol{S}_v = \begin{bmatrix}\boldsymbol{E} & \boldsymbol{0}\end{bmatrix}$ and the definitions (2.8) and (2.35) are used. Then, the null-space projector (4.43) results having the form

$$\boldsymbol{N}_c(\boldsymbol{q}) = \begin{bmatrix}\boldsymbol{0} & -\frac{1}{m}\boldsymbol{M}_{v\omega}(\boldsymbol{q}) & -\frac{1}{m}\boldsymbol{M}_{vq}(\boldsymbol{q})\\ \boldsymbol{0} & \boldsymbol{E} & \boldsymbol{0}\\ \boldsymbol{0} & \boldsymbol{0} & \boldsymbol{E}\end{bmatrix}. \tag{A.8}$$

By considering a partitioning $\boldsymbol{J}_j^{\oplus}(\boldsymbol{q}) = \begin{bmatrix}\boldsymbol{J}_{jv}^{\oplus}(\boldsymbol{q}) & \boldsymbol{J}_{j\omega}^{\oplus}(\boldsymbol{q}) & \boldsymbol{J}_{jq}^{\oplus}(\boldsymbol{q})\end{bmatrix}$, and by partitioning the Adjoint matrix in the mapping in (2.17) as $\boldsymbol{J}_j(\boldsymbol{q}) = \begin{bmatrix}\begin{bmatrix}\boldsymbol{R}_{jb}(\boldsymbol{q})\\ \boldsymbol{0}\end{bmatrix} & \begin{bmatrix}\boldsymbol{R}_{jb}(\boldsymbol{q})[\boldsymbol{o}_{jb}(\boldsymbol{q})]^{\wedge}\\ \boldsymbol{R}_{jb}(\boldsymbol{q})\end{bmatrix} & \boldsymbol{J}_{jq}(\boldsymbol{q})\end{bmatrix}$, the circumcentroidal mapping (4.42) results in

$$\boldsymbol{J}_{jv}^{\oplus}(\boldsymbol{q}) = \boldsymbol{0}, \tag{A.9a}$$

$$\boldsymbol{J}_{j\omega}^{\oplus}(\boldsymbol{q}) = \begin{bmatrix}[\boldsymbol{o}_{jc}(\boldsymbol{q})]^{\wedge}\boldsymbol{R}_{jb}(\boldsymbol{q})\\ \boldsymbol{R}_{jb}(\boldsymbol{q})\end{bmatrix} \tag{A.9b}$$

$$\boldsymbol{J}_{jq}^{\oplus}(\boldsymbol{q}) = \boldsymbol{J}_{jq}(\boldsymbol{q}) - \frac{1}{m}\begin{bmatrix}\boldsymbol{R}_{jb}(\boldsymbol{q})\\ \boldsymbol{0}\end{bmatrix}\boldsymbol{M}_{vq}(\boldsymbol{q}), \tag{A.9c}$$

and, in turn, (4.45) results in (4.46), as

$$\boldsymbol{\nu}_j^{\oplus} = \boldsymbol{J}_j^{\oplus}(\boldsymbol{q})\boldsymbol{\upsilon} = \begin{bmatrix}\boldsymbol{0} & \boldsymbol{J}_{j\omega}^{\oplus}(\boldsymbol{q}) & \boldsymbol{J}_{jq}^{\oplus}(\boldsymbol{q})\end{bmatrix}\begin{bmatrix}\boldsymbol{v}_b\\ \boldsymbol{\omega}_b\\ \dot{\boldsymbol{q}}\end{bmatrix} = \boldsymbol{J}_{j\omega}^{\oplus}(\boldsymbol{q})\boldsymbol{\omega}_b + \boldsymbol{J}_{jq}^{\oplus}(\boldsymbol{q})\dot{\boldsymbol{q}}. \tag{A.10}$$

APPENDIX B

Error coordinates

Herein, the expressions of the error coordinates used throughout the text, as well as the associated Jacobians, are specified. Given a desired CoM position $\boldsymbol{o}_{c_d}$, the CoM position and velocity errors are denoted by $\tilde{\boldsymbol{x}}_c \in \mathbb{R}^3$ and $\tilde{\boldsymbol{v}}_c \in \mathbb{R}^3$, respectively, and are defined as

$$\tilde{\boldsymbol{x}}_c = \boldsymbol{o}_{c_d c}, \qquad \tilde{\boldsymbol{v}}_c = \boldsymbol{v}_{c_d c}. \tag{B.1}$$

The time derivative of the CoM error is trivially

$$\dot{\tilde{\boldsymbol{x}}}_c = \tilde{\boldsymbol{v}}_c. \tag{B.2}$$

For parameterizing rotation errors, a quaternion-based coordinates representation is adopted herein. Considering a general rotation matrix $\boldsymbol{R}_{xy}$, let the symbols $\boldsymbol{\epsilon}_{xy} \in \mathbb{R}^3$ and $\eta_{xy} \in \mathbb{R}$ denote the vector and scalar part, respectively, of the unit quaternion extracted from $\boldsymbol{R}_{xy}$. Let us consider a desired frame $\mathcal{B}_d$ for the base, which is located on the origin of $\mathcal{B}$ but has axes that are aligned towards desired directions; a base rotation error and a base angular velocity error are denoted by $\tilde{\boldsymbol{x}}_{b,rot} \in \mathbb{R}^3$ and $\tilde{\boldsymbol{\omega}}_b \in \mathbb{R}^3$, respectively, and are defined as

$$\tilde{\boldsymbol{x}}_{b,rot} = 2\boldsymbol{\epsilon}_{b_d b}, \qquad \tilde{\boldsymbol{\omega}}_b = \boldsymbol{\omega}_{b_d b}. \tag{B.3}$$

The time derivative $\dot{\tilde{\boldsymbol{x}}}_{b,rot}$ is related to $\tilde{\boldsymbol{\omega}}_b$ by the coordinates Jacobian $\boldsymbol{J}_{\tilde{x}_{b,rot}}(\tilde{\boldsymbol{x}}_{b,rot}) \in \mathbb{R}^{3\times 3}$, as

$$\dot{\tilde{\boldsymbol{x}}}_{b,rot} = \boldsymbol{J}_{\tilde{x}_{b,rot}}(\tilde{\boldsymbol{x}}_{b,rot})\tilde{\boldsymbol{\omega}}_b, \qquad \boldsymbol{J}_{\tilde{x}_{b,rot}}(\tilde{\boldsymbol{x}}_{b,rot}) = \eta_{b_d b}\boldsymbol{E} + [\boldsymbol{\epsilon}_{b_d b}]^\wedge. \tag{B.4}$$

Given desired frames $\mathcal{B}_d$ and $\mathcal{E}_d$ for the base and the end-effector, respectively, roto-translation errors and velocity errors are denoted by $\tilde{\boldsymbol{x}}_b \in \mathbb{R}^6$ and $\tilde{\boldsymbol{\nu}}_b \in \mathbb{R}^6$ for the base, and $\tilde{\boldsymbol{x}}_e \in \mathbb{R}^6$ and $\tilde{\boldsymbol{\nu}}_e \in \mathbb{R}^6$ for the end-effector. They are defined as

$$\tilde{\boldsymbol{x}}_b = \begin{bmatrix} \boldsymbol{o}_{b_d b} \\ 2\boldsymbol{\epsilon}_{b_d b} \end{bmatrix}, \qquad \tilde{\boldsymbol{\nu}}_b = \boldsymbol{\nu}_{b_d b}, \tag{B.5a}$$

$$\tilde{\boldsymbol{x}}_e = \begin{bmatrix} \boldsymbol{o}_{e_d e} \\ 2\boldsymbol{\epsilon}_{e_d e} \end{bmatrix}, \qquad \tilde{\boldsymbol{\nu}}_e = \boldsymbol{\nu}_{e_d e}, \tag{B.5b}$$

The time derivative $\dot{\tilde{\boldsymbol{x}}}_b$ and $\dot{\tilde{\boldsymbol{x}}}_e$ are related to the error velocities by coordinates Jacobians $\boldsymbol{J}_{\tilde{x}_b}(\tilde{\boldsymbol{x}}_b) \in \mathbb{R}^{6\times 6}$ and $\boldsymbol{J}_{\tilde{x}_e}(\tilde{\boldsymbol{x}}_e) \in \mathbb{R}^{6\times 6}$, respectively, as

$$\dot{\tilde{\boldsymbol{x}}}_b = \boldsymbol{J}_{\tilde{x}_b}(\tilde{\boldsymbol{x}}_b)\tilde{\boldsymbol{\nu}}_b, \qquad \boldsymbol{J}_{\tilde{x}_b}(\tilde{\boldsymbol{x}}_b) = \begin{bmatrix} \boldsymbol{E} & \boldsymbol{0} \\ \boldsymbol{0} & \eta_{b_d b}\boldsymbol{E} + [\boldsymbol{\epsilon}_{b_d b}]^\wedge \end{bmatrix}, \tag{B.6a}$$

$$\dot{\tilde{\boldsymbol{x}}}_e = \boldsymbol{J}_{\tilde{x}_e}(\tilde{\boldsymbol{x}}_e)\tilde{\boldsymbol{\nu}}_e, \qquad \boldsymbol{J}_{\tilde{x}_e}(\tilde{\boldsymbol{x}}_e) = \begin{bmatrix} \boldsymbol{E} & \boldsymbol{0} \\ \boldsymbol{0} & \eta_{e_d e}\boldsymbol{E} + [\boldsymbol{\epsilon}_{e_d e}]^\wedge \end{bmatrix}. \tag{B.6b}$$

An advantage of the adopted quaternion representation is that coordinates Jacobians cannot grow unbounded, and that in contact the quaternion renders a task-consistent compliant interaction. [Nat03, p.13].

APPENDIX C

Additional equations for definition of controllers

C.1. Addendum to Section 3.1.1

To construct a null space which satisfies the condition (3.5), the following map is chosen [Ott08, PCY99]

$$\boldsymbol{J}_n(\boldsymbol{q}_m) = \left(\boldsymbol{Z}(\boldsymbol{q}_m)\boldsymbol{M}(\boldsymbol{q}_m)\boldsymbol{Z}(\boldsymbol{q}_m)^T\right)^{-1}\boldsymbol{Z}(\boldsymbol{q}_m)\boldsymbol{M}(\boldsymbol{q}_m), \tag{C.1}$$

where $\boldsymbol{Z}(\boldsymbol{q}_m) \in \mathbb{R}^{r\times(6+n_m)}$ is a so-called base matrix [CW93] which spans the null space of $\begin{bmatrix}\boldsymbol{L}(\boldsymbol{R}_b,\boldsymbol{q})\\ \boldsymbol{J}_e(\boldsymbol{q}_m)\end{bmatrix}$, i.e., it satisfies the property

$$\begin{bmatrix}\boldsymbol{L}(\boldsymbol{R}_b,\boldsymbol{q})\\ \boldsymbol{J}_e(\boldsymbol{q}_m)\end{bmatrix}\boldsymbol{Z}(\boldsymbol{q}_m)^T = \boldsymbol{0}. \tag{C.2}$$

Given (C.2), it is straightforwardly seen that the choice (C.1) satisfies the condition (3.5). Note that, by partitioning the null-space base matrix as $\boldsymbol{Z}(\boldsymbol{q}_m) = \begin{bmatrix}\boldsymbol{Z}_b(\boldsymbol{q}_m) & \boldsymbol{Z}_m(\boldsymbol{q}_m)\end{bmatrix}$, where $\boldsymbol{Z}_b(\boldsymbol{q}_m) \in \mathbb{R}^{r\times 6}$ and $\boldsymbol{Z}_m(\boldsymbol{q}_m) \in \mathbb{R}^{r\times n_m}$, the property (C.2) results in the condition

$$\boldsymbol{J}^*_{em}(\boldsymbol{q}_m)\boldsymbol{Z}_m(\boldsymbol{q}_m)^T = \boldsymbol{0}, \tag{C.3}$$

which says that $\boldsymbol{Z}_m$ is the null-space base matrix of the generalized Jacobian[1]. Based on (C.3), given the partitioning $\boldsymbol{J}_n(\boldsymbol{q}_m) = \begin{bmatrix}\boldsymbol{J}_{nb}(\boldsymbol{q}_m) & \boldsymbol{J}_{nm}(\boldsymbol{q}_m)\end{bmatrix}$ of the null-space mapping in base and manipulator sub-blocks, they are given by

$$\boldsymbol{J}_{nb} = \boldsymbol{0}, \tag{C.4a}$$

$$\boldsymbol{J}_{nm}(\boldsymbol{q}_m) = \left(\boldsymbol{Z}_m(\boldsymbol{q}_m)\boldsymbol{M}^*_m(\boldsymbol{q}_m)\boldsymbol{Z}_m(\boldsymbol{q}_m)^T\right)^{-1}\boldsymbol{Z}_m(\boldsymbol{q}_m)\boldsymbol{M}^*_m(\boldsymbol{q}_m). \tag{C.4b}$$

Note $\boldsymbol{J}_{nm}(\boldsymbol{q}_m)$ results being the dynamically-consistent null-space mapping of the generalized Jacobian $\boldsymbol{J}^*_{em}(\boldsymbol{q}_m)$. Lastly, note that, by straightforward computation, the reduced mapping $\boldsymbol{J}^*_{nm}(\boldsymbol{q}_m)$ in (3.9b) coincides with $\boldsymbol{J}_{nm}(\boldsymbol{q}_m)$.

[1] Algorithms for constructing a null-space base matrix can be found in [Ott08, Sect.4.1].

C.2. Addendum to Section 3.2.1

In order to satisfy the condition (3.22), the following map is chosen

$$\boldsymbol{J}_n(\boldsymbol{q}_m) = \left(\boldsymbol{Z}(\boldsymbol{q}_m)\boldsymbol{M}(\boldsymbol{q}_m)\boldsymbol{Z}(\boldsymbol{q}_m)^T\right)^{-1}\boldsymbol{Z}(\boldsymbol{q}_m)\boldsymbol{M}(\boldsymbol{q}_m), \tag{C.5}$$

where $\boldsymbol{Z}(\boldsymbol{q}_m) \in \mathbb{R}^{r\times(6+n_m)}$ is a so-called base matrix which spans the null space of $\begin{bmatrix}\boldsymbol{J}_b \\ \boldsymbol{J}_e(\boldsymbol{q}_m)\end{bmatrix}$, i.e., it satisfies the property

$$\begin{bmatrix}\boldsymbol{J}_b \\ \boldsymbol{J}_e(\boldsymbol{q}_m)\end{bmatrix}\boldsymbol{Z}(\boldsymbol{q}_m)^T = \boldsymbol{0}. \tag{C.6}$$

Given (C.6), it is easily seen that the choice (C.5) satisfies the condition (3.22). By partitioning $\boldsymbol{Z}(\boldsymbol{q}_m) = \begin{bmatrix}\boldsymbol{Z}_b(\boldsymbol{q}_m) & \boldsymbol{Z}_m(\boldsymbol{q}_m)\end{bmatrix}$ in base and manipulator components $\boldsymbol{Z}_b(\boldsymbol{q}_m) \in \mathbb{R}^{r\times 6}$ and $\boldsymbol{Z}_m(\boldsymbol{q}_m) \in \mathbb{R}^{r\times n_m}$, respectively, the condition (C.6) becomes

$$\boldsymbol{Z}_b(\boldsymbol{q}_m) = \boldsymbol{0}, \qquad \boldsymbol{J}_{em}(\boldsymbol{q}_m)\boldsymbol{Z}_m^T(\boldsymbol{q}_m) = \boldsymbol{0}, \tag{C.7a}$$

where the right equation in (C.7a) corresponds to the orthogonality condition of a fixed-base robot, and says that $\boldsymbol{Z}_m(\boldsymbol{q}_m)$ is the null-space base matrix of the fixed-base Jacobian $\boldsymbol{J}_{em}(\boldsymbol{q}_m)$.
The null-space mapping can be partitioned in base and manipulator components, as $\boldsymbol{J}_n(\boldsymbol{q}_m) = \begin{bmatrix}\boldsymbol{J}_{nb}(\boldsymbol{q}_m) & \boldsymbol{J}_{nm}(\boldsymbol{q}_m)\end{bmatrix}$, where $\boldsymbol{J}_{nb}(\boldsymbol{q}_m) \in \mathbb{R}^{r\times 6}$ and $\boldsymbol{J}_{nm}(\boldsymbol{q}_m) \in \mathbb{R}^{r\times n_m}$. By applying (C.7a) the components can be computed as

$$\boldsymbol{J}_{nb}(\boldsymbol{q}_m) = (\boldsymbol{Z}_m(\boldsymbol{q})\boldsymbol{M}_m(\boldsymbol{q})\boldsymbol{Z}_m(\boldsymbol{q})^T)^{-1}\boldsymbol{Z}_m\boldsymbol{M}_{bm}(\boldsymbol{q})^T, \tag{C.8a}$$

$$\boldsymbol{J}_{nm}(\boldsymbol{q}_m) = (\boldsymbol{Z}_m(\boldsymbol{q})\boldsymbol{M}_m(\boldsymbol{q})\boldsymbol{Z}_m^T(\boldsymbol{q}))^{-1}\boldsymbol{Z}_m(\boldsymbol{q})\boldsymbol{M}_m(\boldsymbol{q}). \tag{C.8b}$$

C.3. Addendum to Section 5.1.1

Considering that for internal velocities it holds Lemma 1, the internal mappings in (5.1) and (5.2) are partitioned in base and joint components, as

$$\boldsymbol{J}_e^{int}(\boldsymbol{q}_m) = \begin{bmatrix}\boldsymbol{0} & \boldsymbol{J}_{em}^{int}(\boldsymbol{q}_m)\end{bmatrix}, \tag{C.9}$$

$$\boldsymbol{J}_n^{int}(\boldsymbol{q}_m) = \begin{bmatrix}\boldsymbol{0} & \boldsymbol{J}_{nm}^{int}(\boldsymbol{q}_m)\end{bmatrix}, \tag{C.10}$$

where $\boldsymbol{J}_{nm}^{int}(\boldsymbol{q}_m) \in \mathbb{R}^{r\times n_m}$, and where (4.18) and (2.61b) are used to compute the joint part of the end-effector mapping. Note that $\boldsymbol{J}_{em}^{int}(\boldsymbol{q}_m) = \boldsymbol{J}_{em}^{*}(\boldsymbol{q}_m) \in \mathbb{R}^{6\times n_m}$, i.e., $\boldsymbol{J}_{em}^{int}(\boldsymbol{q}_m)$ is the generalized Jacobian (3.1). The joint part of the internal mapping in (5.4) is thus

$$\bar{\boldsymbol{J}}_q^{int}(\boldsymbol{q}_m) = \begin{bmatrix}\boldsymbol{J}_{em}^{int}(\boldsymbol{q}_m) \\ \boldsymbol{J}_{nm}^{int}(\boldsymbol{q}_m)\end{bmatrix}. \tag{C.11}$$

The mapping $\boldsymbol{J}_{nm}^{int}(\boldsymbol{q}_m)$ is constructed as follows. By applying (C.9) and (C.10), the condition (5.3) is simplified as

$$\boldsymbol{J}_{em}^{int}(\boldsymbol{q}_m)\boldsymbol{M}_m^{*}(\boldsymbol{q}_m)^{-1}\boldsymbol{J}_{nm}^{int}(\boldsymbol{q}_m)^T = \boldsymbol{0}, \tag{C.12}$$

with $\boldsymbol{M}_m^{*}(\boldsymbol{q}_m)$ being the reduced manipulator inertia in (3.12). The following map is chosen

$$\boldsymbol{J}_{nm}^{int}(\boldsymbol{q}_m) = \left(\boldsymbol{Z}_m(\boldsymbol{q}_m)\boldsymbol{M}_m^{*}(\boldsymbol{q}_m)\boldsymbol{Z}_m(\boldsymbol{q}_m)^T\right)^{-1}\boldsymbol{Z}_m(\boldsymbol{q}_m)\boldsymbol{M}_m^{*}(\boldsymbol{q}_m), \tag{C.13}$$

where $\boldsymbol{Z}_m(\boldsymbol{q}_m) \in \mathbb{R}^{r\times n_m}$ is a base matrix which spans the null space of $\boldsymbol{J}_{em}^{int}(\boldsymbol{q}_m)$, i.e., it satisfies the property

$$\boldsymbol{J}_{em}^{int}(\boldsymbol{q}_m)\boldsymbol{Z}_m(\boldsymbol{q}_m)^T = \boldsymbol{0}. \tag{C.14}$$

Given (C.14), it is easily seen that the choice (C.13) satisfies (C.12).

C.4. Addendum to Section 5.2.1

Considering that for circumcentroidal velocities it holds Lemma 2, the circumcentroidal mappings in (5.18)-(5.21) are partitioned in translation, rotation, and manipulator components, as

$$\boldsymbol{J}_e^{\oplus}(\boldsymbol{q}_m) = \begin{bmatrix}\boldsymbol{0} & \boldsymbol{J}_{e\omega}^{\oplus}(\boldsymbol{q}_m) & \boldsymbol{J}_{em}^{\oplus}(\boldsymbol{q}_m)\end{bmatrix} \in \mathbb{R}^{6\times(6+n_m)}, \tag{C.15}$$

$$\boldsymbol{J}_b^{\oplus}(\boldsymbol{q}_m) = \begin{bmatrix}\boldsymbol{0} & \boldsymbol{J}_{b\omega}^{\oplus}(\boldsymbol{q}_m) & \boldsymbol{J}_{bm}^{\oplus}(\boldsymbol{q}_m)\end{bmatrix} \in \mathbb{R}^{6\times(6+n_m)}, \tag{C.16}$$

$$\boldsymbol{J}_{\omega_b}^{\oplus} = \begin{bmatrix}\boldsymbol{0} & \boldsymbol{E} & \boldsymbol{0}\end{bmatrix} \in \mathbb{R}^{3\times(6+n_m)}. \tag{C.17}$$

$$\boldsymbol{J}_n^{\oplus}(\boldsymbol{q}_m) = \begin{bmatrix}\boldsymbol{0} & \boldsymbol{J}_{n\omega}^{\oplus}(\boldsymbol{q}_m) & \boldsymbol{J}_{nm}^{\oplus}(\boldsymbol{q}_m)\end{bmatrix} \in \mathbb{R}^{r\times(6+n_m)}, \tag{C.18}$$

where[2] $\boldsymbol{J}_{\omega_b}^{\oplus} = \begin{bmatrix}\boldsymbol{0} & \boldsymbol{E}\end{bmatrix}\boldsymbol{J}_b^{\oplus}(\boldsymbol{q}_m)$, where the Jacobian for a robot without reaction wheels in (2.61b) is used for the computation of the circumcentroidal Jacobians, and where $\boldsymbol{J}_{n\omega}^{\oplus}(\boldsymbol{q}_m) \in \mathbb{R}^{r\times 3}$ and $\boldsymbol{J}_{nm}^{\oplus}(\boldsymbol{q}_m) \in \mathbb{R}^{r\times n_m}$. The expressions of the sub-blocks

$$\boldsymbol{J}_{e\omega}^{\oplus}(\boldsymbol{q}_m)=\begin{bmatrix}[\boldsymbol{o}_{ec}(\boldsymbol{q}_m)]^{\wedge}\boldsymbol{R}_{eb}(\boldsymbol{q}_m)\\ \boldsymbol{R}_{eb}(\boldsymbol{q}_m)\end{bmatrix}\in\mathbb{R}^{6\times 3},\ \boldsymbol{J}_{em}^{\oplus}(\boldsymbol{q}_m)=\boldsymbol{J}_{em}(\boldsymbol{q}_m)-\begin{bmatrix}\frac{1}{m}\boldsymbol{R}_{eb}(\boldsymbol{q}_m)\boldsymbol{M}_{vm}(\boldsymbol{q}_m)\\ \boldsymbol{0}\end{bmatrix}\in\mathbb{R}^{6\times n_m}. \tag{C.19}$$

$$\boldsymbol{J}_{b\omega}^{\oplus}(\boldsymbol{q}_m) = \begin{bmatrix}[\boldsymbol{o}_{bc}(\boldsymbol{q}_m)]^{\wedge}\\ \boldsymbol{E}\end{bmatrix} \in \mathbb{R}^{6\times 3}, \quad \boldsymbol{J}_{bm}^{\oplus}(\boldsymbol{q}_m) = -\begin{bmatrix}\frac{1}{m}\boldsymbol{M}_{vm}(\boldsymbol{q}_m)\\ \boldsymbol{0}\end{bmatrix} \in \mathbb{R}^{6\times n_m}. \tag{C.20}$$

In order to construct the null space so that it satisfies the condition (5.22), the following map is chosen

$$\boldsymbol{J}_n^{\oplus}(\boldsymbol{q}_m) = \left(\boldsymbol{Z}(\boldsymbol{q}_m)\boldsymbol{M}(\boldsymbol{q}_m)\boldsymbol{Z}(\boldsymbol{q}_m)^T\right)^{-1}\boldsymbol{Z}(\boldsymbol{q}_m)\boldsymbol{M}(\boldsymbol{q}_m), \tag{C.21a}$$

where $\boldsymbol{Z}(\boldsymbol{q}_m) \in \mathbb{R}^{r\times(n_m+6)}$ is a base matrix for the null space of $\begin{bmatrix}\boldsymbol{J}_{\omega_b}^{\oplus}\\ \boldsymbol{J}_e^{\oplus}(\boldsymbol{q}_m)\end{bmatrix}$, i.e., it satisfies the property

$$\begin{bmatrix}\boldsymbol{J}_{\omega_b}^{\oplus}\\ \boldsymbol{J}_e^{\oplus}(\boldsymbol{q}_m)\end{bmatrix}\boldsymbol{Z}(\boldsymbol{q}_m)^T = \boldsymbol{0}. \tag{C.22}$$

Given (C.22), it is straightforwardly seen that the choice (C.21) satisfies the condition (5.22). Once computed $\boldsymbol{J}_n^{\oplus}(\boldsymbol{q}_m)$ via (C.22), the sub-blocks $\boldsymbol{J}_{n\omega}^{\oplus}(\boldsymbol{q}_m)$ and $\boldsymbol{J}_{nm}^{\oplus}(\boldsymbol{q}_m)$ are readily obtained.
Lastly, given (C.15), (C.17), and (C.18), the circumcentroidal mapping in (5.23) can be partitioned as

$$\bar{\boldsymbol{J}}^{\oplus}(\boldsymbol{q}_m) = \begin{bmatrix}\boldsymbol{0} & \boldsymbol{E} & \boldsymbol{0}\\ \boldsymbol{0} & \boldsymbol{J}_{e\omega}^{\oplus}(\boldsymbol{q}_m) & \boldsymbol{J}_{em}^{\oplus}(\boldsymbol{q}_m)\\ \boldsymbol{0} & \boldsymbol{J}_{n\omega}^{\oplus}(\boldsymbol{q}_m) & \boldsymbol{J}_{nm}^{\oplus}(\boldsymbol{q}_m)\end{bmatrix}, \tag{C.23}$$

[2]The mapping (C.17) means that $\boldsymbol{\omega}_b^{\oplus} = \boldsymbol{\omega}_b$. This interesting detail was already highlighted in Section 4.3.1, and shall come as no surprise. However, note that despite this equivalence the overall transformation adopted herein (see (5.23)) is different than a common free-flyer transformation because it is $\boldsymbol{\nu}_e^{\oplus} \neq \boldsymbol{\nu}_e$.

and, in turn, the relevant columns for use in (4.54), are

$$\bar{\boldsymbol{J}}_{\omega}^{\oplus}(\boldsymbol{q}_m) = \begin{bmatrix} \boldsymbol{E} \\ \boldsymbol{J}_{e\omega}^{\oplus}(\boldsymbol{q}_m) \\ \boldsymbol{J}_{n\omega}^{\oplus}(\boldsymbol{q}_m) \end{bmatrix}, \qquad \bar{\boldsymbol{J}}_{q}^{\oplus}(\boldsymbol{q}_m) = \begin{bmatrix} \boldsymbol{0} \\ \boldsymbol{J}_{em}^{\oplus}(\boldsymbol{q}_m) \\ \boldsymbol{J}_{nm}^{\oplus}(\boldsymbol{q}_m) \end{bmatrix}. \tag{C.24}$$

C.5. Addendum to Section 6.1.1

In the following, definitions of the some symbols used in Section 6.1.1 are provided. The dynamically-consistent projector $\boldsymbol{N}_e^{int}(\boldsymbol{q}_m)$ used in (6.4) is given by

$$\boldsymbol{N}_e^{int}(\boldsymbol{q}_m) = \boldsymbol{E} - \boldsymbol{J}_e^{int}(\boldsymbol{q}_m)^{\#}\boldsymbol{J}_e^{int}(\boldsymbol{q}_m) \in \mathbb{R}^{(n_w+n_m)\times(n_w+n_m)} \tag{C.25}$$

where $\boldsymbol{J}_e^{int}(\boldsymbol{q}_m)^{\#}$ is the dynamically-consistent pseudo-inverse [Kha87] of $\boldsymbol{J}_e^{int}(\boldsymbol{q}_m)$, and is defined as

$$\boldsymbol{J}_e^{int}(\boldsymbol{q}_m)^{\#} = \boldsymbol{M}(\boldsymbol{q}_m)^{-1}\boldsymbol{J}_e^{int}(\boldsymbol{q}_m)^T \left(\boldsymbol{J}_e^{int}(\boldsymbol{q}_m)\boldsymbol{M}(\boldsymbol{q}_m)^{-1}\boldsymbol{J}_e^{int}(\boldsymbol{q}_m)^T\right)^{-1}. \tag{C.26}$$

Considering that for internal velocities it holds Lemma 1, the internal mappings (6.1), (6.2), and (6.3) are partitioned in base and joint components, as

$$\boldsymbol{J}_e^{int}(\boldsymbol{q}_m) = \begin{bmatrix} \boldsymbol{0} & \boldsymbol{J}_{eq}^{int}(\boldsymbol{q}_m) \end{bmatrix}, \tag{C.27}$$
$$\boldsymbol{J}_b^{int}(\boldsymbol{q}_m) = \begin{bmatrix} \boldsymbol{0} & \boldsymbol{J}_{bq}^{int}(\boldsymbol{q}_m) \end{bmatrix}, \tag{C.28}$$
$$\boldsymbol{J}_{\omega_b}^{int}(\boldsymbol{q}_m) = \begin{bmatrix} \boldsymbol{0} & \boldsymbol{J}_{\omega_b q}^{int}(\boldsymbol{q}_m) \end{bmatrix}, \tag{C.29}$$
$$\boldsymbol{J}_{\breve{\omega}_b}^{int}(\boldsymbol{q}_m) = \begin{bmatrix} \boldsymbol{0} & \boldsymbol{J}_{\breve{\omega}_b q}^{int}(\boldsymbol{q}_m) \end{bmatrix}, \tag{C.30}$$
$$\boldsymbol{J}_n^{int}(\boldsymbol{q}_m) = \begin{bmatrix} \boldsymbol{0} & \boldsymbol{J}_{nq}^{int}(\boldsymbol{q}_m) \end{bmatrix}, \tag{C.31}$$

where, by applying the general expression (4.17) for the end-effector and base frames, the Jacobians are given by

$$\boldsymbol{J}_{eq}^{int}(\boldsymbol{q}_m) = \boldsymbol{J}_e(\boldsymbol{q}_m) - \boldsymbol{A}_{eb}(\boldsymbol{q}_m)\boldsymbol{M}_b(\boldsymbol{q}_m)^{-1}\boldsymbol{M}_{bq} \in \mathbb{R}^{6\times(n_w+n_m)}, \tag{C.32}$$
$$\boldsymbol{J}_{bq}^{int}(\boldsymbol{q}_m) = -\boldsymbol{M}_b(\boldsymbol{q}_m)^{-1}\boldsymbol{M}_{bq} \in \mathbb{R}^{6\times(n_w+n_m)}, \tag{C.33}$$
$$\boldsymbol{J}_{\omega_b q}^{int}(\boldsymbol{q}_m) = \boldsymbol{S}_{\omega}\boldsymbol{J}_{bq}^{int}(\boldsymbol{q}_m) \in \mathbb{R}^{3\times(n_w+n_m)}, \tag{C.34}$$

and where $\boldsymbol{J}_{\breve{\omega}_b q}^{int}(\boldsymbol{q}_m) \in \mathbb{R}^{3\times(n_w+n_m)}$. The joint part of the internal mapping in (5.4) is given by by considering that joint part of the internal mapping in (6.7) is

$$\bar{\boldsymbol{J}}_q^{int}(\boldsymbol{q}_m) = \begin{bmatrix} \boldsymbol{J}_{\breve{\omega}_b w}^{int}(\boldsymbol{q}_m) & \boldsymbol{J}_{\breve{\omega}_b m}^{int}(\boldsymbol{q}_m) \\ \boldsymbol{J}_{ew}^{int}(\boldsymbol{q}_m) & \boldsymbol{J}_{em}^{int}(\boldsymbol{q}_m) \\ \boldsymbol{J}_{nw}^{int}(\boldsymbol{q}_m) & \boldsymbol{J}_{nm}^{int}(\boldsymbol{q}_m) \end{bmatrix}. \tag{C.35}$$

The null-space mapping $\boldsymbol{J}_{nq}^{int}(\boldsymbol{q}_m) \in \mathbb{R}^{r\times(n_w+n_m)}$ is constructed as follows. By using (C.27), (C.30), and (C.31), the condition (6.6) of dynamic consistency reduces to

$$\begin{bmatrix} \boldsymbol{J}_{\breve{\omega}_b q}^{int}(\boldsymbol{q}_m) \\ \boldsymbol{J}_{eq}^{int}(\boldsymbol{q}_m) \end{bmatrix} \boldsymbol{M}_q^*(\boldsymbol{q}_m)^{-1}\boldsymbol{J}_{nq}^{int}(\boldsymbol{q}_m)^T = \boldsymbol{0}, \tag{C.36}$$

where $\boldsymbol{M}_q^*(\boldsymbol{q}_m)$ is the reduced joint inertia defined in (2.2.3). The following map is chosen

$$\boldsymbol{J}_{nq}^{int}(\boldsymbol{q}_m) = \left(\boldsymbol{Z}_q(\boldsymbol{q}_m)\boldsymbol{M}_q^*(\boldsymbol{q}_m)\boldsymbol{Z}_q(\boldsymbol{q}_m)^T\right)^{-1}\boldsymbol{Z}_q(\boldsymbol{q}_m)\boldsymbol{M}_q^*(\boldsymbol{q}_m), \tag{C.37}$$

and where $\boldsymbol{Z}_q(\boldsymbol{q}_m) \in \mathbb{R}^{r\times(n_w+n_m)}$ is a null-space base matrix that satisfies the property

$$\begin{bmatrix}\boldsymbol{J}^{int}_{\breve{\omega}_b q}(\boldsymbol{q}_m)\\ \boldsymbol{J}^{int}_{eq}(\boldsymbol{q}_m)\end{bmatrix}\boldsymbol{Z}_q(\boldsymbol{q}_m)^T = \boldsymbol{0}. \tag{C.38}$$

Given the definitions (C.31) and (C.38), and considering the expression of the inverse inertia in (2.49), it is straightforwardly seen that the choice (C.37) satisfies the condition (6.6).
The Jacobians used in the actuation mapping (6.9), are the sub-matrices of the following partitionings in reaction wheels and arm components:

$$\boldsymbol{J}^{int}_{\breve{\omega}_b}(\boldsymbol{q}_m) = \begin{bmatrix}\boldsymbol{J}^{int}_{\breve{\omega}_b w}(\boldsymbol{q}_m) & \boldsymbol{J}^{int}_{\breve{\omega}_b m}(\boldsymbol{q}_m)\end{bmatrix}, \tag{C.39}$$

$$\boldsymbol{J}^{int}_{e}(\boldsymbol{q}_m) = \begin{bmatrix}\boldsymbol{J}^{int}_{ew}(\boldsymbol{q}_m) & \boldsymbol{J}^{int}_{em}(\boldsymbol{q}_m)\end{bmatrix}, \tag{C.40}$$

$$\boldsymbol{J}^{int}_{nq}(\boldsymbol{q}_m) = \begin{bmatrix}\boldsymbol{J}^{int}_{nw}(\boldsymbol{q}_m) & \boldsymbol{J}^{int}_{nm}(\boldsymbol{q}_m)\end{bmatrix}. \tag{C.41}$$

Note that $\boldsymbol{J}^{int}_{em}(\boldsymbol{q}_m) = \boldsymbol{J}^{*}_{em}(\boldsymbol{q}_m)$, i.e., $\boldsymbol{J}^{int}_{em}(\boldsymbol{q}_m)$ is the generalized Jacobian (3.1). Finally, the expressions of the inertias sub-blocks in (6.10) are

$$\boldsymbol{M}^{int}_{\breve{\omega}_b}(\boldsymbol{q}_m) = \left(\boldsymbol{J}^{int}_{\breve{\omega}_b q}(\boldsymbol{q}_m)\boldsymbol{M}^{*}_{q}(\boldsymbol{q}_m)^{-1}\boldsymbol{J}^{int}_{\breve{\omega}_b q}(\boldsymbol{q}_m)^T\right)^{-1} \in \mathbb{R}^{3\times3}, \tag{C.42}$$

$$\boldsymbol{M}^{int}_{e}(\boldsymbol{q}_m) = \left(\boldsymbol{J}^{int}_{eq}(\boldsymbol{q}_m)\boldsymbol{M}^{*}_{q}(\boldsymbol{q}_m)^{-1}\boldsymbol{J}^{int}_{eq}(\boldsymbol{q}_m)^T\right)^{-1} \in \mathbb{R}^{6\times6}, \tag{C.43}$$

$$\boldsymbol{M}^{int}_{n}(\boldsymbol{q}_m) = \boldsymbol{Z}_q(\boldsymbol{q}_m)\boldsymbol{M}^{*}_{q}(\boldsymbol{q}_m)\boldsymbol{Z}_q(\boldsymbol{q}_m)^T \in \mathbb{R}^{r\times r}. \tag{C.44}$$

APPENDIX D

Lemma used in the analysis in Section 6.1.3

The proof of the equation (6.15b) is shown herein. For the sake of brevity, the functional dependence of the matrices is omitted.

Lemma 3. *Given the dynamically-consistent mapping* (6.4)*, it holds* $\boldsymbol{J}_{\omega_b q}^{int}\boldsymbol{J}_{\breve{\omega}_b q}^{int\,\#} = \boldsymbol{E}$.

Proof. By using (6.4) and (C.26), $\boldsymbol{J}_{\breve{\omega}_b}^{int\#}$ can be written as

$$\boldsymbol{J}_{\breve{\omega}_b}^{int\#} = \boldsymbol{M}^{-1}\boldsymbol{N}_e^{int^T}\boldsymbol{J}_{\omega_b}^{int^T}\left(\boldsymbol{J}_{\omega_b}^{int}\boldsymbol{N}_e^{int}\boldsymbol{M}^{-1}\boldsymbol{N}_e^{int^T}\boldsymbol{J}_{\omega_b}^{int^T}\right)^{-1}. \tag{D.1}$$

Then, in order to be $\boldsymbol{J}_{\omega_b}^{int}\boldsymbol{J}_{\breve{\omega}_b}^{int\#} = \boldsymbol{E}$, it must be

$$\boldsymbol{J}_{\omega_b}^{int}\boldsymbol{M}^{-1}\boldsymbol{N}_e^{int^T}\boldsymbol{J}_{\omega_b}^{int^T}\left(\boldsymbol{J}_{\omega_b}^{int}\boldsymbol{N}_e^{int}\boldsymbol{M}^{-1}\boldsymbol{N}_e^{int^T}\boldsymbol{J}_{\omega_b}^{int^T}\right)^{-1} = \boldsymbol{E}, \tag{D.2}$$

where (D.1) was used. By right-multiplying (D.2) times $\left(\boldsymbol{J}_{\omega_b}^{int}\boldsymbol{N}_e^{int}\boldsymbol{M}^{-1}\boldsymbol{N}_e^{int^T}\boldsymbol{J}_{\omega_b}^{int^T}\right)$, it is obtained:

$$\boldsymbol{J}_{\omega_b}^{int}\boldsymbol{M}^{-1}\boldsymbol{N}_e^{int^T}\boldsymbol{J}_{\omega_b}^{int^T} = \boldsymbol{J}_{\omega_b}^{int}\boldsymbol{N}_e^{int}\boldsymbol{M}^{-1}\boldsymbol{N}_e^{int^T}\boldsymbol{J}_{\omega_b}^{int^T}. \tag{D.3}$$

Inserting (C.25) into (D.3), it is

$$\boldsymbol{J}_{\omega_b}^{int}\boldsymbol{M}^{-1}\boldsymbol{N}_e^{int^T}\boldsymbol{J}_{\omega_b}^{int^T} = \boldsymbol{J}_{\omega_b}^{int}\left(\boldsymbol{E} - \boldsymbol{J}_e^{int\#}\boldsymbol{J}_e^{int}\right)\boldsymbol{M}^{-1}\boldsymbol{N}_e^{int^T}\boldsymbol{J}_{\omega_b}^{int^T}, \tag{D.4}$$

$$\boldsymbol{0} = -\boldsymbol{J}_{\omega_b}^{int}\boldsymbol{J}_e^{int\#}\boldsymbol{J}_e^{int}\boldsymbol{M}^{-1}\boldsymbol{N}_e^{int^T}\boldsymbol{J}_{\omega_b}^{int^T}. \tag{D.5}$$

Now, given the property $\boldsymbol{J}_e^{int}\boldsymbol{M}^{-1}\boldsymbol{N}_e^{int^T} = \boldsymbol{0}$ of the dynamically-consistent projector $\boldsymbol{N}_e^{int}$, it is seen that (D.5) is always satisfied, proving that $\boldsymbol{J}_{\omega_b}^{int}\boldsymbol{J}_{\breve{\omega}_b}^{int\#} = \boldsymbol{E}$. Now, by using (6.4) and (2.49), it can be shown that

$$\boldsymbol{J}_{\breve{\omega}_b}^{int\#} = \begin{bmatrix} -\boldsymbol{M}_b^{-1}\boldsymbol{M}_{bq} \\ \boldsymbol{E} \end{bmatrix}\boldsymbol{J}_{\breve{\omega}_b q}^{int\,\#} \tag{D.6}$$

where

$$\boldsymbol{J}_{\breve{\omega}_b q}^{int\,\#} = \boldsymbol{M}_q^{*-1}\boldsymbol{J}_{\breve{\omega}_b q}^{int\,T}\left(\boldsymbol{J}_{\breve{\omega}_b q}^{int}\boldsymbol{M}_q^{*-1}\boldsymbol{J}_{\breve{\omega}_b q}^{int\,T}\right)^{-1}. \tag{D.7}$$

In turn, it results

$$\boldsymbol{J}_{\omega_b}^{int}\boldsymbol{J}_{\breve{\omega}_b}^{int\#} = \begin{bmatrix}\boldsymbol{0} & \boldsymbol{J}_{\omega_b q}^{int}\end{bmatrix}\begin{bmatrix}-\boldsymbol{M}_b^{-1}\boldsymbol{M}_{bq} \\ \boldsymbol{E}\end{bmatrix}\boldsymbol{J}_{\breve{\omega}_b q}^{int\#} = \boldsymbol{J}_{\omega_b q}^{int}\boldsymbol{J}_{\breve{\omega}_b q}^{int\#} = \boldsymbol{E}, \tag{D.8}$$

thereby proving the Lemma. □

By using the relations (6.3) and (C.29), it is

$$\boldsymbol{\omega}_b^{int} = \boldsymbol{J}_{\omega_b q}^{int}\dot{\boldsymbol{q}}. \tag{D.9}$$

By using the relations (6.1), (C.27), (6.4), and (C.30), it can be written

$$\begin{bmatrix}\breve{\boldsymbol{\omega}}_b^{int} \\ \boldsymbol{\nu}_e^{int}\end{bmatrix} = \begin{bmatrix}\boldsymbol{J}_{\breve{\omega}_b q}^{int} \\ \boldsymbol{J}_{eq}^{int}\end{bmatrix}\dot{\boldsymbol{q}}, \tag{D.10}$$

whose inverse is [DOP18]

$$\dot{\boldsymbol{q}} = \boldsymbol{J}_{eq}^{int\#}\boldsymbol{\nu}_e^{int} + \boldsymbol{J}_{\breve{\omega}_b q}^{int\#}\breve{\boldsymbol{\omega}}_b^{int}. \tag{D.11}$$

Then, by inserting (D.11) into (D.9), and inserting the resulting expression into the angular part of the external-internal motion decomposition (4.19) for the base, it is possible to write

$$\boldsymbol{\omega}_b = \breve{\boldsymbol{\omega}}_b^{int} + \boldsymbol{J}_{\omega_b q}^{int}\boldsymbol{J}_{eq}^{int\#}\boldsymbol{\nu}_e^{int} + \boldsymbol{S}_\omega\boldsymbol{A}_{bc}\boldsymbol{M}_c^{-1}\boldsymbol{h}_c, \tag{D.12}$$

wherein Lemma 3 is applied.

APPENDIX E

Proof of consecutive transformation of small adjoint

The aim of this section is to prove (2.14). Let us preliminary state formulas which are used herein [MLS94],[LLM17, p.10]:

$$\boldsymbol{R}\left[\boldsymbol{a}\right]^{\wedge}\boldsymbol{R}^{T}=\left[\boldsymbol{R}\boldsymbol{a}\right]^{\wedge}, \tag{E.1a}$$

$$\left[\boldsymbol{a}+\boldsymbol{b}\right]^{\wedge}=\left[\boldsymbol{a}\right]^{\wedge}+\left[\boldsymbol{b}\right]^{\wedge}, \tag{E.1b}$$

$$\left[\left[\boldsymbol{a}\right]^{\wedge}\boldsymbol{b}\right]^{\wedge}=\left[\boldsymbol{a}\right]^{\wedge}\left[\boldsymbol{b}\right]^{\wedge}-\left[\boldsymbol{b}\right]^{\wedge}\left[\boldsymbol{a}\right]^{\wedge}, \tag{E.1c}$$

for any $\boldsymbol{a},\boldsymbol{b}\in\mathbb{R}^{3}$ and $\boldsymbol{R}^{3\times3}$. Let us express the formula (2.11) for consecutive transformation of relative velocities in translation and rotation components, as

$$\boldsymbol{v}_{xz}=\boldsymbol{R}_{yz}^{T}\boldsymbol{v}_{xy}-\boldsymbol{R}_{yz}^{T}\left[\boldsymbol{o}_{yz}\right]^{\wedge}\boldsymbol{\omega}_{xy}+\boldsymbol{v}_{yz} \tag{E.2}$$

$$\boldsymbol{\omega}_{xz}=\boldsymbol{R}_{yz}^{T}\boldsymbol{\omega}_{xy}+\boldsymbol{\omega}_{yz}, \tag{E.3}$$

where (2.8), (2.9), and (E.1a) are used. Then, the l. h. s. of (2.14) is expressed as

$$\boldsymbol{a}_{xz}=\begin{bmatrix}\left[\boldsymbol{\omega}_{xz}\right]^{\wedge} & \left[\boldsymbol{v}_{xz}\right]^{\wedge}\\ \boldsymbol{0} & \left[\boldsymbol{\omega}_{xz}\right]^{\wedge}\end{bmatrix}=\begin{bmatrix}\left[\boldsymbol{R}_{yz}^{T}\boldsymbol{\omega}_{xy}+\boldsymbol{\omega}_{yz}\right]^{\wedge} & \left[\boldsymbol{R}_{yz}^{T}\boldsymbol{v}_{xy}-\boldsymbol{R}_{yz}^{T}\left[\boldsymbol{o}_{yz}\right]^{\wedge}\boldsymbol{\omega}_{xy}+\boldsymbol{v}_{yz}\right]^{\wedge}\\ \boldsymbol{0} & \left[\boldsymbol{R}_{yz}^{T}\boldsymbol{\omega}_{xy}+\boldsymbol{\omega}_{yz}\right]^{\wedge}\end{bmatrix} \tag{E.4}$$

The first term of the r. h. s. of (2.14) is computed as

$$\boldsymbol{A}_{zy}\boldsymbol{a}_{xy}\boldsymbol{A}_{zy}^{-1}=\begin{bmatrix}\boldsymbol{R}_{yz}^{T} & -\boldsymbol{R}_{yz}^{T}\left[\boldsymbol{o}_{yz}\right]^{\wedge}\\ \boldsymbol{0} & \boldsymbol{R}_{yz}^{T}\end{bmatrix}\begin{bmatrix}\left[\boldsymbol{\omega}_{xy}\right]^{\wedge} & \left[\boldsymbol{v}_{xy}\right]^{\wedge}\\ \boldsymbol{0} & \left[\boldsymbol{\omega}_{xy}\right]^{\wedge}\end{bmatrix}\begin{bmatrix}\boldsymbol{R}_{yz} & \left[\boldsymbol{o}_{yz}\right]^{\wedge}\boldsymbol{R}_{yz}\\ \boldsymbol{0} & \boldsymbol{R}_{yz}\end{bmatrix} \tag{E.5}$$

$$=\begin{bmatrix}\left[\boldsymbol{R}_{yz}^{T}\boldsymbol{\omega}_{xy}\right]^{\wedge} & \left[\boldsymbol{R}_{yz}^{T}\boldsymbol{\omega}_{xy}\right]^{\wedge}\left[\boldsymbol{R}_{yz}^{T}\boldsymbol{o}_{xy}\right]^{\wedge}-\left[\boldsymbol{R}_{yz}^{T}\boldsymbol{o}_{xy}\right]^{\wedge}\left[\boldsymbol{R}_{yz}^{T}\boldsymbol{\omega}_{xy}\right]^{\wedge}+\left[\boldsymbol{R}_{yz}^{T}\boldsymbol{v}_{xy}\right]^{\wedge}\\ \boldsymbol{0} & \left[\boldsymbol{R}_{yz}^{T}\boldsymbol{\omega}_{xy}\right]^{\wedge}\end{bmatrix} \tag{E.6}$$

$$=\begin{bmatrix}\left[\boldsymbol{R}_{yz}^{T}\boldsymbol{\omega}_{xy}\right]^{\wedge} & -\left[\left[\boldsymbol{R}_{yz}^{T}\boldsymbol{o}_{xy}\right]^{\wedge}\boldsymbol{R}_{yz}^{T}\boldsymbol{\omega}_{xy}\right]^{\wedge}+\left[\boldsymbol{R}_{yz}^{T}\boldsymbol{v}_{xy}\right]^{\wedge}\\ \boldsymbol{0} & \left[\boldsymbol{R}_{yz}^{T}\boldsymbol{\omega}_{xy}\right]^{\wedge}\end{bmatrix}, \tag{E.7}$$

$$=\begin{bmatrix}\left[\boldsymbol{R}_{yz}^{T}\boldsymbol{\omega}_{xy}\right]^{\wedge} & \left[\boldsymbol{R}_{yz}^{T}\boldsymbol{v}_{xy}-\boldsymbol{R}_{yz}^{T}\left[\boldsymbol{o}_{xy}\right]^{\wedge}\boldsymbol{\omega}_{xy}\right]^{\wedge}\\ \boldsymbol{0} & \left[\boldsymbol{R}_{yz}^{T}\boldsymbol{\omega}_{xy}\right]^{\wedge}\end{bmatrix}, \tag{E.8}$$

where (E.1) are applied. The second term of the r. h. s. of (2.14) has the form

$$\boldsymbol{a}_{yz} = \begin{bmatrix} [\boldsymbol{\omega}_{yz}]^\wedge & [\boldsymbol{v}_{yz}]^\wedge \\ \mathbf{0} & [\boldsymbol{\omega}_{yz}]^\wedge \end{bmatrix}. \tag{E.9}$$

Then, the r. h. s. of (2.14) results in

$$\boldsymbol{A}_{zy}\boldsymbol{a}_{xy}\boldsymbol{A}_{zy}^{-1} + \boldsymbol{a}_{yz} = \begin{bmatrix} \left[\boldsymbol{R}_{yz}^T\boldsymbol{\omega}_{xy} + \boldsymbol{\omega}_{yz}\right]^\wedge & \left[\boldsymbol{R}_{yz}^T\boldsymbol{v}_{xy} - \boldsymbol{R}_{yz}^T\left[\boldsymbol{o}_{xy}\right]^\wedge\boldsymbol{\omega}_{xy} + \boldsymbol{v}_{yz}\right]^\wedge \\ \mathbf{0} & \left[\boldsymbol{R}_{yz}^T\boldsymbol{\omega}_{xy} + \boldsymbol{\omega}_{yz}\right]^\wedge \end{bmatrix}, \tag{E.10}$$

which is equivalent to (E.4), thereby proving (2.14).

Bibliography

[ADSR+15] J. Artigas, M. De Stefano, W. Rackl, R. Lampariello, B. Brunner, W. Bertleff, R. Burger, O. Porges, A. Giordano, C. Borst, and A. Albu-Schäffer. The OOS-SIM: An on-ground simulation facility for on-orbit servicing robotic operations. In *2015 IEEE International Conference on Robotics and Automation (ICRA)*, May 2015. (Cited on pages 21 and 111)

[Agh09a] F. Aghili. Coordination control of a free-flying manipulator and its base attitude to capture and detumble a noncooperative satellite. In *2009 IEEE/RSJ International Conference on Intelligent Robots and Systems*, pages 2365–2372, Oct 2009. (Cited on pages 17 and 18)

[Agh09b] F. Aghili. Optimal control of a space manipulator for detumbling of a target satellite. In *2009 IEEE International Conference on Robotics and Automation*, pages 3019–3024, May 2009. (Cited on pages 17 and 18)

[Agh12] F. Aghili. A prediction and motion-planning scheme for visually guided robotic capturing of free-floating tumbling objects with uncertain dynamics. *IEEE Transactions on Robotics*, 28(3):634–649, June 2012. (Cited on page 101)

[Agh13] F. Aghili. Pre- and post-grasping robot motion planning to capture and stabilize a tumbling/drifting free-floater with uncertain dynamics. In *2013 IEEE International Conference on Robotics and Automation*, pages 5461–5468, May 2013. (Cited on page 101)

[AJ87] H. Alexander and Cannon Jr. Experiments on the control of a satellite manipulator. *Proceedings of the TEEE American Control Conference*, 1987. (Cited on page 17)

[ALH06] S. Abiko, R. Lampariello, and G. Hirzinger. Impedance control for a free-floating robot in the grasping of a tumbling target with parameter uncertainty. In *Intelligent Robots and Systems, 2006 IEEE/RSJ International Conference on*, pages 1020–1025, Oct 2006. (Cited on page 18)

[AOFH03] A. Albu-Schaffer, C. Ott, U. Frese, and G. Hirzinger. Cartesian impedance control of redundant robots: recent results with the dlr-light-weight-arms.

In *2003 IEEE International Conference on Robotics and Automation (Cat. No.03CH37422)*, volume 3, pages 3704–3709 vol.3, Sep. 2003. (Cited on page 92)

[ASOH07a] Alin Albu-Schäffer, Christian Ott, and Gerd Hirzinger. A unified passivity-based control framework for position, torque and impedance control of flexible joint robots. *The International Journal of Robotics Research*, 26(1):23–39, 2007. (Cited on page 32)

[ASOH07b] Alin Albu-Schäffer, Christian Ott, and Gerd Hirzinger. A unified passivity-based control framework for position, torque and impedance control of flexible joint robots. *The International Journal of Robotics Research*, 26(1):23–39, 2007. (Cited on page 28)

[AVT19] Andrea Antonello, Alfredo Valverde, and Panagiotis Tsiotras. Dynamics and control of spacecraft manipulators with thrusters and momentum exchange devices. *Journal of Guidance, Control, and Dynamics*, 42(1):15–29, 2019. (Cited on page 17)

[BCTW79] Edward V. Bergmann, S.R. Croopnick, J.J. Turkovich, and C.C. Work. An advanced spacecraft autopilot concept. *Journal of Guidance and Control*, 2(3):161–168, 1979. (Cited on page 99)

[BZM92] Franco Bernelli-Zazzera and Paolo Mantegazza. Pulse-width equivalent to pulse-amplitude discrete control of linearsystems. *Journal of Guidance, Control, and Dynamics*, 15(2):461–467, 1992. (Cited on pages 99 and 103)

[CBS+18] P. Colmenarejo, J. Branco, N. Santos, P. Serra, J. Telaar, H. Strauch, A. M. Giordano, M. De Stefano, C. Ott, M. Rainer, D. Henry, J. Jaworski, E. Papadopoulos, G. Visentin, F. Ankersen, and J. Gil-Fernandez. Methods and outcomes of the comrade project - design of robust combined control for robotic spacecraft and manipulator in servicing missions. In *69th International Astronautical Congress*, Sept 2018. (Cited on pages 23, 24, and 97)

[CGA20] D. Calzolari, A. M. Giordano, and A. Albu-Schäffer. Error bounds for pd-controlled mechanical systems under bounded disturbances using interval arithmetic. *IEEE Robotics and Automation Letters*, 5(2):1231–1238, April 2020. (Cited on page 22)

[CGM19a] F. Cavenago, A. M. Giordano, and M. Massari. An approach to contact detection and isolation for free-floating robots based on momentum monitoring. In *2019 IEEE Aerospace Conference*, March 2019. (Cited on page 23)

[CGM19b] F. Cavenago, A. M. Giordano, and M. Massari. Contact force observer for space robots. In *2019 IEEE 58th Conference on Decision and Control (CDC)*, pages 2528–2535, Dec 2019. (Cited on pages 22 and 101)

[CHC+19] J. Cieslak, D. Henry, P. Colmenarejo, N. Santos, J. Branco, P. Serra, J. Telaar, H. Strauch, A.M. Giordano, M. De Stefano, C. Ott, M. J. Reiner, J. Jaworski, E. Papadopoulos, G. Visentin, F. Ankersen, and J. Gil. Assessment of a supervisory fault-hiding scheme in a classical guidance, navigation

and control setup: the e.deorbit mission. In *2019 4th International Conference on Control and Fault-Tolerant Systems (SYSTOL)*, 2019. (Cited on page 22)

[CLG20] D. Calzolari, R. Lampariello, and A. M. Giordano. Singularity maps of space robots and their application to gradient-based trajectory planning. In *Robotics: Science and Systems*, 2020. (Cited on page 22)

[Cra] B. Crawford. Configuration design and efficient operation of redundant multi-jet systems. In *AIAA Guidance, Control, and Flight Mechanics Conference*. (Cited on page 99)

[CS01] Fabrizio Caccavale and Bruno Siciliano. Kinematic control of redundant free-floating robotic systems. *Advanced Robotics*, 15(4):429–448, 2001. (Cited on page 18)

[CW93] C.L.P. Chen and I.D. Walker. A consistent null-space based approach to inverse kinematics of redundant robots. In *IEEE International Conference on Robotics and Automation*, pages 374–381 vol.3, May 1993. (Cited on page 143)

[Dan63] George B. Dantzig. *Linear programming and extensions*. Rand Corporation Research Study. Princeton Univ. Press, 1963. (Cited on page 99)

[DBG+18] M. De Stefano, R. Balachandran, A. M. Giordano, C. Ott, and C. Secchi. An energy-based approach for the multi-rate control of a manipulator on an actuated base. In *2018 IEEE International Conference on Robotics and Automation (ICRA)*, pages 1072–1077, May 2018. (Cited on page 23)

[DOP18] A. Dietrich, C. Ott, and J. Park. The hierarchical operational space formulation: Stability analysis for the regulation case. *IEEE Robotics and Automation Letters*, 3(2):1120–1127, April 2018. (Cited on page 150)

[DP93] S. Dubowsky and E. Papadopoulos. The kinematics, dynamics, and control of free-flying and free-floating space robotic systems. *IEEE Transactions on Robotics and Automation*, Oct 1993. (Cited on page 15)

[DSAG+15] M. De Stefano, J. Artigas, A. Giordano, R. Lampariello, and A. Albu-Schaeffer. On- ground experimental verification of a torque controlled free-floating robot. In *13th Symposium on Advanced Space Technologies in Robotics and Automation 2015 (ASTRA)*, May 2015. (Cited on page 23)

[DSRB+20] M. De Stefano, M. A. Roa, R. Balachandran, A. M. Giordano, H. Mishra, N. Oumer, B. Brunner, M. Lingenauber, M. Stelzer, and R. Lampariello. Design and validation of orbital robotic missions. In Xiu Yan and G. Visentin, editors, *Space Robotics (in press)*. Springer, 2020. (Cited on page 22)

[DT90] S. Dubowsky and M. Torres. Minimizing attitude control fuel in space manipulator systems. In *Proceedings of the International Symposium on AI, Robotics and Automation (i-SAIRAS)*, pages 259–262, 1990. (Cited on page 17)

[DT91] S. Dubowsky and M. A. Torres. Path planning for space manipulators to minimize spacecraft attitude disturbances. In *Proceedings of 1991 IEEE International Conference on Robotics and Automation*, pages 2522–2528 vol.3, Apr 1991. (Cited on page 17)

[DY04a] D. N. Dimitrov and K. Yoshida. Momentum distribution in a space manipulator for facilitating the post-impact control. In *2004 IEEE/RSJ International Conference on Intelligent Robots and Systems (IROS)*, volume 4, pages 3345–3350 vol.4, Sep. 2004. (Cited on page 18)

[DY04b] D. N. Dimitrov and K. Yoshida. Utilization of the bias momentum approach for capturing a tumbling satellite. In *2004 IEEE/RSJ International Conference on Intelligent Robots and Systems (IROS)*, volume 4, pages 3333–3338 vol.4, Sep. 2004. (Cited on page 18)

[ES93] Olav Egeland and Jan Richard Sagli. Coordination of motion in a spacecraft/ manipulator system. *The International Journal of Robotics Research*, 12(4):366–379, 1993. (Cited on page 17)

[FGP14] Pal Johan From, Jan T Gravdahl, and Kristin Y Pettersen. *Vehicle-manipulator systems*. Springer, 2014. (Cited on page 37)

[GCAS18] A. M. Giordano, D. Calzolari, and A. Albu-Schäffer. Workspace fixation for free-floating space robot operations. In *2018 IEEE International Conference on Robotics and Automation (ICRA)*, May 2018. (Cited on pages 21 and 68)

[GDOA20] A. M. Giordano, A. Dietrich, C. Ott, and A. Albu-Schäffer. Coordination of thrusters, reaction wheels, and arm in orbital robots. *Journal of Robotics and Autonomous Systems*, 2020. (Cited on pages 21, 58, and 82)

[GGAS17] A. M. Giordano, G. Garofalo, and A. Albu-Schäffer. Momentum dumping for space robots. In *2017 IEEE 56th Annual Conference on Decision and Control (CDC)*, pages 5243–5248, Dec 2017. (Cited on pages 21, 58, and 68)

[GGDS+16] A. M. Giordano, G. Garofalo, M De Stefano, C. Ott, and A. Albu-Schäffer. Dynamics and control of a free-floating space robot in presence of nonzero linear and angular momenta. In *Proceedings of the 55th IEEE Conference on Decision and Control*, Dec 2016. (Cited on pages 18, 21, 45, and 48)

[GHEO15] Gianluca Garofalo, Bernd Henze, Johannes Englsberger, and Christian Ott. On the inertially decoupled structure of the floating base robot dynamics. 48(1):322 – 327, 2015. 8th Vienna International Conferenceon Mathematical Modelling MATHMOD 2015. (Cited on pages 47, 58, and 60)

[GMGL19] A.P. Gallardo, H. Mishra, A. M. Giordano, and R. Lampariello. Robust estimation of motion states for free-floating tumbling target capture. In *2019 IEEE Aerospace Conference*, March 2019. (Cited on pages 23 and 101)

[GML+20] A. M. Giordano, H. Mishra, R. Lampariello, C. Ott, and A. Albu-Schäffer. Trajectory-tracking control of a space robot relative to a noninertial target. In *IEEE 59th Annual Conference on Decision and Control (CDC) (submitted)*, 2020. (Cited on page 28)

[GO17] G. Garofalo and C. Ott. Energy based limit cycle control of elastically actuated robots. *IEEE Transactions on Automatic Control*, 62(5):2490–2497, May 2017. (Cited on page 86)

[GOA13] G. Garofalo, C. Ott, and A. Albu-Schäffer. On the closed form computation of the dynamic matrices and their differentiations. In *2013 IEEE/RSJ International Conference on Intelligent Robots and Systems*, pages 2364–2359, Nov 2013. (Cited on pages 31, 32, 33, and 44)

[GOA19] A. M. Giordano, C. Ott, and A. Albu-Schäffer. Coordinated control of spacecraft's attitude and end-effector for space robots. *IEEE Robotics and Automation Letters*, 4(2):2108–2115, April 2019. (Cited on pages 21, 62, and 72)

[GPS16] Oscar Biblarz George P. Sutton. *Rocket Propulsion Elements*. Wiley, 9 edition, 2016. (Cited on page 100)

[HCZ+19] D. Henry, J. Cieslak, J. Zenteno Torres, P. Colmenarejo, J. Branco, N. Santos, P. Serra, J. Telaar, H. Strauch, A.M. Giordano, M. De Stefano, C. Ott, M. J. Reiner, J. Jaworski, E. Papadopoulos, G. Visentin, F. Ankersen, and J. Gil. Model-based fault diagnosis and tolerant control: the esa's e.deorbit mission. In *2019 European Control Conference (ECC)*, June 2019. (Cited on page 22)

[IOK99] Tohru Ieko, Yoshimasa Ochi, and Kimio Kanai. New design method for pulse-width modulation control systems via digital redesign. *Journal of Guidance, Control, and Dynamics*, 22(1):123–128, 1999. (Cited on pages 99 and 103)

[JLR+18] S. Jaekel, R. Lampariello, W. Rackl, M. De Stefano, N. Oumer, A. M. Giordano, O. Porges, M. Pietras, B. Brunner, J. Ratti, Q. Muehlbauer, M. Thiel, S. Estable, R. Biesbroek, and A. Albu-Schaeffer. Design and operational elements of the robotic subsystem for the e.deorbit debris removal mission. *Frontiers in Robotics and AI*, 5:100, 2018. (Cited on pages 22 and 23)

[Kha87] O. Khatib. A unified approach for motion and force control of robot manipulators: The operational space formulation. *IEEE Journal of Robotics and Automation*, 3(1):43–53, February 1987. (Cited on pages 20, 41, 46, 58, 63, and 146)

[Kro05] Trond Dagfinn Krovel. Optimal tuning of pwpf modulator for attitude control. Master's thesis, Norwegian University of Science and Technology, 2005. (Cited on page 103)

[LADH08] L. Le Tien, A. Albu-Schaffer, A. De Luca, and G. Hirzinger. Friction observer and compensation for control of robots with joint torque measurement. In *2008 IEEE/RSJ International Conference on Intelligent Robots and Systems*, pages 3789–3795, Sep. 2008. (Cited on page 32)

[LLM17] T. Lee, M. Leok, and N.H. McClamroch. *Global Formulations of Lagrangian and Hamiltonian Dynamics on Manifolds: A Geometric Approach to Modeling and Analysis*. Interaction of Mechanics and Mathematics. Springer International Publishing, 2017. (Cited on page 151)

[LLZ87] Richard W. Longman, Robert E. Lindbergt, and Michael F. Zedd. Satellite-mounted robot manipulators — new kinematics and reaction moment compensation. *The International Journal of Robotics Research*, 6(3):87–103, 1987. (Cited on page 18)

[LMO+18] R. Lampariello, H. Mishra, N. Oumer, P. Schmidt, M. De Stefano, and A. Albu-Schäffer. Tracking control for the grasping of a tumbling satellite with a free-floating robot. *IEEE Robotics and Automation Letters*, 3(4):3638–3645, Oct 2018. (Cited on page 18)

[MDGO19] H. Mishra, M. De Stefano, A. M. Giordano, and C. Ott. A nonlinear observer for free-floating target motion using only pose measurements. In *2019 Annual American Control Conference (ACC)*, June 2019. (Cited on page 22)

[MDGO20] H. Mishra, M. De Stefano, A. M. Giordano, and C. Ott. A geometric controller for fully-actuated robotic capture of a tumbling target. In *2020 Annual American Control Conference (ACC)*, June 2020. (Cited on page 22)

[MDSGO18] H. Mishra, M. De Stefano, A. M. Giordano, and Christian Ott. Tracking control with robotic systems for a moving target: A vector lyapunov function approach. volume 51, pages 471 – 478, 2018. 12th IFAC Symposium on Robot Control SYROCO 2018. (Cited on page 23)

[MGDS+20] H. Mishra, A.M. Giordano, M. De Stefano, R. Lampariello, and C. Ott. Inertially-decoupled equations for hardware-in-the-loop simulation of an orbital robot with external forces. In *2020 IEEE/RSJ International Conference on Intelligent Robots and Systems (IROS)*, 2020. (Cited on page 22)

[MLS94] Richard M. Murray, Zexiang Li, and S. Shankar Sastry. *A Mathematical Introduction to Robotic Manipulation*. CRC Press, Inc., Boca Raton, FL, USA, 1st edition, 1994. (Cited on pages 28, 30, 44, and 151)

[MMA89a] Y. Masutani, F. Miyazaki, and S. Arimoto. Modeling and sensory feedback control for space manipulators. In *Proceedings on the NASA Conference on Telerobotics*, Jan 1989. (Cited on pages 45, 48, and 59)

[MMA89b] Y. Masutani, F. Miyazaki, and S. Arimoto. Sensory feedback control for space manipulators. In *IEEE International Conference on Robotics and Automation*, pages 1346–1351 vol.3, May 1989. (Cited on pages 18, 20, 45, 47, 48, and 53)

[Mor16] Jorge Moreira. Modeling and Control of a Flexible Space Robot for the Capture and Berthing in the ESA e.deorbit Mission. Master's thesis, Technical University of Munich (TUM), 2016. (Cited on page 28)

[MP97] S. A. A. Moosavian and E. Papadopoulos. Control of space free-flyers using the modified transpose jacobian algorithm. In *Proceedings of the 1997 IEEE/RSJ International Conference on Intelligent Robot and Systems. Innovative Robotics for Real-World Applications. IROS '97*, volume 3, pages 1500–1505 vol.3, Sep. 1997. (Cited on page 17)

[MS01] F. Matsuno and K. Saito. Attitude control of a space robot with initial angular momentum. In *2001 IEEE International Conference on Robotics and Automation*, volume 2, pages 1400–1405 vol.2, 2001. (Cited on page 45)

[Nat03] Ciro Natale. *Interaction control of robot manipulators: six degrees-of-freedom tasks*, volume 3. Springer, Heidelberg, 2003. (Cited on page 142)

[NM93] Y. Nakamura and R. Mukherjee. Exploiting nonholonomic redundancy of free-flying space robots. *IEEE Transactions on Robotics and Automation*, 9(4):499–506, Aug 1993. (Cited on page 18)

[NP11] Kostas Nanos and Evangelos Papadopoulos. On the use of free-floating space robots in the presence of angular momentum. *Intelligent Service Robotics*, 4(1):3–15, 2011. (Cited on pages 45 and 49)

[NUY92] D. Nenchev, Y. Umetani, and Kazuya Yoshida. Analysis of a redundant free-flying spacecraft/manipulator system. *IEEE Transactions on Robotics and Automation*, 8(1):1–6, Feb 1992. (Cited on pages 18 and 133)

[NY06a] H. Nakanishi and K. Yoshida. Impedance control for free-flying space robots -basic equations and applications-. In *2006 IEEE/RSJ International Conference on Intelligent Robots and Systems*, Oct 2006. (Cited on pages 17 and 18)

[NY06b] Hiroki Nakanishi and Kazuya Yoshida. Impedance control of free-flying space robot for orbital servicing. *Journal of Robotics and Mechatronics*, 18(5):608–617, 2006. (Cited on page 17)

[NYU91] Dragomir Nenchev, Kazuya Yoshida, and Y Umetani. Analysis, design and control of free-flying space robots using fixed-attitude-restricted jacobian matrix. pages 251–258, 01 1991. (Cited on page 18)

[Oda96] M. Oda. Coordinated control of spacecraft attitude and its manipulator. In *Proceedings of IEEE International Conference on Robotics and Automation*, volume 1, pages 732–738 vol.1, April 1996. (Cited on page 17)

[Oda97] Mitsushige Oda. Motion control of the satellite mounted robot arm which assures satellite attitude stability. *Acta Astronautica*, 41(11):739 – 750, 1997. (Cited on page 17)

[ODAS15] Christian Ott, Alexander Dietrich, and Alin Albu-Schäffer. Prioritized multi-task compliance control of redundant manipulators. *Automatica*, 53:416 – 423, 2015. (Cited on page 87)

[OGL13] David E. Orin, Ambarish Goswami, and Sung-Hee Lee. Centroidal dynamics of a humanoid robot. *Autonomous Robots*, 35(2):161–176, 2013. (Cited on page 35)

[OKY96] M. Oda, K. Kibe, and F. Yamagata. Ets-vii, space robot in-orbit experiment satellite. In *Proceedings of IEEE International Conference on Robotics and Automation*, volume 1, pages 739–744 vol.1, April 1996. (Cited on page 23)

[ONY07] T. Oki, H. Nakanishi, and K. Yoshida. Whole-body motion control for capturing a tumbling target by a free-floating space robot. In *2007 IEEE/RSJ International Conference on Intelligent Robots and Systems*, pages 2256–2261, Oct 2007. (Cited on pages 18 and 133)

[ONY08] T. Oki, H. Nakanishi, and K. Yoshida. Time-optimal manipulator control of a free-floating space robot with constraint on reaction torque. In *2008 IEEE/RSJ International Conference on Intelligent Robots and Systems*, pages 2828–2833, Sep. 2008. (Cited on page 18)

[ONY10] Tomohisa Oki, Hiroki Nakanishi, and Kazuya Yoshida. Time-optimal manipulator control for management of angular momentum distribution during the capture of a tumbling target. *Advanced Robotics*, 24(3):441–466, 2010. (Cited on page 18)

[Ott08] Christian Ott. *Cartesian impedance control of redundant and flexible-joint robots*. Springer, 2008. (Cited on pages 29, 41, 51, 116, 126, 129, and 143)

[PCY99] J. Park, W. Chung, and Y. Youm. On dynamical decoupling of kinematically redundant manipulators. In *Intelligent Robots and Systems, 1999. IROS '99. Proceedings. 1999 IEEE/RSJ International Conference on*, volume 3, pages 1495–1500 vol.3, 1999. (Cited on page 143)

[PD91a] E. Papadopoulos and S. Dubowsky. Coordinated manipulator/spacecraft motion control for space robotic systems. In *Proceedings of 1991 IEEE International Conference on Robotics and Automation*, pages 1696–1701 vol.2, April 1991. (Cited on pages 17, 20, 49, and 54)

[PD91b] E. Papadopoulos and S. Dubowsky. On the nature of control algorithms for free-floating space manipulators. *IEEE Transactions on Robotics and Automation*, 7(6):750–758, Dec 1991. (Cited on page 18)

[PM94] Evangelos Papadopoulos and S. Ali A. Moosavian. Dynamics and control of space free-flyers with multiple manipulators. *Advanced Robotics*, 9(6):603–624, 1994. (Cited on page 17)

[RA06] R. Rastegari and S. A. A. Moosavian. Multiple impedance control of space free-flying robots using virtual object grasp. In *2006 IEEE/RSJ International Conference on Intelligent Robots and Systems*, pages 3125–3130, Oct 2006. (Cited on page 17)

[RMNL11] P Rank, Q Mühlbauer, W Naumann, and K Landzettel. The deos automation and robotics payload. In *Symp. on Advanced Space Technologies in Robotics and Automation, ASTRA, the Netherlands*, 2011. (Cited on page 23)

[RS97] P.V. Kokotovic R. Sepulchre, M. Jankovic. *Constructive Nonlinear Control*. Springer, 1 edition, 1997. (Cited on page 86)

[SA90] J. R Spofford and D. L. Akin. Redundancy control of a free-flying telerobot. *Journal of Guidance, Control, and Dynamics*, 13(3):515–523, 1990. (Cited on page 17)

[SBS+10] Florian Sellmaier, Toralf Boge, Jörn Spurmann, Sylvain Gully, Thomas Rupp, and Felix Huber. On-orbit servicing missions: Challenges and solutions for spacecraft operations. In *American Institute of Aeronautics and Astronautics, Inc.. SpaceOps 2010 Conference, 25,Huntsville, Alabama, USA*, 2010. (Cited on page 23)

[Sid97] Marcel J Sidi. *Spacecraft dynamics and control: a practical engineering approach*, volume 7. Cambridge university press, 1997. (Cited on page 103)

[SK05] L. Sentis and O. Khatib. Control of free-floating humanoid robots through task prioritization. In *Proceedings of the 2005 IEEE International Conference on Robotics and Automation*, April 2005. (Cited on pages 18 and 41)

[SN16] Hiroki Sone and Dragomir Nenchev. Reactionless camera inspection with a free-flying space robot under reaction null-space motion control. *Acta Astronautica*, 128:707 – 721, 2016. (Cited on page 18)

[SSVO09] Bruno Siciliano, Lorenzo Sciavicco, Luigi Villani, and Giuseppe Oriolo. *Robotics: Modelling, Planning and Control*. Springer, 2009. (Cited on page 37)

[SWS96] Leang Shieh, Wei Wang, and John W. Sunkel. Design of pam and pwm controllers for sampled-data interval systems. *Journal of Dynamic Systems, Measurement, and Control*, 118(4):673–682, 1996. (Cited on pages 99 and 103)

[UY87] Yoji Umetani and Kazuya Yoshida. Continuous path control of space manipulators mounted on omv. *Acta Astronautica*, 15(12):981 – 986, 1987. (Cited on page 18)

[UY89] Y. Umetani and K. Yoshida. Resolved motion rate control of space manipulators with generalized jacobian matrix. *IEEE Transactions on Robotics and Automation*, 5(3):303–314, Jun 1989. (Cited on pages 15, 18, 45, and 59)

[UY01] Yoji Umetani and Kazuya Yoshida. Workspace and manipulability analysis of space manipulator. *Transactions of the Society of Instrument and Control Engineers*, E-1(1):1–8, 2001. (Cited on pages 120 and 122)

[VD87] Z. Vafa and S. Dubowsky. On the dynamics of manipulators in space using the virtual manipulator approach. In *Proceedings. 1987 IEEE International Conference on Robotics and Automation*, volume 4, pages 579–585, March 1987. (Cited on page 18)

[VD89] Z. Vafa and S. Dubowsky. The control of space manipulators subject to spacecraft attitude control saturation limits. In *Proceedings of the NASA Conference on Space Telerobotics*, volume 4, January 1989. (Cited on page 17)

[VD90] Z. Vafa and S. Dubowsky. The kinematics and dynamics of space manipulators: The virtual manipulator approach. *The International Journal of Robotics Research*, 9(4):3–21, 1990. (Cited on pages 18 and 75)

[WKCGR18] Markus Wilde, Stephen Kwok Choon, Alessio Grompone, and Marcello Romano. Equations of motion of free-floating spacecraft-manipulator systems: An engineer's tutorial. *Frontiers in Robotics and AI*, 5:41, 2018. (Cited on page 15)

[XS91] Y. Xu and H.Y. Shum. Dynamic control of a space robot with no thrust jets controlled base. *No. CMU-RI-TR-33. Pittsburgh: The Robotics Institutem Carnegie Mellon University*, 1991. (Cited on page 18)

[XSLK92] Y. Xu, H. Y. Shum, J. J. Lee, and T. Kanade. Adaptive control of space robot system with an attitude controlled base. In *Proceedings 1992 IEEE International Conference on Robotics and Automation*, pages 2005–2010 vol.3, May 1992. (Cited on pages 17 and 18)

[XWZY13] Shuanfeng Xu, Hanlei Wang, Duzhou Zhang, and Baohua Yang. Adaptive reactionless motion control for free-floating space manipulators with uncertain kinematics and dynamics. *IFAC Proceedings Volumes*, 46(20):646 – 653, 2013. 3rd IFAC Conference on Intelligent Control and Automation Science ICONS 2013. (Cited on page 18)

[YDN06] K. Yoshida, D. Dimitrov, and H. Nakanishi. On the capture of tumbling satellite by a space robot. In *2006 IEEE/RSJ International Conference on Intelligent Robots and Systems*, pages 4127–4132, Oct 2006. (Cited on pages 18 and 133)

[YNU+04] Kazuya Yoshida, Hiroki Nakanishi, Hiroshi Ueno, Noriyasu Inaba, Takeshi Nishimaki, and Mitsushige Oda. Dynamics, control and impedance matching for robotic capture of a non-cooperative satellite. *Advanced Robotics*, 18(2):175–198, 2004. (Cited on page 18)

[Yos94] K. Yoshida. Practical coordination control between satellite attitude and manipulator reaction dynamics based on computed momentum concept. In *Proceedings of 1999 IEEE/RSJ International Conference on Intelligent Robots and Systems*, volume 3, pages 1578–1585 vol.3, Sep 1994. (Cited on page 18)

[Yos03] Kazuya Yoshida. Engineering test satellite vii flight experiments for space robot dynamics and control: Theories on laboratory test beds ten years ago, now in orbit. *The International Journal of Robotics Research*, 22(5):321–335, 2003. (Cited on page 23)

[YSKU92] K. Yoshida, N. Sashida, R. Kurazume, and Y. Umetani. Modeling of collision dynamics for space free-floating links with extended generalized inertia tensor. In *IEEE International Conference on Robotics and Automation*, pages 899–904 vol.1, May 1992. (Cited on page 18)